Templating Novel Thermotropic Liquid Crystal Phases

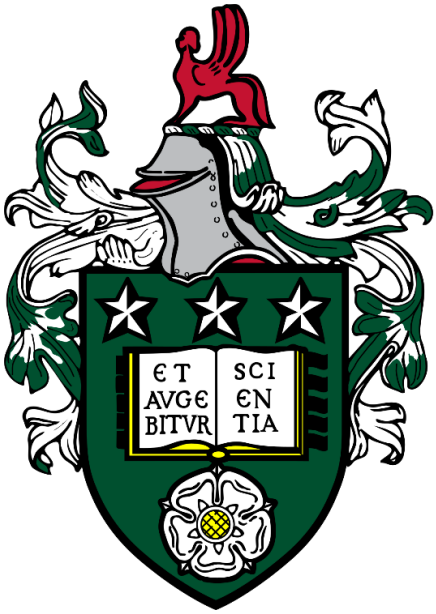

Nina Trbojević

School of Physics and Astronomy

University of Leeds

Submitted in accordance with the requirements for the degree of

Doctor of Philosophy

June 2020

The candidate confirms that the work submitted is her own, except where work which has formed part of jointly-authored publications has been included. The contribution of the candidate and the other authors to this work has been explicitly indicated below. The candidate confirms that appropriate credit has been given within the thesis where reference has been made to the work of others.

Two jointly-authored papers have been included in this thesis:

(1) Trbojevic, N., Read, D. J., & Nagaraj, M. (2017). Dielectric properties of liquid crystalline dimer mixtures exhibiting the nematic and twist-bend nematic phases. Physical Review E, 96(5), 052703.

(2) Trbojevic, N., Read, D. J., & Nagaraj, M. (2019). Metastable room-temperature twist-bend nematic phases via photopolymerization. Physical Review E, 99(6), 062704.

Chapter 3 contains work from paper (1) and Chapters 3 and 4 include work from paper (2). The experimental work was done by Nina Trbojević. Mamatha Nagaraj and Daniel Read contributed to developing the ideas for the work, helping to analyse results and making edits to the drafts of the papers.

Acknowledgements

Firstly, a special thank you goes out to my supervisors, Dr Mamatha Nagaraj and Professor Daniel Read, for taking me on to do research on such an interesting topic. Mamatha radiates sheer brilliance and has been a constant source of encouragement throughout my PhD. She is a role model for all her students, and I could not have wished for a better supervisor. Daniel is an exceptional academic who has been involved in this project from start to finish and has always provided extra support whenever Mamatha was away.

I am incredibly grateful to Professor John Blacker and Dr Bao Nguyen from the iPRD for giving me the opportunity to use their labs. A big thank you to the PhD students and postdocs in iPRD who welcomed me into the group and helped me get set up, especially Nisha, Mike and Rosie. To Stu and Nicole from LEMAS who helped with SEM experiments, and to Dr Verena Görtz for useful synthesis advice. To our Experimental Officer, Dr Dan Baker, for training me on equipment and the ever-entertaining rants. To Glenys, Paula, Amanda and Faith for all admin-related assistance. To members of the Physics workshop and stores for always providing a helping hand, especially Brian Chesworth, who, sadly, passed away last year.

Many thanks to all current and former members of the SMP group for making the time spent in and outside labs entertaining. Particularly Mariam, who is the sort of person one can always rely on and whose constant support I have been lucky enough to receive over the past four years, and Cliff, who is always up for a coffee (beer) break – it has been a pleasure to have him as a mentor and a friend. Thanks also go out to my fantastic office mates from the SMP and Theory groups: Adam, Zach, Matt and Dan, to members of Mamatha's group: Rowan, Bart and Jordan, and to Nikita, for general help during my project.

I would also like to send a special thank you to a number of people outside of the SMP group: my Godparents, Kuma Stana and Kum Đorđe, members of FG Ravna Gora and FG Oplenac, and my go-to ladies, Nataša, Brankica and Danijela, in particular, for their ceaseless encouragement and all the wonderful memories.

Lastly, the biggest thank you goes to my family: my parents, Lila and Mile, my brother, Aleksandar, my aunt and uncle, Auntie Ani and Tečo Jovan, my cousin, Marko, and my grandma, the one and only, Baba Mira ("The Godmother"). It is thanks to their unconditional support that I have reached this milestone, and so I dedicate this thesis to them, and to my three grandparents who are watching from above.

Где ја стадох — ти ћеш поћи!
Што не могох — ти ћеш моћи!
Куд ја нисам — ти ћеш доћи!
Што ја почех — ти продужи!
Још смо дужни — ти одужи!

–Светли гробови–
Јован Јовановић Змај

Where I stopped — you will go!
What I could not — you will do!
Where I did not — you will arrive!
What I began — you continue!
Whatever we owe — you pay back!

–Bright graves–
Jovan Jovanović Zmaj

Abstract

Templating is a bottom-up approach used in materials science, whereby intricate nanoscale features of a 'host' medium are transferred onto a 'guest' matrix through a series of chemical and physical mechanisms. The past few decades have seen a great deal of research on the topic of templating lyotropic liquid crystal phases, mainly for biomedical applications. More recently, thermotropic liquid crystal templating has also sparked research interests, particularly the cholesteric and blue phases, for their applications in tuneable photonic structures. With thermotropic liquid crystal templating being a relatively recent field of research, little is known about the nanoscopic interactions between host liquid crystals and guest polymers that result in the templating effect. This thesis aims to gain a better understanding of how templates are created through the process of surface modification of polymers and which properties of the host liquid crystal can be templated.

Two novel thermotropic mesophases were templated for the first time, namely the twist-bend nematic (N_{TB}) phase and the ferroelectric SmA ($SmAP_F$) phase. The host liquid crystal used to template the N_{TB} phase was a mixture of the dimer CB7CB with the calamitic liquid crystal 5CB. Refilling the N_{TB} template with a nematic mesogen allowed for a better understanding of the electrical and mechanical properties of the N_{TB} phase. A carbosilane-tethered bent-core mesogen exhibiting the $SmAP_F$ phase was synthesised by adapting procedures available in literature, and this mesogen was used for templating the $SmAP_F$ phase. Refilling the $SmAP_F$ template enabled an insight into which properties of the host mesophase can be templated, such as the layered structure, biaxiality and ferroelectric switching.

Samples composed of a monomer and host liquid crystal were thermodynamically-stabilised (photopolymerised) and metastable room temperature N_{TB} phases were formed using this process. All photopolymerised phases showed similar thermal and dielectric properties to the pure host liquid crystals. Residual birefringence was observed in the polymer networks of all polymerised phases when the liquid crystal was in the isotropic state.

Templates were created by washing the host liquid crystal from the polymer matrix. Raman spectroscopy was used for the first time to confirm that the templates were not contaminated with unwashed host liquid crystal. Visualisation of the templates using SEM revealed a clear difference between the template morphologies formed from different host liquid crystals, whereby the general mesoscopic structure of the host mesophase had been templated.

The thermal and dielectric properties of the refilled templates showed that order was being induced in the refilled liquid crystal. The distinction between physical properties of the refilled templates and pure 5CB was especially clear in measurements of permittivity and threshold electric fields. For N_{TB} templates, it was suggested that the nanofeatures of the N_{TB} phase had been templated.

The field of thermotropic liquid crystal templating is still in its infancy, yet it offers a great deal of potential in understanding the elegant interplay of chemical and physical processes in soft matter systems at the nanoscopic scale.

Table of Contents

List of Tables

List of Figures

Abbreviations

* – chiral

a.u. – arbitrary units

Ar – aromatic (ring)

$CDCl_3$ – deuterated chloroform

CH_2Cl_2 – dichloromethane

$CHCl_3$ – chloroform

CN – nitrile group

Cr – crystalline

d (NMR) – doublet

DCC – *N*,*N*′-dicyclohexylcarbodiimide

DMAP – 4-dimethylaminopyridine

DSC – differential scanning calorimetry

EDAC – 1-ethyl-3-(3-dimethylaminopropyl)carbodiimide

EDX – energy-dispersive X-ray spectroscopy

equiv. – equivalent(s)

EtOH – ethanol

h – hour(s)

H_2 – hydrogen

H_2O – water

I/Iso – isotropic

LC – liquid crystal

m (IR) – medium

m (NMR) – multiplet

MeCN – acetonitrile

Mg – magnesium

$MgSO_4$ – magnesium sulphate

min – minute(s)

n – director

N – nematic

N_2 – nitrogen

NaOH – sodium hydroxide

NMR – nuclear magnetic resonance

N_{TB} – twist-bend nematic phase

Pd/C – palladium on activated charcoal

POM – polarising optical microscopy

ppm – parts per million

RMS – root mean square

RT – room temperature

s (IR) – strong

s (NMR) – singlet

SAXS – small angle x-ray scattering

SEM – scanning electron microscopy

SmA – smectic A phase

$SmAP_A$ – polar smectic A phase exhibiting antiferroelectric switching

$SmAP_F$ – polar smectic A phase exhibiting ferroelectric switching

SmC – smectic C

t (NMR) – triplet

THF – tetrahydrofuran

TLC – thin layer chromatography

UV – ultraviolet

w (IR) – weak

w/w – weight by weight concentration

wt% – concentration by weight

δ (NMR)– chemical shift

Nomenclature

E – electric field

E_a – activation energy

f_R – relaxation frequency

P_s – spontaneous polarisation

$T_{I\text{-}SmA}$ – isotropic to SmA phase transition temperature

T_{NI} – nematic to isotropic phase transition temperature

$T_{N\text{-}N_{TB}}$ – nematic to twist-bend nematic phase transition temperature

V – voltage

V_{th} – threshold voltage

μ – dipole moment

ΔH – enthalpy

Δn – birefringence

ΔS – entropy

$\Delta\varepsilon$ – dielectric anisotropy

$\delta\varepsilon$ – dielectric strength

$\varepsilon'_{\parallel}$ – parallel component of the dielectric permittivity

$\varepsilon'_{\perp}$ – perpendicular component of the dielectric permittivity

$\varepsilon'_{average}$ – average permittivity

CHAPTER 1:
Introduction

This introductory chapter will first provide relevant information on liquid crystals, various liquid crystal phases and molecular architectures. The second part of the chapter will discuss fundamentals of reactive mesogens and photopolymerisation of liquid crystal phases followed by a literature review on liquid crystal templating. The motivation for doing the research can be found at the end of the chapter.

1.1 The liquid crystalline phase

We are familiar with materials existing as the three fundamental states: solids, liquids and gases (Figure 1.1). However, a fourth state of matter is also observed between the crystalline and liquid states, known as the liquid crystalline state. As the name suggests, liquid crystals elegantly combine ordering properties of crystalline structures, as well as fluid-like mobility, traditionally associated with isotropic liquids. Thermodynamic phase transitions separate the liquid crystal phase from the solid and liquid states.

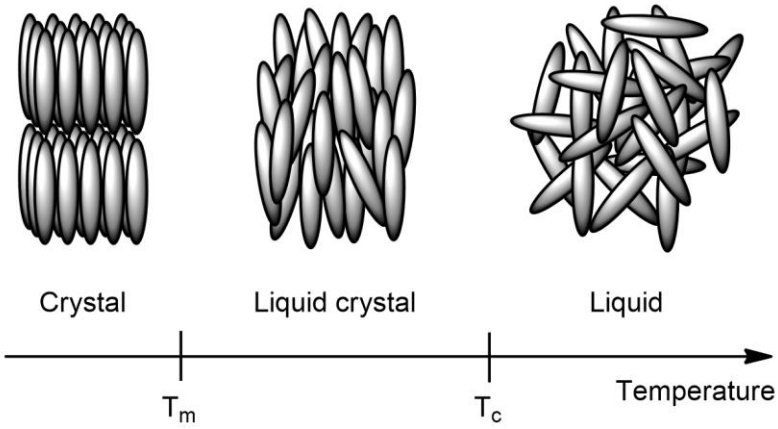

Figure 1.1: Temperature-dependent transitions from the crystalline state through to the isotropic liquid state. The temperature at which the crystal transitions to a liquid crystal phase is called the melting point (T_m) and the temperature at which the liquid crystal phase transitions to the isotropic liquid state is called the clearing point (T_c).

Liquid crystallinity is exhibited by several naturally occurring materials, including DNA, cell membranes and insects' shells.[1] Liquid crystallinity was first observed in

1888[2] by the Austrian Botanist Friedrich Reinitzer. Whilst examining the chemical and physical properties of cholesteryl benzoate, a derivative of cholesterol, Reinitzer observed that the compound had two melting points. Some years later, in 1904, the name 'liquid crystal' was coined by Otto Lehmann.[3] Liquid crystal phases are alternatively known as mesophases, derived from the Ancient Greek word *mésos*, meaning 'in between' or 'intermediate', and for this reason, the molecules that exhibit the liquid crystalline phases are also known as 'mesogens'. As mentioned previously, liquids are isotropic, meaning that the arrangement of molecules are equally disordered in all directions. Liquid crystals, however, exhibit anisotropic behaviour. This means that their physical properties – such as optical, electrical and magnetic behaviour – are dependent on the direction in which they are measured. Anisotropy in the shape of molecules is, therefore, crucial for the formation of liquid crystal phases.

Depending on the nature of the phases they form, liquid crystals can be divided into two general classes: *thermotropic* and *lyotropic* liquid crystals. The behaviour of thermotropic liquid crystals is dependent on temperature: they usually exhibit mesophases either on heating a material from the crystalline solid state, or on cooling from the isotropic liquid state. Lyotropic liquid crystals, on the other hand, are formed on the change of concentration of amphiphilic molecules dispersed in an isotropic medium – for example, surfactant molecules dispersed in water. However, materials such as block copolymers and gemini surfactants[4] can also exhibit a combination of both thermotropic and lyotropic liquid crystalline behaviour, and these are known as *amphotropic* liquid crystals. The experimental work carried out in this thesis includes thermotropic liquid crystals only.

Liquid crystals are well-known for their applications in the manufacturing of displays,[5–8] as well as applications in optical filters and switches,[9] lasers,[10] smart windows[11,12] and biomedicine,[13,14] to name several examples. Due to their high physical and chemical versatility, liquid crystals also offer the potential of novel applications.[15–17]

1.2 Types of mesophases

The three main liquid crystal phases exhibited by thermotropic mesogens are the nematic (N), smectic (Sm) and cholesteric (N*) phases. In all three types of phases, the liquid crystal molecules are aligned along a preferential direction, known as the director ***n***, which is the average orientation of the molecules within the phase. The

extent to which the molecules within a phase are ordered is defined by the order parameter, *S*:

$$S = \frac{1}{2}\langle 3\cos^2\theta - 1\rangle, \qquad (1.1)$$

where θ represents the angle between the director and the long axis of an individual molecule. The order parameter is temperature dependent and is in the range $-\frac{1}{2} < S < 1$. In the isotropic phase, $S = 0$, and in a perfect crystal, $S = 1$ or $S = -\frac{1}{2}$.[18]

The nematic (N) phase

The nematic phase is the simplest type of mesophase. In the nematic phase (Figure 1.2), molecules possess long-range orientational order, but there is no positional order. The name originates from the Ancient Greek *nêma*, meaning 'thread', due to the thread-like defects observed optically (see polarising optical microscopy textures in Figure 2.4). Typically for a nematic phase, the order parameter *S* is between 0.4 and 0.7.[19]

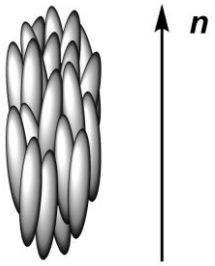

Figure 1.2: Nematic ordering of mesogens along the director ***n***.

The smectic (Sm) phases

Smectic phases, like nematic phases, possess orientational ordering along the director. Compared to nematic phases, however, they have a higher degree of order. Molecules in the smectic phase are arranged in a layered structure with a well-defined interlayer spacing. The name 'smectic' is derived from the Ancient Greek word *smēktikós*, meaning 'cleaning', since, at first, such liquid crystalline phases were observed on ammonium and alkali soaps.[20]

There are many types of smectic mesophases; however, the two that will be focused on in this chapter are the smectic A (SmA) and smectic C (SmC) phases, as these are the ones that are relevant to the rest of the thesis. The smectic A phase is the least ordered smectic phase, where the molecules are arranged in layers and have their long molecular axes perpendicular to the layer planes, and, thus, also to the director

n (Figure 1.3a). If a material exhibits more than one smectic phase, then the SmA phase is observed at the highest mesogenic temperature range. The SmC phase is very similar to the SmA phase, with the difference being that the director is not perpendicular to the layer plane, but tilted at an angle φ (Figure 1.3b).[17] The tilt angle φ is temperature-dependent and usually decreases in value with increasing temperature, and in the SmA phase, $\varphi = 0°$. Within layers of both the SmA and SmC phases, there is no long-range positional ordering between the molecules' centre of mass, but liquid-like fluidity instead.[21]

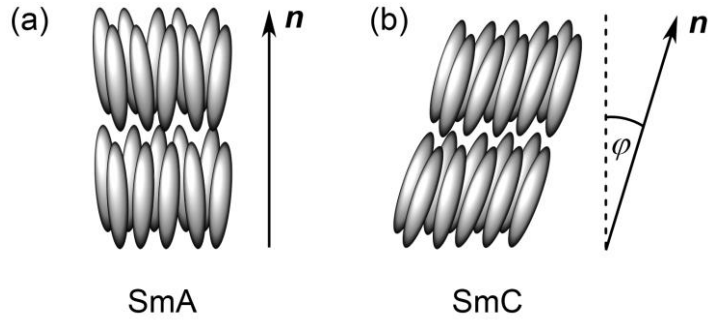

Figure 1.3: The layered arrangement of: (a) the smectic A and (b) the smectic C phase. The director and tilt angle are labelled as ***n*** and φ, respectively.

The cholesteric (N*) phase

The cholesteric, or chiral nematic (N*) phase was first observed in cholesterol derivatives, hence the name 'cholesteric'. The phase exhibits long-range orientational order, like the nematic phase, as well as a twisted structure, whereby the director rotates at an angle perpendicular to the director, to form a helical structure of a certain pitch length (Figure 1.4). The distance at which the director rotates a full 360° around the helical axis is called the pitch, p. However, because ***n*** and ***-n*** are indistinguishable (the director at 0° and 180° are equivalent), the structure repeats itself at every half-pitch distance ($p/2$). The pitch can be sensitive to temperature or chemical composition. Increasing the temperature leads to a shorter pitch, and similarly, decreasing the temperature results in a longer pitch. The pitch of cholesteric compounds can be several hundred nanometres long. If the pitch length falls within the wavelength range of the visible spectrum, shining white light on the material results in the colours corresponding to the pitch length being selectively reflected. Achiral liquid crystals can be mixed with chiral dopants to induce N* phases, and the pitch can be fine-tuned based on the concentration of chiral dopant in the mixture, according the equation:

$$p = \frac{1}{HTP \times c}, \tag{1.2}$$

where HTP is the helical twisting power of the chiral dopant (units in μm^{-1}) and c is the concentration by weight of chiral dopant (expressed in decimals).

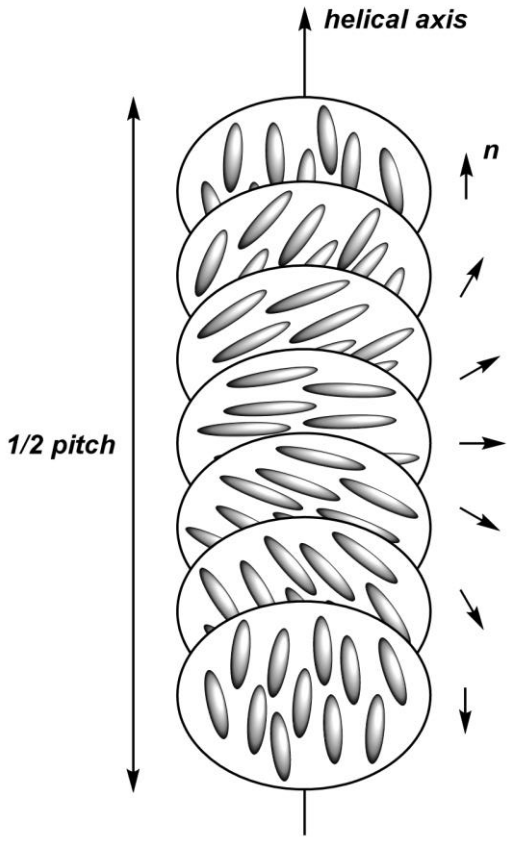

Figure 1.4: A diagram representing a half-pitch distance (a 180° turn of the director) in the cholesteric (chiral nematic, N*) phase. The direction of the helical axis and director ***n*** are labelled.

1.3 Thermotropic liquid crystal architectures

A simple change in the architecture of a liquid crystal molecule can generate a range of fascinating properties and physical phenomena. As previously mentioned, the ability for a molecule to form a liquid crystal phase lies in the balance of order and fluidity. Various architectures of thermotropic liquid crystals exist, such as calamitic, discotic, conic, bent-core and dimeric liquid crystals; however, this thesis focuses on calamitic, bent-core and dimeric mesogen shapes.

Calamitics

Liquid crystals that are calamitic, or rod-shaped, are one of the most widely studied types of liquid crystal. They exhibit cylindrical symmetry across their long molecular axis (the length of the molecule) and tend to consist of a rigid, aromatic core which provides the mesogen with its crystalline behaviour, and a flexible alkyl tail attached to the core which gives the mesogen its flow-like behaviour. The cores can also have polar groups attached, such as fluoride (-F) or nitrile (-CN) groups which provide the mesogen with a dipole moment; these become important when aligning mesogens using an external field.

Calamitic mesogens typically form nematic and smectic mesophases. An example of a calamitic liquid crystal is 4-cyano-4'-pentylbiphenyl, commonly known as 5CB (Figure 1.5). 5CB was first synthesised in 1972 by George Gray, Ken Harrison and John Nash at the University of Hull[22] and it was the first member of the cyanobiphenyl (CB) family to exhibit an enantiotropic liquid crystal phase. It was discovered with the intent of finding a liquid crystal that is stable at room temperature to be used for display applications. The 5CB molecule consists of a rigid biphenyl core, a flexible 5-carbon alkyl chain on one end of the core and a cyano-group (-CN) on the other end. It exhibits the nematic phase between 22.5 °C[22] and 35.5 °C.

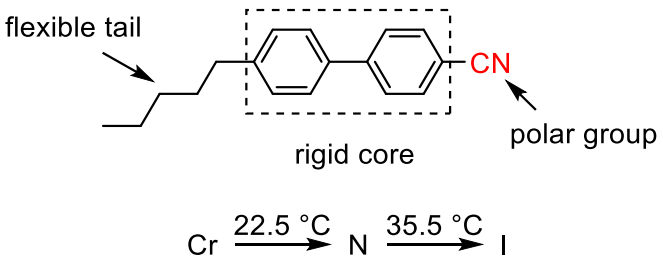

Figure 1.5: The chemical structure and phase sequence of 5CB, a calamitic liquid crystal exhibiting the nematic phase. Different sections of the molecule are labelled.

Bent-cores

Over the past two decades, bent-core liquid crystals (BCLCs), also known as banana or V-shaped liquid crystals, have been a research topic of significant interest. As the name suggests, bent-core molecules possess an aromatic core exhibiting a bent/kinked structure and flexible side chains. Due to the structure of bent-core molecules, they prefer to assemble into layered structures and so they tend to form smectic mesophases.

The bent structure has the potential to give rise to biaxial liquid crystal phases, such as the biaxial SmA phases (discussed in Chapter 5). The biaxial phases possess orthorhombic symmetry with two directors, shown in Figure 1.6: a ***n***-director which is the statistical average orientation of the long molecular axes (the primary axis), and a ***m***-director which lies along the secondary axis, i.e. perpendicular to the primary axis.[23] The first bent-core molecule was synthesised in 1929 by Daniel Vorländer,[24,25] however, they remained unappreciated for many years until a broad range of unusual physical properties were discovered in these materials.[26–30] One of these properties is the presence of ferroelectricity that has been seen even though the mesogens themselves are achiral in nature (discussed in more detail in section 5.1). Bent-core liquid crystals are also known to exhibit fascinating types of liquid crystal phases, an example being the twist-bend nematic (N_{TB}) phase (discussed in detail in Chapter 3).

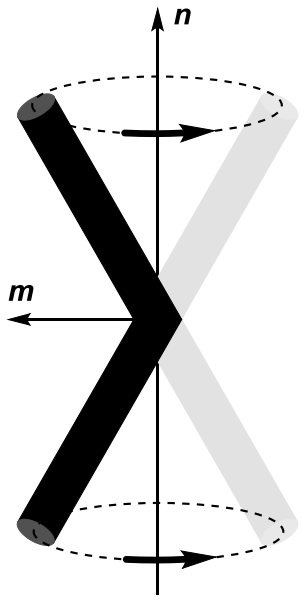

Figure 1.6: A diagram showing the direction of the two directors (***n*** and ***m***) in a bent-core molecule, whereby rotation around the primary axis is occurring.

Dimers

Yet another fascinating class of mesogens are liquid crystal dimers, discovered in 1927 by Daniel Vorländer.[31] A dimeric liquid crystal is composed of two mesogenic units attached through a flexible spacer, generally an alkyl chain. Different combinations of dimeric liquid crystal structures can exist. They can be divided into two broad groups based on their structure: symmetric dimers and non-symmetric dimers,[32] as illustrated in Figure 1.7. In symmetric dimers, the two mesogenic units

are identical – for example, two calamitic units can be joined, or alternatively, two discotic units or two bent-core units. On the other hand, non-symmetric dimers are composed of two different mesogenic units – for example, one calamitic unit attached to a bent-core unit, or a calamitic unit attached to a discotic unit.

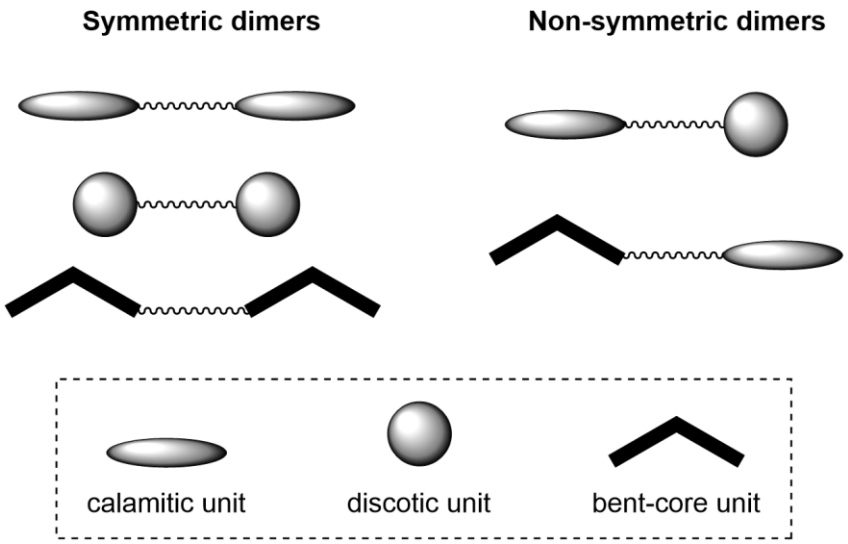

Figure 1.7: A representation of the different combinations of mesogenic units (calamitic, discotic and bent-core) in symmetric and non-symmetric liquid crystals.

An example of liquid crystal dimers are molecules in the CB*n*CB series, where CB refers to 'cyanobiphenyl' and *n* refers to the number of methylene units in the flexible spacer. The molecules in the CB*n*CB series give rise to an 'odd-even' effect (illustrated in Figure 1.8): if the flexible spacer contains an even number of methylene ($-CH_2-$) units, the molecule adopts a linear conformation, whereas an odd number of methylene units results in a bent conformation. The bent conformations exhibit unique physical properties, such as a nematic-nematic transition whereby a spontaneous arrangement of mesogens into helical structures occurs, resulting in the twist-bend nematic (N_{TB}) phase, which, as mentioned previously, will be discussed in detail in Chapter 3.

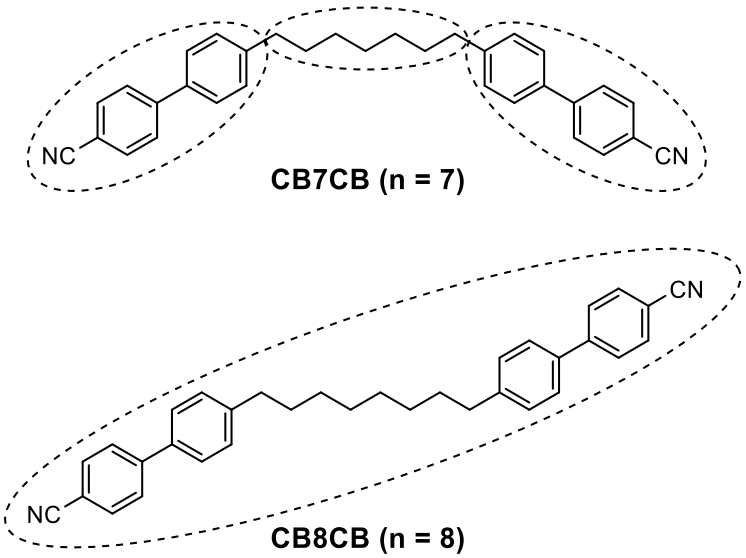

Figure 1.8: An example of the 'odd-even' effect arising from the CB*n*CB series. CB7CB (top molecule) has an odd number of methylene units in the flexible spacer (n = 7) and adopts a bent conformation. CB8CB (bottom molecule) has an even number of methylene units in the spacer (n = 8) and adopts a linear conformation.

1.4 Alignment of liquid crystals

In a liquid crystal device, also known as a 'cell', it is possible to achieve a preferred orientation of the liquid crystal director by surface treatment of the glass substrates and this ultimately determines the optical appearance of the device. The way in which these alignments are generally achieved is by depositing a polyimide onto the surface of the glass substrates which anchors the liquid crystal to the preferred alignment. Two types of alignment are typically used when characterising liquid crystal devices: planar alignment (sometimes referred to as 'homogeneous') and homeotropic alignment, both depicted in Figure 1.9. For a uniaxial nematic liquid crystal in a planar device, the liquid crystal director's orientation is parallel to the glass substrates, whereas in a homeotropic device, the director's orientation is perpendicular to the glass substrates. When the planar polyimide is deposited onto a glass substrate, the director of a nematic liquid crystal will be randomly aligned. To achieve a uniform preferred direction of the director, planar devices can be rubbed with a velvet cloth which creates grooves on the surface of the planar substrate, and the director will lie along the direction of these grooves, i.e. along the 'rubbing direction'.

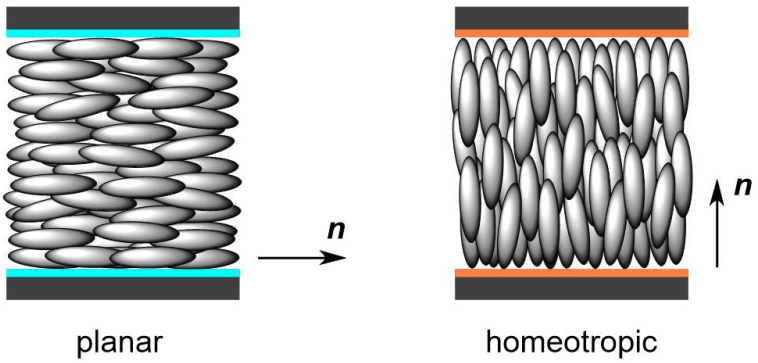

Figure 1.9: A diagram representing the orientation of the nematic liquid crystal director ***n*** in a planar and homeotropic device.

1.5 Elastic properties of liquid crystals

When an external force, such as an electric or magnetic field, is applied to a liquid crystal and exceeds a certain value, deformations to the liquid crystal director occur. These deformations are elastic responses of the director in order to bring the system back to equilibrium. For a nematic phase, there are three main deformations depicted in Figure 1.10: splay (K_{11}), twist (K_{22}) and bend (K_{33}) deformations. In planar devices, the splay elastic constant k_{11} is related to the dielectric anisotropy $\Delta\varepsilon$ of the liquid crystal and its threshold voltage, which will be discussed in Chapter 2.

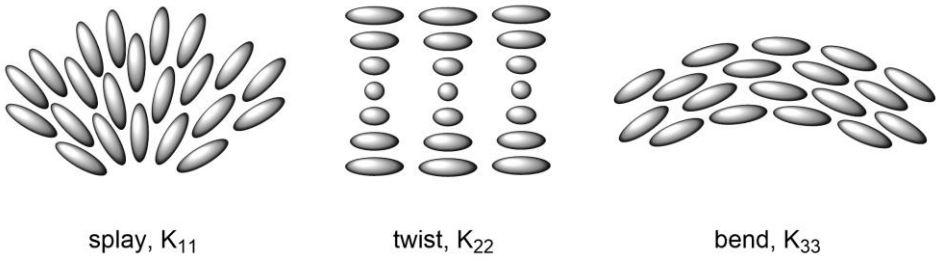

Figure 1.10: A representation of the splay (K_{11}), twist (K_{22}) and bend (K_{33}) deformations for mesogens in a nematic phase.

1.6 Reactive mesogens and photopolymerisation

Photoreactive monomers used in the field of liquid crystals are typically monomers exhibiting liquid crystalline phases (the nematic phase is common) and are, therefore, called reactive mesogens. Their general shape is cylindrical, whereby flexible side chains are attached to a central, polarisable core, and on either side of the molecule, there is a reactive group attached, (for example, an acrylate or methacrylate group),

as illustrated in Figure 1.11a. The commercially available reactive mesogen RM257 – a bifunctional acrylate exhibiting the nematic phase – is commonly used for photopolymerisation. The chemical structure of RM257 is given in Figure 1.11b and its core, flexible tails and reactive acrylate groups are labelled. If a reactive mesogen (RM) possesses two reactive groups, it is referred to as bifunctional, whereas a reactive mesogen possessing one reactive group is monofunctional. Reactive mesogens are widely used for thermodynamically stabilising liquid crystalline structures. The way this is achieved is by mixing a small concentration (usually less than 10%) of reactive bifunctional mesogenic monomer with a low molecular weight liquid crystal that exhibits the mesophase(s) of interest. Of course, a small concentration of photoinitiator is also added to the mixture (typically ~1%) to initiate the polymerisation process. An in-situ photo-initiated polymerisation fixes and stabilises the anisotropic network, and this process is usually referred to as *polymer stabilisation*. Bifunctional monomers are generally used to stabilise structures, however, monofunctional monomers can also be used in combination with bifunctional monomers, and they act as 'terminators' in the polymerisation process.

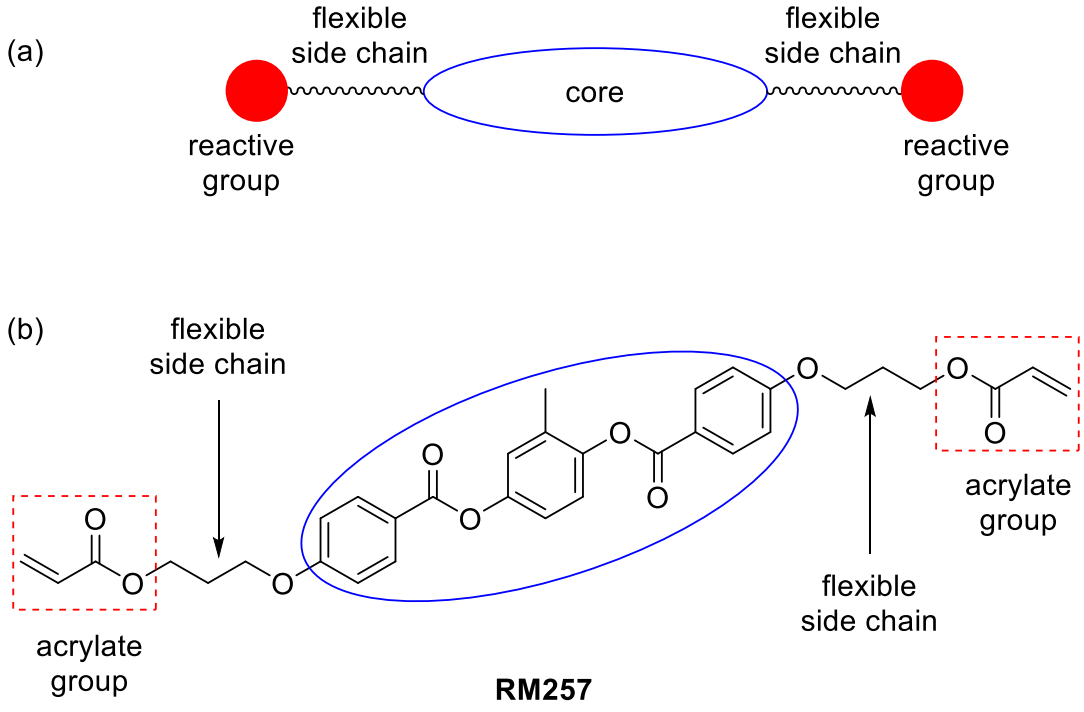

Figure 1.11: (a) A diagram showing the general structure of reactive mesogens consisting of a central core and flexible tails attached to reactive groups on either side of the molecule. (b) The chemical structure of reactive mesogen RM257 with different parts of the molecule labelled.

The way in which the polymerisation mechanism works is the photoinitiator splits into two radicals via photodissociation when in contact with ultraviolet (UV) light[33] – see Figure 1.12. These radicals then attack the double bond of the acrylate groups on either side of the reactive mesogen, which leads to a step-growth polymerisation, ultimately resulting in the formation of a long-chain polymer network. Typically, the polymerisation process should last only a few minutes, but to ensure that complete polymerisation has occurred, the sample can be kept under UV light for longer periods of time. The polymerisation process will usually end when all the monomer has been used up, or alternatively when two radicals recombine, or the UV light source is turned off.

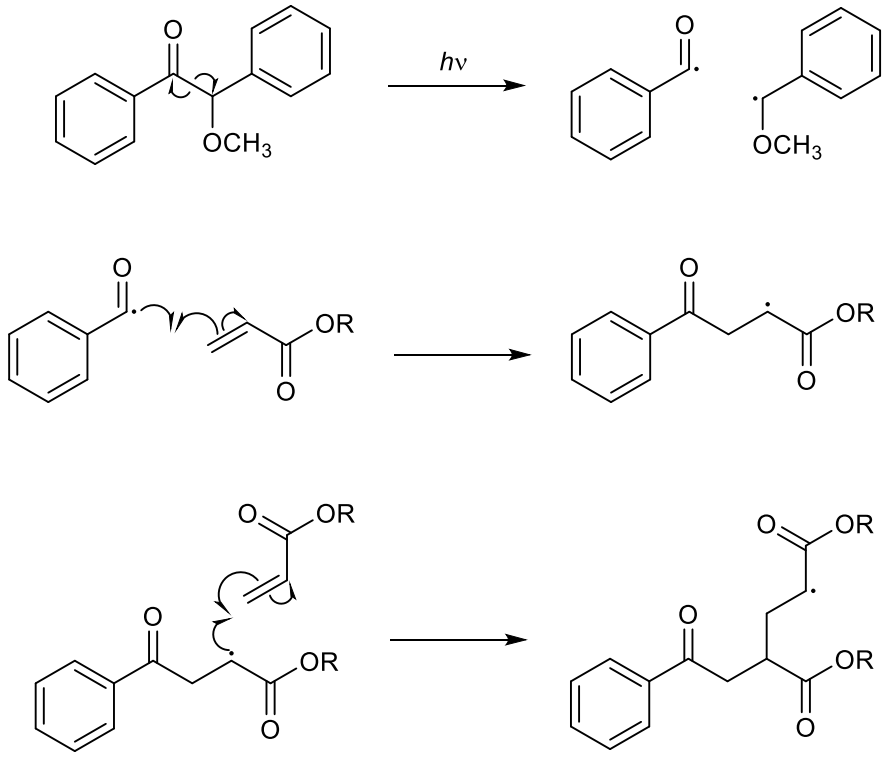

Figure 1.12: Photoinitiator benzoin methyl ether (BME) splits into two radicals when exposed to ultraviolet light (*hν*). These radicals attack the reactive groups of the monomer (in this case the acrylate groups), leading to a step-growth polymerisation.

The way in which polymer stabilisation of liquid crystals works is by stabilising the orientation of the liquid crystal director (alignment) through interactions between the aligned polymer network and the liquid crystal.[34] Polymer stabilisation of liquid crystals provides an enhancement of mechanical stability and improved electro-optical characteristics. In the past, photopolymerisation has been successfully used to extend the temperature range and enhance electro-optic properties of nematic[35–38] and twist-grain boundary[39] phases. Polymer stabilisation of blue phase liquid

crystals leads to a vast array of practical photonic and display applications.[40,41] Polymer stabilisation of cholesteric,[42–45] ferroelectric[46–48] and antiferroelectric[49–51] liquid crystal phases has also been achieved. In these systems, the formation of a polymer network in the lattice of disclinations provides thermal stability for the mesophases over a wide temperature range.

1.7 Liquid crystal templating

The process of transferring liquid crystal features (structural, physical etc.) onto a polymer matrix (or a gel matrix in the case of lyotropic liquid crystals) is referred to as 'liquid crystal templating'. The templates are also referred to as 'scaffolds' in literature. Liquid crystal templating offers great potential in understanding interfacial interactions between liquid crystals and polymers and gels at the nanoscale. At low concentrations in an isotropic medium, surfactants exist as individual molecules, as shown in Figure 1.13a. By increasing the concentration, a threshold (the critical micelle concentration; CMC) is surpassed, and the surfactant molecules combine to form isotropic micellar phases, which are either spherical or cylindrical. Further increasing the concentration results in the formation of lyotropic liquid crystal phases. These liquid crystal phases are (1) hexagonal phases, consisting of hexagonal arrays of cylindrical micelles, (2) cubic phases, and (3) lamellar phases, composed of a layered arrangement of surfactant molecules.

In 1992, Kresge et al.[52] were the first to report the formation of ordered mesoporous frameworks using a liquid crystal templating mechanism. The way this was achieved was through the encapsulation of self-assembled amphiphilic surfactants (lyotropic liquid crystal) using aluminosilicate gels. Finally, the organic surfactant was removed via thermal processing called *calcination*. In addition to calcination,[53–56] the organic surfactant can also be removed via solvent extraction.[57,58] The solvent extraction leaves behind a stable, hexagonal arrangement of hollow cylinders with the diameter of the cylinders (channels) in the range 16-100 Å (or more), i.e. this is a mesoporous molecular sieve. This was a breakthrough in the field of macroscopic ordering of soft matter and, since the discovery, various templates based on lyotropic liquid crystals have been established.[59–71] The size of the pores (channels) can be tailored through the choice of surfactant molecule used to form the template, auxiliary chemicals added to the synthesis mixture and reaction conditions. Examples of surfactants used for lyotropic liquid crystal templating are cetyltrimethylammonium bromide (CTAB; chemical structure shown in Figure 1.13b) and hexadecylamine (HDA).

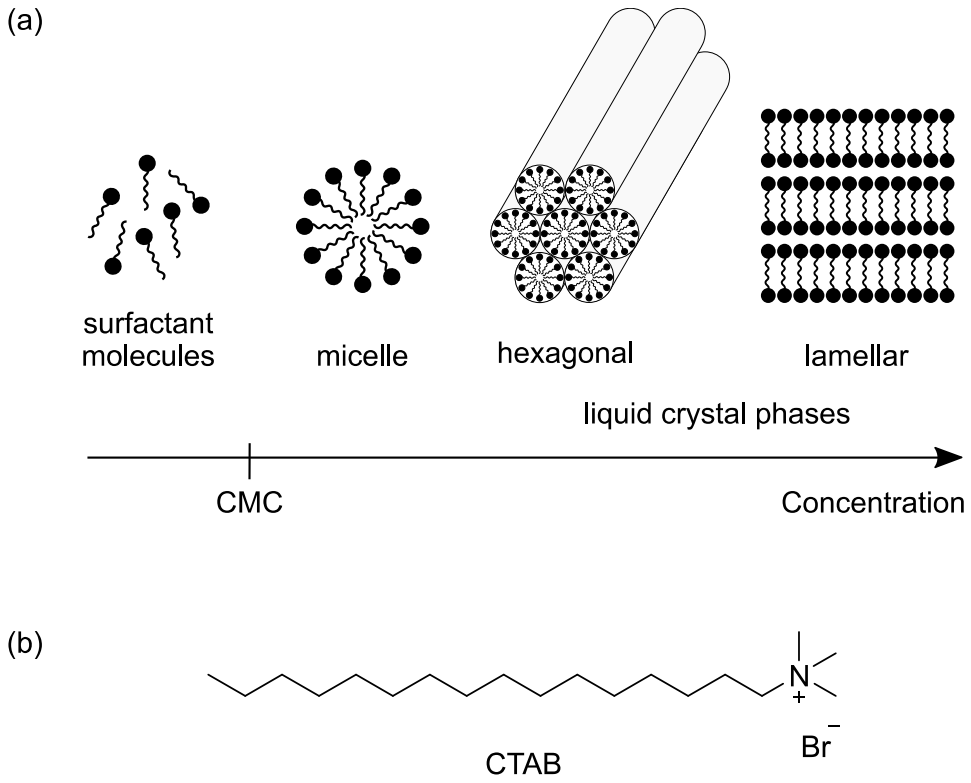

Figure 1.13: (a) Concentration-dependent transition of a surfactant/water system. At low concentrations, surfactants exist as individual molecules. Increasing the concentration leads to the formation of micelles and liquid crystal phases. CMC is the critical micelle concentration. (b) Chemical structure of CTAB (cetyltrimethylammonium bromide).

The templating mechanism proposed by Kresge et al.[52] works as follows. The surfactants pack into hexagonal arrays of cylindrical micelles, with the hydrophobic hydrocarbon chains in the centre of the cylinders and the polar groups of the surfactant facing outwards on the surface of the cylinders, as shown in Figure 1.14. The silicate species then encapsulate the surface of the cylindrical micelles. Another possible route for the templating mechanism is the encapsulation of randomly ordered cylindrical micelles with the silicate species, which then spontaneously assemble into an energetically favourable hexagonal arrangement.[72] The templates (usually inorganic) are formed in a 'skin-tight' fashion around the host templating structures (usually organic) – in this case the hexagonal array of cylindrical surfactant structures – whereby the structural and electronic characteristics of the host templating material are replicated in the inorganic template.[73] The mesoporous silicate materials that are formed through liquid crystal templating have applications in the biomedical field,[74–80] the removal of environmental pollutants,[81–85] chemical catalysis[86–90] and functional devices such as sensors.[91–93]

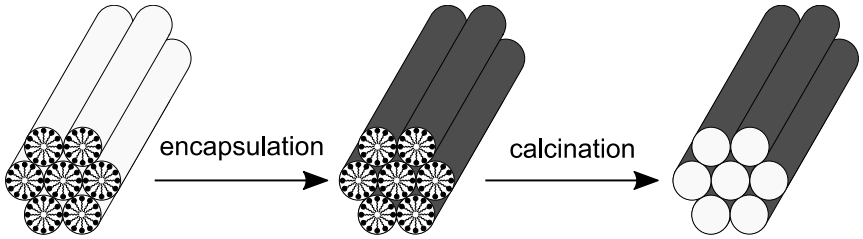

Figure 1.14: A schematic representation of the lyotropic liquid crystal templating mechanism. Cylindrical micelles packed in a hexagonal arrangement are encapsulated with silicate species. The surfactant is removed via calcination to form the template.

Hydrogel templates of lyotropic liquid crystal phases can also be achieved via the photopolymerisation of monomers.[94–101] Hydrogels are composed of a three-dimensional network of cross-linked hydrophilic polymer chains, which enables them to retain large amounts of water (>90%) without being prone to solvation. The hydrogel templates are formed by exposing a homogenous mixture composed of monomers, surfactant/water and photoinitiator to UV light, followed by the removal of surfactant and any unpolymerised material. The templates exhibit nanoscale ordering and retain the original structure of the lyotropic liquid crystal phase. Compared to traditional hydrogel systems, the templated hydrogels exhibit improved mechanical properties and water uptake.

In the last decade or so, templating thermotropic liquid crystal phases has attracted a great deal of attention. Here, the templates are prepared via the photopolymerisation of reactive monomers, as described in Figure 1.15. The sample preparation is similar to the preparation of photopolymerised (polymer-stabilised) liquid crystal phases using monomers; however, larger monomer concentrations are usually used for templating (>10%) to obtain stronger templated films. As is the case for hydrogel templates of lyotropic liquid crystal phases discussed above, in thermotropic liquid crystal templating, a homogenous mixture of liquid crystal, monomer and photoinitiator is exposed to UV light. The unpolymerised liquid crystal and monomer are washed out, which results in the formation of a porous polymer network. This is a template of the host liquid crystal phase, whereby the nano-/microstructures of the liquid crystal phase are expected to be imprinted into the polymer (as is the case in lyotropic liquid crystals). Ultimately, this template can be refilled with a liquid crystal that has different properties to the host liquid crystal used to form the polymer network, and Guo et al.[102] were the first to use this 'washout-refill' method.

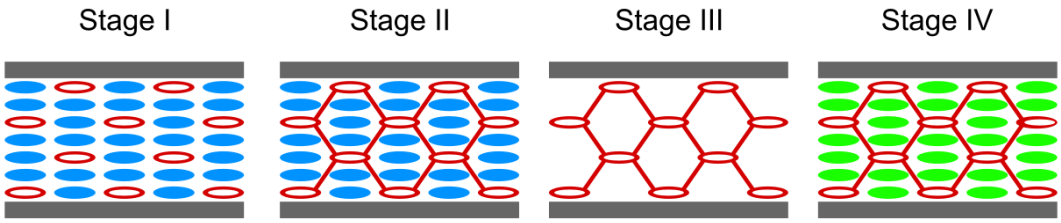

Figure 1.15: A schematic representation of the thermotropic liquid crystal templating procedure. Stage I: A cell is capillary filled with a homogenous mixture of host liquid crystal (blue ovals) and photoreactive monomer (red open ovals). Stage II: The cell is exposed to ultraviolet (UV) light, resulting in the formation of a polymer network – this is the photopolymerised sample. Stage III: The host liquid crystal is washed from the sample, leaving behind a porous polymer network, which is a template of the host liquid crystal phase. Stage IV: The cell can be refilled with a liquid crystal that is different to the host liquid crystal (green ovals).

Cholesteric (N*) liquid crystals have been one of the main areas of focus in thermotropic liquid crystal templating, for their applications in cholesteric liquid crystal films.[102–110] Cholesteric liquid crystal films can be found in nature and they simultaneously reflect both right- and left-circularly polarised light (R-CPL and L-CPL, respectively). Guo et al.[102] developed a single-layer polymer-stabilised liquid crystal film that reflected both R-CPL and L-CPL. The way they achieved this was by forming a polymer template of a left-handed helical structure which was then refilled with a right-handed helical structure. In conventional cholesteric liquid crystals, the reflection intensity of unpolarised light is never greater than 50%, whereas in the refilled template, a reflection intensity of close to 100% was achieved.

An unusual set of mesophases known as blue phases have also been another area of focus in in thermotropic liquid crystal templating. Blue phases are observed in highly chiral liquid crystals between the cholesteric and isotropic phases. They assemble into three-dimensional periodic structures, making them desirable candidates for applications in tuneable photonic devices,[111–117] however, they are usually stable over very small temperature windows. Castles et al.[111] experimentally demonstrated the transfer of liquid crystalline nanostructures to polymers. The blue phase was photopolymerised and the chiral liquid crystal was washed out, whereby the porous template retained the chiral three-dimensional structure of the blue phase. When this template was refilled with the nematic liquid crystal 5CB, the thermal stability of the templated blue phase spanned over a range of 250 °C and the liquid crystal exhibited selective reflection, even though it was achiral in nature.

1.8 Motivation

Templating thermotropic liquid crystal phases is a relatively novel field of research, and little is known about the interactions between the liquid crystal and polymer that lead to the templating effect. The aim of the work undertaken in this thesis is to improve the understanding of the following:

(1) How templating thermotropic mesophases is achieved via the process of surface modification of the polymer (at the interface of the liquid crystal and polymer) during the polymerisation of the homogenous mixture composed of liquid crystal, monomer and photoinitiator;
(2) Which characteristics of the host liquid crystal can be imprinted onto the polymer. These can either be solely characteristics relating to the mesoscopic structure of the host liquid crystal phase, or both structural and physical properties resulting from a specific mesoscopic arrangement of mesogens.

This thesis focuses on templating two liquid crystal phases. The first is the twist-bend nematic (N_{TB}) phase, formed from the spontaneous self-assembly of achiral mesogens into helical structures of nanoscale pitch. The problem with the N_{TB} phase is that it is very difficult to measure its electrical and mechanical properties in pure materials because it is highly viscous. The N_{TB} phase will be templated and then refilled with a different nematic liquid crystal to understand these properties.

The second liquid crystal phase that will be templated is the SmA phase exhibiting ferroelectric switching ($SmAP_F$). The $SmAP_F$ phase is a recently discovered biaxial phase that exhibits macroscopic polarisation. It is the highest-symmetry ferroelectric state possible in a layered structure. An achiral bent-core liquid crystal exhibiting the $SmAP_F$ phase will be synthesised as part of this project. The $SmAP_F$ will be templated and, as for the N_{TB} template, refilled with a nematic liquid crystal to determine if any of its characteristic properties can be templated, such as the layer structure, biaxiality and ferroelectricity.

1.9 Outline of thesis

This thesis is composed of eight chapters. The current chapter provided a background to liquid crystals and their physical properties, as well as a literature review of liquid crystal templating. The procedures and equipment used to undertake the experimental work can be found in Chapter 2. Results on the experimental work are divided into five chapters as follows:

Chapter 3 discusses binary mixtures exhibiting the N_{TB} phase. Two sets of binary mixtures are prepared involving the dimer CB7CB that exhibits the nematic and N_{TB} phases. The first is CB7CB with the calamitic liquid crystal 5CB where an investigation into the dielectric properties is undertaken, and the second is CB7CB mixed with a reactive mesogen.

Chapter 4 uses the mixtures studied in Chapter 3 to create templates of the N_{TB} phase which are then refilled the nematic liquid crystal 5CB.

Chapter 5 discusses the synthesis of the $SmAP_F$ mesogen NT12.

Chapter 6 includes the characterisation of mesogen NT12 and binary mixtures of NT12 with a reactive mesogen.

Chapter 7 uses the binary mixtures from Chapter 6 to create templates of the $SmAP_F$ phase. These templates are then also refilled with 5CB.

A summary of the results can be found at the end of each of the results chapters. Finally, the conclusion can be found in Chapter 8. Supporting information, such as DSC curves and spectroscopic data (NMR/FT-IR spectra) relating to liquid crystal synthesis, is also provided in Appendix I and Appendix II, respectively.

CHAPTER 2:
Experimental methodology

Details about the experimental work undertaken in this thesis can be found in this chapter. Information about the materials used, including their chemical structures, is provided. The chapter also contains information on general sample preparation procedures used for the experimental work, and a background to the characterisation methods used. Information on techniques used for liquid crystal synthesis can also be found in this chapter.

2.1 Materials

The liquid crystals, monomer and photoinitiator used for experimental work are described below and their chemical structures are given in Figure 2.1. The materials were used either in their pure form or as a mixture of two or more compounds.

Liquid crystals

CB7CB: 1′′,7′′-bis(4-cyanobiphenyl-4′-yl)heptane (purchased from SYNTHON Chemicals, Germany). The LC exhibits the nematic and twist-bend nematic phases on heating and cooling. The transition temperatures (°C) on cooling are: Iso 119 N 106 N_{TB} (determined using POM).

5CB: 4′-pentyl-4-biphenylcarbonitrile (purchased from Sigma Aldrich). The LC exhibits the nematic phase on heating and cooling. The transition temperatures (°C) on cooling are: Iso 35.5 N (determined using POM).

8CB: 4′-octyl-4-biphenylcarbonitrile (purchased from Sigma Aldrich). The LC exhibits the nematic and SmA phases on heating and cooling. The transition temperatures (°C) on cooling are: Iso 42 N 34 SmA (determined using POM).

NT12: The LC exhibits the SmA and $SmAP_F$ phases on heating and cooling. The LC was synthesised, and the procedure is described in Chapter 5. The transition temperatures (°C) on cooling are: Iso 162 SmA 141 $SmAP_F$ (determined using POM).

Monomer

RM257: 4-(3-acryloyloxypropyloxy)benzoic acid 2-methyl-1,4-phenylene ester (purchased from SYNTHON Chemicals, Germany). This is a reactive mesogen (RM)

that exhibits the nematic phase on heating and cooling. The transition temperatures determined using the first DSC heating cycle are: Cr 69 N 126 Iso.

Photoinitiator:

BME: benzoin methyl ether (purchased from Sigma Aldrich). Melting point: 47.5–48.5 °C (determined using POM).

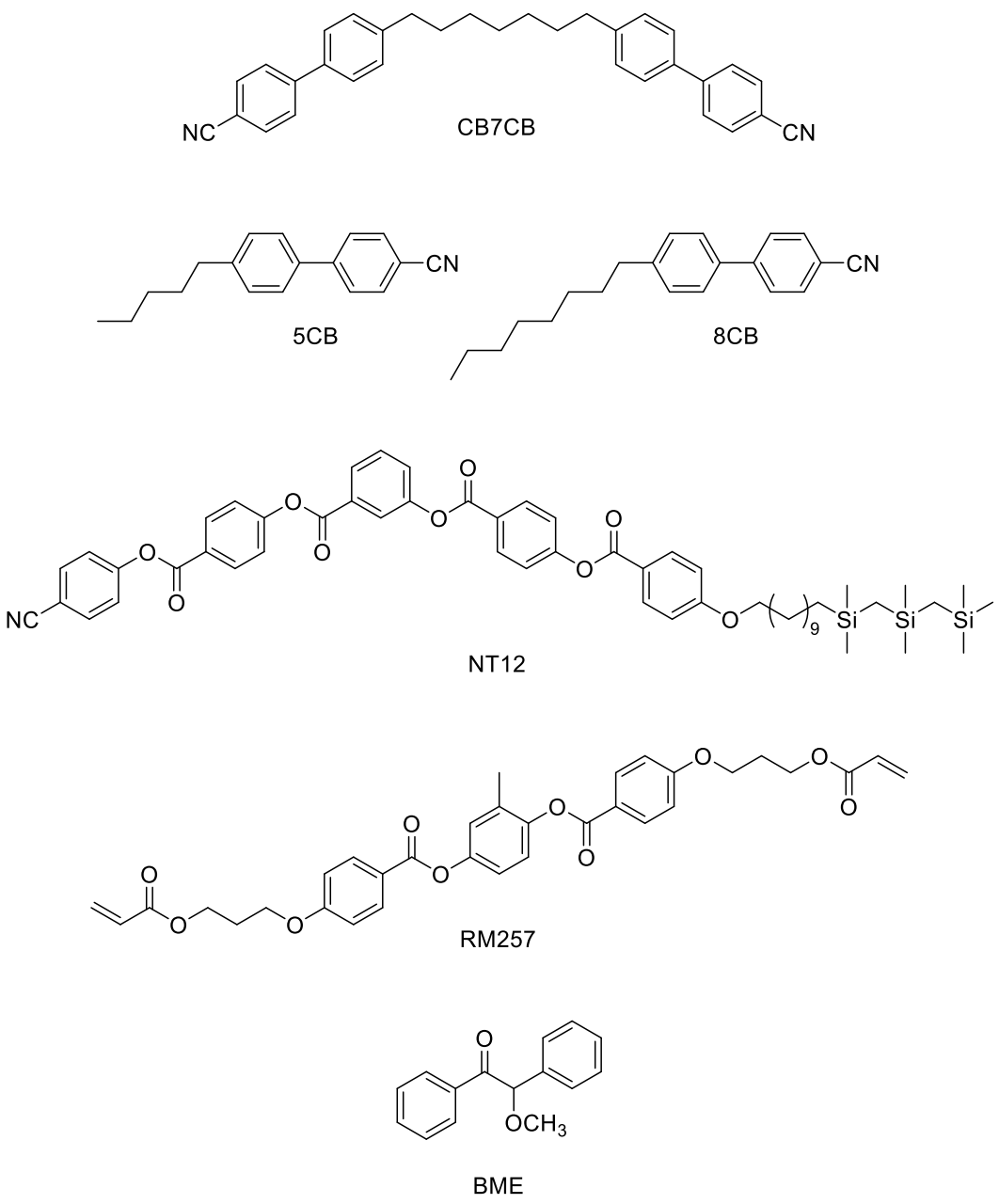

Figure 2.1: Chemical structures of the materials used in this thesis: liquid crystals (CB7CB, 5CB, 8CB, NT12), monomer (RM257) and photoinitiator (BME).

2.2 Preparation of samples

Mixtures

Mixtures with varying concentrations by weight (wt%) were prepared by adding the materials to a 2 ml glass vial at room temperature, either in their solid or liquid crystal form. Dichloromethane (~1 ml) was added to the vial to dissolve all the materials. The contents of the vial were sonicated at room temperature for 30 min and the solvent was removed by allowing it to evaporate on a hotplate at 35-40 °C for at least 12 h.

Homemade cells

Untreated glass slides were cut into small pieces using a glass scorer. The substrates were cleaned by sonicating first in a mixture of soap and deionised water, then in methanol and finally in IPA. The glass substrates were dried in an oven at 70 °C and were then exposed to UV ozone to remove any residual solvent/dirt. The planar alignment material (polyimide SE3510 from Nissan Chemical Corporation) was diluted in dimethylformamide (2:1 parts). This was then deposited onto the centre of the substrate using a pipette. The polyimide was spin-coated onto the glass substrate, within a few minutes of being exposed to UV ozone. The glass substrates were then baked on a hotplate by gradually increasing the temperature from ambient to 180 °C. The substrates were rubbed, and cells were assembled in an antiparallel fashion using UV glue mixed with the desired size of glass spacer beads. The assembled cells were then cured by exposing to UV light of ~365 nm for 1 hour on each side to ensure complete curing.

Filling cells

All cells were filled with pure liquid crystals and mixtures typically in their nematic phase. For experiments relating to the $SmAP_F$ mesogen NT12, cells were filled in the isotropic phase. Mesophase temperature ranges can be found in section 2.1 for pure materials, in Chapter 3 for N_{TB} mixtures and in Chapter 6 for $SmAP_F$ mixtures. Cells that were not filled with mixtures containing polymerisable materials (monomer) were then sealed by placing a small amount of high-temperature UV glue at the cell openings and irradiating with UV light of 365 nm wavelength for 1 h to ensure the UV glue had completely cured. Cells were filled with polymerisable mixtures in the dark room and were not sealed.

Soldering

Indium metal (melting point: 157 °C) was used to solder wires onto cells for electro-optic, dielectric and polarisation experiments. Wires were stripped of 0.5-1 cm of their insulation on both ends. The soldering iron was heated to 190 °C and dabbed into the indium. The metal was deposited both on the stripped section of one end of the wire and on the electrode of the cell, and the two were joined by adding a small amount of extra indium.

Cell gap measurements

Cell gap values were measured with the microscope in reflection mode attached to a HR4000 High-Resolution Spectrometer from the company Ocean Optics (now Ocean Insight) and spectra were taken using the software SpectraSuite 1.6.0_11. To calibrate the software, a mirror was used to capture the bright-field and a black surface was used to capture the dark-field. The empty cell was placed on a black surface and the empty cell gap was measured in several places (wavelengths only in the region between 450 nm and 700 nm were considered) using the equation:

$$d = \frac{\lambda_1 \lambda_2 \, \mathrm{m}}{2\,(\lambda_2 - \lambda_1)}, \tag{2.1}$$

where d = cell gap, λ_1 = lower wavelength value, λ_2 = upper wavelength value, m = number of peaks. The statistical average of multiple cell gap values was taken because the values are almost the same across the area of the empty cell.

Liquid crystal templating procedure

Liquid crystal templating will be discussed in Chapter 4 for the N_{TB} phase and in Chapter 7 for the $SmAP_F$ phase. The general templating procedure used in this thesis is similar to that of templated cholesteric phases and templated blue phases (described in Figure 1.15). The main differences are the concentration of components used in the polymerisable mixtures and the solvents used for washing out non-polymerisable materials. Typical solvents used in literature[102,106,107,111–113,115] include hexane, acetone, ethanol, cyclohexane and THF. Depending on the cell gap, different washing times are also necessary. In general, the larger the cell gap, the shorter the time required to wash out non-polymerisable materials from the cell.

The templating procedure used in this thesis is as follows. A cell was capillary filled on the microscope hot stage with a mixture composed of liquid crystal(s), RM257 and BME, either in the nematic or isotropic phase. The sample was cooled to a

temperature corresponding to the liquid crystal phase of interest. The cell was then irradiated with UV light of ~365 nm for 2 hours to ensure complete polymerisation of the sample, during which a constant temperature of the sample was maintained. The sample was left in a 30 ml glass jar filled with acetone for several days to completely wash out the host liquid crystal and leave behind the polymer network template. While the cell was being washed in acetone, a difference between washed and unwashed areas of the cell could usually be distinguished, as shown in Figure 2.2a. The cell was dried by placing it on a hotplate at 30 °C for approx. 1 h. As the sample dried, a white polymer film formed across the cell (as shown in Figure 2.2b).

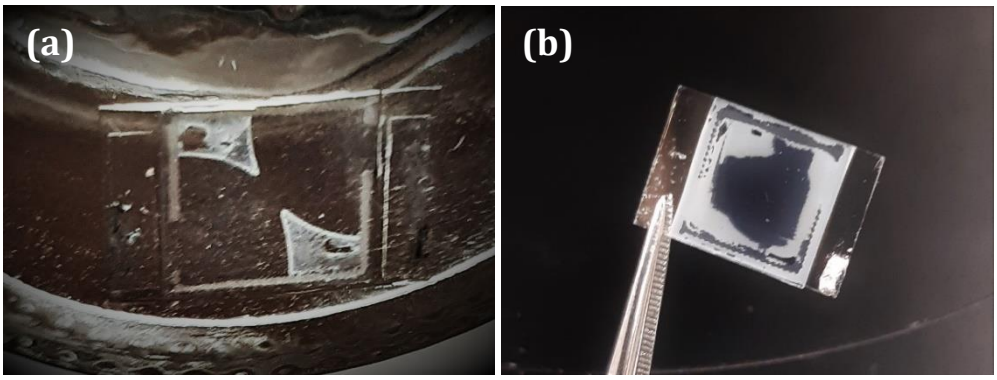

Figure 2.2: (a) A cell in acetone with the top left and bottom right corners representing areas of the cell that have not yet been washed. (b) A white polymer film forming across the cell as the sample dries.

2.3 Characterisation of mesophases

2.3.1 Polarising optical microscopy (POM)

Polarising optical microscopy (POM) is a fundamental technique for distinguishing between isotropic and anisotropic phases. Optical anisotropy, or birefringence (Δn), is a phenomenon observed in liquid crystals whereby polarised light experiences two refractive indices. It is defined as $\Delta n = n_e - n_o$, where n_e is the extraordinary refractive index (parallel to the director $\boldsymbol{n}$ in uniaxial liquid crystals), and n_o is the ordinary refractive index (perpendicular to the director) – see Figure 2.3. When the plane of polarised light from the first polariser passes through the liquid crystal, it becomes elliptically polarised (diffracted) due to birefringence and, therefore, it can pass through the second polariser (called the 'analyser'), which is aligned at a 90° angle to the first polariser. As a result, coloured textures that are characteristic of specific liquid crystal phases can be observed, and these are best obtained when the

liquid crystal material is cooled from its isotropic state. On the other hand, an isotropic liquid would appear black between crossed polarisers because the plane of polarised light from the polariser would not get diffracted when passing through the liquid and, as a result, would get blocked by the analyser.

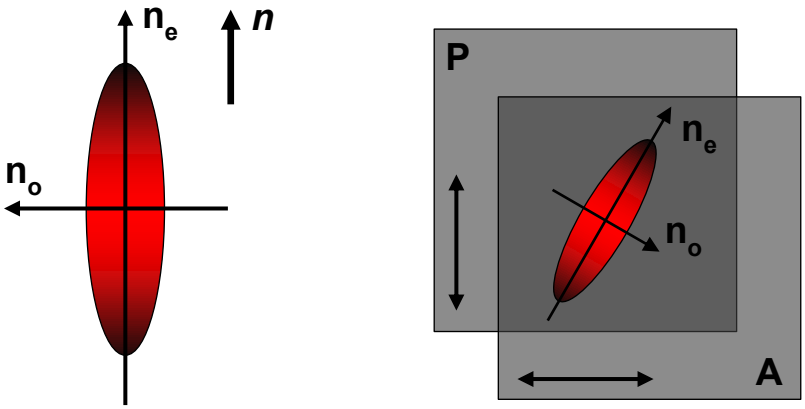

Figure 2.3: A diagram showing the direction of the ordinary and extraordinary refractive indices, n_o and n_e, respectively. When n_o and n_e are not parallel to the crossed polarisers, the liquid crystal transmits lights from the polariser (P) to the analyser (A).

Liquid crystals can align themselves homeotropically between two untreated glass substrates. In this case, the light passing through the polariser experiences only one of the material's refractive indices and does not get diffracted, as is the case for isotropic liquids. Therefore, the homeotropically aligned sample appears black. When the rubbing direction of rubbed planar cells (see section 1.4) is parallel to either the polariser or analyser, the sample will appear dark for a nematic sample, because the director lies along the rubbing direction. Figure 2.4 shows the typical textures observed for a nematic liquid crystal between untreated glass substrates. The black lines represent *schlieren* textures and are observed when the liquid crystal director lies parallel to the crossed polarisers.

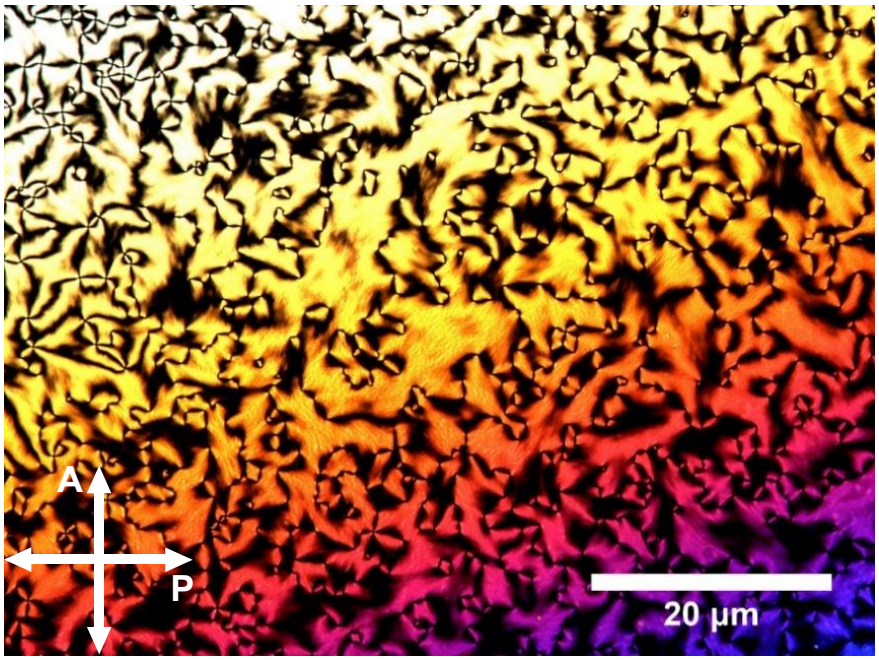

Figure 2.4: Coloured texture of the nematic phase when the liquid crystal is viewed between two untreated glass substrates using polarising optical microscopy (POM).

The setup used for carrying out polarising optical microscopy (POM) and electro-optic experiments is shown in Figure 2.5. POM experiments were carried out using a Leica DM2700P polarisation microscope. A Linkam THMS600 hot stage connected to a Linkam T95-PE temperature controller was used to control the sample temperature. Phase transition temperatures were usually determined at cooling rates of 0.1 °C/min on cooling from the isotropic phase. Pictures were taken using the digital camera Invenio 5DII from the company DeltaPix that was controlled using the software DeltaPix InSight version 4.1.3.

Figure 2.5: The experimental setup for electro-optic experiments: a polarising optical microscope, hot stage, temperature controller and electrical kit.

2.3.2 Differential scanning calorimetry (DSC)

Differential scanning calorimetry (DSC) measures the thermodynamic events occurring in a liquid crystal material on heating and cooling, such as transitions between the solid and liquid crystal phases, between two mesophases or the transition to the isotropic phase. These transitions can be classed as either first order or second order. A melting point (T_m, shown in Figure 2.6), for example, is a strongly first-order transition. Here, the change in free energy G is assumed to be zero ($\Delta G = 0$), and so if there is a change in entropy of the system, the enthalpy can be measured using $\Delta H = T\Delta S$. Transitions between two mesophases, on the other hand, are considered to be weakly first order, or sometimes second order. This means there is no change in entropy (and enthalpy) of the system during the phase transition. A transition from a liquid crystal phase to an isotropic phase (T_c in Figure 2.6) is also weakly first order, with enthalpy values at around 1 kJ/mol.

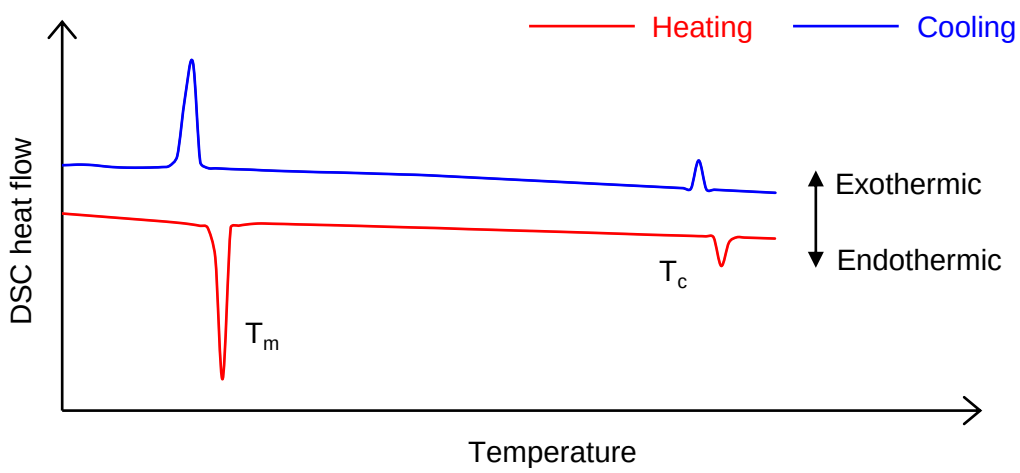

Figure 2.6: DSC curves showing a heating and cooling cycle of a thermotropic liquid crystal. T_m and T_c indicate the melting and clearing points, respectively.

In the DSC experiment, the heat capacity (C_p) of a material is measured as a function of temperature. A sample and a reference crucible are heated electrically at a constant rate (usually 5-20 °C/min), whereby the same temperature is maintained in both. When a phase transition occurs, the temperature in the sample crucible will typically change significantly relative to that of the reference. This results in a peak in the DSC curve (Figure 2.6) from which the enthalpy associated with the corresponding transition can be calculated. It is important to note that DSC experiments should be complementary to optical microscopy experiments. This is because textural changes identified optically do not necessarily lead to phase transitions in DSC data, and vice versa.

For DSC experiments, a DSC Q20 V24.11 Build 124 was used. Heating and cooling cycles were performed at a constant rate. The software Universal Analysis 2000 version 4.5A from the company TA Instruments was used to analyse DSC curves. The phase transition peaks were integrated (see Figure 2.7) to obtain the associated latent heat value (J/g enthalpies) of the transition, from which enthalpies (ΔH) in kJ/mol were calculated based on the molar mass (M) of the material using the equation:

$$\Delta H = latent\ heat \times M. \qquad (2.2)$$

The total molar mass of a binary mixture was calculated based on the molar mass of each component and their concentration by weight (X and Y, in decimals), i.e.:

$$M(mixture) = X \times M(component\ 1) + Y \times M(component\ 2), \qquad (2.3)$$

where $0 < X < 1$, $0 < Y < 1$, and $X + Y = 1$.

Dimensionless entropies of phase transitions ($\Delta S/R$) were then calculated using:

$$\Delta S = \frac{\Delta H}{RT}, \tag{2.4}$$

where ΔH is the calculated phase transition enthalpy, R is the gas constant with a value of 8.314 J mol^{-1} K^{-1}. T is the onset temperature (in kelvin) obtained from integration of the peaks using the DSC software (see Figure 2.7).

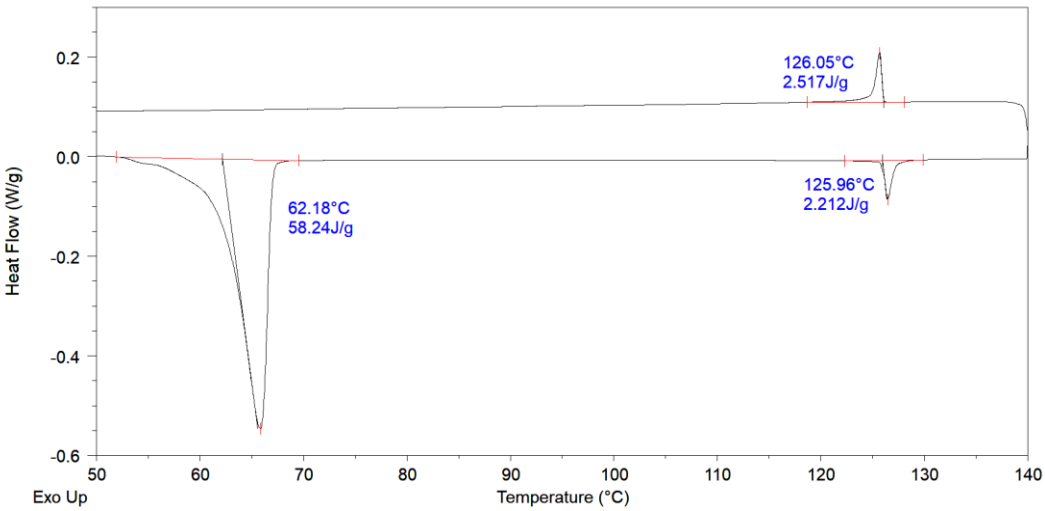

Figure 2.7: An example of the DSC curves of RM257, measured a rate of 2 °C/min showing the integration parameters (onset temperature and latent heat) for each phase transition peak. The bottom and top curves show the first heating cycle and first cooling cycle, respectively.

2.3.3 Dielectric spectroscopy

Dielectric spectroscopy measures the dielectric properties of a material, such as frequency-dependent relaxation processes occurring within molecules. It is an excellent technique to probe conformational distributions and changes in liquid crystalline structures. Dielectric properties are important for determining if the liquid crystal is suitable for technological applications. The response of a liquid crystal to an applied electric field is governed by its dielectric constant, or dielectric permittivity, ε', which is the real part of a complex dielectric permittivity ε^*:

$$\varepsilon^* = \varepsilon' + i\varepsilon'', \tag{2.5}$$

where ε'' is the imaginary part of the dielectric permittivity. ε' corresponds to the ability of a material to store electric charge and it is a measure of its polarisability, i.e. a material with a high permittivity polarises more compared to a material with low permittivity, and, in turn, stores more electric energy.

The electron-withdrawing cyano-group (-CN) of 5CB gives the molecule a permanent dipole moment (μ) along the director ***n*** (the long molecular axis). When exposed to a sufficiently strong electric field in a planar device, the liquid crystal becomes polarised and the dipole moment aligns with the electric field (see Figure 2.8, left molecule). Permittivity is related to polarisability (α) in such a way that the separation of negative and positive charge for 5CB is along the long molecular axis, and so the permittivity along the long molecular axis ($\varepsilon'_{\parallel}$) will be larger than along the short molecular axis ($\varepsilon'_{\perp}$), resulting in a positive dielectric anisotropy material ($\Delta\varepsilon$, where $\Delta\varepsilon = \varepsilon_{\parallel} - \varepsilon_{\perp}$). In a derivative of 5CB which has a fluoride group attached to the lateral ortho- or meta- positions of the Ph-CN ring (see Figure 2.8, right molecule), the dipole moment will lie perpendicular to the long molecular axis of the molecule. Therefore, when the dipole moment aligns with the applied electric field, in this case, the separation of charge will be measured along the short molecular axis, i.e. $\varepsilon'_{\perp}$ is larger than $\varepsilon'_{\parallel}$, resulting in a negative $\Delta\varepsilon$ material.

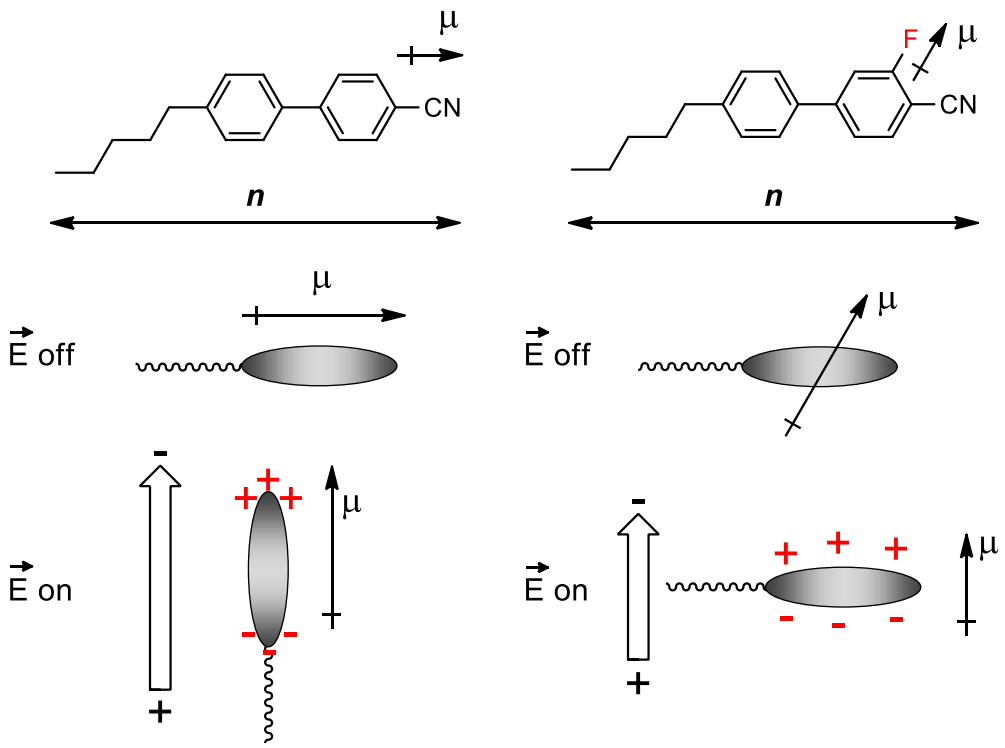

Figure 2.8: The dipole moment (μ) aligns along the director ***n*** in 5CB (left molecule). For a derivative of 5CB with a laterally substituted fluoride group (right molecule), μ lies perpendicular to the director. When a sufficiently strong electric field is applied to the molecules, the dipole moment aligns with the electric field and, as a result, 5CB has a positive dielectric anisotropy ($\Delta\varepsilon$), whereas the laterally-substituted derivative has a negative $\Delta\varepsilon$.

Dielectric spectroscopy experiments will be discussed in Chapter 3, Chapter 4, Chapter 6 and Chapter 7. Measurements were taken using an Agilent E4980A Precision LCR Meter and the setup is shown in Figure 2.9. Planar cells (AWAT PPW, Poland) having a square indium tin oxide (ITO) electrode area of sheet resistance 15Ω/□ were used for all dielectric experiments.

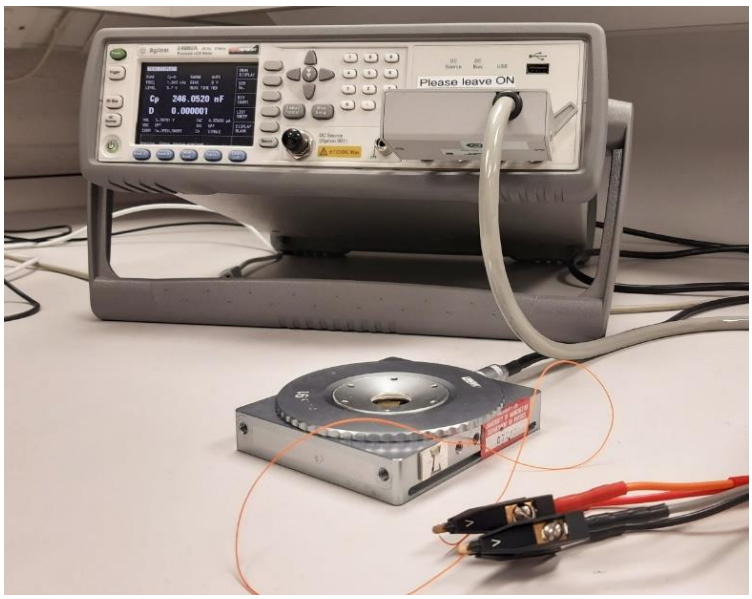

Figure 2.9: The setup for dielectric spectroscopy experiments. The cell is placed on the temperature-controlled hot stage and connected to the spectrometer through the wires.

Firstly, the capacitance of the empty cell (C_o) was measured at 0.1 V_{RMS} as a function of frequency between 20 Hz and 2 MHz. The cell was then filled with the liquid crystal in the nematic or isotropic phase, and capacitance measurements were taken for a range of temperatures on cooling at a rate of 0.5 or 1 °C/min. Temperatures were stabilised for 120 s before measurements were taken. An example graph of capacitance as a function of frequency is given in Figure 2.10 for CB7CB.

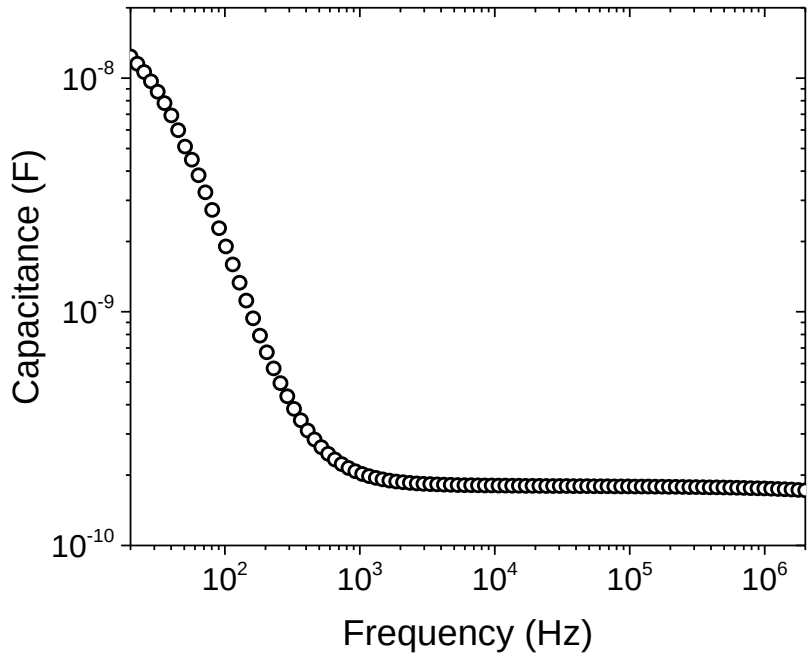

Figure 2.10: A plot of capacitance as a function of frequency for CB7CB at 110 °C (0.1 V_{RMS}).

The data analysis software OriginPro by OriginLab Corporation was used for calculating and fitting dielectric data. Permittivity (ε') values for planar and homeotropic alignment of devices can be calculated by dividing the filled cell capacitance with the empty cell capacitance, i.e.:

$$\varepsilon' = \frac{C_{LC}}{C_o}, \tag{2.6}$$

where ε' is permittivity, C_o is empty cell capacitance, and C_{LC} is the filled cell capacitance. Alternatively, permittivity can also be measured using the formula:

$$\varepsilon' = \frac{C_{LC}\, d}{\varepsilon_o\, A}, \tag{2.7}$$

where d is the cell gap, ε_o is the permittivity of free space, and A is the ITO electrode area. In this thesis, permittivity values of filled cells were calculated using the formula $\varepsilon' = C_{LC}/C_0$. The associated errors in ε' were found to be 10% and they were determined by comparing the permittivities obtained from square electrode cells with the permittivities obtained using guard ring cells.

In order to obtain the dielectric strength and frequencies of relaxation processes, the dielectric loss was fitted using WinFIT software (a screenshot of the curve fitting software is given in Figure 2.11), according to the Havriliak-Negami equation:[118]

$$\varepsilon^*(\omega) = \varepsilon' - i\varepsilon'' = \varepsilon_\infty + \sum_{k=1,2} \frac{\Delta\varepsilon_k}{[1 + (i\omega\tau_k)^{\alpha_k}]^{\beta_k}} - \frac{i\sigma_{DC}}{\omega\varepsilon_0}, \quad (2.8)$$

where $\omega = 2\pi f$ (f is the frequency in Hz) and ε_0 is the permittivity of free space, ε_∞ is the permittivity at the high-frequency limit, $\Delta\varepsilon_k$ is the strength of the relaxation mode and σ_{DC} is the DC conductivity. The relaxation time is characterised by τ_k and the parameters α_k and β_k describe the shape of the spectra. For a Debye relaxation $\alpha = \beta = 1$, and for a Cole-Cole distribution $\alpha < 1$ and $\beta = 1$.[118] The frequency of the relaxation (f_R) can be calculated from the relaxation time τ_k, where $f_R = 1/(2\pi\tau_k)$.

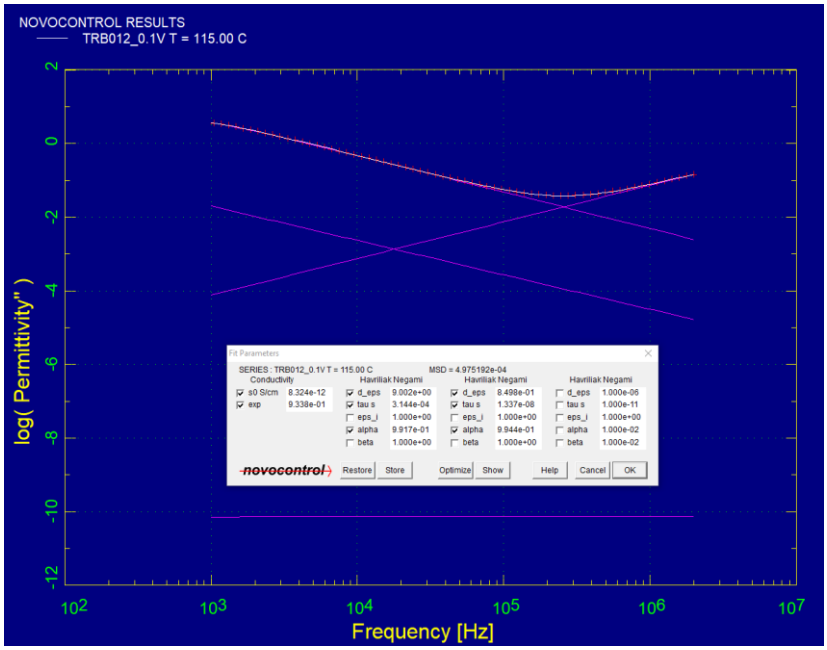

Figure 2.11: An example of curve fitting using the WinFIT software.

For binary CB7CB and 5CB mixtures in Chapter 3, the permittivities measured in the homeotropic geometry of the nematic phase were compared to those obtained from 1/V extrapolation (permittivity at infinite applied voltage), and the values of permittivity were within ±0.5.

2.3.4 Threshold voltage

Exposing a liquid crystal device to a sufficiently strong electric field causes a distortion of the liquid crystal director, known as the Fréedericksz transition.[119] The minimum voltage applied to the liquid crystal device for the Fréedericksz transition to occur is known as the threshold voltage (V_{th}). The threshold voltage can be determined from the point of intersection of the two lines shown in the inset of Figure 2.12 and will be discussed in Chapter 4.

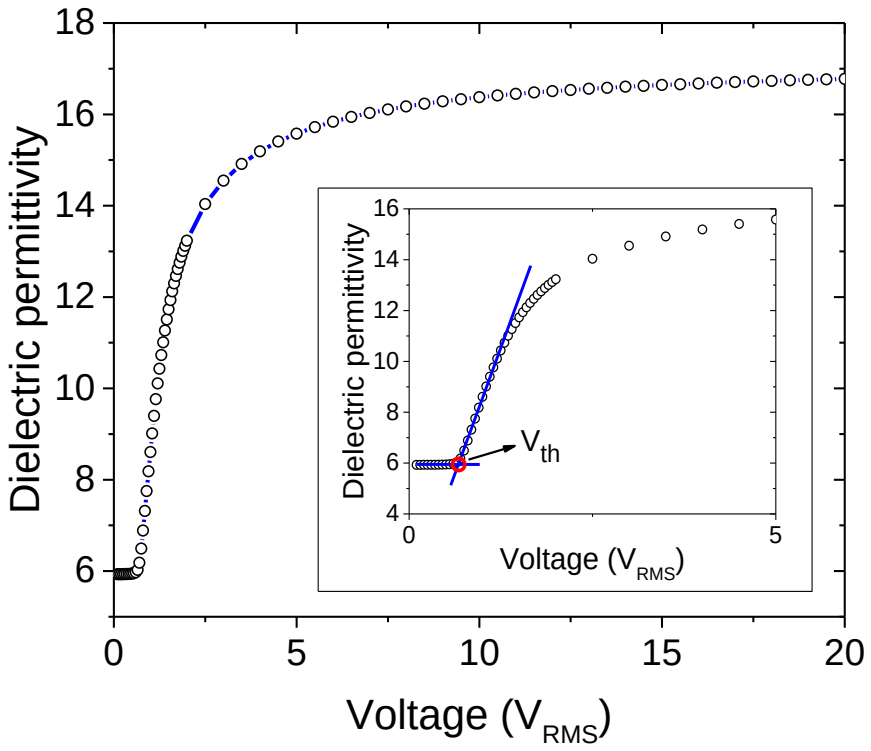

Figure 2.12: A representative plot of permittivity as a function of voltage for 5CB at 25 °C in a 10 μm planar cell. The inset shows the threshold voltage (V_{th}) at the point of intersection of the two lines, marked with a circle.

2.3.5 Spontaneous polarisation

Subjecting a liquid crystal device to an external electric field allows for polar ordering (ferroelectric/antiferroelectric) to be identified in liquid crystal phases. Applying an electric field to a polar liquid crystal phase induces a flow of current (I_{total}) which consists of a total of three contributions. These are charge-up current to the capacitor (I_c), current due to polarisation switching (I_p) and current that arises from the flow of ions (I_i):

$$I_{total} = I_c + I_p + I_i. \tag{2.9}$$

The second term (I_p) is needed to determine spontaneous polarisation, however contributions from I_c and I_i are inevitable. Experimentally, alternating triangular[120] or rectangular[121] waveforms are applied to polar liquid crystals in electro-optic switching experiments, known as the 'current pulse method'. In a planar device, the alternating electric field reorients the liquid crystal director (and dipole moment) in the opposite direction. This induces a flow of current and switching of the spontaneous polarisation (P_s), where peaks (due to I_p) are observed in each half

period of the applied wave. Applying a triangular wave, however, is more advantageous compared to the square wave, as the I_p contribution can be separated more easily from the total current (I_{total}).[122]

Ferroelectric materials (see section 5.1 for more details) show single current peaks in each half period of the triangular waveform, such as those shown in Figure 2.13, whereas antiferroelectric materials show double peaks. This is due to two switchings occurring: one from the ferroelectric (+P) to antiferroelectric state, and the other from the antiferroelectric to the ferroelectric (-P) state. The frequency of the applied electric field at which the switchings are probed is also important. If the frequency is too high, it is easy for the direct switching from the ferroelectric (+P) to the ferroelectric (-P) state to occur without passing through the antiferroelectric state. This would result in the observation of a single peak in each half period of the applied triangular waveform, as opposed to double peaks in each half period.

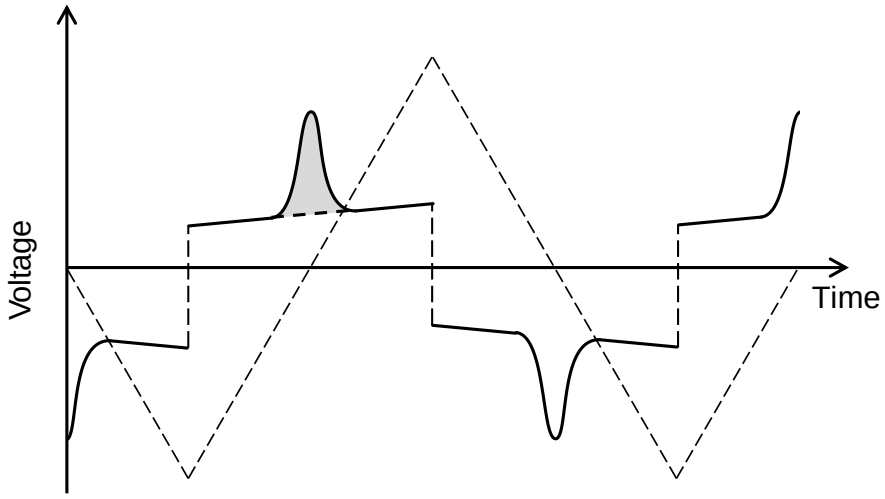

Figure 2.13: A graph showing the current response of a ferroelectric liquid crystal when a triangular wave is applied to the sample. Ferroelectric liquid crystals give rise to a single peak (shaded) in each half period of the triangle wave. The dashed line under the peak represents the baseline.

The magnitude of spontaneous polarisation (P_s) can be calculated by integrating the area under the switching peak (shaded in grey in Figure 2.13):

$$P_s = \frac{1}{2A}\int I\, dt, \tag{2.10}$$

where A is the electrode area of the liquid crystal device, I is the current measured, and t is time. This equation can also be expressed as the following:

$$P_s = \frac{\text{Area under curve}}{2RA}, \tag{2.11}$$

where R is the resistance, and this equation will be used for calculations of spontaneous polarisation of the $SmAP_F$ phase in Chapter 6 and Chapter 7.

Wires were soldered onto a planar parallel-rubbed AWAT cell of electrode area 0.25 cm^2 and known cell gap. The cell was filled with the $SmAP_F$ liquid crystal NT12 and the experimental setup was assembled as shown in the circuit diagram in Figure 2.14. Measurements were recorded for a range of temperatures on cooling the sample from the isotropic phase at a fixed voltage by generating a triangular wave. In the $SmAP_F$ phase, a single output voltage peak at each half-triangle wave was present due to ferroelectric switching. Using Ohm's Law ($V = IR$), the measured current I can be calculated. The estimated error in P_s was 6% and this was determined by comparing P_s values from repeated experiments.

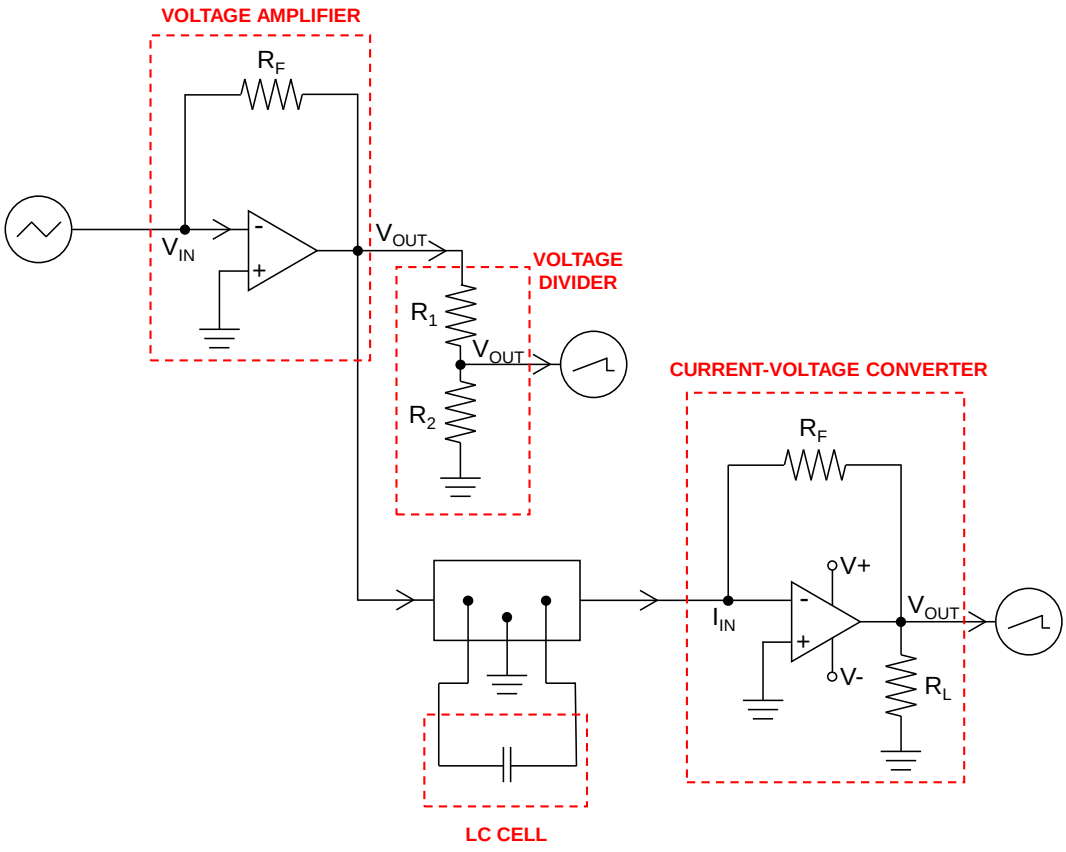

Figure 2.14: A circuit diagram of the experimental setup for spontaneous polarisation measurements. Components representing the liquid crystal cell, voltage amplifier/divider and current-voltage converter are labelled with dashed rectangles.

2.3.6 Small-angle X-ray scattering (SAXS)

X-ray scattering provides information about the supramolecular liquid crystalline structure by which a mesophase can be unambiguously identified. The smectic phases are periodically ordered in one direction with an equal interlayer distance *d* (Figure 2.15).[24] An incident X-ray beam hits the mesogen and is scattered by its electron shell. The X-ray is scattered at an angle θ (the angle between the incident ray and the layer plane). The incident and scattered X-ray beams both form an angle of θ with the layer plane, which is equal to a total of 2θ. After scattering, the X-rays from adjacent layers interfere with each other, which can either be constructive or destructive.

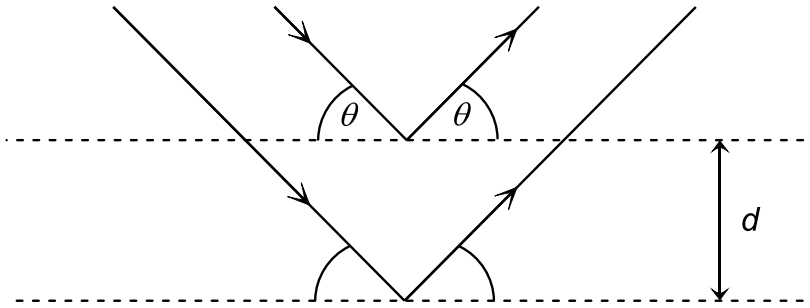

Figure 2.15: X-rays scattering at an angle θ in layers of spacing *d*.

If the X-rays interfere with each other in phase, constructive interference occurs, satisfying Bragg's Law:

$$n\,\lambda = 2\,d\,sin\theta, \qquad (2.12)$$

where *n* is a positive integer, λ is the wavelength of the incident X-ray, *d* is the layer spacing, and θ is the glancing angle (the angle between the X-ray beam and the layer plane). In a smectic phase, the interlayer distance *d* can be measured by incorporating the glancing angle θ into equation 2.12.

SAXS experiments will be discussed in Chapter 6 for pure NT12. Measurements were taken using a Xeuss 2.0. SAXS instrument connected to a Dry Scroll Vacuum Pump (Agilent Technologies). The temperature was controlled using a TermoTek Circulator. A SAXS detector Dectris Pilatus 3R 200K-A (sample-detector distance of 344 mm) was used to record 1D scattering patterns. Silver behenate was used as a peak-profile calibration standard. A quartz glass capillary of 1.5 mm diameter was filled with NT12 in solid form and wax-sealed, as shown in Figure 2.16. Measurements were taken on cooling from 150 °C with a stabilisation time of 10 min for each temperature and an exposure time of 10 min.

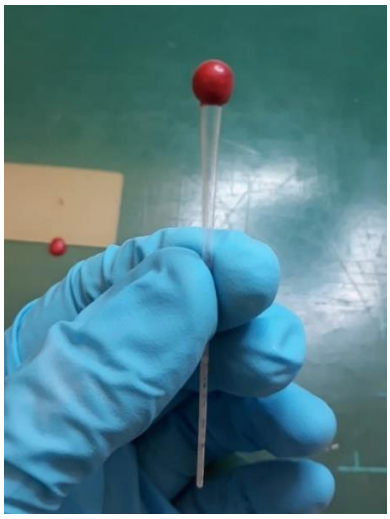

Figure 2.16: A wax-sealed 1.5 mm quartz capillary.

For mesogen NT12 in Chapter 6, Gaussian fitting of the peak of highest intensity for each SAXS profile was carried out to obtain the q value (in $Å^{-1}$). The temperature-dependent layer spacing (d, in Å) was calculated using the equation:

$$q = \frac{2\pi}{d}. \tag{2.13}$$

2.3.7 Scanning electron microscopy (SEM)

Scanning electron microscopy was used to image polymer templates and the experiments will be discussed in Chapter 4 and Chapter 7. Washed cells (see templating procedure in section 2.2) were cracked open by hand and placed on an aluminium stub using a double-sided carbon sticker. Additional carbon paint was added to the edge to help with conductivity. The sample was then coated with ~15 nm of conductive carbon (Figure 2.17) using a Quorum Q150TE evaporative coater. The surface of the sample was imaged using a Hitachi ultra-high resolution SU8230 scanning electron microscope. For energy-dispersive X-ray spectroscopy (EDX) experiments in Chapter 6, an Oxford instruments XMax 80 mm^2 silicon drift detector (SDD) was used.

Figure 2.17: Pictures of an SEM sample: a cracked open cell is placed on an aluminium stub and coated with conductive carbon.

2.3.8 Raman spectroscopy

Raman spectroscopy measurements will be discussed in Chapter 4 and Chapter 6. Raman spectra were acquired using a Renishaw inVia Raman Microscope equipped with a 515.32 nm solid state laser set to provide ~1 mW of power to the samples. The spectra were collected using Renishaw's WiRE data acquisition software connected to a charge coupled detector (CCD). The 1 mW incident laser power was combined with an exposure time of 10 s and 5% laser intensity, and the objective (20×) was used for focussing, scanning a circular area of diameter ~4 mm.

2.3.9 Birefringence

Birefringence measurements will be discussed in Chapter 4 and Chapter 7. The birefringence (Δn) was measured using a Berek compensator, an optical device containing a thin sheet of birefringent material cut perpendicular to the optical axis. The compensator was inserted into the polarising optical microscope at a 45° angle to the crossed polarisers. The cell was rotated on the microscope stage so that the director of the liquid crystal cell was positioned perpendicular to the fast axis of the birefringent material. The sheet of birefringent material can then be tilted to introduce an additional phase shift to the light that passes through it. The magnitude of the phase shift depends on the tilt angle of the birefringent material, which can be read off the compensator. The additional retardance introduced by the compensator will have 'compensated' for the retardance of the liquid crystal in the cell, and so the two cancel out. The retardance (ΔΓ) introduced can be calculated using the equation:

$$\Delta\Gamma = n_o d_c \sqrt{\left(1 - \frac{sin^2\alpha}{n_o^2}\right) - \left(1 - \frac{sin^2\alpha}{n_e^2}\right)}, \quad (2.14)$$

where d_c is the thickness of the compensator's birefringent material, α is the tilt angle, and n_o and n_e are the compensator's ordinary and extraordinary refractive index, respectively. The refractive indices are related to the wavelength of light (λ) and can be calculated using the equation:[123]

$$n_{o,e} = \sqrt{A_{o,e} + \frac{B_{o,e}}{\lambda^2 - C_{o,e}}}, \quad (2.15)$$

where A, B and C are constants corresponding to the compensator's birefringent material. For the birefringence experiments in Chapter 4 and Chapter 7: λ = 589 nm, A_o = 5.913, A_e = 7.197, $B_o = 2.441\times10^5$, $B_e = 3.322\times10^5$, $C_o = 8.03\times10^4$, $C_e = 8.43\times10^4$. The birefringence of the liquid crystal (with an associated error of 5%) can then be calculated from the retardance (ΔΓ) and cell gap (d) using the equation:

$$\Delta n = \frac{\Delta\Gamma}{d}. \quad (2.16)$$

2.4 Liquid crystal synthesis

This section gives information on general experimental procedures that were used for the liquid crystal synthesis in Chapter 5.

Solvents and reagents

All solvents and reagents were provided by the supplier and used for experiments without further distillation or purification.

Thin layer chromatography (TLC)

TLC is a useful technique for determining the purity of a compound. Silica gel on aluminium TLC sheets (20×20 cm) coated with fluorescent indicator F_{254} (purchased from Merck) were cut using a guillotine into four 5×20 cm strips. A baseline (~1 cm away from the long side of the strips) was marked with a pencil across the length of the strips and these were then cut into smaller plates perpendicular to the marked lines. The crude products and reference (starting) materials were dissolved in acetone or dichloromethane in separate vials to make suitable concentrations of sample. These were then dabbed onto the baseline of the TLC plate using a capillary.

The plates were then placed into a developing jar containing an appropriate eluent (either one solvent or a mixture of solvents) that would allow for optimal separation of the components of the crude products. The plates were taken out of solution before the eluent reached the top of the plate and were visualised under UV light of 254 nm. If a compound is pure, only one spot should be visualised under UV light, whereas two or more spots can typically be observed for impure/crude compounds. An example is given in the TLC plate in Figure 2.18, where the pure compound (right side of the TLC plate) shows only one spot, whereas the impure compound (left side of the TLC plate) separates into multiple spots. The impure compounds separate into multiple spots because the impurities usually have different polarities to the pure product.

Figure 2.18: A TLC plate showing an impure compound (left side of plate) separating into multiple spots after the eluent was passed through the plate, and a pure compound (right side of plate) showing only one spot.

Column chromatography

Column chromatography was used for the purification of crude materials. Silica gel Type 60 with a particle diameter size 40-63 μm purchased from Sigma Aldrich was used for purification. A column equipped with a filter was packed as follows: silica gel, sand, dry-loaded crude product, sand. To prepare the crude for dry-loading onto the column, the crude product was dissolved in DCM and some silica gel was added to the flask, then the contents of the flask were reduced on a rotary evaporator. An appropriate eluent was passed through the column to purify the crude compound.

NMR spectroscopy

The NMR spectra were recorded at room temperature using a Bruker AV3HD 9.4 T NMR spectrometer (AV3HD-400). ^{1}H-NMR spectra were recorded at a frequency of 400 MHz and ^{13}C-NMR spectra at 101 MHz. Deuterated chloroform ($CDCl_3$) and deuterated acetone (acetone-d6) were used as solvents. The chemical shift (δ) of compounds is given in ppm (parts per million).

Infrared spectroscopy

Measurements were carried out using an ALPHA FT-IR spectrometer from the company Bruker. Measurements were taken at room temperature over a range of 4000 to 400 cm^{-1}, with the samples either in the solid or liquid form. The spectroscopic software OPUS (Bruker) was used to analyse the spectra.

CHAPTER 3:
Liquid crystalline mixtures exhibiting the nematic and twist-bend nematic phases

In this chapter, an introduction to the twist-bend nematic (N_{TB}) phase will be given, followed by a discussion on experimental results obtained for binary mixtures exhibiting the nematic and N_{TB} phases. Some of these materials will be used later in Chapter 4 to obtain templated structures of the twist-bend nematic phase. A detailed investigation of the dielectric properties of binary CB7CB and 5CB mixtures is also given, and the influence of the calamitic mesogen 5CB on the dielectric properties and phase behaviour of the N_{TB} material CB7CB is discussed in detail.

3.1 The twist-bend nematic (N_{TB}) phase

As previously mentioned in section 1.2, the simplest liquid crystalline phase is the nematic phase, where mesogens exhibit orientational order along the director, ***n***, and no long-range positional order is present. One of the important findings of recent years is the discovery of a new type of nematic phase, known as the twist-bend nematic (N_{TB}) phase.[124–132] In the twist-bend nematic phase, in addition to the orientational order, the mesogens spontaneously self-assemble into a helical structure with an extremely short pitch length, in the order of less than 10 nm.[133–135] The way in which the helical structure is achieved is through the simultaneous twisting and bending of the director in space, hence the name 'twist-bend' nematic (Figure 3.1). The twist-bend nematic phase was predicted independently by Meyer[136] and Dozov.[137] Panov et al.[124] were the first to give evidence of a first-order phase transition from the nematic phase to a second nematic phase, at the time denoted as the N_x phase.

It is remarkable that the helical structure in the twist-bend nematic phase is spontaneously generated, and the phase exhibits degenerate domains of opposite handedness arising from symmetry breaking, even though the constituent molecules are **achiral** in nature.[138] Overall the phase attains a structure where the local nematic director ***n*** lies at a 'tilt' angle (θ) with respect to a helical axis ***h*** (Figure 3.1). The N_{TB} director can be described as: $\boldsymbol{n} = (sin\theta\ cos\varphi, sin\theta\ sin\varphi, cos\theta)$, where the azimuthal angle $\varphi = t_{TB}h$ and $t_{TB} = 2\pi/p_{TB}$ (p_{TB} is the pitch of the helix). For the N_{TB} phase, the temperature-dependent tilt angle θ falls in the range between 0 and $\pi/2$ radians, and,

in the case of the nematic phase, $\theta = 0$. In the cholesteric phase (see section 1.2), the director's tilt angle is at 90° to the helical axis, and so the twist-bend nematic phase represents a link between the nematic and cholesteric phases.

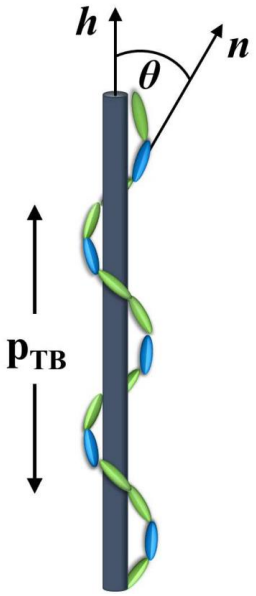

Figure 3.1: A simplified schematic representation of the twist-bend nematic (N_{TB}) phase exhibited by liquid crystal dimers: p_{TB} represents the pitch of the helix, consisting of three dimer molecules; θ represents the tilt angle; ***n*** and ***h*** are the direction of the director and the helical axis, respectively.

Twist-bend nematic liquid crystals have attracted a great deal of attention for a number of reasons, including the possibility of achieving microsecond response times[125,133] when an external electric field is applied across the sample, making them promising for applications in fast-switching photonic and electro-optic devices. Varanytsia and Chien[139] report a sub-millisecond electro-optic switching time of a dimer exhibiting the N_{TB} phase, and suggest the prospects of using these materials for applications in 3D liquid crystal displays and as active retarders for quantum computing. Besides the potential for novel applications, the discovery of the twist-bend nematic phase represents a significant scientific breakthrough because it is the fifth phase discovered as part of the nematic 'family', the first being the chiral nematic (N*) phase discovered by Reinitzer in 1888.[2]

The twist-bend nematic phase has been observed in molecules of various architectures, including dimers,[140–142] trimers,[143,144] and bent-core liquid crystals.[145–147] As previously mentioned in section 1.3, dimeric liquid crystals consist of two mesogenic units linked together via a flexible spacer. The nature, length and

parity of the flexible spacer decide the angle between the two mesogenic units and, hence, the conformation of the dimer.[148] The twist-bend nematic phase has not been templated before and will be carried out in Chapter 4 with the aim of further understanding the physical and electrical properties of the N_{TB} phase, which are difficult to measure in pure materials due to the high viscosity of the N_{TB} phase.[149–152] However, it is important to first understand the physical and electrical properties of the pure N_{TB} liquid crystal and its binary mixtures.

Dielectric properties have previously been studied for pure dimeric liquid crystals of both positive and negative dielectric anisotropies that exhibit the twist-bend nematic phase, i.e. where the dipoles align parallel or perpendicular to the long mesogenic axes, respectively.[153–155] Variation in conformations and their population distribution gives an insight into the molecular shape of the liquid crystal, which is an important feature in determining phase behaviour and physical properties.[156–164] This is based on the principle that a change in the molecular conformation would change the mean-square dipole moment, which provides a direct link to the molecular shape. The mean-square dipole moment is an averaged vector sum of dipoles. For dimeric liquid crystals having terminal polar groups on the mesogenic units, a change in the molecular shape or orientation of the liquid crystal would result in variation of the direction and magnitude of the dipole moment. This would, in turn, affect the dielectric anisotropy of the material. For liquid crystal phases, two components of the dielectric permittivity (perpendicular and parallel) can be measured over a range of frequencies, which allows for the mean-square dipole moment to be measured perpendicular and parallel to the applied electric field.

The dimer CB7CB, exhibiting the nematic and N_{TB} phases, will be used for experiments in this chapter. Figure 3.2 shows the characteristic textures of the N_{TB} phase viewed using polarised optical microscopy (POM) on cooling from the isotropic phase. Figure 3.2a shows a combination of typical N_{TB} rope-like and broken-fan-shaped textures between untreated glass substrates, and Figure 3.2b shows the difference between the textures of the N_{TB} and nematic phases (both labelled) in a planar cell.

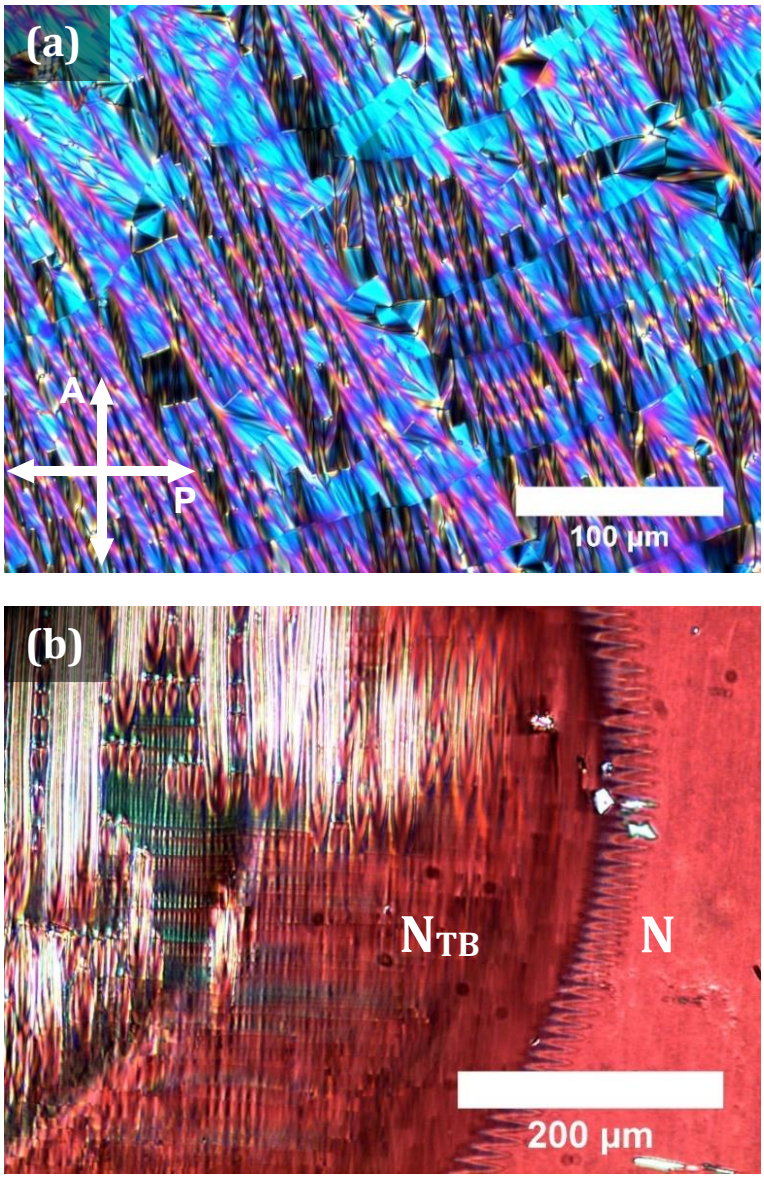

Figure 3.2: POM images showing: (a) characteristic N_{TB} rope-like textures and broken-fan-shaped textures between untreated glass slides, and (b) a clear difference between the N_{TB} (left) and nematic (right) phases in a 10 µm planar cell. Crossed polariser (P) and analyser (A) are labelled and the length of the scale bars are shown.

3.2 Binary mixtures with a calamitic liquid crystal

A series of binary mixtures of CB7CB and 5CB were prepared to understand the influence of the calamitic liquid crystal 5CB on phase transition temperatures and stability of the N_{TB} phase, and a systematic investigation of the thermal and dielectric properties is presented. The CB7CB liquid crystal exhibits the nematic and N_{TB} phases, whereas 5CB exhibits the nematic phase. A complete phase diagram of CB7CB and 5CB mixtures is provided with a detailed investigation of the phase transition

temperatures, transition enthalpies and dielectric properties. The mixtures are labelled as 'M' followed by a number indicating the wt% of 5CB in the mixture.

3.2.1 Phase diagram

The chemical structures and transition temperatures of CB7CB and 5CB are given in Figure 3.3a. CB7CB consists of two rigid cyanobiphenyl mesogenic units linked via a flexible 7-unit methylene spacer. The cyano- groups lie along the long molecular axes of the two mesogenic units and are the largest contributors to the total dipole moment of the liquid crystal. 5CB is a monomeric liquid crystal having a similar molecular structure to that of the monomer of CB7CB.

Figure 3.3b shows the phase diagram of binary CB7CB and 5CB mixtures obtained using POM. The transition temperatures that were measured are comparable to those reported in literature.[165] At room temperature and above, the N_{TB} phase is observed in mixtures with a concentration of up to 45 wt% of 5CB. As the concentration of 5CB increases, the phase diagram clearly shows a linear decrease in the isotropic to nematic and the nematic to N_{TB} phase transition temperatures, as well as an increase in the width of the nematic phase. The mixtures were carefully investigated by POM to check for any visible phase separation, however, no noticeable immiscibility of the two liquid crystals is observed across the phase diagram.

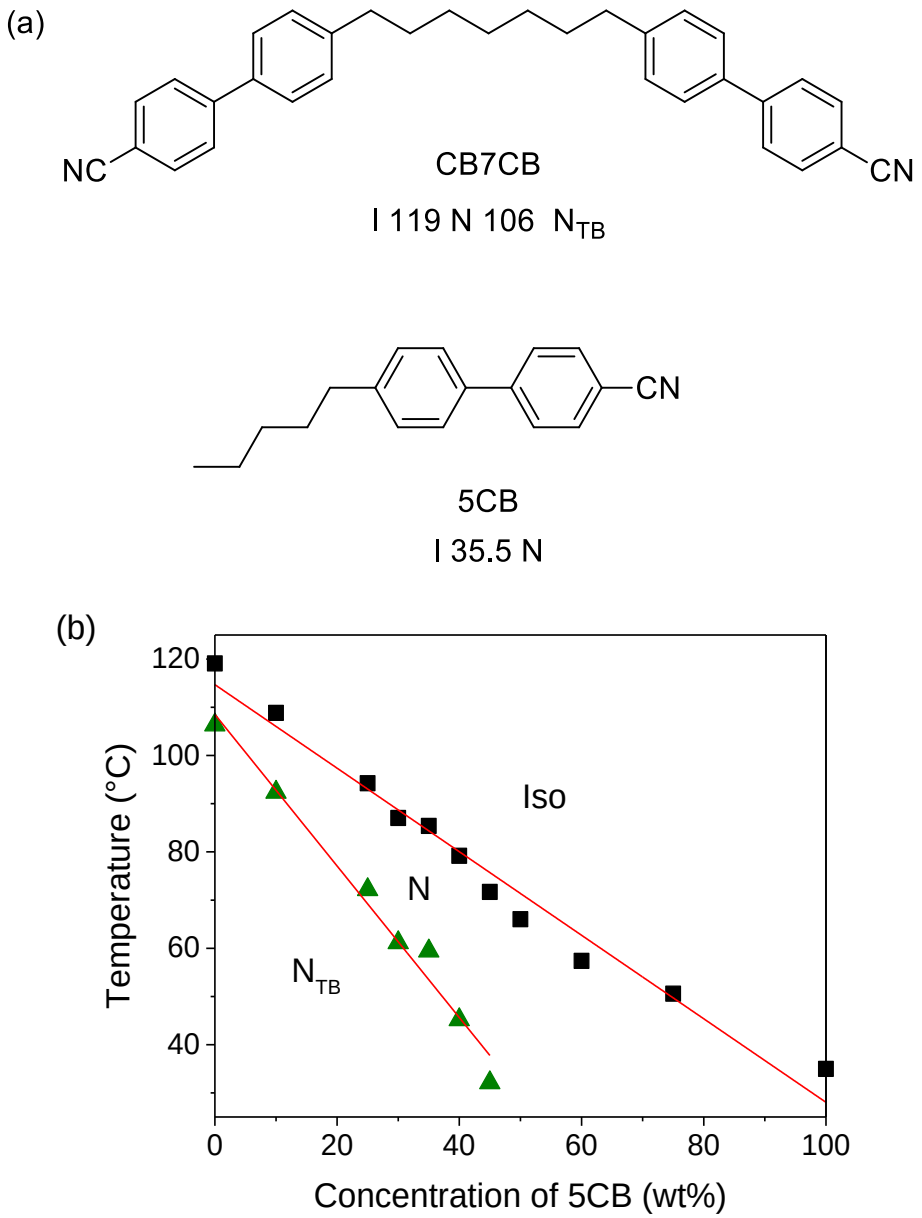

Figure 3.3: (a) Chemical structures and phase sequence of CB7CB and 5CB. (b) Phase diagram of the binary mixtures of CB7CB and 5CB obtained using POM. The lines represent linear fits to both the Iso-N and N-NT$_B$ transition temperatures.

3.2.2 Differential scanning calorimetry

Table 3.1 lists the phase transition temperatures of the pure CB7CB and 5CB liquid crystals and their mixtures, as well as phase transition enthalpies (ΔH) obtained from the second cooling cycles of differential scanning calorimetry (DSC) experiments. Crystallisation temperatures are not reported as the samples tend to supercool. DSC curves of the second heating and cooling cycles of CB7CB, 5CB and mixtures M10 and M40 are provided in Appendix I.

Table 3.1: A list of transition temperatures (in °C, obtained using POM) and enthalpies (Δ*H*) of phase transitions in kJ/mol (obtained from a single measurement using DSC) for the second cooling cycles (10 °C/min rate) of binary CB7CB+5CB mixtures. T_{NI} – nematic to isotropic phase transition temperature; $T_{N\text{-}N_{TB}}$ – nematic to N_{TB} phase transition temperature. Values that were not measurable are represented with a dash (-).

Compound	5CB (wt%)	T_{NI}	Δ*H*	$T_{N\text{-}N_{TB}}$	Δ*H*
CB7CB	0	119.1	0.90	106.3	1.19
M10	10	108.8	0.68	92.4	0.46
M25	25	94.3	0.62	72.2	0.18
M30	30	87.0	0.69	61.2	0.16
M35	35	85.4	0.50	59.4	no peak
M40	40	79.2	0.60	45.2	no peak
M45	45	71.7	0.26	32.1	no peak
M50	50	66.0	0.46	-	-
M60	60	57.4	0.55	-	-
M75	75	50.6	0.71	-	-
5CB	100	35.0	0.58	-	-

The DSC curve of CB7CB shows a clear first order N-N_{TB} phase transition with an associated enthalpy of 1.19 kJ/mol. Furthermore, the magnitude of heat capacity for the N-N_{TB} transition in CB7CB is higher than that of other dimeric liquid crystals which exhibit the N_{TB} phase.[166] It is to be noted that in pure CB7CB, the enthalpy of the isotropic to nematic transition (0.90 kJ/mol) is slightly lower than the N to N_{TB} transition (1.19 kJ/mol). This was also the case for the second heating cycle, in which the enthalpies of the N-Iso and N_{TB}-N transitions were 0.75 kJ/mol and 0.92 kJ/mol, respectively. The pure CB7CB liquid crystal has been investigated by DSC before and the enthalpy of phase transition mentioned in this work are comparable to previous studies.[141,167]

Figure 3.4 shows plots of enthalpies and entropies (inset) of the Iso-N and N-N_{TB} phase transitions of the binary mixtures as a function of concentration, obtained from single measurements. As the concentration of 5CB increases, on the left-hand side of

the diagram in Figure 3.4, the Iso-N enthalpies decrease from being 0.90 kJ/mol for pure CB7CB, to 0.26 kJ/mol for 45 wt% of 5CB in CB7CB. The corresponding entropies of isotropic-nematic phase transitions (given as an inset in Figure 3.4) also show a similar trend, from 0.28 (for pure CB7CB) to 0.09 (for mixture M45; 45 wt% of 5CB in CB7CB). On the right-hand side of the enthalpy and entropy diagrams, as the concentration of 5CB increases, an increase in both the enthalpy and entropy of the Iso-N transition is observed. The scatter of the entropies of the Iso-N transition in the binary mixtures is in the range 0.09–0.27 and the enthalpies are of similar magnitude across the phase diagram. It is important to emphasise that, as the concentration of 5CB increases, the energies associated with the N-N_{TB} phase transition are *reduced significantly*, from 1.19 kJ/mol for pure CB7CB to 0.16 kJ/mol for M30 (30 wt% of 5CB in CB7CB), as shown in Figure 3.4. The corresponding entropy of the N-N_{TB} transition also decreases from 0.38 for pure CB7CB to 0.06 for mixture M30 (Figure 3.4 inset). It is to be noted that when the concentration of 5CB is increased beyond 30 wt%, no measurable enthalpies for the N-N_{TB} transition were observed: mixtures M35, M40 and M45 do not show a discernible N-N_{TB} transition peak in their DSC curves (for the DSC curve of mixture M40, see Appendix I). However, in all three mixtures, at the N-N_{TB} phase transition, clear textural changes between the nematic and N_{TB} phases are observed using POM, with focal conic and rope-like textures characteristic of the N_{TB} phase. As the concentration of 5CB increases in the binary mixtures, the entropy associated with the N-N_{TB} phase transition decreases (the energy difference between the N and N_{TB} phases decreases). This indicates that an increase in 5CB concentration results in the N-N_{TB} transition becoming more second order or weakly first order (compared to a clear first order N-N_{TB} transition in pure CB7CB). On further increasing the 5CB concentration (≥ 50 wt%), the mixtures exhibit only the nematic phase above room temperature and the enthalpies of the isotropic-nematic transition show a slight increase (see M50, M60 and M75 in Table 3.1, and Figure 3.4). Further, the enthalpy of the Iso-N transition in M50 is 0.12 kJ/mol lower than that of pure 5CB. This might be due to the fact, that compared to the sharper Iso-N transition peak observed for 5CB, where the width of the peak ΔT = 6 °C, the DSC curve of M50 shows a broader Iso-N transition peak with ΔT = 10 °C (ΔT is the difference in the two temperatures between which the transition peak is integrated to obtain enthalpy values). Mixture M60 also shows a broad isotropic to nematic transition peak, having ΔT = 13 °C.

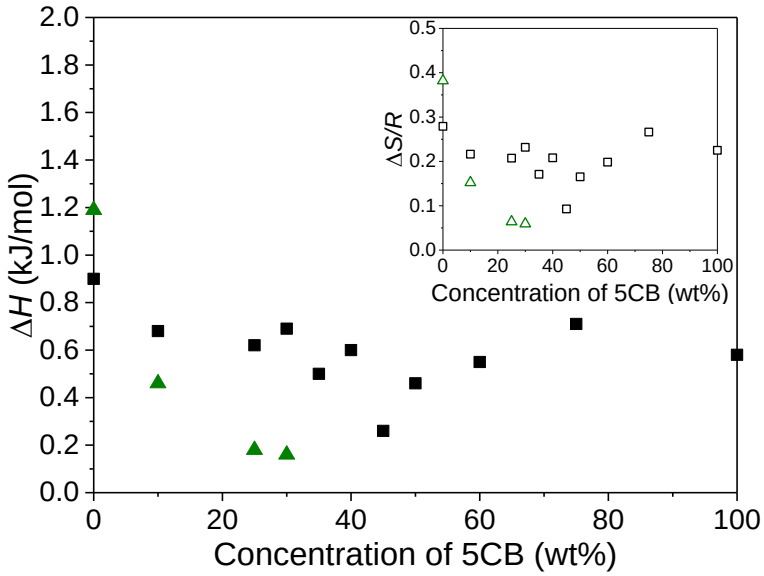

Figure 3.4: Plots of enthalpies (ΔH) and dimensionless entropies ($\Delta S/R$; inset) of phase transitions for binary CB7CB+5CB mixtures as a function of concentration. Values were obtained from single measurements (second cooling cycle). Squares and triangles represent Iso-N and N-N_{TB} phase transitions, respectively.

3.2.3 Dielectric spectroscopy

The plots in Figure 3.5 show the real part of the dielectric permittivity (ε') at 10 kHz as a function of reduced temperature and only the isotropic and nematic phases are labelled. Closed symbols represent $\varepsilon'_{\perp}$ (obtained by applying 0.1 V_{RMS} to the device) and open symbols represent $\varepsilon'_{||}$ (obtained by applying 20 V_{RMS} to the device; for more information, see section 2.3.3). Figure 3.5a is the permittivity data for pure 5CB and mixtures M50, M60 and M75, and these materials exhibit only the nematic phase above room temperature. The dielectric permittivity data for the mixtures which exhibit both the N_{TB} and nematic phases is split into two plots for clarity, which are given in Figure 3.5b and Figure 3.5c. Pure 5CB and the two mixtures M60 and M75 (that exhibit the nematic phase only) have similar isotropic permittivities, as shown in Figure 3.5a. On cooling from the isotropic phase, $\varepsilon'_{\perp}$ (closed symbols) decreases in the nematic phase for all binary mixtures and pure materials (shown in all plots in Figure 3.5), whereas $\varepsilon'_{||}$ (open symbols) increases in Figure 3.5a,b. This indicates a positive dielectric anisotropy for the materials in their nematic phase across the temperature range. On the other hand, pure CB7CB and mixtures M10, M25 and M30 (Figure 3.5c) show a decrease in $\varepsilon'_{||}$ with decreasing temperature in the nematic phase (more details are provided later). With respect to the permittivity in the N_{TB} phase,

binary mixtures with a smaller 5CB concentration, i.e. M10, M25 and M30, show a significant drop in $\varepsilon'_{||}$ close to the N to N_{TB} phase transition (Figure 3.5c).

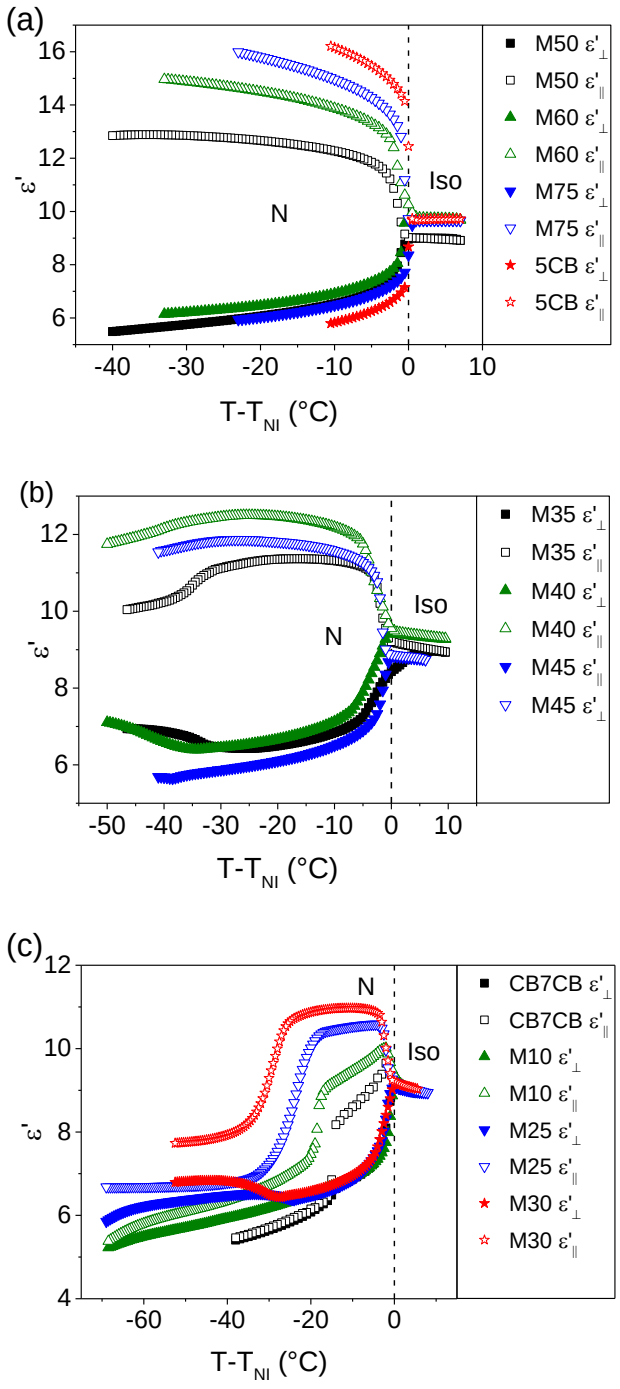

Figure 3.5: Plots of permittivity (ε') as a function of reduced temperature for both perpendicular ($\varepsilon'_{\perp}$) and homeotropic ($\varepsilon'_{||}$) alignment of the director at 10 kHz for: (a) 5CB, M50, M60, M75; (b) M35, M40, M45; (c) CB7CB, M10, M25, M30. Closed symbols represent $\varepsilon'_{\perp}$ and open symbols represent $\varepsilon'_{||}$.

A plot of dielectric permittivity ($\varepsilon'_{\perp}$ and $\varepsilon'_{||}$) as a function of concentration for a fixed temperature of T-T_{NI} = -5 °C is shown in Figure 3.6a. On increasing the concentration of 5CB, $\varepsilon'_{||}$ increases linearly by a considerable amount, from 9.08 for pure CB7CB to 15.48 for pure 5CB. The slope of the linear fit is 0.066. In contrast to this, the values of $\varepsilon'_{\perp}$ do not change significantly; instead, they show a slight decrease, from 7.25 in pure CB7CB, to 6.25 in pure 5CB. The change in permittivity in the nematic and N_{TB} phases results in a considerable deviation in the average permittivity from the isotropic phase (details discussed later). Figure 3.6b shows the dielectric anisotropy (Δε) as a function of 5CB concentration at T-T_{NI} = -5 °C in the nematic phases of the liquid crystals. Clearly, as more 5CB is added to the dimer, Δε increases linearly from 1.24 (in pure CB7CB), to 7.41 (in the 75 wt% 5CB mixture, M75). The slope of the linear fit is 0.079.

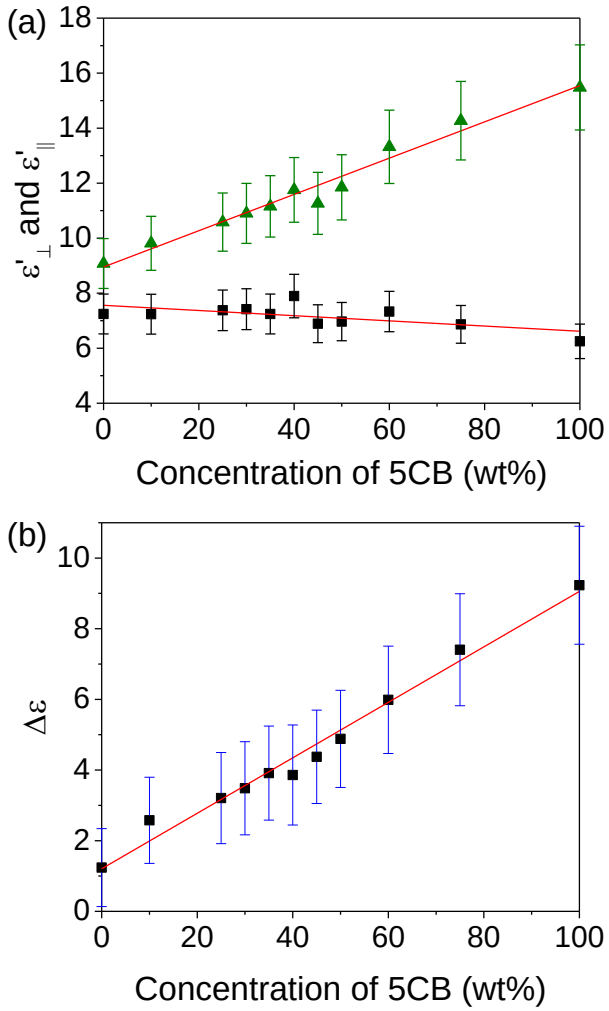

Figure 3.6: (a) $\varepsilon'_{\perp}$ (squares) and $\varepsilon'_{||}$ (triangles) as a function of concentration, and (b) dielectric anisotropy (Δε) as a function of concentration. For both plots, measurements were taken at T-T_{NI} = -5 °C at 10 kHz, and the straight lines represent linear fits to the data set.

Assuming cylindrical symmetry of the liquid crystals, the average dielectric permittivity is calculated as an average of the permittivity contributions measured along the long and short molecular axes: $\varepsilon'_{average} = (\varepsilon_{\parallel} + 2\varepsilon_{\perp})/3$. In pure cyanobiphenyls, a decrease in $\varepsilon'_{average}$ at the nematic to isotropic transition has been attributed to the antiparallel correlation of the dipole moment in the nematic phase of the liquid crystals. Likewise, a decrease in the average dielectric permittivity at the isotropic to nematic phase transition in cyanobiphenyl-based odd dimers (dimers having an odd number of alkyl units in the spacer chain) has been observed before.[157] Such behaviour has been attributed to a shift in the distribution of the conformer population at the isotropic to nematic phase transition. Specifically, a significant decrease of $\varepsilon'_{average}$ in pure dimeric liquid crystals indicates an increase in the average number of bent conformers. In general, the reduction in $\varepsilon'_{average}$ suggests a strong decrease in the mean-square dipole moment upon cooling from the isotropic state. The cyanobiphenyl-based dimers with an odd number of spacer units exhibit bent and hairpin conformations. The bent conformers have a zero mean-square dipole moment if the angle between the terminal dipoles is greater than 90°. This gives rise to a non-zero contribution to the orientational dielectric permittivity. In contrast, hairpin conformers have a small angle between the terminal polar groups, resulting in a large mean-square dipole contribution to $\varepsilon'_{||}$, and hence to $\varepsilon'_{average}$.

Figure 3.7a-d show plots of the real part of the dielectric permittivity and the average value as a function of temperature. Figure 3.7a corresponds to M25 – a mixture exhibiting the nematic and N_{TB} phases, and Figure 3.7b corresponds to M50 – a mixture exhibiting only the nematic phase. Dielectric permittivity plots for pure CB7CB and 5CB have also been presented for comparison in Figure 3.7c and Figure 3.7d, respectively. The mixture M50 (Figure 3.7b), which only exhibits the nematic phase, behaves in a similar way to pure 5CB (Figure 3.7d), showing very little change in the average dielectric permittivity across the temperature range of the isotropic and nematic phases (Figure 3.7b, open triangles). On the other hand, the mixture M25 (Figure 3.7a) shows a significant reduction in $\varepsilon'_{average}$, which is similar to the behaviour of pure CB7CB (Figure 3.7c). It should be noted that at lower temperatures in the N_{TB} phase of CB7CB, Δε reduces considerably and becomes zero, indicating the possibility of dual frequency responses. In the N_{TB} phase of the binary mixtures, however, Δε remains positive throughout the temperature range. It should also be noted that permittivity measurements given here correspond to a frequency of 10 kHz, as opposed to permittivities obtained in the range 1 MHz to 1.8 GHz in literature.[128]

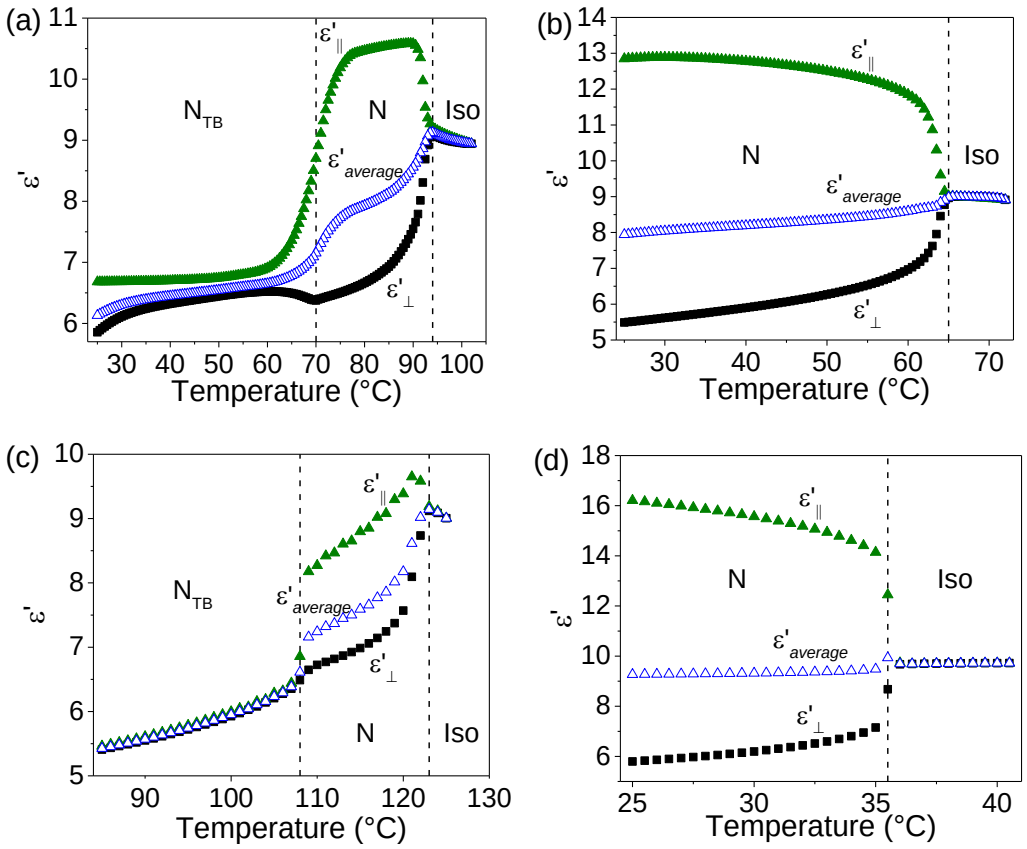

Figure 3.7: Plots of parallel ($\varepsilon'_{||}$), perpendicular ($\varepsilon'_{\perp}$) and average permittivity ($\varepsilon'_{average}$) at 10 kHz measured over the isotropic, nematic and twist-bend nematic phases for: (a) M25; (b) M50; (c) CB7CB; (d) pure 5CB.

A plot of average permittivity as a function of reduced temperature for a set of binary mixtures is given in Figure 3.8a. Closed symbols represent mixtures that only exhibit the nematic phase and open symbols represent mixtures with both the nematic and N_{TB} phases. As the temperature decreases, the mixtures which form the N_{TB} phase (M10, M30 and M40) show a clear reduction in the average dielectric permittivity. Figure 3.8b shows the average permittivity as a function of concentration at various temperatures below T_{NI}. A linear increase in $\varepsilon'_{average}$ as a function of composition is seen for binary mixtures exhibiting the N_{TB} phase (0 – 40 wt% 5CB), with $\varepsilon'_{average}$ increasing from 7.77 for pure CB7CB to 9.07 for the 40 wt% mixture, where both values correspond to $\varepsilon'_{average}$ at $T-T_{NI} = -6$ °C. The $\varepsilon'_{average}$ values for the 45 wt% and 50 wt% 5CB mixture further decrease (compared to the 40 wt% mixture), and then there is a sudden increase in $\varepsilon'_{average}$ for the 60 wt% 5CB mixture. The 60 wt% and 75 wt% mixtures have an average permittivity very similar to those of pure 5CB.

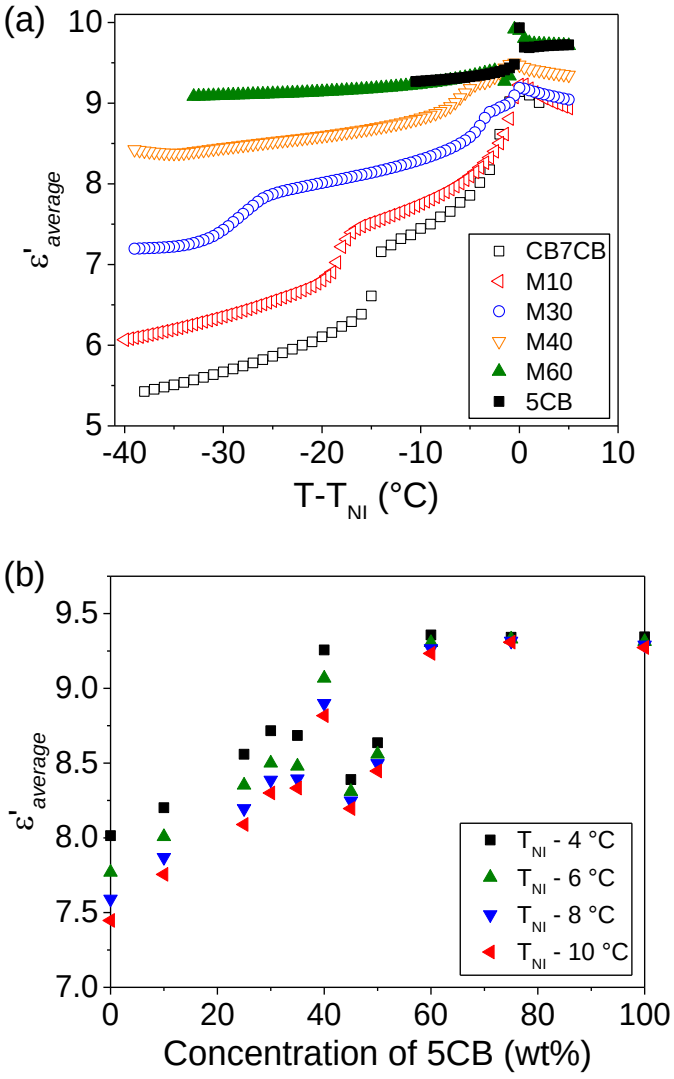

Figure 3.8: Plots of average permittivity ($\varepsilon'_{average}$) at 10 kHz measured over temperatures of the isotropic, nematic and N_{TB} phases: (a) as a function of reduced temperature, and (b) as a function of concentration of 5CB in the nematic phase.

The imaginary part of the dielectric permittivity (ε'') was measured as a function of frequency for all binary mixtures and pure materials in planar and homeotropic devices. In a planar device, for pure 5CB and mixtures exhibiting only the nematic phase, such as M50, M60 and M75, there are no relaxations observed within the measured frequency window. In contrast, pure CB7CB and mixtures exhibiting the N_{TB} phase do show a single relaxation peak (P1) in the measured frequency window. A relaxation peak was observed in both planar ($P1_{\perp}$) and homeotropic ($P1_{||}$) device geometries at temperatures corresponding to the N_{TB} phase (mixture M45 in a planar device, however, did not show a relaxation peak). A representative plot of ε'' as a function of frequency for the binary N_{TB} mixture M25 is given in Figure 3.9. As the sample is cooled from the isotropic state, no relaxations were observed in the

frequency range 1 kHz to 2 MHz in the nematic phase, however, a relaxation peak ($P1_{\perp}$) appears close to the nematic to N_{TB} phase transition. On further cooling, $P1_{\perp}$ shifts to lower frequencies, falling between the 10^4–10^5 Hz frequency range at ~25 °C (marked with a rectangle in Figure 3.9).

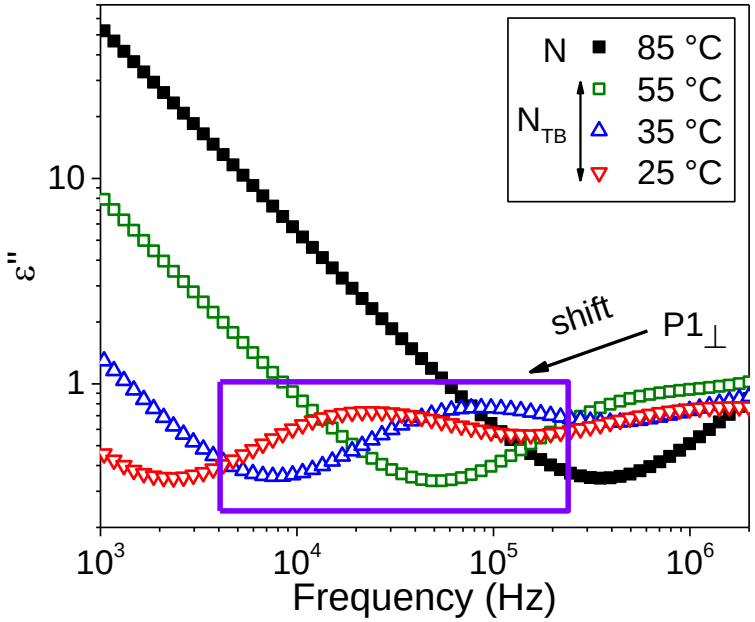

Figure 3.9: Plots of the imaginary part of the dielectric permittivity (ε'') as a function of frequency in the mixture M25 (25 wt% 5CB in CB7CB), measured in a 10 μm planar cell. The relaxation peak is labelled with a rectangle.

The dielectric loss was fitted to the Havriliak-Negami equation[118] (2.8) to obtain the relaxation frequencies (f_R) and dielectric strengths ($\delta\varepsilon$) of peak P1. The relaxation frequency and dielectric strength of P1 are given as a function of reduced temperature in Figure 3.10 for CB7CB and all binary mixtures in which the N_{TB} phase is observed. Figure 3.10a,b show the relaxation frequency and dielectric strength of $P1_{\perp}$ and Figure 3.10c,d show the same for $P1_{||}$. The lowest temperature at which dielectric properties are measured ranges between 25 – 45 °C, hence the temperature windows given in Figure 3.10 vary. The most important feature to note is that the relaxation frequencies of the dimer and all binary mixtures (M10 – M45, irrespective of the alignment of the director) decrease on cooling, as is shown in Figure 3.10a,c. The dielectric strength given in Figure 3.10b,d generally increases on cooling, and also tends to increase in value as the concentration of 5CB in the mixtures increases. However, in Figure 3.10b, the dielectric strength of $P1_{\perp}$ in pure CB7CB (square symbols) shows a slight decrease (at $T\text{-}T_{N\text{-}N_{TB}}$ = -28 °C, $\delta\varepsilon$ = 0.11 and at $T\text{-}T_{N\text{-}N_{TB}}$ = -58 °C, $\delta\varepsilon$ = 0.10). The relaxation peak emerges at different frequencies for different mixtures. For example, in Figure 3.10c,

M25 becomes measurable at a higher frequency than CB7CB, but also has a smaller frequency window compared to CB7CB. A link can be made between the concentration of 5CB in the mixtures and the temperature at which $P1_{\perp}$ emerges in the measurable frequency window in Figure 3.10a: as the concentration of 5CB decreases, the temperature at which P1 becomes measurable shifts further away from the N-N_{TB} phase transition. For example, for mixture M35, peak $P1_{\perp}$ becomes measurable at $T\text{-}T_{N\text{-}N_{TB}}$ = -5 °C, whereas for CB7CB, the peak becomes measurable at $T\text{-}T_{N\text{-}N_{TB}}$ = -28 °C. Mixture M45 (45 wt% 5CB in CB7CB) in Figure 3.10c also shows $P1_{||}$ in the nematic phase (close to the N-N_{TB} transition) as well as in the N_{TB} phase (the boundary between the N and N_{TB} phases is represented with a vertical, dashed line on the graph).

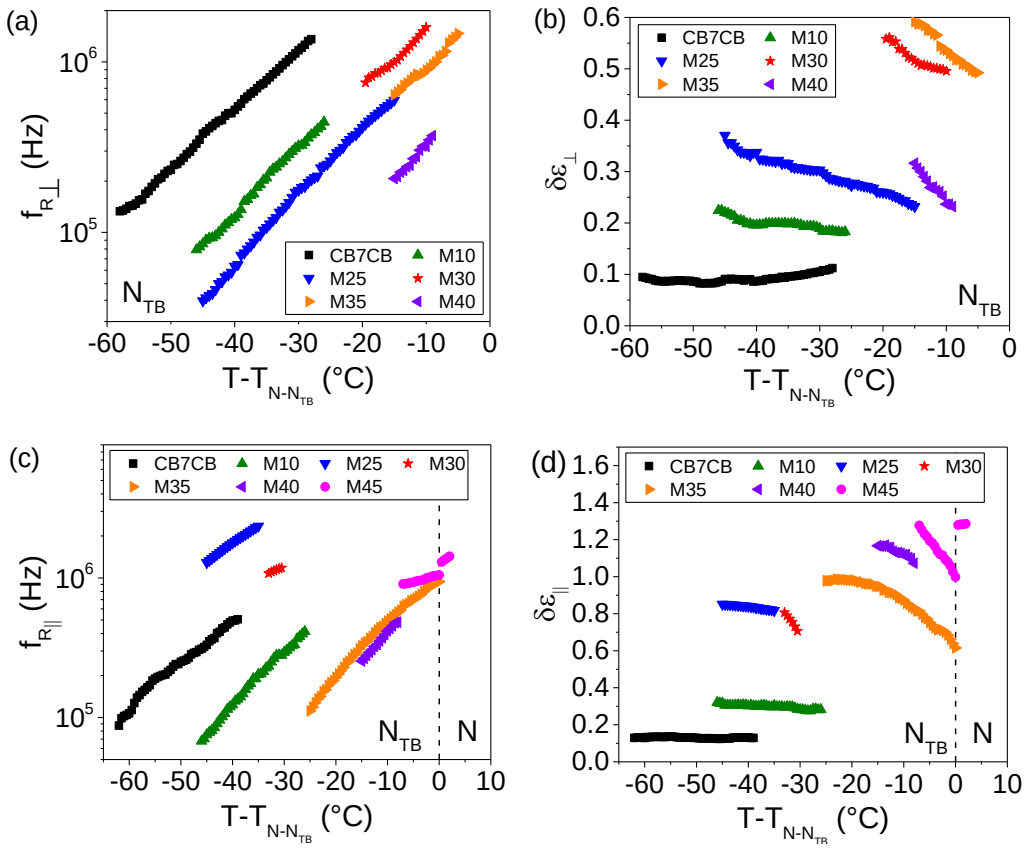

Figure 3.10: (a) Relaxation frequency (f_R) as a function of reduced temperature for perpendicular alignment of the director; (b) dielectric strength ($\delta\varepsilon$) as a function of reduced temperature for perpendicular alignment of the director; (c) f_R for parallel alignment of the director; (d) $\delta\varepsilon$ for parallel alignment of the director.

The dipole moment of the nematic and N_{TB} phases of CB7CB results in two relaxation modes involving rotational dynamics, represented in Figure 3.11. One is a precessional motion at high frequencies (in the order of ~10^7 Hz), where the rigid

cyanobiphenyl units rotate around the director. The other is a flip-flop motion (or 'end-over-end' motion) that occurs at lower frequencies (in the order of ~10^6 Hz), where the cyanobiphenyl units reorient parallel to the director (i.e. rotation around the short molecular axis).[158,163,168] For the pure dimer CB7CB and its binary mixtures with 5CB studied in this chapter, the relaxation peak P1 is temperature-dependent and shifts towards lower frequencies on cooling, as seen in Figure 3.10a,c. This relaxation is generally correlated to the flip-flop motion of the dipolar cyanobiphenyl groups parallel to the director, and has been observed in previous studies of dimers.[128,131,153,158] However, because the population of symmetric bent conformers is dominant in the N_{TB} phase, whereby the longitudinal dipole moment is zero, Merkel et al.[169,170] assign this lower frequency relaxation as the spinning rotation of the transverse component of the dipole moment, i.e. rotation of the long axis.

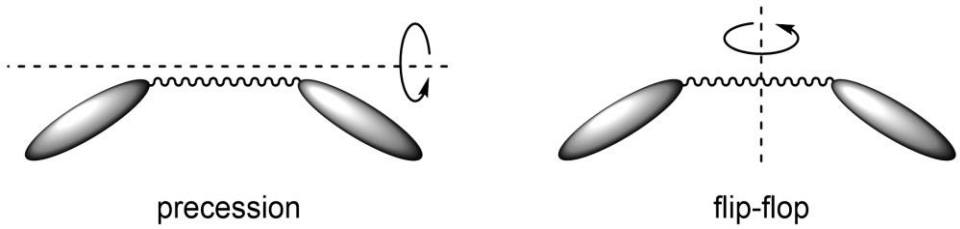

Figure 3.11: Schematic representation of precessional and flip-flop motions in symmetric dimers.

To understand the relationship between the activation energy of the relaxation process P1 and the concentration of 5CB in the binary mixtures, the temperature-dependent relaxation frequencies were fitted to the Arrhenius equation. A plot of $\log_{10}$ values of the relaxation frequencies of P1 as a function of the inverse of temperature (1/T) is given in Figure 3.12a for mixture M25 (25 wt% 5CB in CB7CB). Figure 3.12b shows $\log_{10}$ values of relaxation frequencies as a function 1/T for mixtures M10 – M40 that exhibit the N_{TB} phase. Activation energies (E_a) of P1 in the N_{TB} phase are calculated from the gradient of the $\log_{10}(f_R)$ vs 1/T plot, and are given in Figure 3.12c as a function of the concentration of 5CB, where errors calculated from the linear fit are also included. The graph in Figure 3.12c shows that for perpendicular alignment of the director (square symbols), the 40 wt% mixture has E_a = 31.90 ± 1.09 kJ/mol and E_a of pure CB7CB (32.90 kJ/mol) fits within the error of the measurements for the 40 wt% mixture. This implies that for all binary N_{TB} mixtures, the activation energy remains almost constant. This can be compared to the enthalpies of the isotropic to nematic phase transitions of the binary CB7CB and 5CB mixtures in Figure 3.4, which are all of similar magnitude across the phase diagram. The 25 wt% and 30 wt% of 5CB

mixtures in homeotropic devices both clearly deviate in comparison to their planar devices (Figure 3.12b,c). For the 25 wt% mixture in a planar device, E_a = 32.62 kJ/mol, and in a homeotropic device, E_a = 19.92 kJ/mol. For the 30 wt% mixture in a planar device E_a = 27.22 kJ/mol, whereas for the homeotropic device E_a = 12.07 kJ/mol. This could be due to the fact that for these two mixtures, the activation energies in homeotropic devices were calculated for a data set at a smaller temperature window compared to the planar devices – in Figure 3.12b, for the 30 wt% mixture, $P1_{||}$ is observed only across a 2.5 °C temperature window. It is also noted that the activation energies of the 10 wt% 5CB and the 40 wt% 5CB mixtures are very similar in both perpendicular and homeotropic devices.

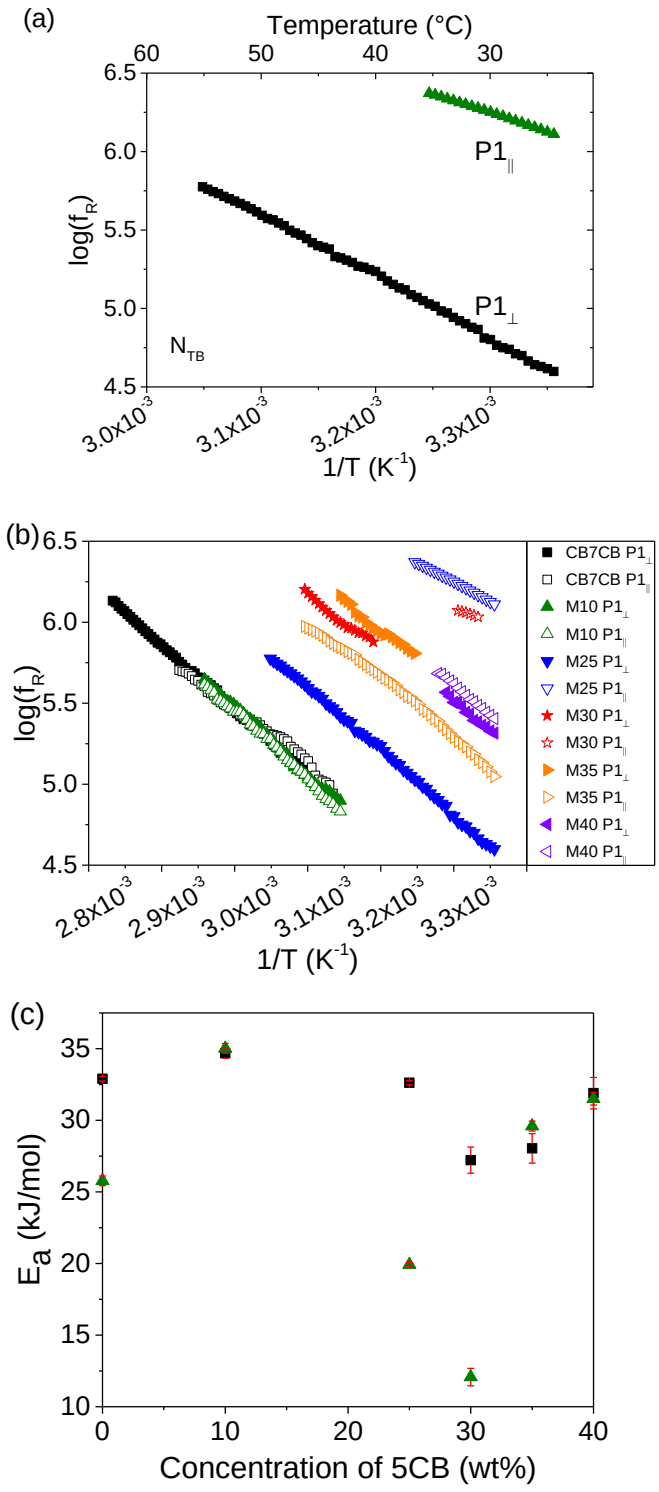

Figure 3.12: Relaxation frequency (f_R) as a function of 1/T, for both perpendicular and parallel alignment of the director of: (a) M25; (b) mixtures M10 – M40 exhibiting the N_{TB} phase. (c) Activation energy (E_a) as a function of 5CB concentration for pure CB7CB and mixtures M10 – M40. E_a is calculated for the N_{TB} phase and errors are obtained from the error of the linear fit. Squares and triangles represent activation energies for perpendicular and parallel alignment of the director, respectively.

3.3 Binary mixtures with a reactive mesogen

The previous section of this chapter discussed how the addition of a calamitic liquid crystal influences the twist-bend nematic phase. In this section, a series of binary mixtures of CB7CB and reactive mesogen RM257 were prepared to understand the influence that a photopolymerisable monomer has on the phase behaviour of the N_{TB} material, and this will be compared to the influence of the calamitic liquid crystal. Photopolymerisation of these CB7CB+RM257 mixtures will be carried out in Chapter 4. The reactive mesogen RM257 (introduced in section 1.6) is a bifunctional mesogen. It possesses two reactive groups (in this case acrylates) which can, in the presence of a photoinitiator, react to form a polymer network via photopolymerisation. The mixtures are labelled as 'PM' (polymerisable mixture), followed by a number standing for the concentration by weight (wt%) of RM257. A photoinitiator will be added to these mixtures in section 4.1 to form photopolymerised N_{TB} phases.

The chemical structures of CB7CB and RM257 are given in Figure 2.1 and the phase diagram of the binary CB7CB+RM257 mixtures is shown in Figure 3.13. Initially, as the concentration of RM257 is increased, there is a gradual decrease (by 7 °C) in the isotropic-nematic transitions (T_{NI}) for concentrations between 0 wt% and 30 wt% RM257. At higher concentrations, T_{NI} increases to 18 °C above the minimum T_{NI}. The addition of the calamitic liquid crystal in Figure 3.3 results in a linear decrease in T_{NI}. As the concentration of monomer increases, the N-N_{TB} transition temperature decreases linearly and the width of the nematic phase increases, which is also the case for mixtures of CB7CB and 5CB in Figure 3.3. At room temperature and above, the N_{TB} phase is observed in mixtures containing up to 40 wt% RM257, and at higher concentrations, only the nematic phase is observed. Similarly, in the case of mixtures with 5CB, the N_{TB} phase was observed in mixtures containing up to 45 wt% of 5CB (Figure 3.3). The N_{TB} phases in all binary CB7CB+RM257 mixtures supercool to room temperature and crystallise within a few hours. The width of the nematic phase increases considerably as the monomer concentration increases, ranging approximately 70 °C at 40 wt% RM257. Interestingly, in the mixture PM30 (30 wt% RM257), an additional transition is observed at 45 °C, which corresponds to a transition from the N_{TB} phase to a smectic phase (Figure 3.14a).

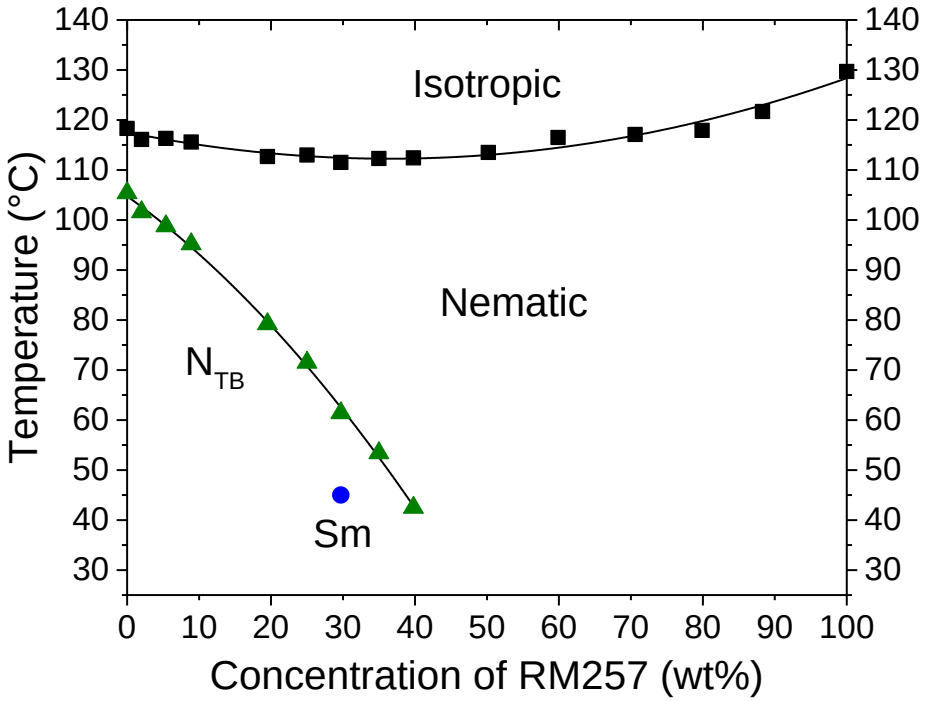

Figure 3.13: Phase diagram of binary CB7CB+RM257 mixtures. ■ – Isotropic-nematic transition (T_{NI}); ▲ – nematic-N_{TB} transition; ● – N_{TB}-smectic (Sm) transition. The lines serve as guides to the eye and do not represent a theoretical fit.

The smectic phase was also observed in mixtures containing 25 wt%, 35 wt% (Figure 3.14b) and 40 wt% (Figure 3.14c) of RM257. However, these data points are omitted in the phase diagram in Figure 3.13, as the N_{TB}-Sm transition was highly second order and determining the exact transition temperature was difficult. A 2 µm planar antiparallel rubbed AWAT cell was filled with the mixture PM30 and an electric field was applied at three temperatures on cooling, at 90 °C, 55 °C and 20 °C, corresponding to the nematic, N_{TB} and smectic phase, respectively. At 20 $V_{0\text{-pk}}$, the nematic phase almost completely switches (Figure 3.14d), whereas the N_{TB} (Figure 3.14e) and smectic phases (Figure 3.14f) do not switch completely as they are more ordered than the nematic phase of the same material.

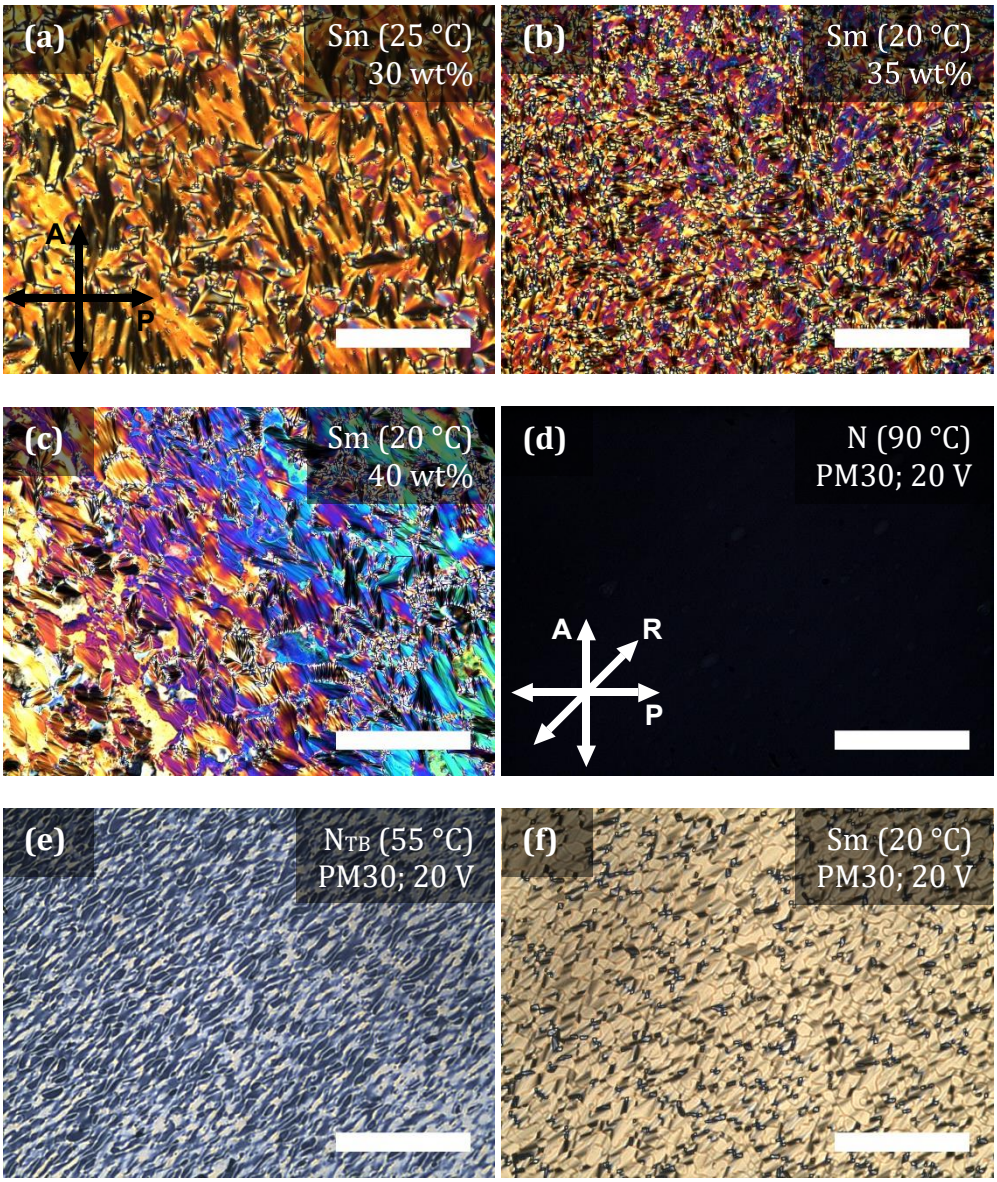

Figure 3.14: POM images of the smectic phase in CB7CB+RM257 mixtures between cover slips, with RM257 concentration of: (a) 30 wt% (PM30) at 25 °C; (b) 35 wt% at 20 °C; (c) 40 wt% at 20 °C. Mixture PM30 (30 wt% RM257) in a 2 µm planar cell at 20 $V_{0\text{-}pk}$ in the: (d) nematic phase at 90 °C; (e) N_{TB} phase at 55 °C; (f) smectic phase at 20 °C, which corresponds to the same phase as (a). The crossed polarisers and rubbing direction (R) are labelled and the length of the scale bar is 100 µm.

The nature of the phase transitions in the binary mixtures was further investigated by differential scanning calorimetry (DSC). Figure 3.15 shows the effect of monomer concentration on the enthalpies and entropies (Figure 3.15 inset) of phase transitions in the binary CB7CB+RM257 mixtures.

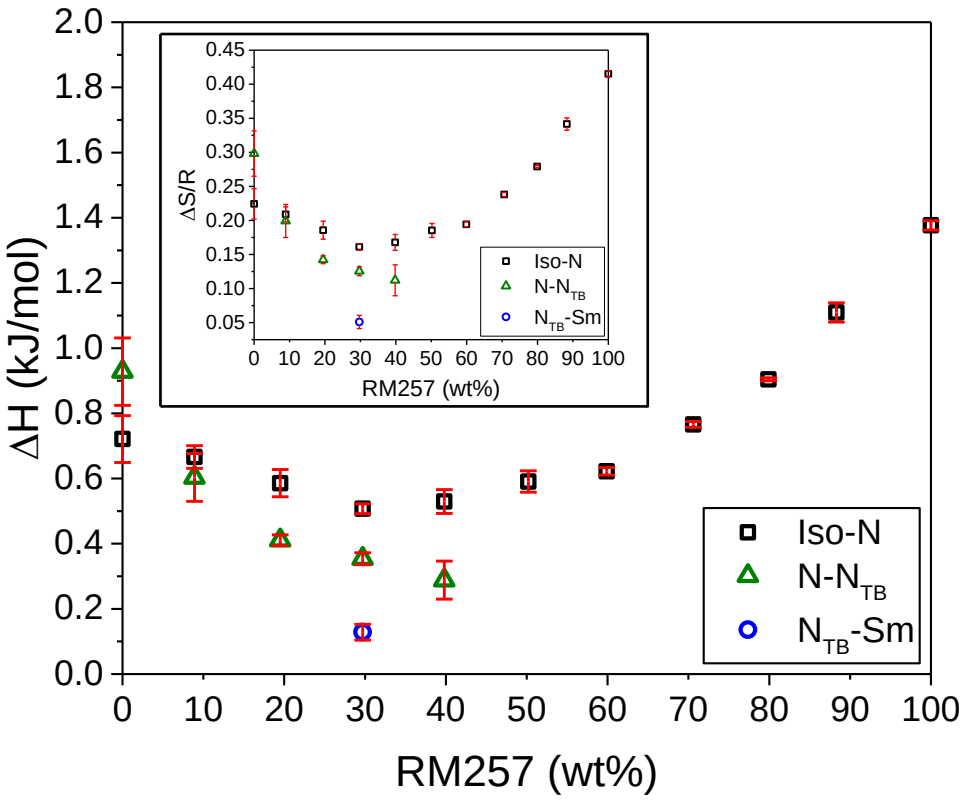

Figure 3.15: Plots of enthalpies and dimensionless entropies (inset) of the phase transitions of CB7CB and RM257 mixtures as a function of concentration. □ – Isotropic-nematic transition; △ – N to N_{TB} transition; ○ – N_{TB} to smectic transition. Errors were obtained from the standard deviation of corresponding phase transition enthalpies from 3 cooling cycles.

As the concentration of RM257 is increased, a linear decrease in N-N_{TB} transition enthalpies and entropies between 10 wt% and 40 wt% of RM257 is observed, similar to what is observed for mixtures of up to 30 wt% 5CB in Figure 3.4. The enthalpy of the N-N_{TB} transition of the mixture containing 30 wt% RM257 is approx. 3 times smaller than that of CB7CB. When 30 wt% of calamitic liquid crystal is added, however, the enthalpy of the N-N_{TB} transition is approx. 6 times smaller than that of pure CB7CB, as can be seen in Figure 3.4. For the PM30 sample, an additional peak in the DSC curve could be distinguished around room temperature (shown in Figure 3.16), with an associated enthalpy of 0.10 kJ/mol. This corresponds to the N_{TB} to smectic transition in the mixture, as seen using POM in Figure 3.14a. However, in the

PM40 mixture, a DSC peak corresponding to the N_{TB}-Sm transition was not observed, even though textural changes from a broken-fan like N_{TB} texture to smectic focal conics were observed by polarised optical microscopy (Figure 3.14c). Induced smectic phases have previously been observed in binary mixtures of N_{TB} materials.[171]

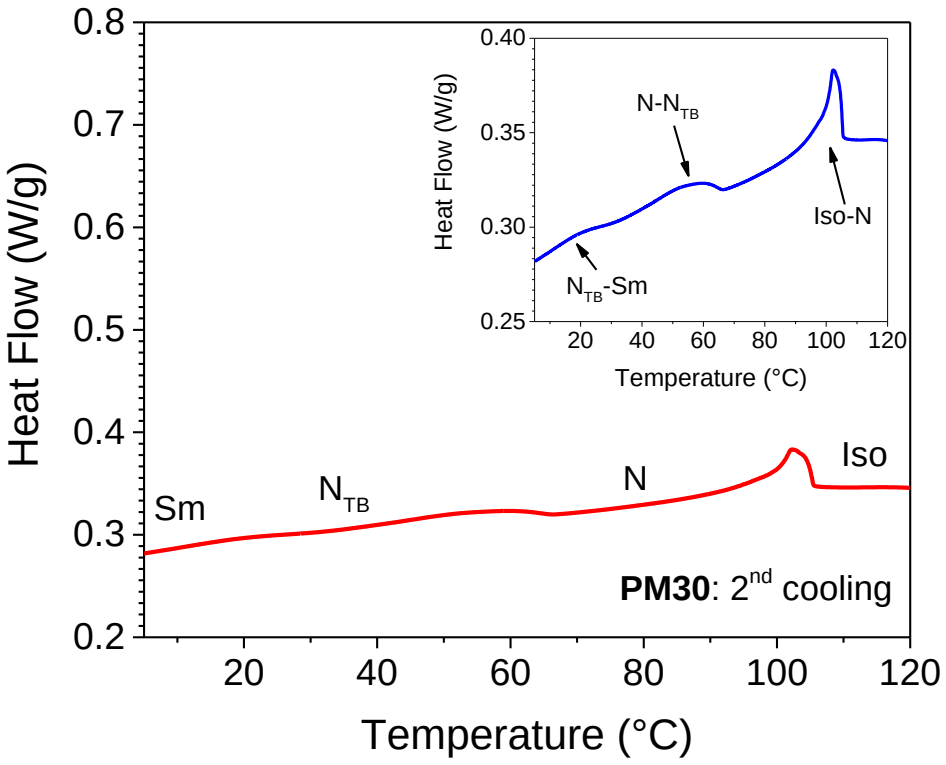

Figure 3.16: DSC curve of the second cooling cycle (10 °C/min) of PM30 (30 wt% RM257) with the different phases labelled (Iso – isotropic; N – nematic; N_{TB} – twist-bend nematic; Sm – smectic). A more defined DSC curve with arrows pointing to the transition peaks is included as an inset.

3.4 Summary of results

The results in this chapter are divided into two parts, both considering binary mixtures composed of CB7CB exhibiting the nematic and twist-bend nematic phases. Section 3.2 provided a detailed investigation of the thermal and dielectric properties of a series of binary CB7CB+5CB mixtures, with the aim to understand the influence of the calamitic liquid crystal 5CB on the phase transition temperatures and dielectric properties of the dimeric liquid crystal. A phase diagram of the two-component system is presented in Figure 3.3b, which shows that the N_{TB} phase is observed (above room temperature) in mixtures of up to 45 wt% of 5CB. As the concentration of the calamitic liquid crystal is increased, there is a linear decrease in the phase transition

temperatures and an increase in the width of the nematic phase. For DSC measurements, an increase in the concentration of the calamitic liquid crystal resulted in a *significant decrease* in the associated energies of the N-N_{TB} phase transitions, compared to a first order transition seen in the pure dimer (with $\Delta S/R = 0.38$). No measurable enthalpies could be obtained for the N-N_{TB} transition at 5CB concentrations of more than 30 wt%, even though these mixtures showed a sharp transition between the nematic *schlieren* texture to the focal conic and rope-like textures of the N_{TB} phase when observed by POM.

The real and imaginary parts of the dielectric permittivity for both planar and homeotropic alignment of the liquid crystal in the nematic and N_{TB} phases of the binary mixtures showed two important features. The first was a significant decrease in the average dielectric permittivity as a function of temperature for mixtures forming the N_{TB} phase (see Figure 3.8a). Interestingly, this decrease was seen even in the nematic phase, prior to the N_{TB} transition and indicates an increase in the population of bent conformers. The second important feature was the observation of a single relaxation peak for all binary mixtures exhibiting the N_{TB} phase, which emerged in the N_{TB} phase and on decreasing the temperature shifted towards lower frequencies (in the 10^4–10^5 Hz range). A combination of these two features could be used to indicate the presence of a twist-bend nematic phase in the absence of POM and DSC measurements, and similar dielectric relaxations of N_{TB} materials will be discussed in Chapter 4. Relaxation frequencies (f_R) for all binary CB7CB+5CB mixtures and pure materials decreased on cooling from the isotropic state. The relaxation peak correlated to the flip-flop motion of the dipolar groups parallel to the director. The relaxation frequencies were fitted to the Arrhenius equation from which activation energies of mixtures exhibiting the N_{TB} phase were calculated. No significant variation in the activation energy was observed as the 5CB concentration was changed in the binary mixtures.

Section 3.3 provided an investigation into binary mixtures of CB7CB and monomer RM257, exhibiting the nematic and N_{TB} phases. Both the nematic and N_{TB} phases are observed in mixtures containing up to 40 wt% of RM257; all other mixtures exhibit only the nematic phase. As the concentration of RM257 increases, the nematic to twist-bend nematic transition temperatures decrease linearly and the width of the nematic phase increases significantly. This is also the case when the calamitic liquid crystal is added to CB7CB. The nature of the phase transitions in the binary mixtures was further investigated by DSC, and a decrease in the N-N_{TB} transition enthalpies and entropies between 0 wt% and 40 wt% of RM257 is observed. Compared to the

addition of polymerisable monomer to CB7CB, the addition of calamitic liquid crystal results in a greater decrease in the enthalpy of the N-N_{TB} transition. An induced smectic phase was observed below the N_{TB} phase for mixtures containing between 25 wt% and 40 wt% of RM257 – textural changes from a broken-fan N_{TB} texture to smectic focal conics were observed by POM. However, these transitions were very smooth and so a DSC second order transition from the N_{TB} to the smectic phase could only be distinguished for the 30 wt% mixture. In the following chapter, these binary CB7CB+RM257 mixtures will be used to create photopolymerised N_{TB} phases and templates of the N_{TB} phase.

CHAPTER 4:
Templating the nanostructures of the twist-bend nematic phase

This chapter establishes a procedure for templating the ultrastructure of the twist-bend nematic (N_{TB}) phase. Building on the experimental results discussed in the previous chapter, the nematic and N_{TB} phases mentioned in this chapter are formed from a mixture of CB7CB and 5CB. The aim of choosing the N_{TB} phase for templating includes gaining a deeper understanding of its mechanical and electrical properties, which are difficult to measure conventionally due to the high viscosity of the phase. The templates are formed via photopolymerisation, which allows for surface modification of the polymer using the host liquid crystal phase. A detailed investigation of the physical and structural properties of the templated N_{TB} phase will be provided and comparisons will be made with a template of the nematic phase. The templates are refilled with the nematic liquid crystal 5CB to understand the influence of the templated structures on the physical properties of the refilled liquid crystal.

4.1 Photopolymerised twist-bend nematic phases

4.1.1 Advantages of photopolymerisation

With the exception of a trimeric liquid crystal that has been shown to exhibit the twist-bend nematic phase at room temperature,[143] the N_{TB} phase typically exists at elevated temperatures and over a narrow temperature interval below the isotropic or nematic phases. In addition, the phase generally supercools to room temperature and crystallises within a few hours, as observed for N_{TB} materials previously discussed in Chapter 3. In order to template the N_{TB} phase and/or to ensure that the N_{TB} materials are suitable for practical applications, materials that exhibit the N_{TB} phase are required to (1) be stable at room temperature, (2) exhibit the phase across a broad range of temperatures, and (3) be readily made from commercially available precursors. One way of meeting these requirements is to thermodynamically stabilise the liquid crystal phase using reactive mesogens, as discussed in section 1.6. In principle, this approach can also be applied to the twist-bend nematic phase in order to extend the temperature range over which the phase is stable. Photopolymerisation

of the N_{TB} phase has previously been carried out by Panov et al.[172] to demonstrate its usefulness in exploring complex hierarchical structures of the N_{TB} phase.

4.1.2 Thermal stability of photopolymerised N_{TB} phases

Following the results obtained in Chapter 3 for binary mixtures composed of CB7CB and RM257 (labelled as 'PM', followed by a number standing for the concentration by weight of RM257), photoinitiator BME (benzoin methyl ether) was added to the mixtures that exhibited the N_{TB} phase. The chemical structures of all of the materials are provided in Figure 2.1. Homemade planar cells of 3 μm spacing were filled in the isotropic phase and polymerised in the supercooled N_{TB} phase.

The thermal stability of the polymerised samples was investigated. It was found that when the polymerised samples were left at room temperature, the N_{TB} phase remained stable for the whole period of testing, i.e. several months, and so will be referred to as 'metastable'. In comparison, the supercooled N_{TB} phases, before polymerisation, crystallised within a few hours. Also, the polymerised samples exhibit the N_{TB} phase over a temperature range of up to 80 °C (calculated from room temperature to the N-N_{TB} phase transition temperature on cooling). There is very little change in the nematic-isotropic transition temperature of the polymerised samples compared to before polymerisation. However, the N-N_{TB} transition temperature in the polymerised samples increases slightly in mixtures composed of a smaller concentration of monomer: by 2.5 °C in the 2 wt% mixture and by 4.5 °C in the 5.5 wt% mixture.

The behaviour of polymerised samples upon heating from the metastable N_{TB} phase will now be discussed. Polymerised samples with <10 wt% monomer show clear textural changes from the rope-like N_{TB} texture at room temperature, to the homogeneous nematic texture, and subsequently to the isotropic dark texture. An example of the phase transitions is given in Figure 4.1 for the polymerised 2 wt% monomer mixture (PM2).

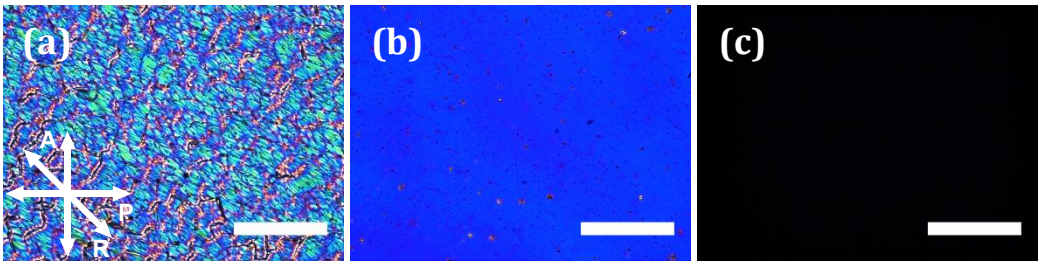

Figure 4.1: POM images of the polymerised PM2 (2 wt% RM257) sample on heating: (a) room temperature, (b) 105 °C, and (c) 110 °C. The crossed polariser (P) and analyser (A) are labelled, and the rubbing direction (R) is marked. The length of the scale bar is 100 μm.

Samples with higher monomer concentration (≥10 wt%) also indicate similar interesting characteristics. These are shown in the POM images in Figure 4.2 for the polymerised PM20 sample. Polymerised PM20 exhibits typical N_{TB} rope-like textures at 25 °C (Figure 4.2a). On heating, the birefringence of the sample changes very slightly in the temperature range between 25 °C and 105 °C. At temperatures above ~105 °C, there is a noticeable change in birefringence (see Figure 4.2b). Further heating results in a more evident decrease in birefringence at temperatures above ~118 °C (Figure 4.2c). It should be noted that the temperatures 105 °C and 118 °C are close to the N_{TB}-N and N-Iso transition temperatures in pure CB7CB. This transition has been further confirmed by DSC experiments, which are summarised in Table 4.1. The complementary DSC curves for the second heating cycles of pure CB7CB and polymerised PM20 are provided in Appendix I. Two enthalpy peaks (Table 4.1) are observed for the polymerised PM20 sample, which correspond to temperatures at which the N_{TB}-N and N-Iso transitions are observed in pure CB7CB.

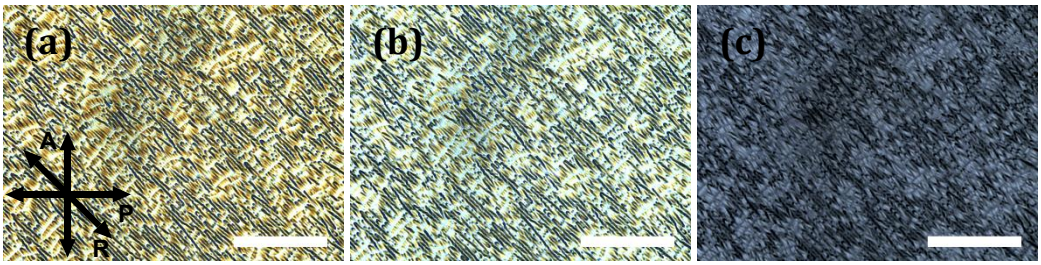

Figure 4.2: POM images of the N_{TB} textures of polymerised PM20 in a 3 μm planar cell at: (a) 25 °C, (b) 115 °C, (c) 120 °C. The rubbing direction (R) is marked with respect to the crossed polarisers. The length of the scale bar is 100 μm.

Table 4.1: Enthalpy (ΔH) of phase transitions for pure CB7CB and the polymerised N_{TB} sample PM20 (CB7CB with 20 wt% RM257). Values were obtained from a single measurement second heating cycle. Iso – isotropic, N – nematic, N_{TB} – twist-bend nematic.

Sample	Temperature (°C)	ΔH (kJ/mol)
CB7CB (pure)	101.7 (N_{TB}-N)	0.75
	113.7 (N-Iso)	0.92
PM20 – polymerised	95.7	0.79
	109.9	0.49

In addition, in Figure 4.2c at 120 °C, which is above the isotropic transition temperature of pure CB7CB, the polymer network retains a small residual birefringence. Residual birefringence above the liquid crystal's clearing temperature is observed for all photopolymerised N_{TB} mixtures irrespective of the monomer concentration. This is also true for the 2 wt% sample (PM2) discussed earlier in this section, where residual birefringence is observed at 110 °C, but it is not clear in the image in Figure 4.1c due to the low concentration of monomer. In addition to the residual birefringence, for monomer concentrations ≥10 wt%, the polymer network also clearly shows the textural features of the N_{TB} phase even above 120 °C, as shown in Figure 4.2c. The residual birefringence observed in polymerised samples above the liquid crystal's clearing temperature is most likely due to the aligned polymer network inducing orientational order in the isotropic phase of the liquid crystal, at the interface of the liquid crystal and polymer. Such residual birefringence has been noted previously for polymer-stabilised liquid crystals.[37,173]

4.1.3 Comparisons between polymerised N_{TB} and SmA phases

To provide a comparison with polymerised N_{TB} phases, polymerised SmA phases were also tested. Samples composed of the liquid crystal 8CB and RM257 monomer in 98/2 wt% and 90/10 wt% ratios were prepared, and they are named 8CB-RM-2 and 8CB-RM-10, respectively. Before polymerisation, the mixtures exhibit both the nematic and SmA phases: the nematic to SmA transition in 8CB-RM-2 is at 30.2 °C and in 8CB-RM-10 it is at 23.1 °C. The mixtures were then polymerised in the SmA phase and heated from room temperature. POM images of the polymerised SmA phases of 8CB-RM-2 and 8CB-RM-10 contained in planar cells are given in Figure 4.3.

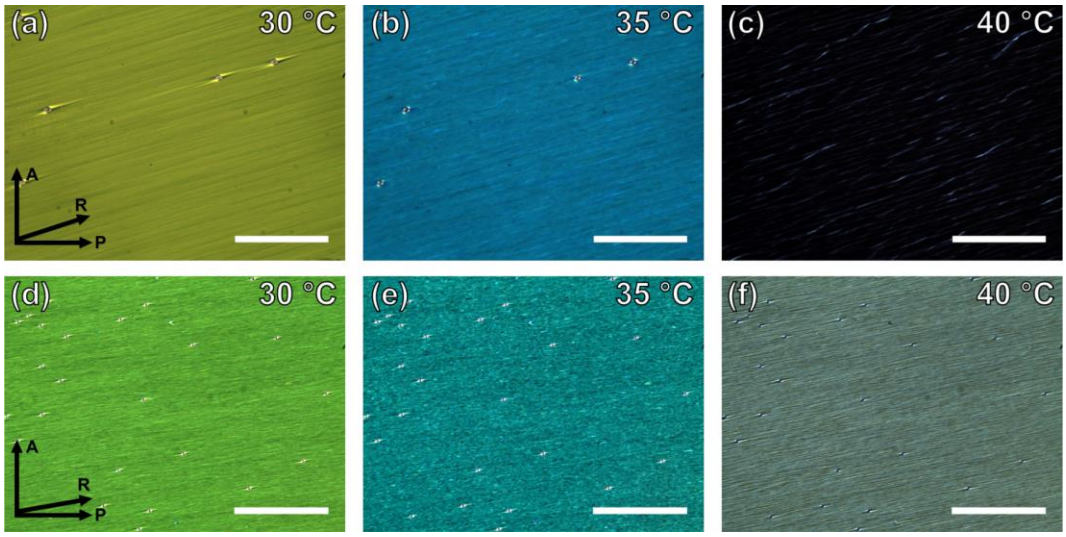

Figure 4.3: POM images of the polymerised SmA phase of 8CB-RM-2 and 8CB-RM-10, on heating in a 5µm planar cell. (a), (b) & (c) The sample with 2 wt% monomer (8CB-RM-2); the length of the scale bar is 100 µm. (d), (e) & (f) The sample with 10 wt% monomer (8CB-RM-10); the length of the scale bar is 200 µm. The rubbing direction R is labelled with respect to the crossed polarisers.

In both polymerised SmA samples, similar behaviour to the CB7CB mixtures occurs on heating: (1) a change in birefringence occurs at ~35 °C, a temperature close to the SmA-N transition of pure 8CB, (2) a significant decrease in birefringence is observed at ~40 °C (which corresponds to the T_{NI} of pure 8CB), and (3), the polymer networks retain the textural features of the SmA phase throughout the entire heating experiment, even above 40 °C. Also, the polymer networks in both the 2% and 10% polymerised SmA samples exhibit residual birefringence above the temperature corresponding to the isotropic transition of the pure liquid crystal (Figure 4.3c and Figure 4.3f), as was observed in polymerised N_{TB} samples (Figure 4.2c). The changes in birefringence that appear on heating both the polymerised N_{TB} and SmA samples suggest that the unpolymerised liquid crystals that are not a part of the polymeric network are transitioning to the isotropic state at these temperatures. This transition has been further confirmed by DSC experiments which are summarised in Table 4.2. The complementary DSC curves for the second heating cycles of pure 8CB and polymerised 8CB-RM-10 are provided in Appendix I. The polymerised 8CB-RM-10 sample shows one transition at 43.6 °C with an associated enthalpy of 0.70 kJ/mol (Table 4.2). Even though a clear change in birefringence is observed using POM at ~35 °C (Figure 4.3) a DSC peak corresponding to this transition was not distinguishable (note the small enthalpy of 0.07 kJ/mol associated with the SmA-N transition in pure 8CB). For the polymerised 8CB-RM-10 sample, even though a

SmA-N peak cannot be distinguished in DSC experiments, it can be deduced that there is a transition from the SmA to the N phase, based on changes in birefringence close to the temperature corresponding to the SmA to N transition of pure 8CB. The SmA phase in the 10% sample shows an increase in the width of the SmA phase. Before polymerisation, the N-SmA transition occurs at 23.1 °C and after polymerisation, changes in birefringence occur at ~35 °C, which is similar to the N-SmA transition of pure 8CB.

Table 4.2: Enthalpy (ΔH) of phase transitions for the second heating cycles of pure 8CB and polymerised 8CB-RM-10 (8CB with 10 wt% RM257) obtained from a single measurement. Iso – isotropic, N – nematic, SmA – smectic A.

Sample	Temperature (°C)	ΔH (kJ/mol)
8CB (pure)	34.1 (SmA-N)	0.07
	41.0 (N-Iso)	0.60
8CB-RM-10 – polymerised	43.6	0.70

It can be concluded that, the polymerised SmA samples optically behave similarly to the polymerised N_{TB} samples based on (1) the birefringence changes that occurs on heating at temperatures close to the SmA-N transition of pure 8CB, (2) the residual birefringence above the isotropic transition of the pure liquid crystals, and (3) phase transition peaks observed in DSC measurements,

4.1.4 Dielectric spectroscopy

A comparison of PM20 before and after polymerisation was made using dielectric spectroscopy and the data is given in Figure 4.4. Plots of permittivity (ε') at 10 kHz and 100 kHz as a function of temperature are given in Figure 4.4a and Figure 4.4c for PM20 before and after polymerisation, respectively. Dielectric loss as a function of frequency is also provided for PM20 before and after polymerisation, in Figure 4.4b and Figure 4.4d, respectively. The plot of permittivity as a function of temperature for PM20 before polymerisation in Figure 4.4a shows a similar trend to the graphs of $\varepsilon'_{\perp}$ as a function of temperature for binary CB7CB+5CB mixtures that exhibited the N_{TB} phase, discussed in section 3.2.3. As the temperature decreases in Figure 4.4a, a decrease in the permittivity at the isotropic to nematic phase transition is observed

at ~114 °C. There is a further decrease in permittivity at ~75 °C – in POM experiments, this temperature corresponds to the nematic to N_{TB} transition of PM20 before polymerisation. The relaxation peak labelled with a rectangle in Figure 4.4b is characteristic of the N_{TB} phase (as previously discussed in section 3.2.3); it emerges on cooling from the nematic phase and shifts towards lower frequencies on cooling.

After polymerising PM20, the graph of ε' as a function of temperature in Figure 4.4c resembles that of pure CB7CB (in Figure 3.7c). There is a change in permittivity at two points in the measured temperature window: one at ~115 °C and one just above 100 °C. These changes in permittivity can be compared to the POM experiments of polymerised PM20 in Figure 4.2, where a noticeable change in birefringence is observed at ~105 °C, and a more evident decrease in birefringence is observed at temperatures above ~118 °C. The plot of dielectric loss as a function of frequency for polymerised PM20 in Figure 4.4d also shows the characteristic N_{TB} relaxation peak (labelled with a rectangle) that shifts to lower frequencies on cooling to lower temperatures. The drop in permittivity in Figure 4.4a at ~75 °C (before polymerisation) has shifted considerably after polymerisation, where it appears just above 100 °C in Figure 4.4c. In addition, after polymerisation, the range of the nematic phase (labelled with vertical dashed lines) has decreased and the range of the N_{TB} phase has increased. This is because the isotropic transition before polymerisation is determined from the mixture of two liquid crystals, i.e. CB7CB and RM257, whereas after polymerisation, a polymer network is formed from RM257 and so the isotropic transition of the polymerised sample will mainly be determined only from CB7CB. Therefore, in polymerised PM20, liquid crystalline behaviour very similar to that of CB7CB is observed.

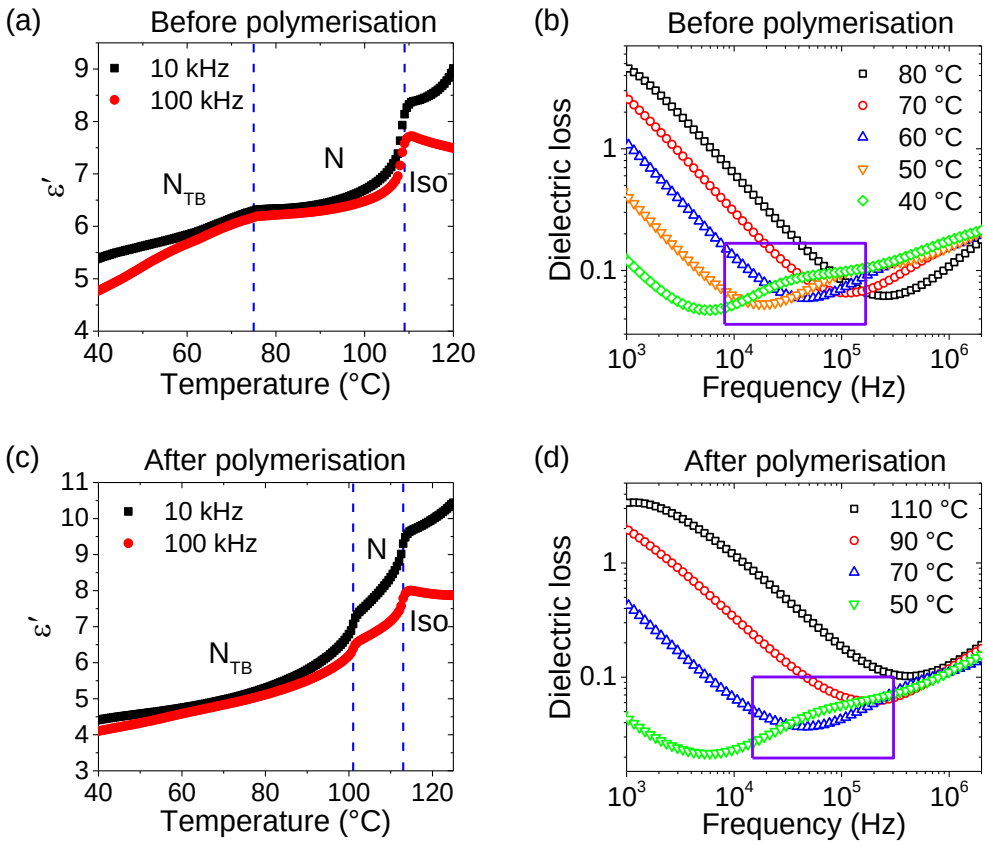

Figure 4.4: Plots of dielectric permittivity as a function of temperature and dielectric loss as a function of frequency measured at 0.1 V_{RMS} in 10 µm planar cell at various temperatures for: (a) & (b) PM20 before polymerisation; (c) & (d) PM20 polymerised in the N_{TB} phase.

The dielectric loss data before and after polymerisation was fitted to the Havriliak-Negami equation (2.8) to determine the relaxation frequencies (f_R) and dielectric strength ($\delta\varepsilon$) of the characteristic N_{TB} peak (labelled with a rectangle in Figure 4.4b and Figure 4.4d) as a function of reduced temperature. The fitted dielectric loss data before and after polymerisation is given in Figure 4.5 and this is compared to the fitted data for pure CB7CB. As the temperature decreases, there is a linear decrease in the relaxation frequencies for CB7CB and PM20 before and after polymerisation, as shown in Figure 4.5a. The temperatures at which the peak becomes measurable is similar both before polymerisation (triangle symbols) and after polymerisation (circle symbols) – they are closer to the N-N_{TB} transition temperature compared to pure CB7CB. The frequency at which the peak becomes measurable is lower for unpolymerised PM20 (~256 kHz) compared to pure CB7CB (~1.17 MHz) and polymerised PM20 (~1.15 MHz). The dielectric strength of the peak before polymerisation (open circle symbols) in Figure 4.5b is slightly higher than that of pure CB7CB and shows a decrease in value as the temperature decreases. For example, at

$T_{N\text{-}N_{TB}}$ = -30 °C, δε = 0.11 for unpolymerised PM20 and δε = 0.10 for pure CB7CB. After polymerisation (open triangle symbols), however, there is a reduction in dielectric strength, with δε = 0.07 at $T_{N\text{-}N_{TB}}$ = -30 °C. The plot of dielectric strength for polymerised PM20 is similar to that of pure CB7CB – as the temperature decreases, the dielectric strength also generally decreases, but at temperatures below $T_{N\text{-}N_{TB}}$ ≈ -45 °C, the strengths begin to increase.

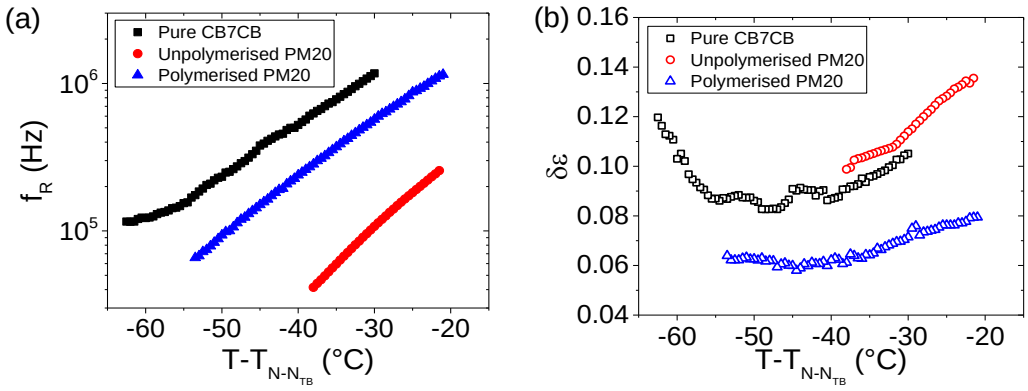

Figure 4.5: Fitted dielectric loss data as a function of reduced temperature for pure CB7CB and mixture PM20 before and after polymerisation: (a) relaxation frequency (f_R), and (b) dielectric strength (δε) of the characteristic relaxation peak.

4.2 Characteristics of twist-bend nematic templates

4.2.1 Preparing the templating mixture

In order to achieve templated polymer structures, it is preferable to have the phase of interest at room temperature, so that processes such as 'washing out' the host liquid crystal can easily be carried out. In order to achieve this, 5CB was also added to the mixtures of CB7CB and RM257 discussed in section 3.3, in order to reduce the transition temperatures (mixtures were prepared according to the procedure described in section 2.2). Note: the addition of 5CB is not required to make templates of the N_{TB} phase. The results from section 4.1 show that a monomer concentration of 20 wt% gives a stable N_{TB} phase and polymer films of sufficient strength to carry out electron microscopy experiments. Therefore, the concentration of RM257 was fixed to 20 wt%. The transition temperatures of the ternary mixtures are given in Figure 4.6. In these mixtures, as the concentration of 5CB+RM257 increases, the temperature range across which the N_{TB} phase exists gets suppressed, which was also observed for CB7CB+5CB mixtures in section 3.2.1. Both the isotropic-N and N-N_{TB} transitions

decrease as more 5CB+RM257 is added, and at CB7CB concentrations of 40 wt% and 50 wt%, the N_{TB} phase is not observed above room temperature.

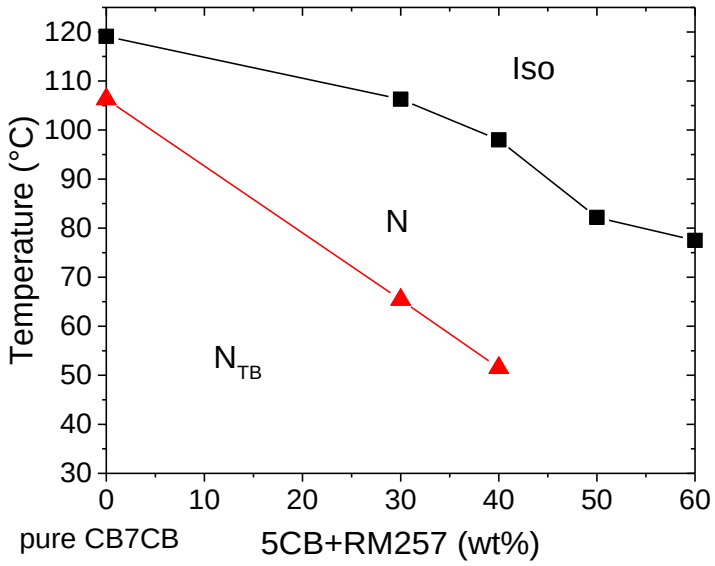

Figure 4.6: Transition temperatures of ternary CB7CB+5CB+RM257 mixtures with the concentration of RM257 fixed at 20 wt% in all mixtures. Square symbols represent the isotropic to nematic transition and triangle symbols represent the nematic to N_{TB} transition. The lines serve as guides to the eye and do not represent a theoretical fit.

The mixture composed of CB7CB (70 wt%), 5CB (10 wt%) and RM257 (20 wt%) was chosen for templating experiments and will be referred to as 'NTB20' throughout the chapter.

In the next step, photoinitiator was added to the mixture NTB20 to enable photopolymerisation of the sample when exposed to UV light. The photoinitiator used was BME (see Figure 2.1 for chemical structure) and the mixtures were made in the cleanroom in yellow light to prevent unwanted photopolymerisation of the samples whilst contained in vials or cells. Three concentrations of BME with respect to mixture NTB20 were tested in 2 µm planar cells: 0.1 wt%, 1 wt% and 6.5 wt%, and Table 4.3 gives the phase transition temperatures for each mixture before polymerisation.

Table 4.3: Phase transition temperatures of the mixture NTB20 composed of CB7CB (70 wt%), 5CB (10 wt%) and RM257 (20 wt%) at different concentrations of BME (before polymerisation).

BME (wt%)	T_{NI} (°C)	$T_{N\text{-}N_{TB}}$ (°C)
0.1	101.8	60.8
1.0	88.1	57.5
6.5	Phase separation	-

Increasing the BME concentration from 0.1 wt% to 1 wt% decreases the nematic phase range by ~10 °C (the melting temperature of BME is 47.5–48.5 °C). A higher concentration of BME (6.5 wt%) induced phase separation within the sample, as shown in Figure 4.7 where crystals began to form in the isotropic phase. A BME concentration of 0.1 wt% was chosen for templating the N_{TB} phase.

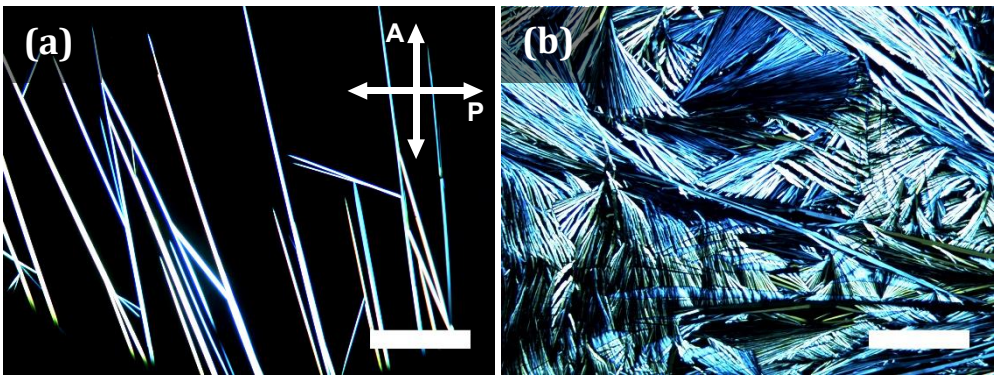

Figure 4.7: POM images of mixture NTB20 with 6.5 wt% BME added to the mixture, showing phase separation: (a) crystal formation as the LC transitions to the isotropic phase (68 °C), and (b) crystallisation of the entire sample on cooling (50 °C). The length of the scale bar is 300 µm.

Devices of 2 µm, 5 µm and 20 µm spacing were filled with mixture NTB20 to check the alignment of the N_{TB} phase (see Figure 4.8). The N_{TB} textures in cells with a 2 µm and 5 µm cell gap (Figure 4.8a and Figure 4.8b, respectively) were found to have smaller domain sizes compared to the 20 µm cell in Figure 4.8c, and so 2 µm and 5 µm cells were mainly used for templating experiments.

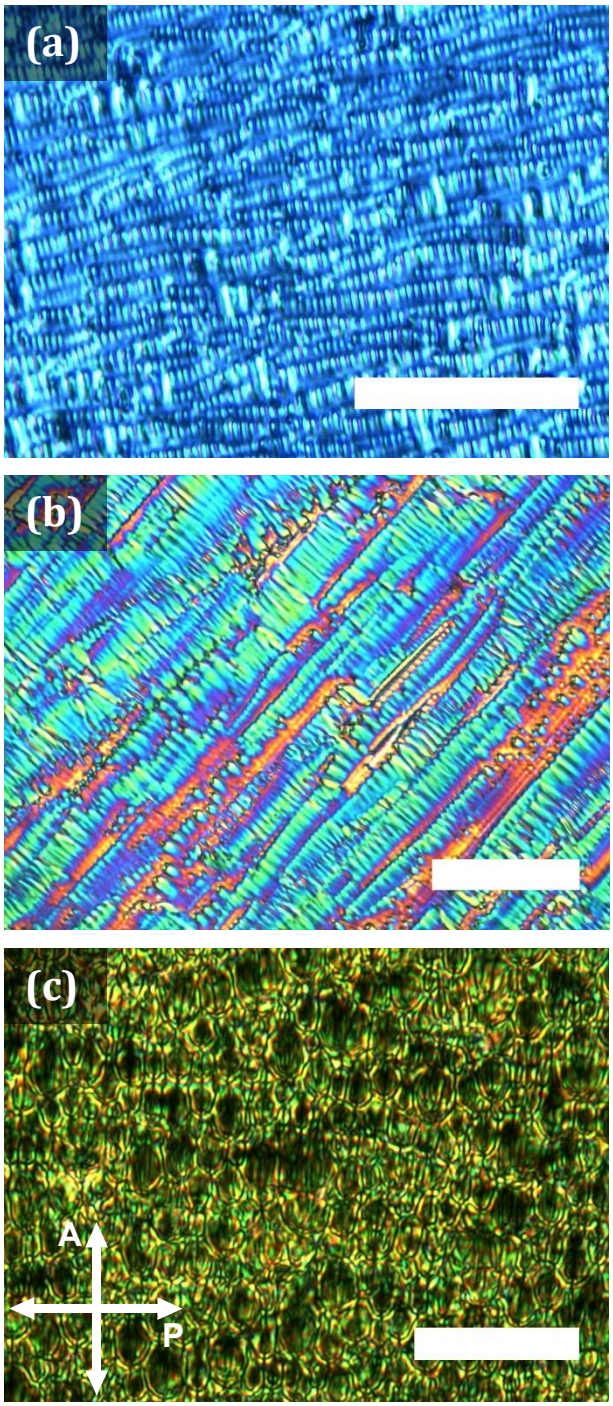

Figure 4.8: POM images of the N_{TB} alignment of mixture NTB20 in planar cells of different cell gap: a) 2 μm; b) 5 μm; c) 20 μm. The length of the scale bar is 50 μm.

4.2.2 Properties of polymerised N_{TB} phases

Planar cells were filled with the templating mixture NTB20 in the isotropic phase (110 °C). The samples were then cooled at 5 °C/min to the supercooled N_{TB} phase at 25 °C, and then photopolymerised by exposing to UV light for 2 h. Note: before exposing the samples to UV light, a test to check for signs of crystallisation was carried out by keeping the temperature constant at 25 °C. After 3 hours, the sample did not crystallise.

The polymerised N_{TB} sample was heated to test its thermal stability and POM images of polymerised NTB20 in a 5 μm planar cell are provided in Figure 4.9. At room temperature, the sample is in the N_{TB} phase. There is little difference in the birefringence up to ~80 °C (Figure 4.9b), and above this temperature, the birefringence decreases gradually (Figure 4.9c,d). Between 98 °C and 99 °C (Figure 4.9e), there is a significant decrease in birefringence, which corresponds to the nematic to isotropic transition of the mixture of CB7CB and 5CB liquid crystals that form the N_{TB} templating mixture NTB20 (composed of 70 wt% CB7CB, 10 wt% 5CB and 20 wt% RM257). Residual birefringence was observed above 99 °C. As discussed previously, an explanation for this could be that the alignment of the N_{TB} phase templated into the polymer network is inducing order in the isotropic phase of the liquid crystal, close to the interface of the polymer and the liquid crystal. The polymerised NTB20 sample behaves the same as polymerised PM20 (the binary mixture of CB7CB with 20 wt% RM257 that was discussed in section 4.1). The difference between mixtures NTB20 and PM20 is that NTB20 is also composed of the calamitic liquid crystal 5CB, which was used to lower the transition temperatures of the sample. Hence the lower isotropic transition temperature for polymerised NTB20 (98-99 °C) compared to polymerised PM20 (~118 °C).

To further investigate the residual birefringence in the polymerised NTB20 sample, the polymerised N_{TB} sample was heated to temperatures well above 99 °C (Figure 4.9f-l) – note that the boiling point of 5CB is above 140 °C. The N_{TB} polymer template slowly began to degrade at temperatures around 300 °C (Figure 4.9k) and the sample was heated to a maximum temperature of 400 °C, whereby the polymer transitioned to a liquid state (Figure 4.9l). Residual birefringence was observed over the entire temperature range from 99 °C (Figure 4.9e) until the point of polymer degradation, i.e. over a temperature range of ~200 °C.

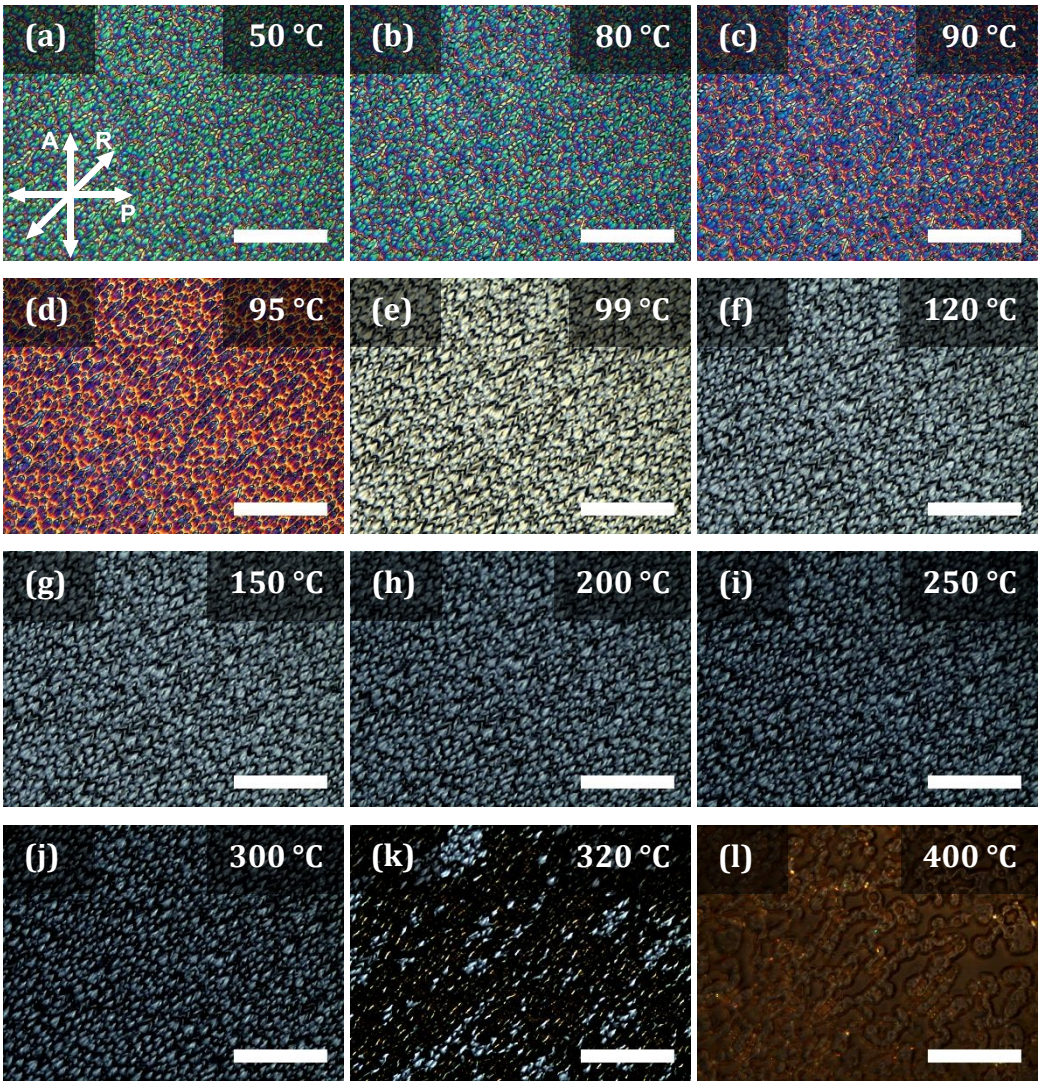

Figure 4.9: POM images of the polymerised NTB20 sample in a 5 μm planar cell on heating from room temperature. Corresponding temperatures are labelled on each image. Residual birefringence is observed from 99 °C until the polymer template degrades. At 400 °C, the polymer is transitioning to a liquid. The length of the scale bar in each image is 100 μm.

4.2.3 Comparisons between different templated structures

To provide a comparison with templated N_{TB} structures, the nematic phase of mixture NTB20 was also photopolymerised. Figure 4.10a compares the dielectric permittivity measured at 0.1 V_{RMS} between 25 °C and 125 °C for three different polymerised samples: (1) polymerised RM257 (i.e. pure polymer) in a 5 μm planar cell, (2) the templating mixture NTB20 polymerised in the N_{TB} phase in a 2 μm cell, and (3) NTB20 polymerised in the nematic phase in a 2 μm cell. Across a range of 100 °C, polymerised RM257 network does not show a significant change in permittivity. For the polymerised N_{TB} and N samples in Figure 4.10a, generally the properties of the unpolymerised mixture of CB7CB and 5CB liquid crystals are being measured. This is why the permittivities of the polymerised N_{TB} and nematic phases in Figure 4.10a are similar, although, naturally, there are contributions from the polymer network that surrounds the liquid crystals. On cooling from 125 °C in Figure 4.10a, a decrease in permittivity is observed at ~93 °C and corresponds to the isotropic to nematic transition temperature of the unpolymerised mixture of CB7CB and 5CB liquid crystals. Optically, however, this transition (decrease in birefringence) was observed at ~99 °C for the polymerised N_{TB} phase (note: when the polymerised N_{TB} sample was heated, residual birefringence was observed until ~300 °C, as discussed earlier in section 4.2.2). On further cooling, there is also a decrease in permittivity at ~78 °C, corresponding to the N-N_{TB} transition of the bulk unpolymerised CB7CB+5CB liquid crystal. The isotropic, nematic and N_{TB} regions are labelled in Figure 4.10a for the polymerised N and N_{TB} samples. The permittivities in the nematic phase range of the polymerised N phase are slightly lower than those of the polymerised N_{TB} phase. The permittivities have also been plotted as a function of reduced temperature ($T-T_{NI}$) and are given in Figure 4.10b, where the isotropic, nematic and N_{TB} phase regions have been labelled. Note that the permittivity in the isotropic region ($T-T_{NI} > 0$) remains almost constant.

The permittivities of the polymerised N_{TB} and N phases in Figure 4.10a are similar to those of the polymerised N_{TB} phase of PM20 (CB7CB mixed with 20 wt% of RM257) in Figure 4.4c, discussed earlier in section 4.1.4. The difference, however, are the temperatures at which the decrease in permittivity at the isotropic to nematic and nematic to N_{TB} transitions are observed. In polymerised NTB20, the changes in permittivity occur at lower temperatures compared to polymerised PM20. This is expected because the NTB20 mixture also includes 5CB, which was added to the mixture with the aim of lowering the temperatures of the N-N_{TB} and nematic-isotropic transitions.

A comparison between the dielectric loss data of the polymerised N_{TB} phase (Figure 4.10c) and the polymerised nematic phase (Figure 4.10d) can be made. For the polymerised N_{TB} phase, the characteristic N_{TB} relaxation peak (labelled with a rectangle in Figure 4.10c) emerges on cooling, at temperatures corresponding to the N_{TB} phase in Figure 4.10a and it shifts towards lower frequencies. On the other hand, the polymerised nematic phase does not show any distinguishable relaxations on cooling in the measured frequency window. There is clearly a difference in dielectric loss data for polymerised nematic and N_{TB} phases, even though the same mixture NTB20 (composed of 70 wt% CB7CB, 10 wt% 5CB and 20 wt% RM257) was used for photopolymerisation. This would indicate that, during photopolymerisation of the nematic phase, nematic ordering is being imprinted onto the polymer network. Due to this, the unpolymerised CB7CB and 5CB liquid crystals exhibit different dielectric properties in the polymerised nematic and polymerised N_{TB} phases, i.e. a characteristic N_{TB} relaxation peak is observed in the polymerised N_{TB} sample (Figure 4.10c), whereas this peak is not observed in the polymerised nematic sample (Figure 4.10d).

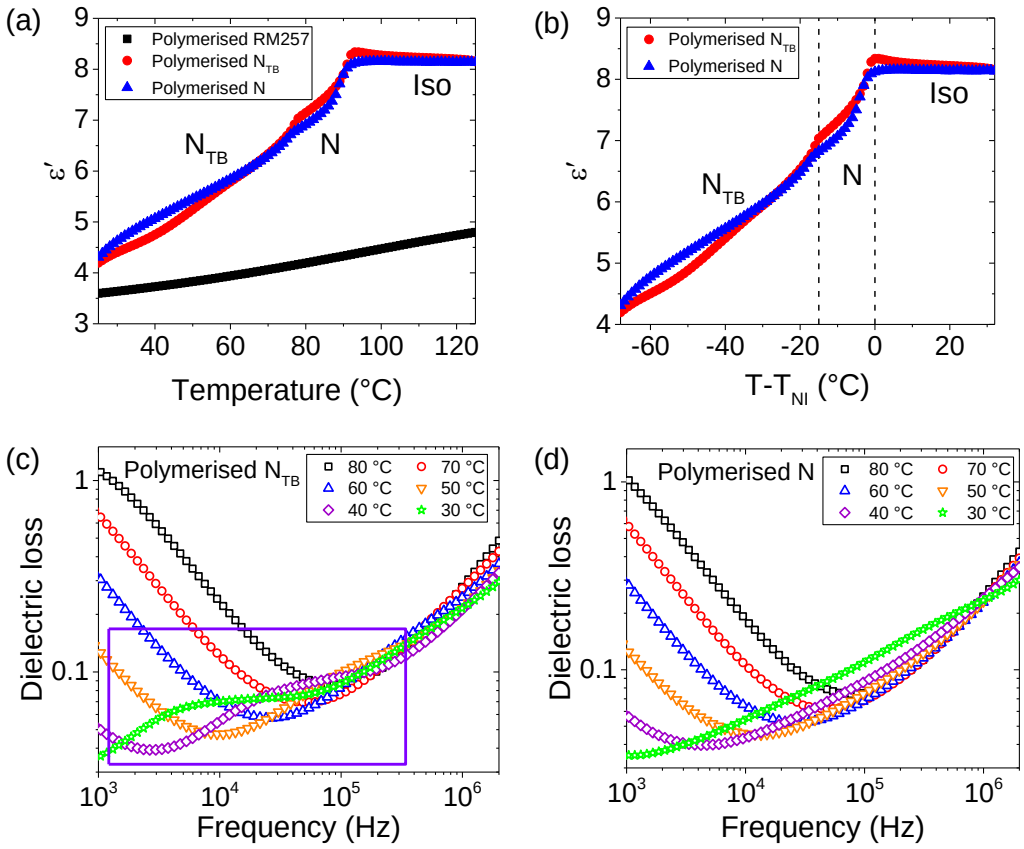

Figure 4.10: (a) Dielectric permittivity (ε') at 100 kHz measured at 0.1 V_{RMS} in a 5 µm planar cell as a function of: (a) temperature, and (b) reduced temperature ($T-T_{NI}$). Dielectric loss as a function of frequency measured at 0.1 V_{RMS} in a 2 µm planar cell between 80 °C and 30 °C for: (c) NTB20 polymerised in the N_{TB} phase (the relaxation peak shifts to lower frequencies on cooling and it is labelled with a rectangle), and (d) NTB20 polymerised in the nematic phase.

4.2.4 Creating the template of the N_{TB} phase

To create a polymer template of the liquid crystal phase, the host liquid crystal is washed from the polymerised samples using acetone, to leave behind a porous polymer network. The CB7CB and 5CB host liquid crystals were washed from the photopolymerised N_{TB} samples by placing the cell into a beaker containing acetone for one or more days, depending on the cell gap. The washing procedure for cells with a smaller gap (2 µm) tended to last longer than those with a larger cell gap (10 µm). The cell was then dried on a hotplate at 30 °C, whereby a white polymer film was formed across the cell (see Figure 2.2b). This indicated that the host liquid crystal was washed out and that the polymer network had been formed. This polymer film scatters light, as seen in the POM image in Figure 4.11a.

Further, Raman spectroscopy was used to ensure that the host liquid crystal is completely washed out and that there are no traces of it left in the template. This was possible due to the fact that the liquid crystals CB7CB and 5CB both possess nitrile (-CN) groups and the polymer network (constructed from RM257) does not, which allowed for tracing of the Raman peak corresponding to the –CN group throughout the washing procedure. For chemical structures of CB7CB, 5CB and RM257, see Figure 2.1. Figure 4.11b shows the Raman spectra of the photopolymerised samples (composed of liquid crystals CB7CB and 5CB, and polymerised RM257) and the washed samples (consisting of only polymerised RM257). The polymerised sample is represented with a dashed blue line and the washed sample is represented with a red solid line. The Raman spectrum of the polymerised sample shows an important peak at ~2227 cm^{-1} (labelled with a rectangular box). This peak corresponds to the Raman shift of nitrile groups of the liquid crystals, which is present for the polymerised samples but is absent after washing. This means that the host liquid crystal has been completely washed out of the sample, which is important, as any leftover liquid crystal could interfere with further experiments discussed later in this chapter. In addition, the strong peak at ~1605 cm^{-1} in the spectrum of the polymerised sample corresponds to the Raman shift of aromatic C=C bonds. Aromatic rings are present in both the liquid crystals and the polymer network, therefore the peak at ~1605 cm^{-1} is observed in both the polymerised and washed samples. There is, however, a significant decrease in the intensity of this peak in the washed sample compared to the polymerised sample, which is expected because the liquid crystals CB7CB and 5CB – which make up a total of 80 wt% of the templating mixture NTB20 – have been removed in the washed sample.

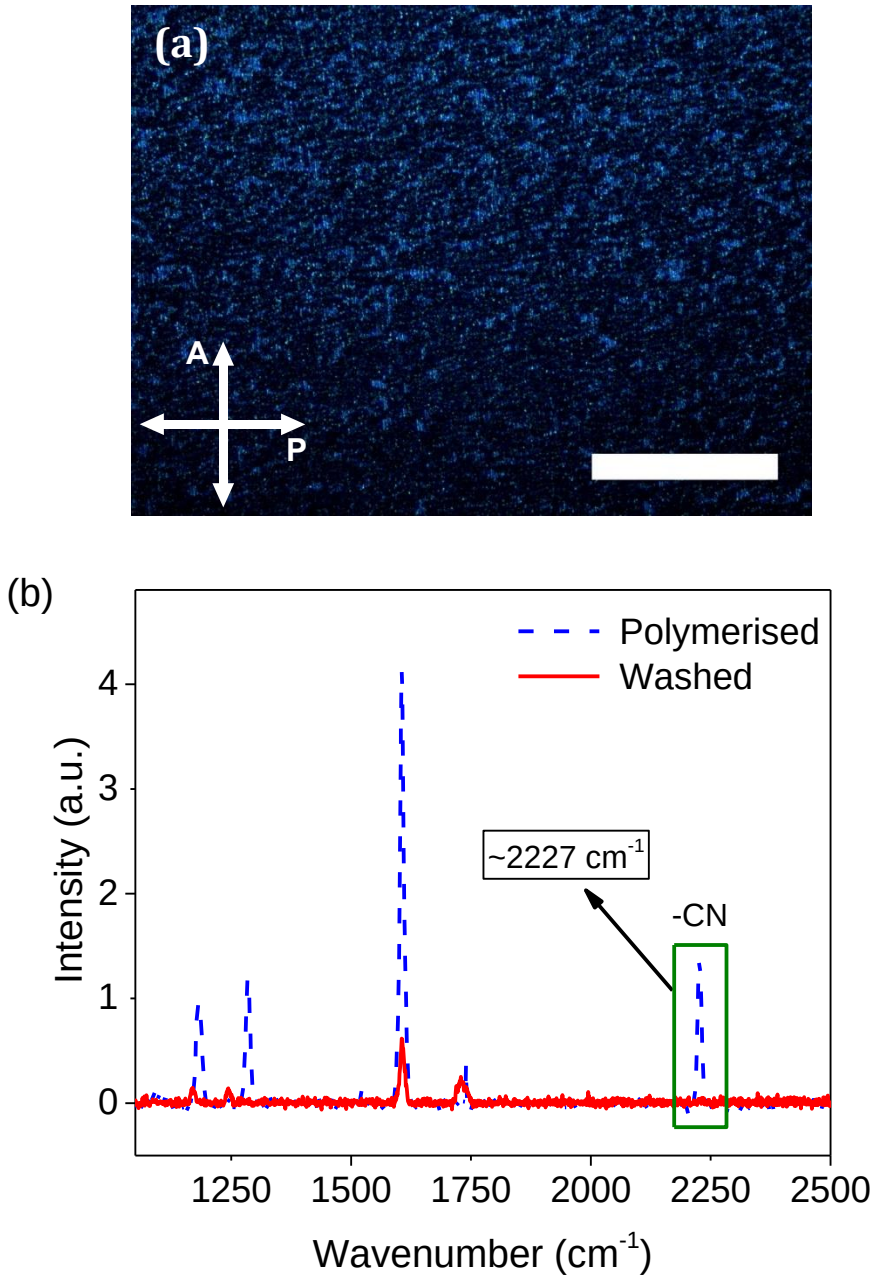

Figure 4.11: (a) POM image of the N_{TB} polymer template in a planar 2 µm cell at 25 °C. The scale bar length is 200 µm. (b) Comparison of the Raman spectra of the polymerised (dashed line) and washed sample (full line). The nitrile (-CN) peak is labelled with a rectangle.

Even though acetone worked well as a washing solvent, the non-polar solvent hexane was also used to test its suitability as a washing solvent. A comparative study of 'washing' using acetone and hexane as solvents by Raman spectroscopy is given in Figure 4.12. The blue line represents the Raman spectrum of the sample where washing was carried out using hexane as the solvent, and the red line represents washing using acetone. It is clear from the spectra that the nitrile (-CN) peak is absent

from the spectrum where acetone was used. However, the nitrile peak is still present in the spectrum where hexane was used. Therefore, for further templating experiments, acetone was used to wash out host liquid crystals.

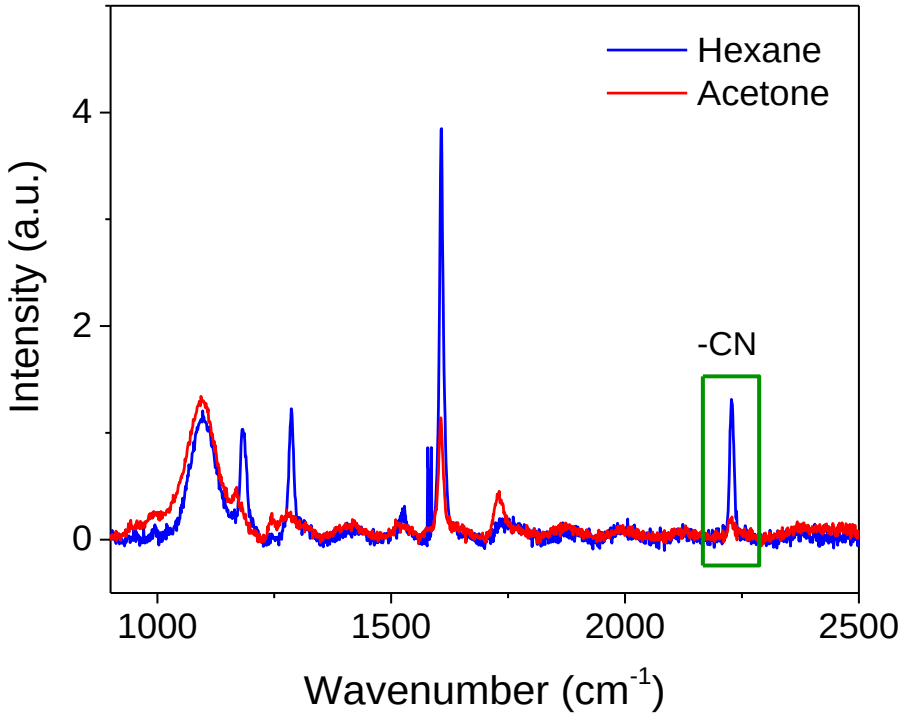

Figure 4.12: Raman spectra of samples washed using hexane (blue line) and acetone (red line) in a planar 2 µm cell. The nitrile (-CN) peak is present in the spectrum of the sample washed with hexane. Therefore, hexane is an unsuitable solvent for washing out the host liquid crystal.

4.2.5 Porosity of polymer templates

Figure 4.13 shows plots of the real (ε') part of the dielectric permittivity as a function of frequency for N_{TB} templates (circle symbols) and nematic templates (triangle symbols), i.e. washed samples. The networks were probed with a measuring voltage of 0.1 V_{RMS} in 2 µm planar cells at 25 °C. The permittivities of both the N_{TB} and N polymer networks are greater than 1 (i.e. greater that the permittivity of an empty cell), which, in addition to the Raman data in Figure 4.12, confirms that acetone does wash out the host liquid crystal but the polymer network is still intact in the cell. The permittivity of the nematic template in Figure 4.13 (triangle symbols) is slightly higher than the permittivity of the N_{TB} template (circle symbols). Taking into consideration a 10% error in permittivity, however, the permittivities of both templates fall within error of each other. At 10 kHz, the permittivity of the N_{TB}

template is 1.40±0.14, and the permittivity of the nematic template is 1.50±0.15, and both templates consist of only polymerised RM257. Comparing these values to the permittivity of polymerised RM257 at 10 kHz gives an indication of the porosity of the network. At 10 kHz, the permittivity of polymerised RM257 (square symbols) is 3.77±0.38, meaning that the N_{TB} template takes up 37±5% of the volume of the interior of the cell [(1.40±0.14)/(3.77±0.38)], and the nematic template takes up 40±6% [(1.50±0.15)/(3.77±0.38)] of the volume (the rest is air), indicating that the N_{TB} and nematic templates have similar porosities (within error). It is expected that the two templates have similar porosities because they are made up from the same material (NTB20). Because the samples were polymerised in different phases, the difference between the N_{TB} and nematic templates would be in the physical properties they exhibit when they are refilled with a nematic liquid crystal, which will be discussed later in section 4.2.7. Methods such as mercury porosimetry, image analysis, thermoporometry and cryoporometry have been used in literature[174–180] to measure porosity in soft matter materials.

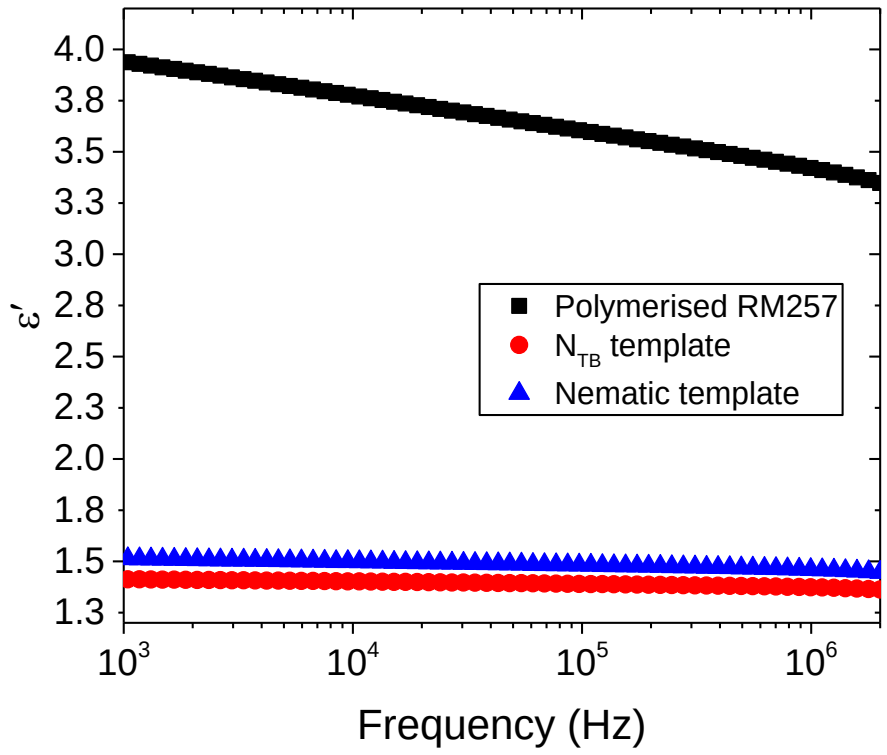

Figure 4.13: Plots of the dielectric permittivity as a function of frequency at 25 °C for polymerised RM257 and templates (washed samples) of the N_{TB} and nematic phases. The measurements were taken at 0.1 V_{RMS} in a 5 µm planar cell for polymerised RM257 and in 2 µm cells for the N_{TB} and N templates.

4.2.6 Morphologies of templated structures

Scanning electron microscopy (SEM) imaging was used to visualise the orientation of polymer strands in different templated phases. Firstly, SEM imaging of the polymerised N_{TB} material (before washing) was tested. The SEM image of the photopolymerised N_{TB} phase of mixture NTB20 is given in Figure 4.14a, and the corresponding POM image is shown in Figure 4.14b (with the rubbing direction *R* marked). As observed in the SEM image, the polymer strands cannot be clearly distinguished, due to the 'soft' areas around the strands (labelled with ovals) which arise from the liquid crystals. Due to this, for further SEM imaging experiments, all of the liquid crystal was first washed out of the cell, which was confirmed using Raman spectroscopy. The cell was then cracked open by hand, and each of the two glass substrates had a relatively equal amount of polymer on them.

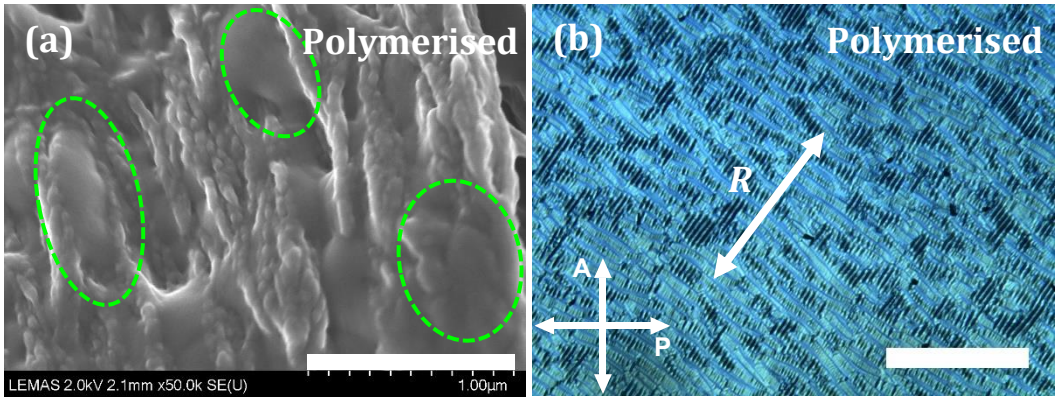

Figure 4.14: SEM (a) and POM (b) images of the photopolymerised N_{TB} phase of mixture NTB20. In the SEM image, the three ovals represent areas where polymer strands cannot be distinguished, and the scale bar is labelled in the image. The rubbing direction *R* in the POM image is labelled. The length of the scale bar in the POM image is 100 µm.

SEM was carried out on the N_{TB} template, formed from polymerising NTB20 at $T\text{-}T_{N\text{-}N_{TB}} \approx -35$ °C in a planar 2 µm cell. SEM images of the N_{TB} template are given in Figure 4.15a and Figure 4.15b, and the corresponding POM image of the N_{TB} phase is given in Figure 4.15c. The SEM images in Figure 4.15 show a well-defined network of the polymerised mesogen. In the N_{TB} phase (Figure 4.15a), the vertical strands in the SEM image are spaced approximately 2 µm apart, which is equivalent to the distance between the stripes in the corresponding POM image (Figure 4.15c). The SEM image shows that the polymer strands form at an angle (α) with respect to the rubbing direction (*R*). The angle α is approximately 35° and this value falls within the range of

the tilt angle (θ) of CB7CB, deduced from birefringence measurements at $T\text{-}T_{N\text{-}N_{TB}} \approx -35$ °C reported in literature.[181] This suggests that the helical axis of the N_{TB} phase lies along the rubbing direction and the polymer strands follow the orientation of the local nematic director ***n*** (labelled in Figure 4.15a). Therefore, it is possible that angle α (also labelled in Figure 4.15a) corresponds to the tilt angle θ. This also suggests that photopolymerising the N_{TB} phase at different temperatures below the $N\text{-}N_{TB}$ transition could be used as a means of measuring the temperature-dependent N_{TB} tilt angle.

The N_{TB} template was then compared with a template of the SmA phase formed from mixture 8CB-RM-10 (8CB with 10 wt% RM257, discussed in section 4.1.3), polymerised in a 5 μm planar cell. The SEM images of the SmA template are given in Figure 4.15e, and the corresponding POM image is given in Figure 4.15f. In the case of the SmA sample (Figure 4.15d), the director ***n*** lies along the rubbing direction *R* and the network of polymer strands is clearly aligned parallel to the director.

The polymer strands in both the N_{TB} and SmA templates (Figure 4.15b and Figure 4.15e) show close packing of individual polymer strands and the packing gives them a 'smooth' appearance. The individual polymer strands are labelled with a rectangle and their width is in the range 50-100 nm.

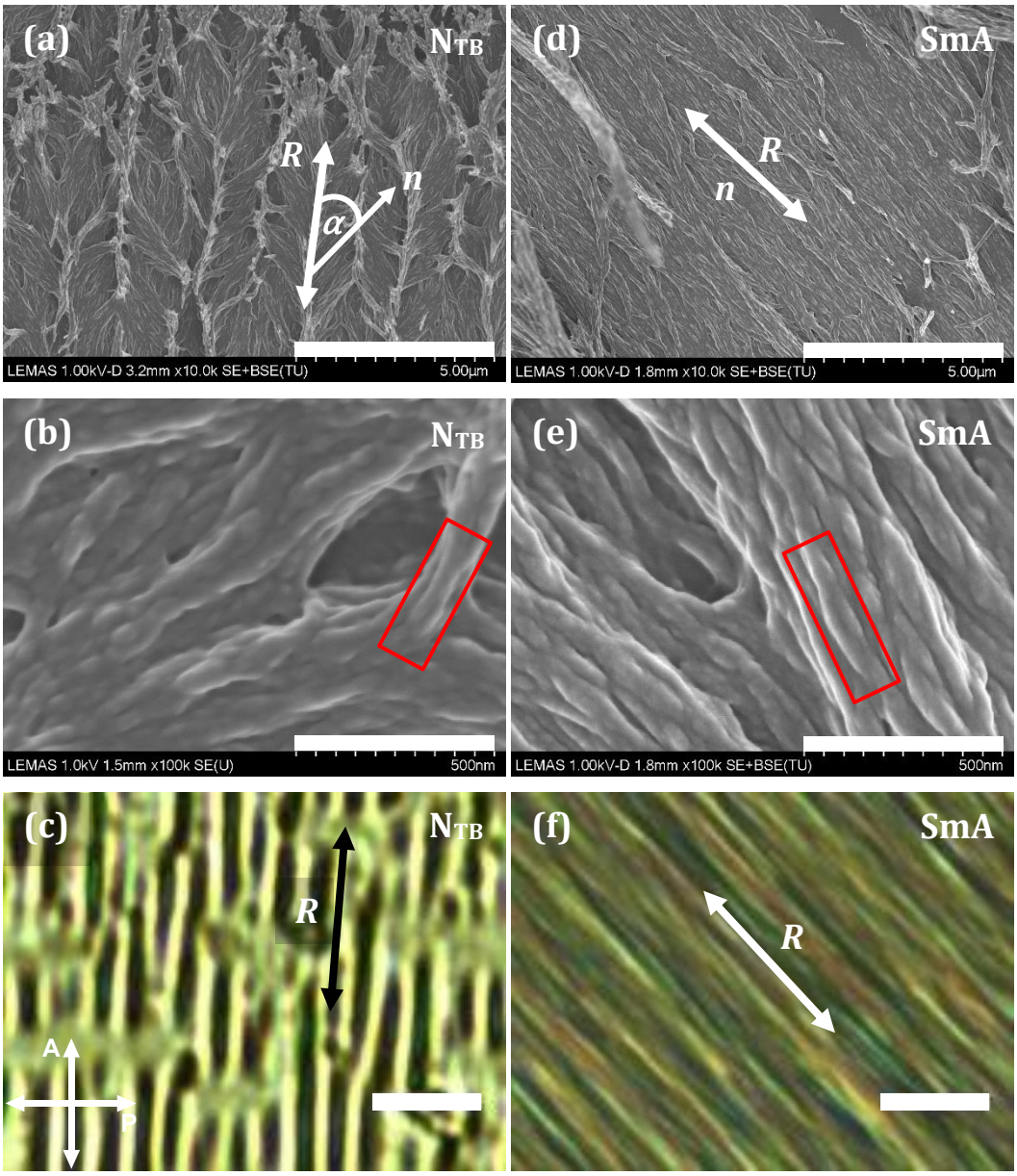

Figure 4.15: SEM images of templates of the N_{TB} phase (a,b) and the SmA phase (d,e). The corresponding POM image of the N_{TB} phase (c) and SmA (f) phase are also given. The rubbing direction (*R*) is marked and the length of the scale bar for POM images is 5 µm. The scale bars for SEM images are labelled in each individual image.

Figure 4.16 shows SEM images of templates of the nematic and isotropic phases formed from mixture NTB20 in 2 µm planar cells. There is a clear difference between the templates of the N_{TB} (Figure 4.15a,b), nematic (Figure 4.16a,b) and isotropic (Figure 4.16c,d) phases formed from mixture NTB20.

The nematic phase in Figure 4.16a shows the polymer strands uniformly following the orientation of the nematic director ***n*** along a preferred direction (labelled with an arrow) that corresponds to the cell's rubbing direction (*R*). The polymer network of

the nematic template appears less ordered than in the N_{TB} template (Figure 4.15a). The rectangular box in Figure 4.16a represents a 'flat' area of the sample, where the polymer has been ripped off the second glass substrate whilst cracking open the cell. On the other hand, molecules in the isotropic phase exhibit a lack of orientational order, and this is observed in Figure 4.16c where polymer strands are oriented in all directions. The individual polymer strands in Figure 4.16b and Figure 4.16d (labelled with a red rectangle) are approximately 50 nm wide.

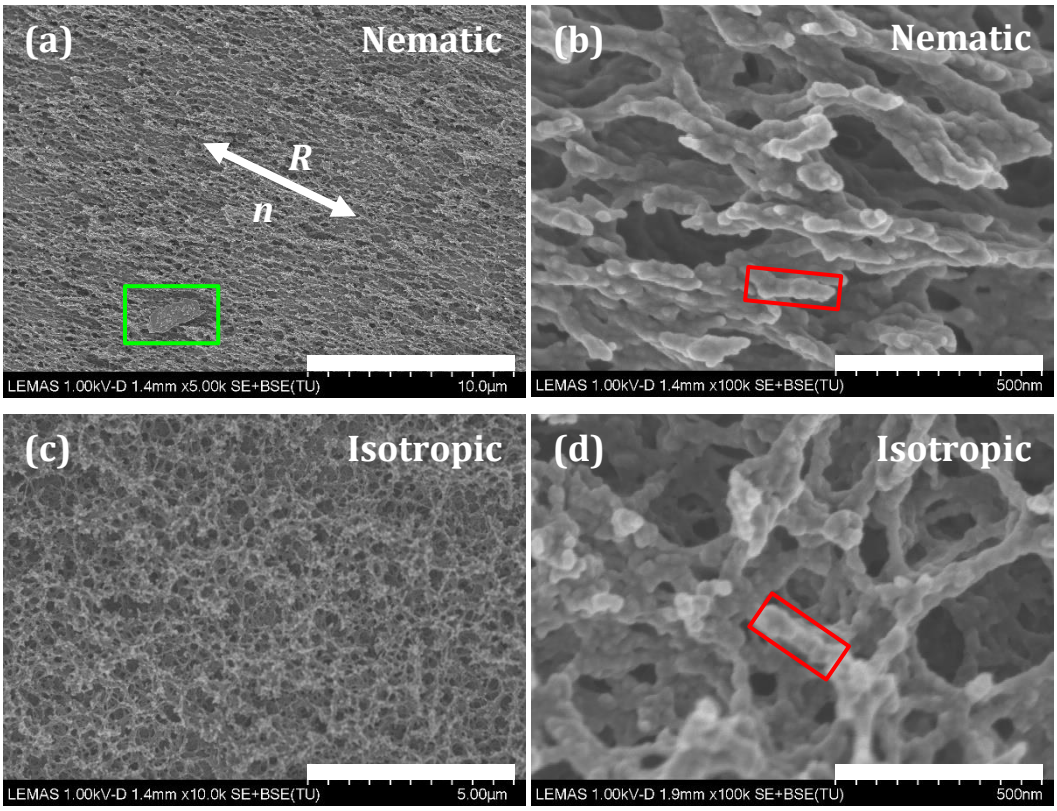

Figure 4.16: SEM images of templates of the nematic phase (a,b) and the isotropic phase (d,e). The individual polymer strands are labelled with a red rectangle. The scale bar for SEM images is labelled in individual images.

The mixture NTB20 was polymerised in all three of its phases: N_{TB} (Figure 4.15b), nematic (Figure 4.16b) and isotropic (Figure 4.16d), where the N_{TB} phase is the most ordered phase out of the three, and the isotropic phase is the least ordered. The N_{TB} phase – being the most ordered out of the three phases – shows a smooth appearance of the polymer strands. The isotropic template, on the other hand, has a bead-like texture, whereas the texture of the nematic template is in between smooth and bead-like. Note that the texture of the polymer strands in the SmA template (Figure 4.15e) is similar to that of the N_{TB} template. In addition, it appears that the degree of order of the host liquid crystal phase that was used for templating has an influence on how

the individual polymer strands are packed in the template. In section 4.2.5, it was discussed that the N_{TB} and nematic templates have similar porosities. However, the morphology of the networks is different for the N_{TB}, nematic and isotropic templates. The individual polymer strands in the N_{TB} template appear more tightly packed compared to the nematic and isotropic templates, and the N_{TB} template does not appear to show as many voids (pores) compared to the nematic and isotropic templates. In contrast to this, the isotropic template appears to have the most voids. It has been noted before that curing at higher temperatures results in larger voids in the polymer network,[182–184] i.e. a lower degree of order in the system leads to larger voids. The morphology of the polymer networks can also be controlled through factors such as the concentration of monomer[185–187] and the choice of monomer.[188–190] The morphology of the N_{TB} and nematic templates affects the dielectric properties of the refilled templates which will be discussed in the following section.

4.2.7 Physical properties of refilled templates

The templates (washed samples) were refilled with the calamitic liquid crystal 5CB that only exhibits the nematic phase. This was done in order to (1) understand the influence of the templated networks on the refilled liquid crystal, and (2) investigate if any physical properties of the host liquid crystal can be imprinted into the polymer network. The refilling process using 5CB is shown in Figure 4.17 and the time taken to completely refill a template lasted approximately one day.

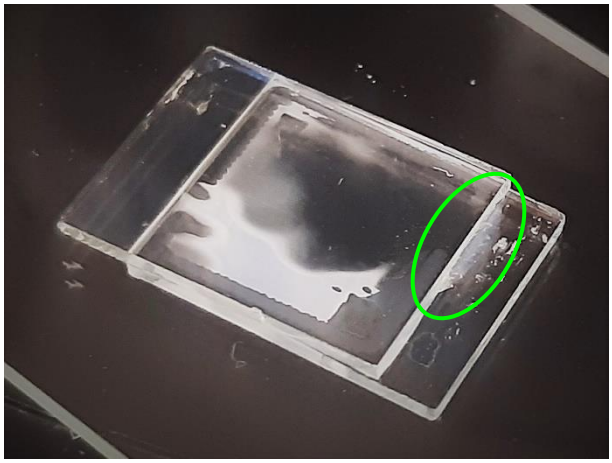

Figure 4.17: The refilling process at room temperature using 5CB: the transparent area represents the template that has been refilled with 5CB, and the white area represents the template that is yet to be refilled. The 5CB liquid crystal is placed at the cell opening (labelled with an oval) and the template is refilled via capillary action.

The N_{TB} template refilled with 5CB was heated from room temperature, and POM generally showed a decrease in birefringence between 35 °C and 36 °C (the clearing temperature of pure 5CB is at 35.5 °C). Residual birefringence was observed in the isotropic state of the liquid crystal, as was the case for polymerised N_{TB} phases in section 4.2.2. The residual birefringence gradually decreases as the refilled N_{TB} template is heated further into the isotropic state of the liquid crystal (further above the nematic-isotropic transition of 5CB).

Figure 4.18a shows a plot of birefringence as a function of electric field for both the refilled N_{TB} template and pure 5CB. Corresponding POM images of the refilled N_{TB} template (1.9 μm planar cell) at 0 V_{RMS}, 20 V_{RMS} and 50 V_{RMS} are also provided in Figure 4.18b. As shown in Figure 4.18a, the birefringence at 29 °C in the absence of an electric field (0 V/μm) is ~60% lower for the refilled N_{TB} template ($\Delta n = 0.10 \pm 0.01$) compared to pure 5CB ($\Delta n = 0.17 \pm 0.01$). When 1 V/μm is applied, the pure 5CB sample shows a significant decrease in birefringence (approx. a 4-fold decrease compared to Δn at 0 V/μm), whereas the refilled N_{TB} template does not. Instead, as the applied electric field increases, the birefringence of the refilled N_{TB} template decreases linearly, and at 10 V/μm, $\Delta n = 0.06 \pm 0.01$ (Figure 4.18b at 20 V_{RMS}). Increasing the applied field further results in a continued decrease in birefringence, and at ~25 V/μm, $\Delta n = 0.03 \pm 0.01$ (see Figure 4.18b at 50 V_{RMS}). When the field was removed, the textures and birefringence were monitored by eye using POM. The birefringence gradually increased and within 5 min, the liquid crystal director returned to its original planar texture/configuration (before an electric field was applied to the refilled sample). 5CB, on the other hand, relaxes in less than 1 s when the electric field is removed.[191] The decrease in birefringence in the refilled N_{TB} template as the applied electric field increases is similar to the effect of heating (discussed above), where the refilled template exhibits a continual decrease in residual birefringence above the clearing temperature of 5CB. Across an applied electric field window of 10 V/μm (Figure 4.18a), the birefringence of the refilled N_{TB} template has only decreased from $\Delta n = 0.10 \pm 0.01$ at 0 V/μm to $\Delta n = 0.06 \pm 0.01$ at 10 V/μm, which is not significant. Comparing this to pure 5CB, an applied field of only 1 V/μm results in a significant decrease in birefringence, from $\Delta n = 0.17 \pm 0.01$ at 0 V/μm to $\Delta n = 0.04 \pm 0.01$ at 1 V/μm. The birefringence of the refilled N_{TB} template at 10 V/μm ($\Delta n = 0.06 \pm 0.01$) is still greater than the birefringence of pure 5CB at 1 V/μm ($\Delta n = 0.04 \pm 0.01$). This means that the templated order of the N_{TB} phase is clearly having an anchoring effect on the refilled 5CB liquid crystal at the polymer/liquid

crystal interface, which is making it difficult for the liquid crystal director to switch when an electric field is applied.

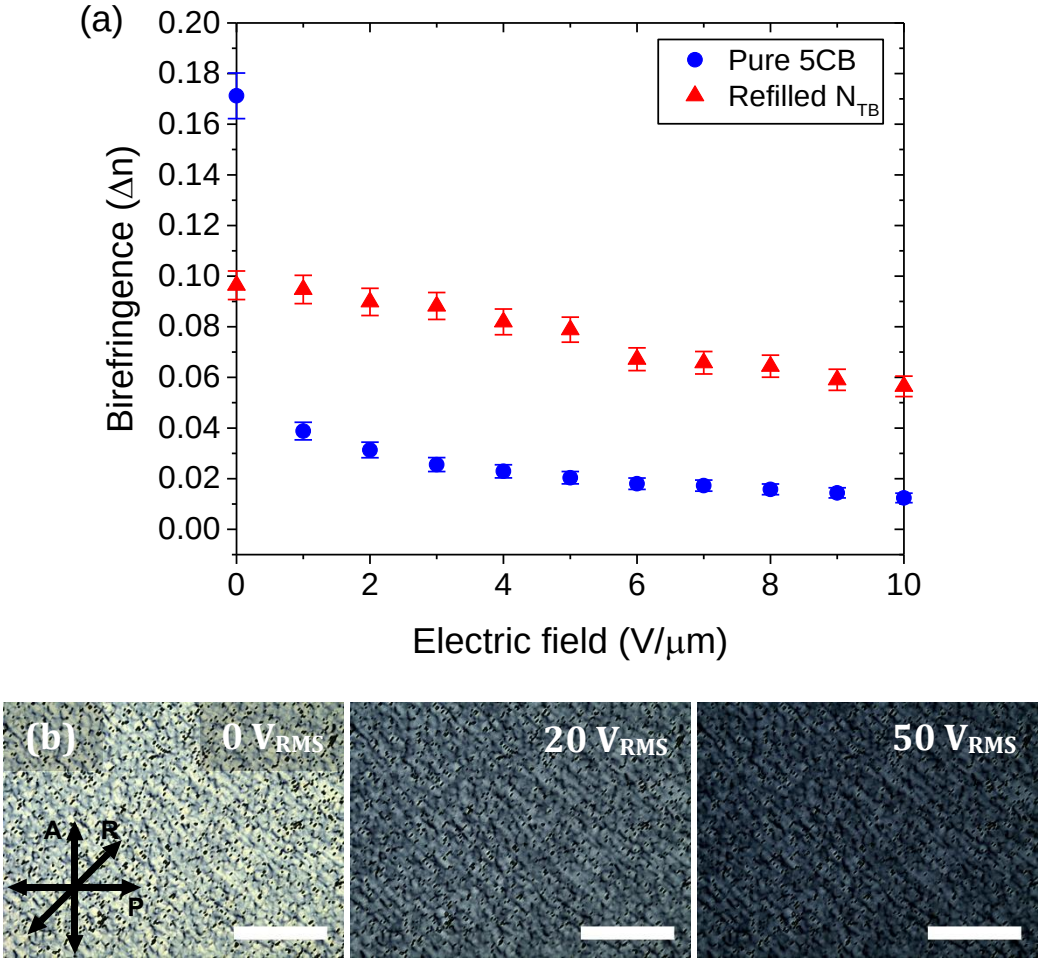

Figure 4.18: (a) Birefringence as a function of electric field (V/μm) at 29 °C for pure 5CB and the N_{TB} template that has been refilled with 5CB. (b) POM images of the refilled N_{TB} template (29 °C) in a 1.9 μm planar cell at $0V_{RMS}$, 20 V_{RMS} and 50 V_{RMS}. The length of the scale bar is 100 μm.

Dielectric spectroscopy measurements were carried out on the N_{TB} and nematic templates that were refilled with 5CB in order to compare their dielectric behaviour to pure 5CB – the data is given in Figure 4.19.

The plot of dielectric permittivity as a function of temperature at 10 kHz for refilled templates and 5CB is shown in Figure 4.19a. The plot also includes data for polymerised RM257 (100% polymer). The net permittivity of the refilled N_{TB} and N templates ($\varepsilon'_{refilled}$) in the isotropic phase can be calculated based on three factors: (1) the permittivity of pure 5CB (ε'_{LC}) in the isotropic phase, (2) the permittivity of the polymer (i.e. polymerised RM257), and (3) the ratio of the permittivity of the

template (washed sample) and the permittivity of the polymer (polymerised RM257). These can be incorporated into the equation:

$$\varepsilon'_{refilled} = x\varepsilon'_{polymer} + (1-x)\varepsilon'_{LC}, \quad (4.1)$$

where x is the porosity of the template, i.e. the ratio of the permittivity of the N_{TB} or N template and the permittivity of polymerised RM257, at a particular frequency and temperature.

Based on porosity calculations in section 4.2.5 (Figure 4.13) for washed samples (templates) at 10 kHz, x = 0.37±0.05 for the N_{TB} template and x = 0.40±0.06 for the nematic template. At 40 °C – a temperature corresponding to the isotropic phase of pure 5CB and the refilled templates – the permittivity value at 10 kHz for polymerised RM257 (the polymer) is 3.93±0.39, and for pure 5CB it is 9.72±0.97. Incorporating these values into equation 4.1, the permittivity of the refilled N_{TB} template at 40 °C is calculated to be ε' = 7.58±0.82, and the experimental permittivity value at 40 °C (ε' = 7.58±0.76) matches the calculated value of 7.58±0.82. Likewise, at 40 °C, the permittivity of the refilled nematic template is calculated to be ε' = 7.40±0.87, and the permittivity obtained experimentally at 40 °C (ε' = 8.17±0.82) is within the error of the calculated value. The calculated permittivities of the refilled N_{TB} template (ε' = 7.58±0.82) and the refilled nematic template (ε' = 7.40±0.87) are very similar. This is expected for the calculated permittivities because the N and N_{TB} templates are made up of the same polymer. The experimental values obtained at 40 °C, however, are slightly higher for the refilled nematic template (ε' = 8.17±0.82) compared to the refilled N_{TB} template (ε' = 7.58±0.76). The difference in permittivities of the nematic and N_{TB} phases can be attributed to a shift in the population of bent and hairpin molecular conformations, as discussed in Chapter 3. The templated polymer networks clearly have a memory of this effect, and so the N_{TB} template is influencing the 5CB at the polymer/liquid crystal interface differently to that of the nematic template. To further investigate this, the difference between the permittivities of the isotropic and nematic phases ($\varepsilon'_{iso}-\varepsilon'_{nematic}$) is plotted as a function of temperature for pure 5CB and the refilled N_{TB} and nematic templates, as shown in Figure 4.19b. For all three samples, the isotropic permittivity (ε'_{iso}) corresponds to the permittivity at 45 °C obtained from Figure 4.19a. The plot of $\varepsilon'_{iso}-\varepsilon'_{nematic}$ vs temperature in Figure 4.19b clearly shows a bigger difference in $\varepsilon'_{iso}-\varepsilon'_{nematic}$ for pure 5CB, compared to the refilled templates. When comparing the refilled N and N_{TB} templates in Figure 4.19b, the difference in values of $\varepsilon'_{iso}-\varepsilon'_{nematic}$ of the two refilled templates show that the N_{TB} template influences the refilled liquid crystal differently compared to the nematic template. In both refilled N and N_{TB} templates, the nematic director is distorted at the

polymer/liquid crystal interface in such a way that there is now less of a difference between the isotropic value and the nematic value in the template. This is showing a bigger effect in the refilled N_{TB} template compared to the refilled nematic template.

Dielectric loss for refilled N_{TB} and nematic templates and pure 5CB measured at 25 °C as a function of frequency is given in Figure 4.19c. At higher frequencies (>100 kHz), there are no relaxations in the measured frequency window either for pure 5CB or for the refilled nematic template. However, for the refilled N_{TB} template (red circle symbols), the shape of the curve is rounding off at ~1 MHz, which is not the case for the refilled nematic template. This indicates that it is likely that a weak relaxation peak characteristic of the N_{TB} phase could be emerging, as observed in Figure 4.10c for the polymerised N_{TB} sample. The peak was fitted to the Havriliak-Negami equation (2.8) and the fitted data is given in Figure 4.19d. The frequency and strength of the fitted peak are: f_R = 5.55 MHz and $\delta\varepsilon$ = 1.6 (note the strength of the peak is greater than the ones obtained in Figure 3.10b). It appears as though the imprinted polymer template is inducing N_{TB}-like characteristics in the refilled nematic liquid crystal.

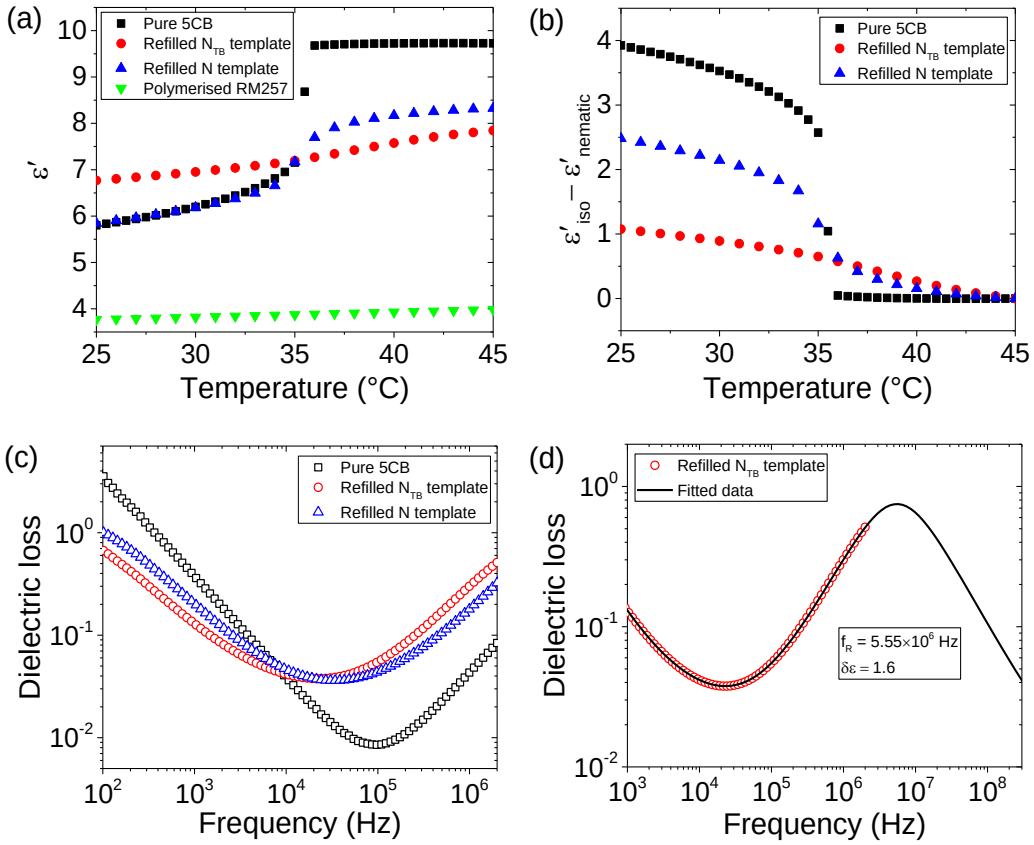

Figure 4.19: Dielectric data measured at 0.1 V_{RMS} for N_{TB} and nematic templates refilled with 5CB (1.9 µm planar cells), and data pure 5CB (measured in a 10 µm planar cell) is given as a comparison: (a) permittivity (ε') at 10 kHz as a function of temperature, (b) $\varepsilon'_{iso}-\varepsilon'_{nematic}$ at 10 kHz as a function of temperature, (c) dielectric loss as a function of frequency at 25 °C, and (d) the emerging peak exhibited by the refilled N_{TB} template, fitted to the Havriliak-Negami equation.

In order to further understand the influence of the template on the refilled liquid crystal, the nematic liquid crystal in the refilled template was subjected to an external electric field and the capacitance of the device as a function of the applied field was measured. This experiment allows for an understanding of the anchoring at the interface of the polymer network and the refilled liquid crystal, as well as a quantification of the elastic properties of the N_{TB} phase itself. The latter has proven to be extremely difficult in pure liquid crystals due to the high viscosity of the N_{TB} phase. For this reason, the method of templating-refilling was established, allowing for a new way to quantify the physical properties of the viscous mesophases. Permittivity was measured as a function of voltage in the refilled N_{TB} and nematic templates. The plots are given in Figure 4.20a for the refilled N_{TB} template and in Figure 4.20b for the refilled nematic template. The data was measured in the nematic phase (25 °C, 29 °C

and 33 °C), just above the nematic-isotropic transition (37 °C), and in the isotropic phase (41 °C).

In Figure 4.20a, the ε' vs voltage curves are smooth (note the smooth linear decrease in Δn as a function of electric field in Figure 4.18a) and show signs of saturation at higher applied voltages (>15 V), i.e. as the voltage continues to increase above ~15 V, the change in permittivity becomes less significant. The refilled N_{TB} template shows an increase in permittivity between 0.1 V and 20 V in the isotropic phase of the liquid crystal at 37 °C and 41 °C. However, the permittivity values for each of these two temperatures at 0.1 V (ε' = 7.26±0.73 at 37 °C and ε' = 7.43±0.74 at 41 °C) and 20 V (ε' = 8.59±0.86 at 37 °C and ε' = 8.02±0.80 at 41 °C) are within error of each other (the error is 10%). The reason that a slight increase is observed in the isotropic phase of the refilled N_{TB} template is most likely due to induced nematic ordering at the interface of the polymer and 5CB liquid crystal. On the other hand, the refilled nematic template in Figure 4.20b does not show signs of saturation at higher voltages – as the applied voltage is increased above ~12.5 V, the permittivities increase linearly. In both the refilled N_{TB} and nematic templates, the director has not completely switched at 20 V_{RMS}. This can also be compared to the refilled N_{TB} template in Figure 4.18b at 20 V_{RMS}, where birefringence is still observed.

The threshold voltages were calculated from the point of intersection of two linear fits: one to the slope (5-10 V for Figure 4.20a and 12.5-20 V for Figure 4.20b) and one to the flat region which corresponds to values before the director reorients under the applied field (0.1-0.4 V for Figure 4.20a and 0.1-5 V for Figure 4.20c). The threshold voltages were converted into threshold electric field values and are given in Figure 4.20c for 25 °C, 29 °C and 33 °C. The threshold electric field values of pure 5CB are also included in Figure 4.20c as a comparison. The errors in threshold electric field were obtained through propagation of the errors corresponding to the linear fits. The threshold electric fields of both the refilled N_{TB} and nematic templates are greater than the threshold electric field of 5CB, and all three show a linear increase as the temperature decreases. At 25 °C, the threshold of the refilled N_{TB} template (~1.74 V/μm) is approx. 25 times greater than that of pure 5CB (~0.07 V/μm). The refilled nematic template (~5.51 V/μm), on the other hand, is approx. 80 times greater than the threshold field of pure 5CB.

The morphologies of the templates (discussed in section 4.2.6) are clearly having a significant influence on the threshold electric field values of the refilled templates, where the threshold electric field values of the refilled nematic template are approx. 3-fold greater than the refilled N_{TB} template. The tighter-packed polymer strands of

the N_{TB} template (Figure 4.15b) are exhibiting a smaller anchoring effect at the interface of the polymer and 5CB, compared to the nematic template (Figure 4.16b) which appears to exhibit more voids than the N_{TB} template. Due to the smaller anchoring effect of the N_{TB} template, the 5CB director is switching from a planar to homeotropic configuration more easily in the N_{TB} template compared to the nematic template, hence the lower threshold voltages/electric field values. It is expected that the threshold electric field values of the refilled nematic template would be smaller than the refilled N_{TB} template because the nematic phase is less ordered than the N_{TB} phase. However, the viscosity of the N_{TB} phase in pure liquid crystals makes it difficult to measure its threshold voltages. The different threshold voltages of refilled N_{TB} and nematic templates and the emergence of a relaxation peak in the refilled N_{TB} template (Figure 4.19c&d) strongly suggest that the nanostructures of the N_{TB} phase have been templated. This also suggests that it is possible that the threshold voltage of the N_{TB} phase is smaller than the threshold voltage of the nematic phase in pure liquid crystals.

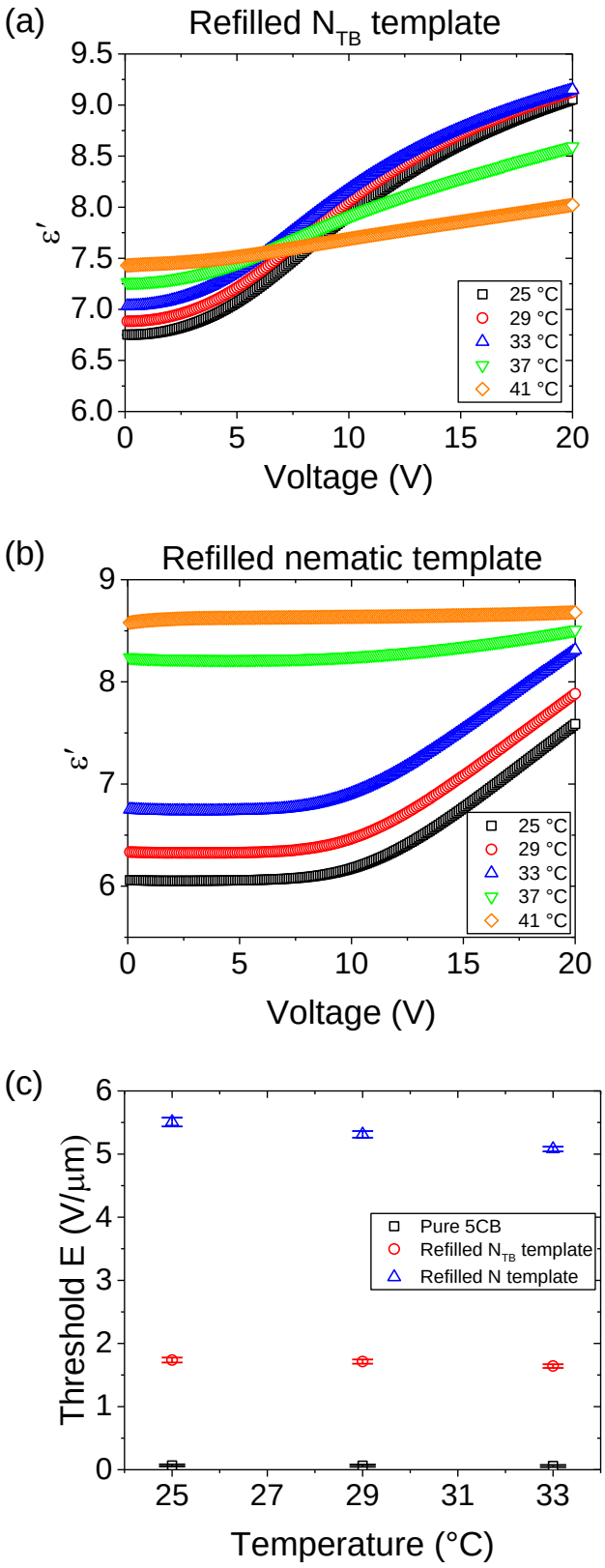

Figure 4.20: Plots of dielectric permittivity (measured at 10 kHz in a 1.9 μm planar cell) as a function of voltage for: (a) the N_{TB} template refilled with 5CB, (b) the nematic template refilled with 5CB. (c) Threshold electric fields (E) at 25 °C, 29 °C and 33 °C for N_{TB} and nematic templates refilled with 5CB (1.9 μm planar cells) compared to those of pure 5CB (10 μm planar cell).

4.3 Summary of results

Section 4.1 discussed photopolymerisation of twist-bend nematic phases exhibited by binary CB7CB and RM257 mixtures, to successfully form metastable room temperature N_{TB} phases. In all photopolymerised samples, the N_{TB} phase existed over a temperature range of up to 80 °C. Residual birefringence was observed in the polymer network on heating the samples above the isotropic transition of the unpolymerised liquid crystal. Dielectric spectroscopy measurements of unpolymerised and polymerised N_{TB} samples were compared. The permittivity as a function of temperature showed isotropic, nematic and N_{TB} regions before and after polymerisation. After polymerisation, a change in the range of the nematic and N_{TB} phases was observed and the polymerised sample showed similar permittivities to pure CB7CB. In addition, the relaxation peak characteristic of the N_{TB} phase was present before and after polymerisation. On cooling, it shifted to lower frequencies and the strength of the peak generally decreased. The polymerised N_{TB} phase showed a similar trend in dielectric strength to CB7CB.

Templated N_{TB} structures were created through the photopolymerisation of the N_{TB} phase exhibited by a mixture composed of CB7CB, 5CB and RM257, and were discussed in section 4.2. The photopolymerised phase exhibited residual birefringence throughout the entire isotropic phase of the liquid crystal, until the template began to degrade at ~300 °C. Dielectric properties of the photopolymerised N_{TB} phase were compared to the photopolymerised nematic phase, both of which were created from the same mixture. Plots of permittivity as a function of temperature for polymerised N_{TB} and polymerised nematic phases were similar. However, the relaxation peak characteristic of the N_{TB} phase was observed in the polymerised N_{TB} phase, whereas it was not for the polymerised nematic phase. This suggested that nematic ordering was imprinted into the polymer network.

Templates of the liquid crystal phase were created by washing out the host liquid crystal. Raman spectroscopy determined that the liquid crystal had been entirely removed from the template during the washing procedure. Dielectric spectroscopy was used as a technique to measure the porosity of the N_{TB} and nematic templates, which were both found to have similar porosities. The morphologies of the templates were imaged using SEM and the width of individual polymer strands was in the range 50-100 nm for all templated phases. The general mesoscopic structure of the N_{TB} phase had been templated. In the N_{TB} template, it was suggested that the polymer strands were assembled at an angle that corresponded to the tilt angle of the nematic

director with respect to the direction of the helical axis. This suggests that photopolymerisation of the N_{TB} phase could be used as a means of measuring the tilt angle of the N_{TB} phase. The texture of the polymer strands in the N_{TB} template appeared smoother compared to the nematic and isotropic templates, which had a more bead-like texture. In addition, the polymer strands in the N_{TB} template appeared closely packed, whereas in the nematic and isotropic templates there appeared to be more voids.

The template was refilled with 5CB to understand how surface modification of the polymer network influences the refilled system, and to see which physical properties of the host liquid crystal can be templated. For refilled templates, a change in birefringence is observed between 35 °C and 36 °C, which corresponds to the clearing temperature of pure 5CB, and residual birefringence was observed in the isotropic phase of 5CB. An electric field was applied to the refilled N_{TB} template, which showed a linear decrease in optical birefringence as the electric field increased. Dielectric permittivity as a function of temperature showed that the N_{TB} template influences the refilled liquid crystal differently to that of the nematic template. There was a smaller difference between the isotropic and nematic permittivities in the templates compared to pure 5CB, where the effect was greater for the refilled N_{TB} template compared to the refilled nematic template. Dielectric loss as a function of frequency showed no relaxations for the refilled nematic template, but a relaxation peak appeared to emerge in the refilled N_{TB} template. Threshold electric fields for refilled N_{TB} and nematic templates were calculated and compared to those of pure 5CB. The threshold electric fields for all three samples showed a linear increase on cooling. The threshold electric fields of both the refilled N_{TB} and nematic templates were greater than those of 5CB. The threshold electric fields of the refilled nematic template were almost 3-fold greater in value compared to the refilled N_{TB} template. It was suggested that the nanostructures of the N_{TB} phase have been imprinted into the polymer network.

CHAPTER 5:
Synthesis of a bent-core mesogen exhibiting the ferroelectric smectic A ($SmAP_F$) phase

In this chapter, an achiral bent-core liquid crystal exhibiting the ferroelectric smectic A ($SmAP_F$) phase will be synthesised and used in Chapter 7 for templating. The $SmAP_F$ phase was discovered in the past decade and it is the highest symmetry (C_{2v}) polar fluid phase achievable in smectic systems. It exhibits macroscopic ferroelectric order because of its unique physical properties.

5.1 Polarity in liquid crystal phases

When considering individual molecules, liquid crystals are generally polar. The calamitic mesogen 5CB, for example, consists of a polar nitrile group attached to the alkyl-tethered biphenyl core, which gives the molecule a permanent dipole moment. However, in a liquid crystal medium, neighbouring 5CB molecules collectively arrange themselves so that the dipole moments between neighbouring molecules are antiparallel. This results in the cancellation of the dipoles and an overall non-polar liquid crystal phase.

Bent-core mesogens (introduced in section 1.3), on the other hand, arrange themselves as effectively as possible in a liquid crystal medium. The mesogens stack side-by-side because of their bent molecular shape, and, in doing so, they tend to form lamellar structures, i.e. smectic phases. When subjected to an external electric field, the combination of both the close-packed environment[192] and the tendency to form layers results in polar ordering within individual layers, with a direction that is parallel to the layer planes. In the case of calamitic liquid crystals, in-layer polarisation is possible only in the presence of simultaneous director tilt and molecular chirality.[193] However, chiral materials are expensive to synthesise, therefore, a great amount of research has gone into discovering achiral materials that exhibit spontaneous polarisation.[194–208]

Today, we are familiar with spontaneous polarisation in smectic phases exhibited by achiral bent-core mesogens. Polarisation effects in SmA phases formed by non-chiral bent-core mesogens was suggested in 1992 by Brand, Cladis and Pleiner,[209] and such phases are called polar smectic A phases, or SmAP phases (see Figure 5.1), where the 'P' stands for 'polar'. In the simplest case, there are two SmAP subphases: (1) the

$SmAP_F$ phase, where the in-layer polarisation points in the same direction for all layers, i.e. ferroelectric, and (2) the $SmAP_A$ phase, where the polarisation between neighbouring layers points in opposite directions, i.e. antiferroelectric. Ferroelectric liquid crystals are promising candidates for applications in fast-switching electro-optic devices.[210–214] In 1996,[215] the first achiral bent-core material exhibiting ferroelectricity in its SmC phase was discovered. Several years later, the first ever observation of a SmAP subphase was made by Eremin et al.[216] in a liquid crystal possessing a cyano-substituted central core. The material exhibited antiferroelectric switching. In addition, another example of a SmAP subphase is the $SmAP_R$ phase (the 'R' subscript stands for 'random'), whereby the in-layer polarisation between neighbouring layers is arranged randomly, as shown in Figure 5.1. The $SmAP_R$ phase was discovered in 2003 by Pociecha et al.[217] In 2006, Shimbo et al.[218] demonstrated that a transition from the $SmAP_R$ to the $SmAP_F$ phase can be induced by applying an electric field parallel to the layer plane. In 2011, the first $SmAP_F$ material was synthesised by Reddy et al.[219] The $SmAP_F$ phase is the highest symmetry (C_{2v}) polar fluid phase possible in a layered system and it exhibits macroscopic ferroelectric ordering. The $SmAP_F$ phase has been observed over a temperature range of more than 50 °C, and it exhibits well-aligned textures in rubbed Teflon cells (it is difficult to obtain uniformly-aligned smectic phases of bent-core mesogens because they are usually formed directly below the isotropic phase). The reason why it has taken so long to discover the $SmAP_F$ phase (between 1996 and 2011) is because the molecular design of most bent-core liquid crystals favours antiferroelectric ordering because it is stabilised by energetic and entropic effects[27,220] (see the following paragraph for more details). Shortly after the discovery of the $SmAP_F$ phase, a modulated $SmAP_F$ ($SmAP_{Fmod}$) phase was also observed.[221]

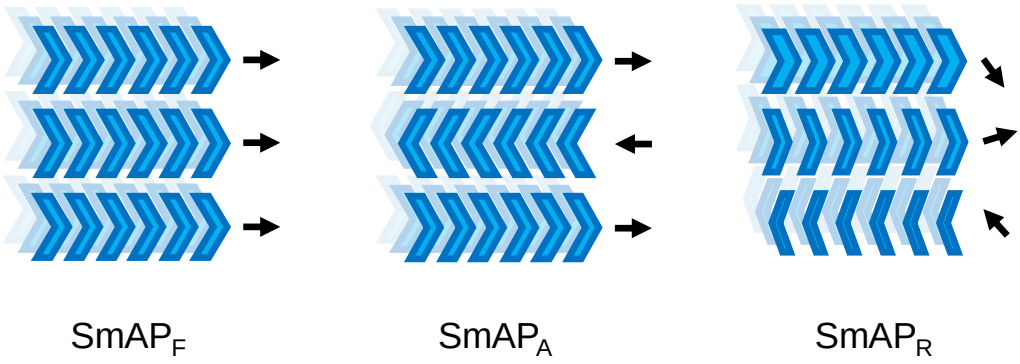

Figure 5.1: A schematic representation of the polar smectic A (SmAP) subphases, where arrows represent the direction of in-layer polarisation. The SmAP$_F$ phase (the 'F' stands for ferroelectric), where in-layer polarisation points in the same direction in all layers. The SmAP$_A$ phase, exhibiting antiparallel ordering of in-layer polarisation between neighbouring layers (the 'A' stands for antiferroelectric). The SmAP$_R$ phase, where in-layer polarisation is randomly aligned (the 'R' stands for random).

For this project, the SmAP$_F$ liquid crystal that was originally designed by Reddy et al.[219] was re-synthesised (named 'NT12') to further understand the physical properties of the SmAP$_F$ phase and to use the phase for templating in Chapter 7. The details of the synthesis are given in section 5.2. The molecular structure of NT12 is shown in Figure 5.2a. The structure is composed of a bent-core consisting of ester linkages, and a carbosilane tail tethered to the bent-core. Liquid crystals with ester groups in the bent-core are known to form spontaneously polar fluid smectic layers, typically having a tilted molecular axis (SmC) and exhibiting antiferroelectric behaviour.[222–227] This particular molecule (NT12), however, favours the formation of non-tilted layers, due to a single alkyl tail tethered to the bent-core (as opposed to two tails, one tethered to either end of the bent-core). Single tails attached to bent-cores (see Figure 5.2b) lead to more freedom of movement between layers, and hence, a decrease in their in-plane entropic pressure.[228] Now, because there is more free volume between the layers (which is energetically unfavourable), out-of-layer fluctuations of the tails into the adjacent layers occurs. These favour the arrangement of the tails in a synclinic fashion, which leads to antiferroelectric ordering. However, the presence of the carbosilane group disfavours out-of-layer fluctuations of the tails into adjacent layers, [219] and so the tails arrange in an anticlinic fashion, resulting in ferroelectric ordering of the in-layer polarisation between layers.

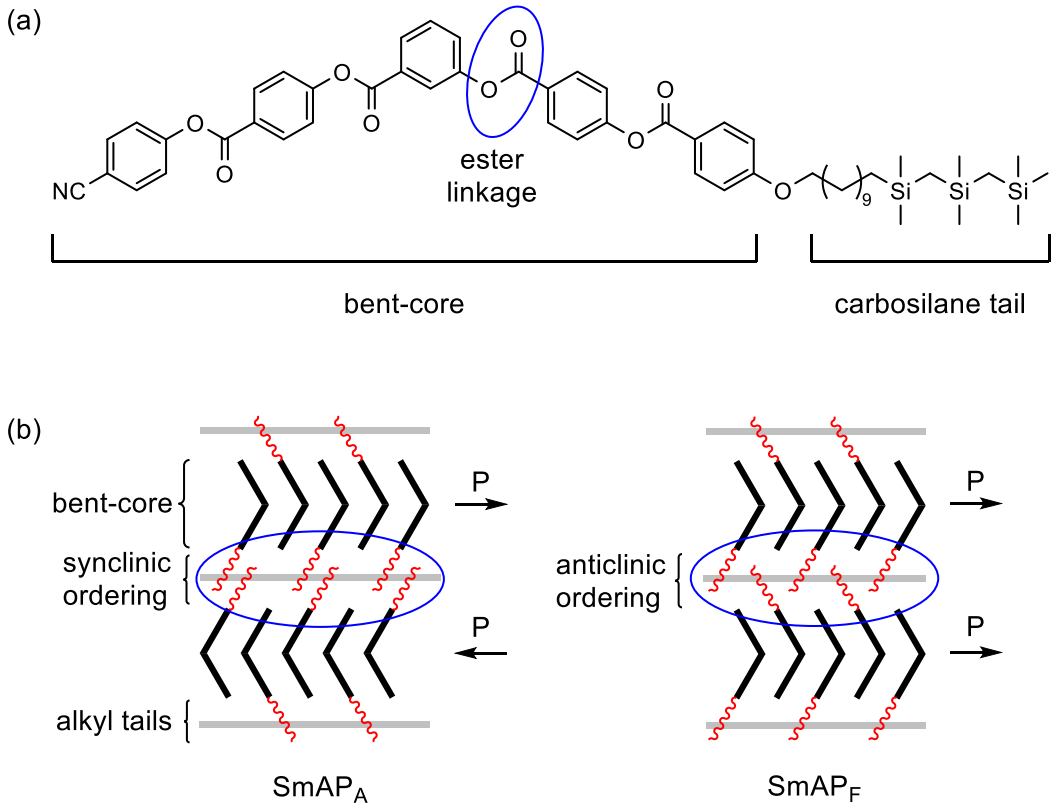

Figure 5.2: (a) Chemical structure of the bent-core mesogen exhibiting the SmA and SmAP$_F$ phases. (b) A diagram demonstrating synclinic and anticlinic ordering of molecular tails in the SmAP$_A$ and SmAP$_F$ phases, respectively.

5.2 Synthesis of mesogen NT12

The synthesis of the $SmAP_F$ mesogen NT12 consisted of a total of twelve steps and these are outlined in Scheme 1, Scheme 2 and Scheme 3. The synthesis of the bent-core part of the molecule involved alternating esterification and hydrogenation reactions. To form the target $SmAP_F$ liquid crystal, the final products from Scheme 2 and Scheme 3 couple together via an esterification reaction. The mechanism of the esterification reactions using DMAP and EDAC is demonstrated in Scheme 4. $^{1}H/^{13}C$ NMR spectra and FT-IR spectra for all synthesised compounds can be found in Appendix II.

Scheme 1:

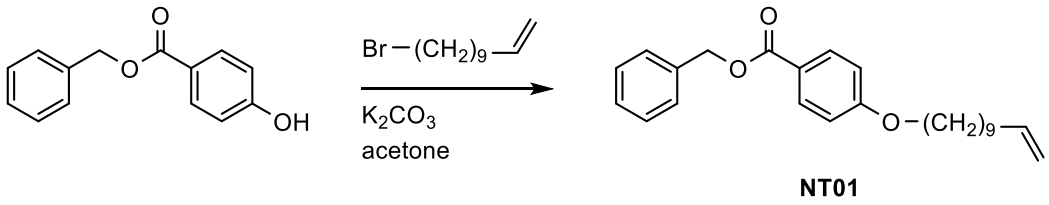

NT01

Scheme 2:

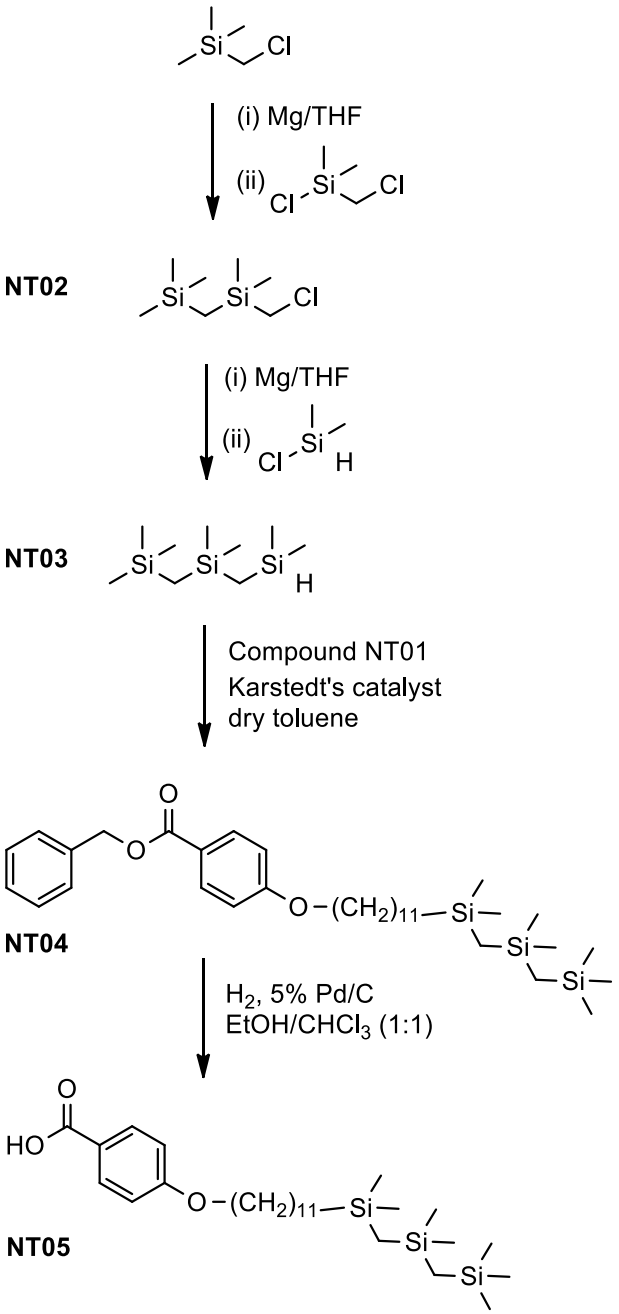
(i) Mg/THF
(ii)
NT02
(i) Mg/THF
(ii)
NT03
Compound NT01
Karstedt's catalyst
dry toluene
NT04
H2, 5% Pd/C
EtOH/CHCl3 (1:1)
NT05

Scheme 3:

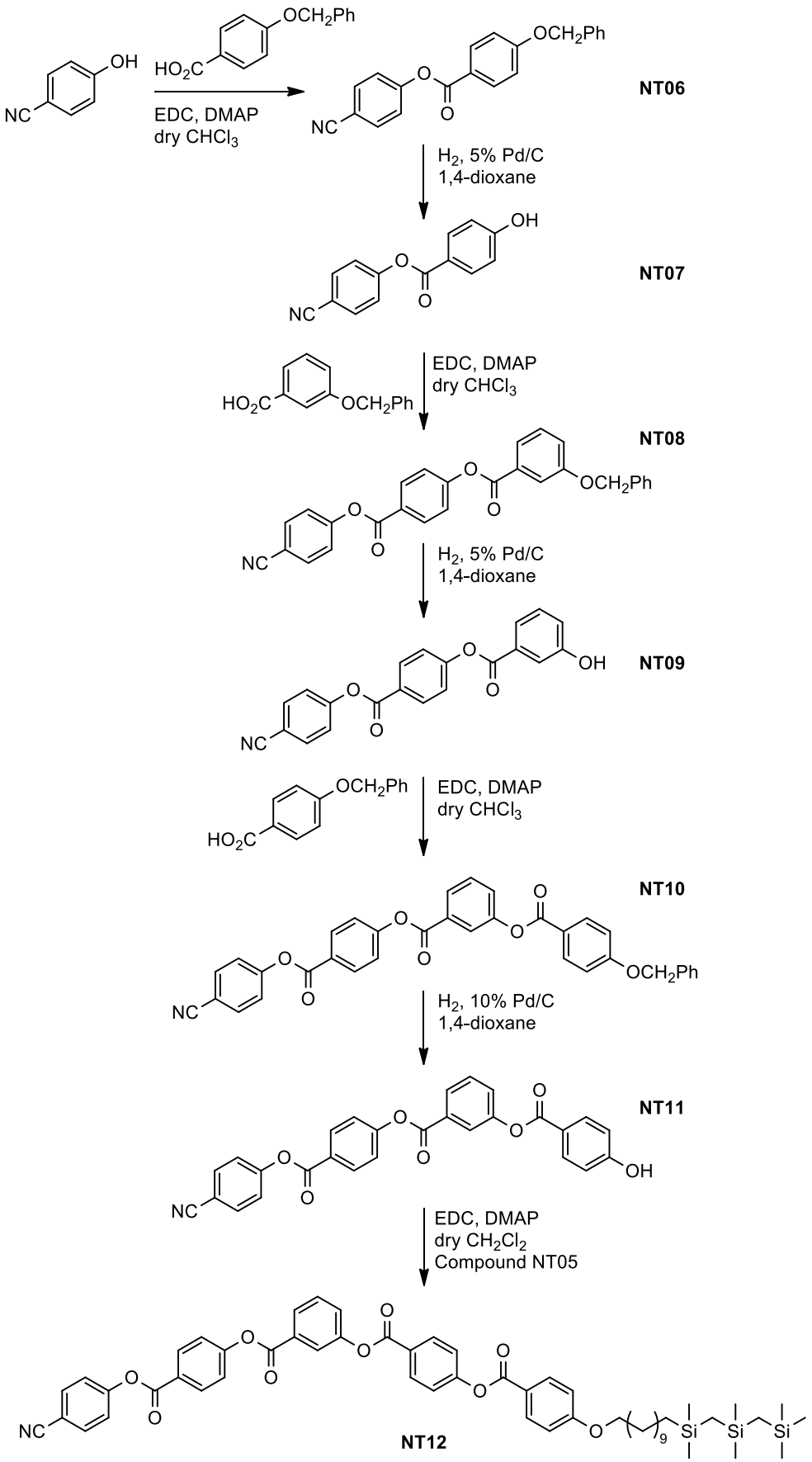
OCH2Ph
HO2C
OH
NC
EDC, DMAP
dry CHCl3
NT06
H2, 5% Pd/C
1,4-dioxane
NT07
NT08
NT09
NT10
H2, 10% Pd/C
1,4-dioxane
NT11
EDC, DMAP
dry CH2Cl2
Compound NT05
NT12
Si

Scheme 4 – Esterification reaction:

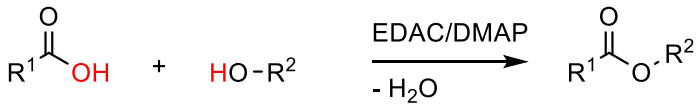

Mechanism:

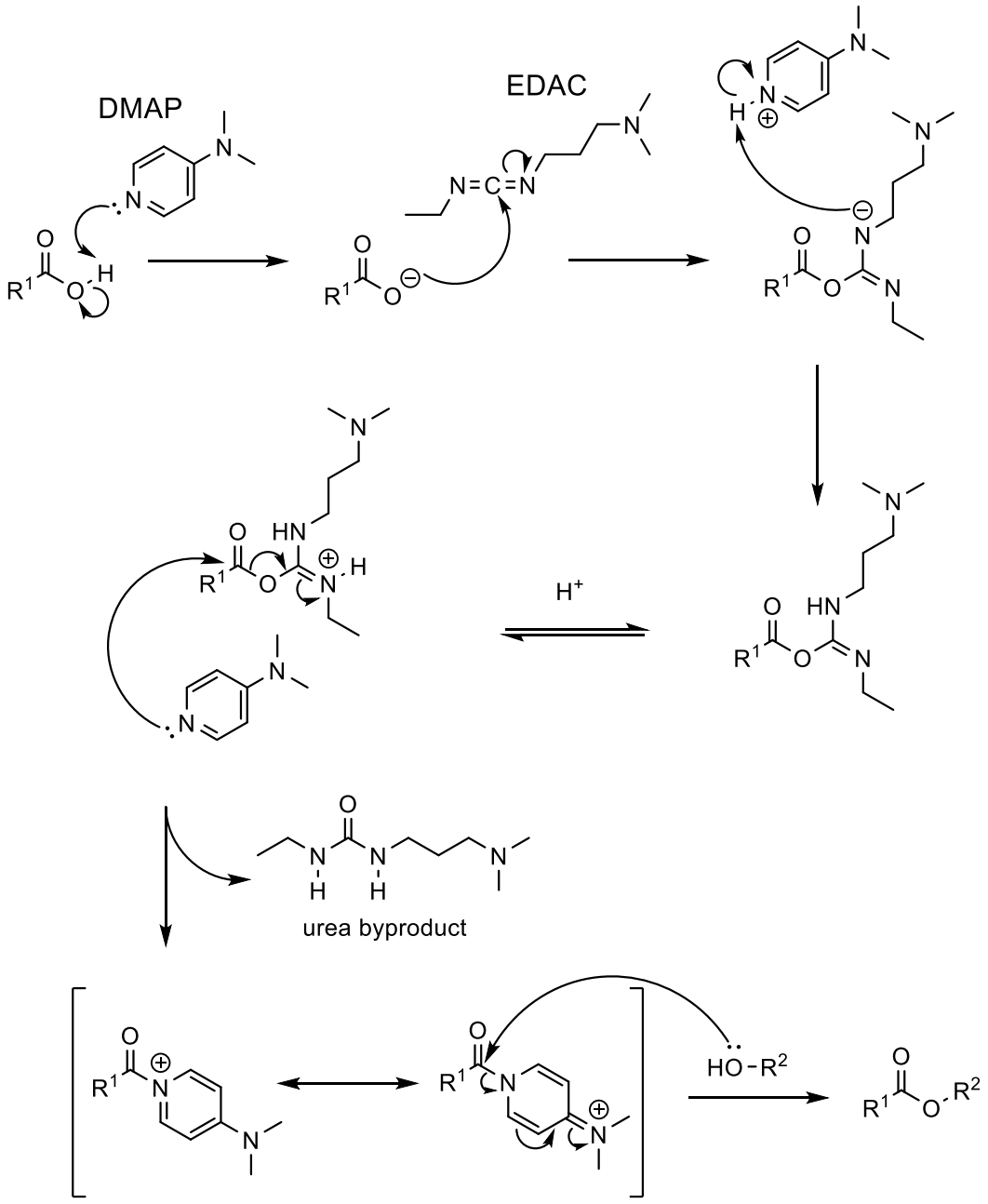

Benzyl 4-(undec-10-en-1-yloxy)benzoate [NT01]

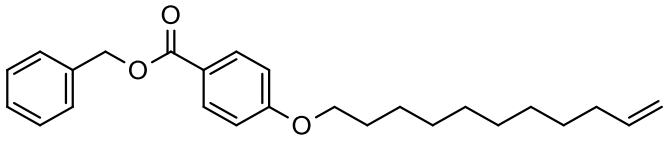

$C_{25}H_{32}O_3$
(380.53)

NT01 was prepared according to a procedure by Zhu et al.[221] 11-Bromo-1-undecene (13.27 g, 56.9 mmol) was added via a syringe to a mixture of benzyl 4-hydroxybenzoate (13.45 g, 58.9 mmol) and potassium carbonate (25.62 g, 185.4 mmol) whilst stirring in acetone (350 ml) at RT under a N_2 atmosphere. The reaction was then refluxed for 3 days. Once cooled to RT, the solvent was removed under reduced pressure. Diethyl ether (200 ml) was added to the residue, followed by filtration of the insoluble material through celite. The filtrate was washed with 10% (w/w) NaOH solution (3 × 100 ml) and brine (3 × 100 ml), and then dried over $MgSO_4$ and filtered. The solvent was removed under reduced pressure to give NT01 as a colourless oil in 72% yield (15.56 g, 40.9 mmol). No further purification was undertaken.

^{1}H-NMR (400 MHz, $CDCl_3$): δ = 8.08–7.95 (m, 2H), 7.48–7.29 (m, 5H), 6.93–6.86 (m, 2H), 5.91–5.74 (m, 1H), 5.34 (s, 2H), 5.04–4.88 (m, 2H), 4.00 (t, *J* = 6.6 Hz, 2H), 2.09–1.99 (m, 2H), 1.85–1.73 (m, 2H), 1.51–1.23 (m, 12H) ppm.

^{13}C-NMR (101 MHz, $CDCl_3$): δ = 166.3, 163.1, 139.2, 136.4, 131.7, 128.6, 128.1, 128.1, 122.3, 114.2, 114.1, 68.2, 66.4, 33.8, 29.5, 29.4, 29.4, 29.1, 28.9, 26.0 ppm.

FT-IR: $\tilde{\nu}$ = 3067 (w), 3034 (w), 2925 (m), 2853 (m), 2076 (w), 1713 (s), 1640 (w), 1605 (s), 1580 (w), 1510 (m), 1456 (m), 1421 (w), 1375 (w), 1312 (m), 1249 (s), 1165 (s), 1097 (s), 1009 (m), 909 (m), 846 (m), 768 (s), 750 (m), 732 (m), 695 (s), 649 (m), 632 (w), 599 (w), 585 (w), 510 (m) cm^{-1}.

(Chloromethyl)dimethyl((trimethylsilyl)methyl)silane [NT02]

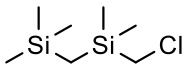

$C_7H_{19}ClSi_2$
(194.85)

NT02 was prepared according to a procedure by Reddy et al.[219] Oven-dried Mg turnings (8.91 g, 366.5 mmol) and an iodine crystal were added to an oven-dried 3-neck flask equipped with a condenser, dropping funnel and septum. Dry THF (60 ml) was added to the flask whilst the reaction was stirred at RT under a nitrogen atmosphere, followed by 9 drops of 1,2-dibromoethane. The Grignard reagent was activated after 15 min (indicated by a change in colour from orange/brown to colourless). A solution of (chloromethyl)trimethylsilane (40.68 g, 331.6 mmol) in 40 ml of dry THF was added dropwise to the 3-neck flask at RT over approx. 1 h. The reaction was left to reflux for 2 h and then cooled to RT. A solution of chloro(chloromethyl)dimethylsilane (45.08 g, 315.1 mmol) in 40 ml of dry THF was then added dropwise to the flask at RT over approx. 35 min. The reaction mixture was then left to reflux for 3 days. The reaction mixture was cooled to RT, deionised H_2O (150 ml) was added, followed by hexane (100 ml). The aqueous phase was extracted with hexane (3 × 50 ml) and the combined hexane phases were dried over $MgSO_4$. The solvent was removed under reduced pressure to yield 76% (46.37 g, 238.0 mmol) of NT02 as a colourless oil.

^{1}H-NMR (400 MHz, $CDCl_3$): δ = 2.70 (s, 2H, -$SiCH_2Si$-), 0.09 (s, 6H, -$Si(CH_3)_2$-), 0.00 (s, 9H, -$Si(CH_3)_3$), -0.19 (s, 2H, -CH_2Cl) ppm.

^{13}C-NMR (101 MHz, $CDCl_3$): δ = 31.1, 0.0, -0.1, -3.3 ppm.

FT-IR: $\tilde{\nu}$ = 2954 (m), 2898 (w), 1396 (w), 1354 (w), 1250 (m), 1175 (w), 1105 (w), 1052 (m), 830 (s), 764 (m), 687 (m), 655 (w), 635 (w), 601 (w), 550 (w) cm^{-1}.

((Dimethylsilyl)methyl)dimethyl((trimethylsilyl)methyl)silane [NT03]

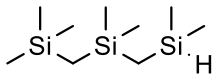

$C_9H_{26}Si_3$
(218.56)

NT03 was prepared according to a procedure that is similar to the synthesis of compound NT02. Oven-dried Mg turnings (3.90 g, 160.4 mmol) and an iodine crystal were added to an oven-dried 3-neck flask equipped with a condenser, dropping funnel and septum. Dry THF (65 ml) and then 2-3 drops of 1,2-dibromoethane were added to the flask and the reaction was stirred under a N_2 atmosphere at RT. Once the Grignard reaction was initiated, a solution of compound NT02 (26.59 g, 135.5 mmol) in 25 ml of dry THF was added dropwise at RT over a period of 20 min. The reaction was left to reflux for 2 h and was then cooled to RT. Chlorodimethylsilane (12.91 g, 136.5 mmol) was then added dropwise over approx. 20 min at 0 °C. The reaction mixture was then left to stir at RT for 41 h. Deionised water (200 ml) was added to the reaction mixture, followed by hexane (100 ml). The aqueous phase was extracted with hexane (3 × 50 ml) and the combined hexane phases were dried over $MgSO_4$ and filtered. The filtrate was reduced to give NT03 as a colourless oil in a 76% yield (22.54 g, 103.1 mmol) and this was used for the following reaction without further purification.

^{1}H-NMR (400 MHz, $CDCl_3$): δ = 3.99–3.91 (m, 1H, Si-H), 0.07 (d, J = 3.6 Hz, 6H, -Si(CH_3)$_2$H), 0.03 (s, 6H, -Si(CH_3)$_2$-), 0.00 (s, 9H, -Si(CH_3)$_3$), -0.24–-0.27 (m, 4H, 2 × -SiCH_2Si-) ppm.

^{13}C-NMR (101 MHz, $CDCl_3$): δ = 3.7, 1.4, 0.4, 0.0, -2.9 ppm.

FT-IR: $\tilde{\nu}$ = 2954 (m), 2899 (w), 2109 (m), 1420 (w), 1355 (w), 1249 (s), 1052 (s), 890 (s), 860 (m), 827 (s), 811 (s), 763 (s), 684 (m), 659 (w), 630 (m), 588 (w), 542 (w) cm^{-1}.

Benzyl 4-((11-(((dimethyl((trimethylsilyl)methyl)silyl)methyl)dimethylsilyl) undecyl)oxy)benzoate [NT04]

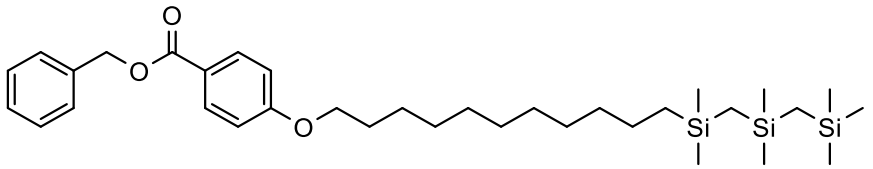

$C_{34}H_{58}O_3Si_3$
(599.09)

NT04 was prepared according to a procedure by Reddy et al.[219] NT01 (15.40 g, 40.5 mmol) was stirred at RT in dry toluene (100 ml). To this mixture, NT03 (11.17 g, 51.1 mmol) in dry toluene (15 ml) was added, followed by the addition of Karstedt's catalyst [platinum-divinyltetramethyldisiloxane complex in xylene; Pt concentration: 2.1 - 2.4%] (1.55 ml). The reaction was shielded from light by covering the flask with aluminium foil and was then left to stir at RT for 2 days. The reaction underwent a colour change – upon the addition of the catalyst, it was a pale-yellow colour, then gradually turned to dark brown. The crude product was reduced and purified using flash chromatography with hexane as the eluent. The eluate was reduced, and deionised H_2O (100 ml) and hexane (400 ml). The aqueous phase was extracted with hexane (3 × 150 ml) and the combined hexane phases were dried over $MgSO_4$ and filtered. The filtrate was reduced to give NT04 as a brown oil in a 79% yield (19.19 g, 32.0 mmol), which was used for the following reaction without further purification.

^{1}H-NMR (400 MHz, $CDCl_3$): δ = 8.02–7.96 (m, 2H, Ar-H), 7.44–7.27 (m, 5H, Ar-H), 6.89–6.84 (m, 2H, Ar-H), 5.31 (s, 2H, Ar-CH_2-), 3.97 (t, *J* = 6.6 Hz, 2H, Ar-OCH_2-), 1.82–1.71 (m, 2H, -OCH_2*CH_2*-), 1.47–1.18 (m, 16H, 8 × CH_2), 0.50–0.41 (m, 2H, -CH_2*CH_2*Si-), 0.05–-0.07 (m, 21H, 2 × Si $(CH_3)_2$, 1 × Si $(CH_3)_3$), -0.29 (d, *J* = 9.6 Hz, 4H, 2 × -Si-CH_2-Si-) ppm.

^{13}C-NMR (101 MHz, $CDCl_3$): δ = 164.7, 161.6, 134.9, 130.2, 127.1, 126.6, 126.6, 120.8, 112.6, 66.7, 64.9, 32.2, 28.2, 28.1, 28.1, 27.9, 27.6, 24.5, 22.5, 16.6, 4.3, 2.5, 1.0, 0.0, -1.9 ppm.

FT-IR: $\tilde{\nu}$ = 2949 (m), 2923 (m), 2853 (m), 1716 (m), 1606 (m), 1580 (w), 1510 (m), 1456 (w), 1421 (w), 1375 (w), 1312 (w), 1248 (s), 1166 (m), 1098 (m), 1049 (m), 1010 (m), 830 (s), 808 (s), 768 (s), 694 (s), 649 (m), 599 (w), 530 (w), 510 (w) cm^{-1}.

4-((11-(((dimethyl((trimethylsilyl)methyl)silyl)methyl)dimethylsilyl) undecyl)oxy)benzoic acid [NT05]

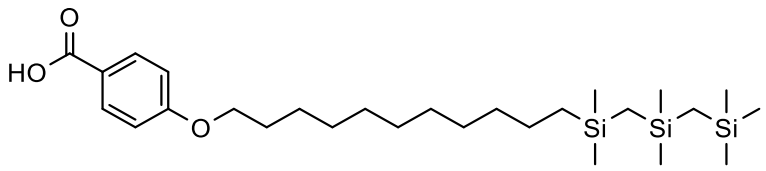

$C_{27}H_{52}O_3Si_3$
(508.97)

NT05 was prepared according to a procedure by Reddy et al.[219] NT04 (15.18 g, 25.3 mmol) and 5% Pd on activated charcoal catalyst (Pd/C; 3.01 g) were stirred at RT in a 1:1 mixture of EtOH/$CHCl_3$ (200 ml). The reaction mixture was evacuated and backfilled with N_2 four times. The reaction was then left to stir in an atmosphere of hydrogen at RT for 4 h. The catalyst was filtered through celite and the filtrate was reduced and dried under vacuum to yield NT05 as an almost colourless solid in a 99% yield (12.73 g, 25.0 mmol), which was used without further purification.

^{1}H-NMR (400 MHz, $CDCl_3$): δ = 8.05–8.00 (m, 2H), 6.94–6.87 (m, 2H), 4.00 (t, *J* = 6.5 Hz, 2H), 1.84–1.73 (m, 2H), 1.49–1.39 (m, 2H), 1.38–1.19 (m, 14H), 0.50–0.40 (m, 2H), 0.05–-0.05 (m, 21H), -0.27–-0.33 (m, 4H) ppm.

^{13}C-NMR (101 MHz, $CDCl_3$): δ = 169.2, 162.2, 130.9, 117.4, 112.7, 66.8, 32.2, 28.1, 27.9, 27.6, 27.6, 26.8, 26.1, 25.5, 24.5, 22.5, 16.6, 4.3, 2.6, 1.0, 0.0, -1.9 ppm.

FT-IR: $\tilde{\nu}$ = 2950 (m), 2919 (m), 2851 (m), 2672 (w), 2559 (w), 2066 (w), 1979 (w), 1672 (m), 1605 (m), 1577 (w), 1513 (w), 1467 (w), 1433 (m), 1306 (m), 1250 (s), 1159 (m), 1127 (w), 1105 (w), 1036 (s), 959 (w), 942 (w), 905 (w), 831 (s), 802 (s), 770 (s), 722 (m), 685 (m), 645 (m), 598 (w), 550 (m), 505 (m) cm^{-1}.

4-Cyanophenyl 4-benzyloxybenzoate [NT06]

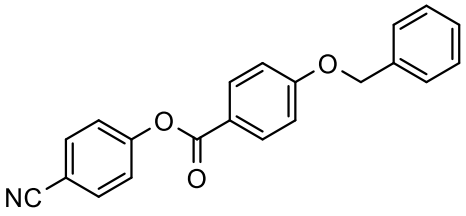

$C_{21}H_{15}NO_3$
(329.36)

NT06 was prepared according to an adapted procedure by Sadashiva et al.[228] 4-Benzyloxybenzoic acid (24.61 g, 107.8 mmol), 4-hydroxybenzonitrile (12.86 g, 108.0 mmol) and DMAP (1.21 g, 10.7 mmol) were stirred in dry $CHCl_3$ (400 ml) at RT for 25 min. The flask was then placed in an ice bath and EDAC (21.87 g, 189.8 mmol) was added. The flask was kept in the ice bath for 5 min after the addition of EDAC and was then allowed to heat back up to RT. When EDAC was added, the reaction turned clear (it was cloudy before the addition of EDAC), and 30 min after the addition of EDAC, precipitate began to form. The reaction was stirred at RT for a further 48 h. The crude reaction was washed with deionised H_2O (3 × 200 ml) and the organic layer was dried over $MgSO_4$ and filtered. The filtrate was reduced and washed with acetone to yield NT06 as a colourless solid in a 73% yield (25.76 g, 78.2 mmol).

^{1}H-NMR (400 MHz, $CDCl_3$): δ = 8.14 (d, *J* = 8.8 Hz, 2H, Ar-H), 7.73 (d, *J* = 8.6 Hz, 2H, Ar-H), 7.47–7.30 (m, 7H, Ar-H), 7.07 (d, *J* = 8.9 Hz, 2H, Ar-H), 5.17 (s, 2H, -OCH_2Ph) ppm.

^{13}C-NMR (101 MHz, $CDCl_3$): δ = 164.0, 163.5, 154.4, 136.0, 133.7, 132.5, 128.8, 128.4, 127.5, 123.0, 121.1, 118.4, 114.9, 109.6, 70.3 ppm.

FT-IR: $\tilde{\nu}$ = 3434 (w), 3099 (w), 3065 (w), 2946 (w), 2883 (w), 2229 (m), 2116 (w), 2050 (w), 1949 (w), 1922 (w), 1898 (w), 1793 (w), 1725 (s), 1601 (m), 1575 (m), 1507 (m), 1494 (m), 1464 (w), 1455 (w), 1418 (w), 1381 (m), 1328 (w), 1316 (w), 1305 (w), 1270 (m), 1250 (m), 1195 (m), 1159 (m), 1120 (m), 1105 (m), 1067 (m), 996 (w), 982 (m), 919 (w), 886 (m), 849 (m), 815 (m), 799 (m), 762 (s), 753(s), 724 (w), 695 (s), 648 (w), 630 (w), 572 (w), 549 (s), 522 (m), 510 (m) cm^{-1}.

4-Cyanophenyl 4-hydroxybenzoate [NT07]

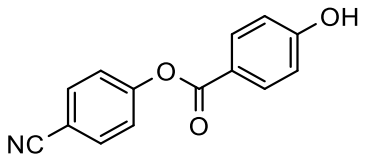

$C_{14}H_9NO_3$
(239.23)

NT07 was prepared according to a an adapted procedure by Sadashiva et al.[228] To a 250 ml flask, NT06 (7.67 g, 23.3 mmol), 5% Pd/C catalyst (1.53 g) and 1,4-dioxane (100 ml) were added and the flask was evacuated and backfilled with N_2 three times at RT. The reaction was heated to 57 °C under an atmosphere of N_2 and then exposed to an atmosphere of H_2 for 22 h. The reaction mixture was cooled to RT and filtered through celite. The filtrate was reduced to give NT07 as an almost colourless solid in a 96% yield (5.34 g, 22.3 mmol).

^{1}H-NMR (400 MHz, acetone-d6): δ = 9.41 (s, 1H, Ar-OH), 8.11–8.03 (m, 2H, Ar-H), 7.94–7.87 (m, 2H, Ar-H), 7.56–7.49 (m, 2H, Ar-H), 7.05–6.98 (m, 2H, Ar-H) ppm.

^{13}C-NMR (101 MHz, acetone-d6): δ = 163.7, 162.8, 154.8, 133.7, 132.5, 123.4, 120.0, 118.0, 115.6, 109.4 ppm.

FT-IR: $\tilde{\nu}$ = 3347 (m), 3104 (w), 2230 (m), 2113 (w), 2015 (w), 1996 (w), 1923 (w), 1731 (s), 1611 (m), 1593 (m), 1512 (m), 1496 (m), 1449 (w), 1411 (w), 1373 (w), 1356 (w), 1287 (m), 1266 (s), 1214 (s), 1165 (s), 1113 (m), 1068 (s), 1012 (m), 954 (w), 875 (m), 841 (m), 807 (m), 758 (m), 725 (w), 707 (w), 686 (m), 635 (m), 615 (m), 550 (s), 504 (m) cm^{-1}.

4-((4-Cyanophenoxy)carbonyl)phenyl 3-(benzyloxy)benzoate [NT08]

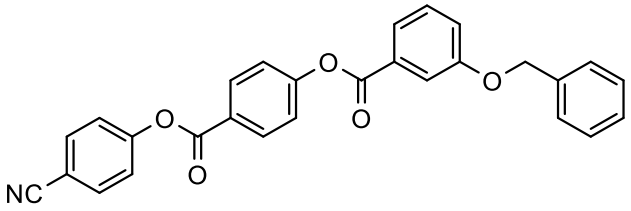

$C_{28}H_{19}NO_5$
(449.46)

The synthesis procedure of NT08 was similar to that of compound NT06.

Setup: NT07 (7.91 g, 33.1 mmol, 1 equiv.)

3-benzyloxybenzoic acid (7.56 g, 33.1 mmol, 1 equiv.)

EDAC (6.12 g, 39.4 mmol, 1.2 equiv.)

DMAP (0.42 g, 3.44 mmol, 0.1 equiv.)

dry $CHCl_3$ (100 ml)

The reaction was stirred at RT for 13 h. The crude was mixed with silica gel and reduced. This was then flushed through a pad of silica gel using chloroform. The resulting filtrate was reduced to yield NT08 as an almost colourless solid.

Yield: 7.72 g, 17.2 mmol, 52%, almost colourless solid.

^{1}H-NMR (400 MHz, $CDCl_3$): δ = 8.31–8.25 (m, 2H, Ar-H), 7.85–7.72 (m, 4H, Ar-H), 7.49–7.26 (m, 11H, Ar-H), 5.16 (s, 2H, -OCH_2Ph) ppm.

^{13}C-NMR (101 MHz, $CDCl_3$): δ = 164.4, 163.6, 159.0, 155.6, 154.2, 136.3, 133.8, 132.0, 130.2, 129.9, 128.7, 128.3, 127.6, 126.2, 122.9, 122.3, 121.2, 118.3, 115.9, 110.0, 70.3 ppm.

FT-IR: $\tilde{\nu}$ = 3100 (w), 3067 (w), 2887 (w), 2227 (w), 2128 (w), 1927 (w), 1817 (w), 1729 (s), 1601 (m), 1581 (m), 1500 (m), 1485 (m), 1453 (m), 1417 (m), 1392 (w), 1313 (w), 1291 (w), 1273 (s), 1216 (m), 1166 (m), 1114 (w), 1083 (w), 1067 (m), 1013 (m), 929 (w), 906 (w), 889 (w), 867 (m), 846 (w), 830 (w), 798 (w), 743 (s), 698 (m), 679 (m), 631 (w), 549 (m), 528 (w), 502 (w) cm^{-1}.

4-((4-Cyanophenoxy)carbonyl)phenyl 3-hydroxybenzoate [NT09]

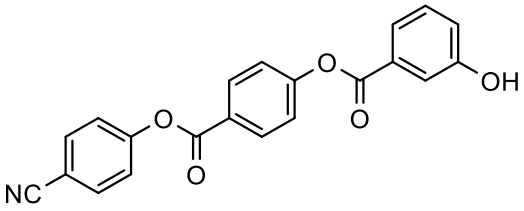

$C_{21}H_{13}NO_5$
(359.34)

The synthesis procedure of NT09 was similar to that of compound NT07.

Setup: NT08 (7.70 g, 17.1 mmol)

5 % Pd/C catalyst (1.53 g)

1,4-dioxane (75 ml)

The reaction mixture was stirred in an atmosphere of hydrogen for 12 h at 57 °C. The reaction was cooled to RT and filtered through celite. The filtrate was reduced to yield NT09 as an almost colourless solid.

Yield: 6.07 g, 16.9 mmol, 99%, almost colourless solid.

^{1}H-NMR (400 MHz, acetone-d6): δ = 8.87 (s, 1H, Ar-OH), 8.35–8.28 (m, 2H, Ar-H), 7.97–7.91 (m, 2H, Ar-H), 7.73–7.52 (m, 6H, Ar-H), 7.48–7.41 (m, 1H, Ar-H), 7.25–7.18 (m, 1H, Ar-H) ppm.

^{13}C-NMR (101 MHz, acetone-d6): δ = 164.1, 163.4, 157.7, 154.5, 133.8, 131.8, 130.4, 130.0, 126.6, 123.4, 122.5, 121.2, 121.1, 118.0, 116.4, 109.8 ppm.

FT-IR: $\tilde{\nu}$ = 3284 (m), 3105 (w), 3068 (w), 2247 (m), 2142 (w), 2020 (w), 1929 (w), 1728 (s), 1560 (m), 1587 (m), 1501 (m), 1485 (m), 1450 (w), 1417 (m), 1379 (w), 1337 (w), 1294 (w), 1266 (m), 1237 (m), 1193 (s), 1168 (m), 1116 (w), 1072 (w), 1055 (m), 1014 (w), 997 (w), 931 (w), 903 (w), 873 (m), 847 (w), 824 (w), 803 (w), 751 (s), 688 (m), 646 (w), 626 (w), 550 (m), 506 (w) cm^{-1}.

4-((4-cyanophenoxy)carbonyl)phenyl 3-((4-(benzyloxy)benzoyl)oxy)benzoate [NT10]

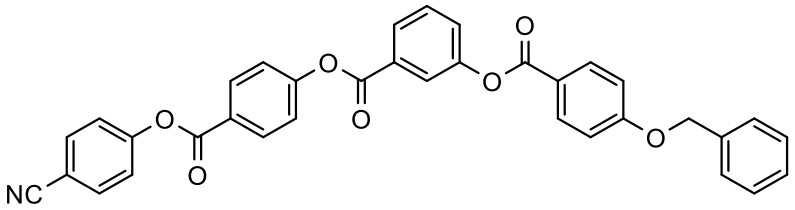

$C_{35}H_{23}NO_7$
(569.57)

The synthesis procedure of NT10 was similar to that of compound NT06.

Setup: NT09 (6.04 g, 16.8 mmol, 1 equiv.)

4-benzyloxybenzoic acid (3.84 g, 16.8 mmol, 1 equiv.)

EDAC (4.57 g, 29.4 mmol, 1.8 equiv.)

DMAP (0.21 g, 1.72 mmol, 0.1 equiv.)

dry $CHCl_3$ (75 ml)

The reaction was stirred at RT for 27 h. The crude was mixed with silica gel and reduced. This was then flushed through a pad of silica gel using chloroform. The resulting filtrate was reduced and dissolved in chloroform (200 ml) and washed with deionised H_2O (3 × 100 ml). The organic layer was dried over $MgSO_4$ and filtered to yield NT10 as an almost colourless solid.

Yield: 6.46 g, 11.3 mmol, 68%, almost colourless solid.

^{1}H-NMR (400 MHz, $CDCl_3$): δ = 8.31–8.25 (m, 2H, Ar-H), 8.21–8.02 (m, 4H, Ar-H), 7.78–7.73 (m, 2H, Ar-H), 7.64–7.33 (m, 11H, Ar-H), 7.11–7.05 (m, 2H, Ar-H), 5.17 (s, 2H, -OCH_2Ph) ppm.

^{13}C-NMR (101 MHz, $CDCl_3$): δ = 164.7, 163.7, 163.5, 163.3, 161.5, 161.4, 155.4, 154.2, 151.3, 136.0, 133.8, 132.5, 132.1, 130.4, 129.9, 128.8, 128.3, 127.7, 127.7, 127.5, 126.3, 123.8, 122.9, 122.9, 122.2, 121.5, 118.3, 114.9, 110.0, 70.3 ppm.

FT-IR: $\tilde{\nu}$ = 3073 (w), 2229 (w), 2117 (w), 2011 (w), 1927 (w), 1735 (s), 1719 (s), 1601 (m), 1505 (m), 1468 (w), 1445 (w), 1414 (w), 1391 (w), 1312 (w), 1246 (m), 1201 (s), 1157 (s), 1053 (s), 1009 (m), 995 (m), 916 (m), 880 (w), 864 (w), 841 (m), 795 (w), 759 (m), 752 (m), 734 (m), 694 (m), 673 (m), 657 (w), 631 (w), 593 (w), 568 (w), 549 (m), 505 (m) cm^{-1}.

4-((4-cyanophenoxy)carbonyl)phenyl 3-((4-hydroxybenzoyl)oxy)benzoate [NT11]

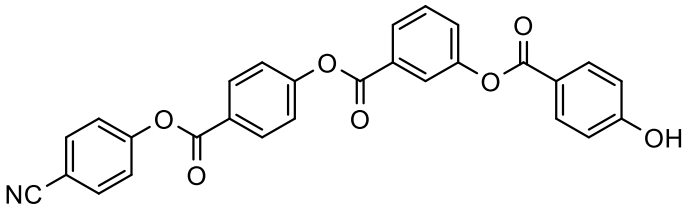

$C_{28}H_{17}NO_7$
(479.44)

The synthesis procedure of NT11 was similar to that of compound NT07.

Setup: NT10 (6.44 g, 11.3 mmol)

5 % Pd/C catalyst (0.65 g)

1,4-dioxane (65 ml)

The reaction mixture was stirred in an atmosphere of hydrogen for 24 h at 57 °C. The reaction was cooled to RT and filtered through celite. The filtrate was reduced, mixed with silica gel and CH_2Cl_2, and reduced again. This was flushed through a pad of silica gel with CH_2Cl_2. The filtrate was reduced to yield NT11 as an almost colourless solid.

Yield: 4.67 g, 9.74 mmol, 86%, almost colourless solid.

^{1}H-NMR (400 MHz, acetone-d6): δ = 9.38 (s, 1H, Ar-OH), 8.36–8.29 (m, 2H), 8.19–8.05 (m, 4H), 7.97–7.91 (m, 2H), 7.77–7.57 (m, 6H), 7.06–7.00 (m, 2H) ppm.

^{13}C NMR (101 MHz, acetone-d6): δ = 162.6, 154.5, 151.6, 133.8, 132.5, 131.8, 130.0, 127.9, 127.3, 127.3, 126.9, 126.7, 123.6, 123.4, 122.6, 118.0, 115.5, 109.8 ppm.

FT-IR: $\tilde{\nu}$ = 3379 (w), 3072 (w), 2962 (w), 2231 (w), 2096 (w), 2026 (w), 2007 (w), 1918 (w), 1734 (s), 1702 (s), 1591 (s), 1507 (m), 1440 (m), 1414 (w), 1373 (w), 1311 (w), 1248 (s), 1200 (s), 1157 (s), 1053 (s), 1012 (m), 912 (m), 875 (w), 845 (m), 796 (w), 740 (m), 687 (m), 633 (w), 571 (w), 549 (m), 502 (w) cm^{-1}.

4-((4-cyanophenoxy)carbonyl)phenyl 3-((4-((4-((11-(((dimethyl((trimethylsilyl)methyl)silyl)methyl)dimethylsilyl)undecyl)oxy)benzoyl)oxy)benzoyl)oxy)benzoate [NT12]

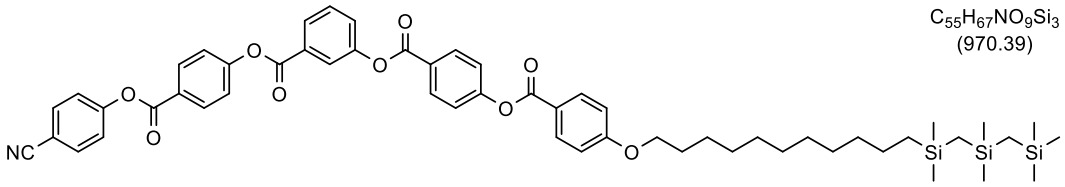

NT12 was prepared according to a procedure by Reddy et al. [219] NT11 (3.86 g, 8.05 mmol), NT05 (3.99 g, 7.84 g) and DMAP (0.13 g, 1.06 mmol) were stirred in dry CH_2Cl_2 (75 ml) for 15 min. The flask was then placed in an ice bath for 3 min and EDAC (1.41 g, 9.08 mmol) was added. The flask was kept in the ice bath for 5 min and was then allowed to heat back to RT. The reaction was left to stir at RT for 44 h. The crude was purified using column chromatography, with $CHCl_3$ as the eluent. The eluate was reduced, dissolved in $CHCl_3$ (250 ml) and washed with 2% aqueous acetic acid (3 × 100 ml), cold 10% NaOH solution (3 × 100 ml) and deionised H_2O (150 ml). The organic phase was dried over MgSO4, filtered and reduced. This was then crystallised from MeCN and the precipitate was filtered, washed with MeCN and dried under vacuum to give NT12 as an almost colourless solid in a 19% yield (1.48 g, 1.53 mmol). This was not purified further.

^{1}H-NMR (400 MHz, $CDCl_3$): δ = 8.31–8.24 (m, 4H, Ar-H), 8.16–8.03 (m, 4H, Ar-H), 7.76–7.71 (m, 2H, Ar-H), 7.64–7.51 (m, 2H, Ar-H), 7.43–7.34 (m, 6H, Ar-H), 7.00–6.94 (m, 2H, Ar-H), 4.04 (t, *J* = 6.5 Hz, 2H, Ar-OCH_2-), 1.85–1.77 (m, 2H, Ar-OCH_2*CH_2*-), 1.52–1.20 (m, 16H, -CH_2-), 0.49–0.43 (m, 2H, -Si*CH_2*CH_2), 0.04–-0.04 (m, 21H, 1 × $Si(CH_3)_3$, 2 × $Si(CH_3)_2$), -0.27–-0.32 (m, 4H, 2 × -$SiCH_2$Si) ppm.

^{13}C-NMR (101 MHz, $CDCl_3$) δ = 162.8, 162.4, 162.2, 162.1, 154.2, 153.9, 152.7, 149.6, 132.3, 131.0, 130.6, 130.4, 129.0, 128.5, 126.4, 126.1, 124.8, 122.2, 121.5, 120.8, 120.7, 119.4, 116.8, 113.0, 108.5, 66.9, 32.2, 28.2, 28.1, 28.1, 27.9, 27.6, 24.5, 22.5, 16.6, 4.3, 2.6, 1.0, 0.0, -1.9 ppm.

FT-IR: $\tilde{\nu}$ = 3074 (w), 2950 (m), 2921 (m), 2852 (m), 2232 (w), 1922 (w), 1732 (s), 1602 (m), 1509 (m), 1481 (w), 1445 (m), 1414 (m), 1311 (w), 1248 (s), 1211 (s), 1162 (s), 1115 (w), 1053 (s), 1016 (m), 916 (w), 831 (s), 809 (s), 752 (s), 737 (m), 684 (m), 624 (w), 578 (w), 548 (w), 506 (w) cm^{-1}.

***Learning the hard way*: useful tips for future reference**

(1) Initially, DCC (*N*,*N'*-dicyclohexylcarbodiimide) was used as the esterification coupling reagent (instead of EDAC). However, DCC is moisture sensitive, therefore, the yield of the esterification reactions using DCC was relatively low compared to the reactions where EDAC was used as the coupling reagent. In addition, when using DCC, the crude product was difficult to purify using column chromatography as the dicyclohexyl urea by-product has a similar polarity to that of the product.

(2) For hydrogenation reactions, rather than only purging with nitrogen, the reaction flask should be evacuated and backfilled with nitrogen at room temperature whilst the starting material, catalyst and solvent are vigorously stirring in the flask. The aim of doing this procedure is to get rid of any air trapped in the solvent (the solvent is not dry). When the solvent begins to bubble, the flask can be backfilled with nitrogen. This procedure should be repeated several times to ensure no air is present in the reaction flask, as this will prevent the potential formation of side-products. Note: a cold liquid nitrogen trap should be used for this procedure to avoid evaporated solvent getting into the vacuum pump during the evacuation procedure.

(3) Care should be taken when carrying out hydrogenation reactions. Avoid leaving the reactions to run for too long as this can lead to the formation of side products. The hydrogenation reactions should regularly be monitored using thin layer chromatography. There is also a possibility of the nitrile group getting reduced.

(4) For the purification of the three crude esterification reaction products NT06, NT08 and NT10 (Scheme 3), washing the crude products with acetone works well. This can be used as an alternative to crystallising the crude from acetonitrile/chloroform (as stated in the original paper[219]).

(5) Generally, a final step in the synthesis of liquid crystals involves the purified liquid crystal material being passed through a column of aluminium oxide, in order to remove any remaining ions. However, passing this particular liquid crystal through a (neutral) aluminium oxide column led to decomposition of the material, which was monitored using TLC.

(6) Care should be taken so that deuterated NMR solvents do not contain any moisture. Sometimes a singlet peak can be seen in the ^{1}H-NMR spectrum with a chemical shift that corresponds to H_2O (~1.56 ppm in $CDCl_3$ and ~2.84 ppm in

acetone d-6). This can lead to confusion whether the singlet peak is due to the reaction product catching moisture or if there is moisture within the NMR solvent.

(7) For hydrogenation reactions, a binary mixture of solvents including EtOH is generally used, because EtOH acts as a source of hydrogen. However, for the three hydrogenation steps in Scheme 3, the solvent 1,4-dioxane used in the original procedure[228] worked well.

(8) NMR solvents with tetramethylsilane (TMS) added as a standard should be avoided for compounds containing silane groups. This is because the chemical shifts of protons with neighbouring Si atoms appear at a similar chemical shift to the TMS singlet peak at 0 ppm. This is especially important when integrating peaks in ^{1}H-NMR spectra.

CHAPTER 6:
Investigations into the $SmAP_F$ phase

This chapter investigates the ferroelectric smectic A phase ($SmAP_F$) exhibited by the mesogen NT12 synthesised in Chapter 5. The $SmAP_F$ phase is the highest-symmetry layered ferroelectric state possible and it exhibits macroscopic polarisation stabilised by dipolar intermolecular interactions. The characterisation of pure NT12 is discussed first, followed by characterisation of binary mixtures of NT12 with the polymerisable monomer RM257. These mixtures will then be used in Chapter 7 to form templates of the $SmAP_F$ phase.

6.1 Characterisation of mesogen NT12

The chemical structure of NT12 is given in Figure 6.1a. A homeotropically-aligned cell was used to distinguish between the uniaxial SmA and biaxial $SmAP_F$ phases, which has previously been reported in literature for biaxial materials.[229–233] The sample was cooled from the isotropic state. As is shown in Figure 6.1b, at 155 °C the uniaxial SmA phase is optically dark, whereas at 130 °C in the biaxial $SmAP_F$ phase, birefringence is observed. The phase sequence of NT12 on cooling was determined using POM and was found to be: Iso 162 °C SmA 141 °C $SmAP_F$ (the phase sequence is given in Figure 6.1a). The isotropic-SmA and SmA-$SmAP_F$ phase transitions were determined using planar and homeotropic cells, respectively. Figure 6.1c shows that a fairly good homeotropic alignment can also be achieved between untreated cover slips, where the sample is optically dark in the SmA phase at 150 °C, and birefringence is observed in the $SmAP_F$ phase at 130 °C.

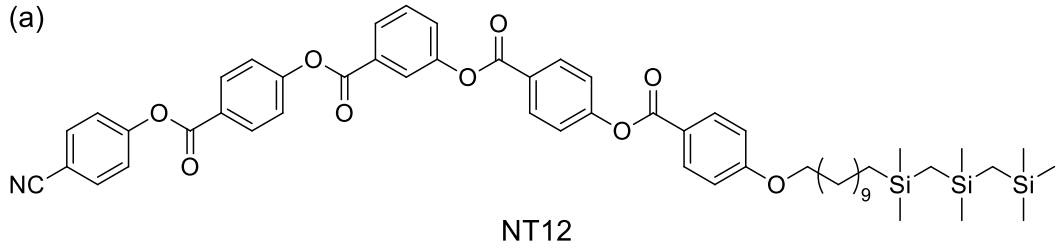

NT12

I 162 SmA 141 $SmAP_F$

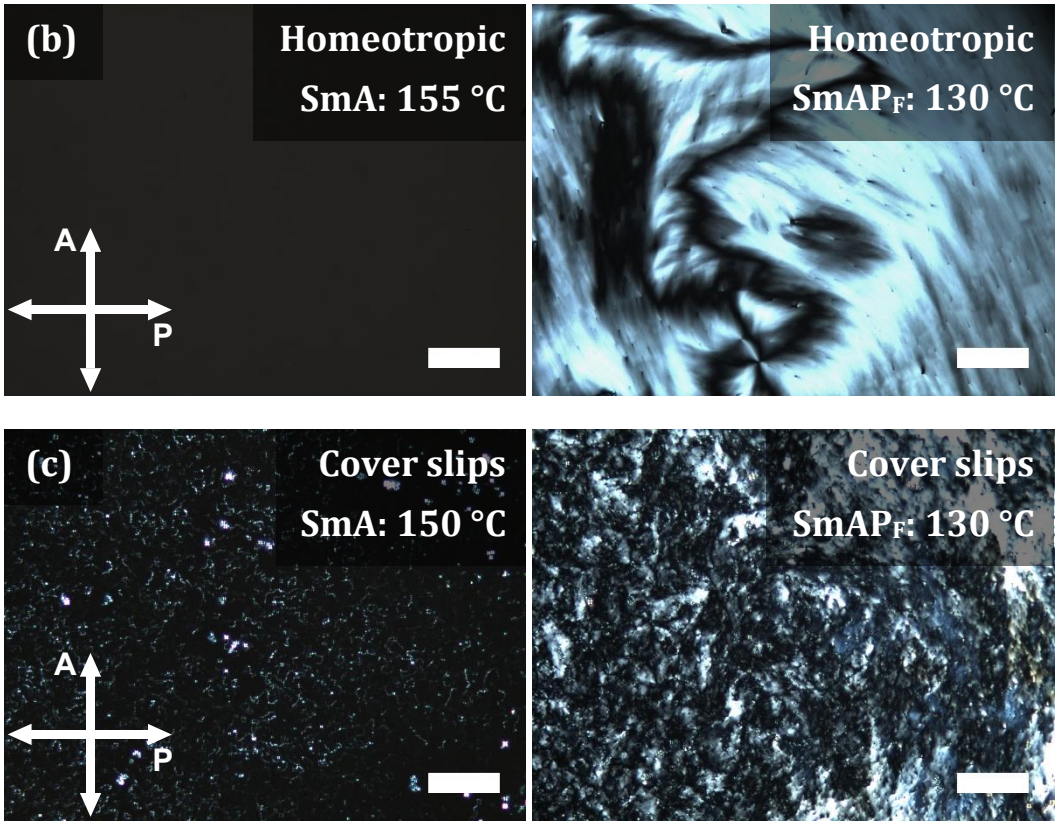

Figure 6.1: (a) The chemical structure and phase sequence of NT12. POM images of NT12: (b) in a 20 µm homeotropic cell at 155 °C (SmA) and 130 °C ($SmAP_F$), and (c) between untreated cover slips at 150 °C (SmA) and 130 °C ($SmAP_F$). The crossed polariser (P) and analyser (A) are labelled and the length of the scale bar is 100 µm.

A 5 μm planar cell was filled with NT12 at 160 °C (close to its clearing temperature of 162 °C) to identify any characteristic textures and features of the SmA and $SmAP_F$ phases. On cooling from the isotropic phase, small focal conic domains with a smooth texture are observed in the SmA phase at 145 °C, as seen in Figure 6.2. As the sample was further cooled, in the $SmAP_F$ phase at 125 °C, a 'brushed' texture in the focal conic domains is observed and the direction of the brushes is labelled with arrows in Figure 6.2 at 125 °C. As the sample is cooled below 100 °C, streaks appear that have a direction that is approximately perpendicular to the direction of the brushes. The directions of these streaks are labelled for two focal conic domains in Figure 6.2 at 95 °C, with an arrow encompassed by an oval. Further cooling results in the appearance of the streaks becoming more prominent (see 90 °C and 85 °C). Similar streaks have previously been observed in POM experiments for the $SmAP_F$[234] and $SmAP_A$[235] phases. Below 80 °C, the sample begins to crystallise, and sometimes textures of lower birefringence are observed, such as those depicted across the majority of the POM image at 25 °C in Figure 6.2. These textures of lower birefringence form along the same direction as the streaks discussed above.

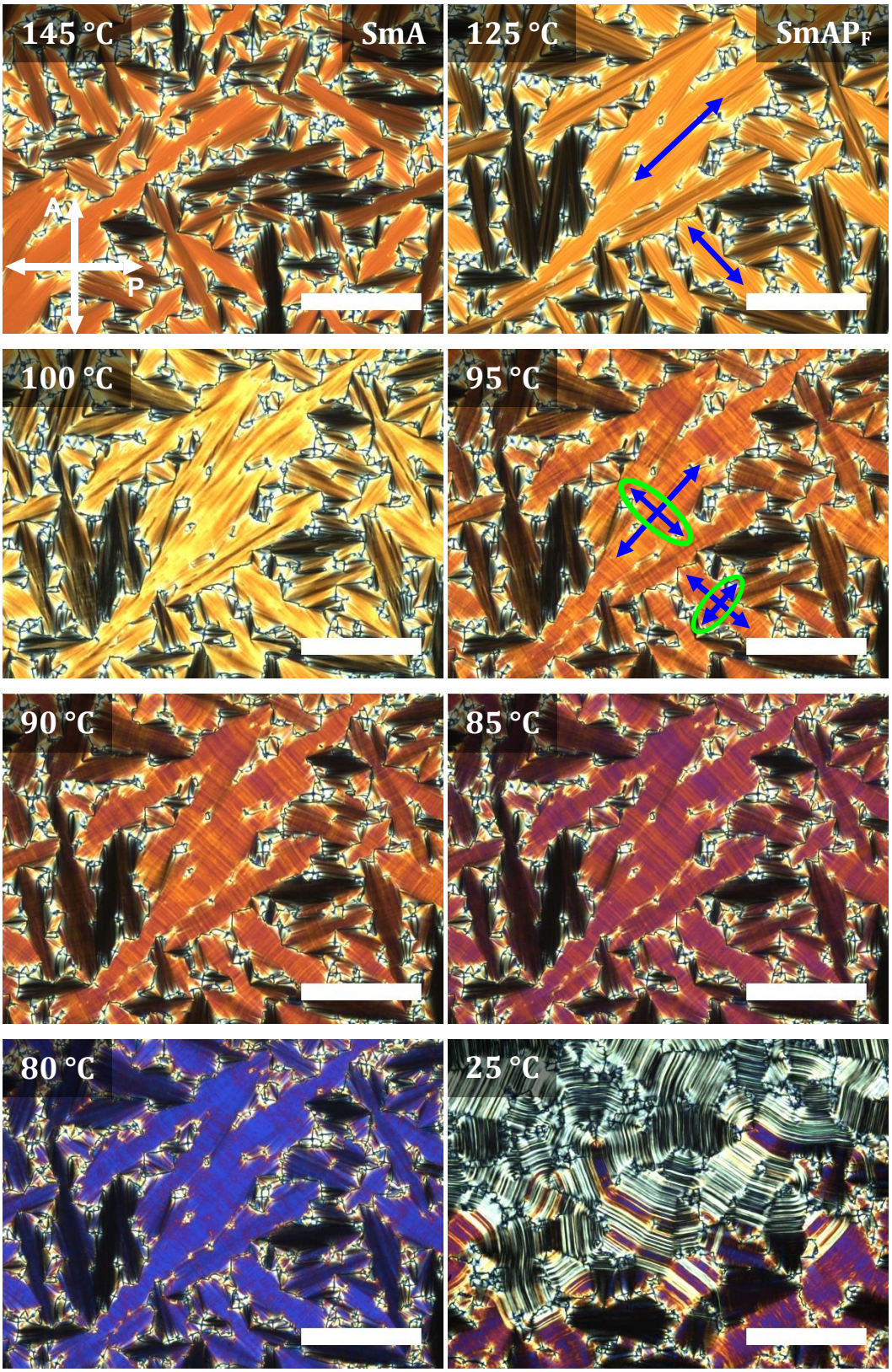

Figure 6.2: POM images of NT12 in a 5 μm planar cell taken on cooling from the isotropic state. The temperatures corresponding to each image are labelled. The length of the scale bar is 100 μm. The polariser and analyser are labelled.

Next, the electro-optical behaviour of NT12 was tested in a 10 µm planar cell. Subjecting the sample to an electric field results in a more homogeneous alignment with larger focal conic domains, compared to when no field is applied. Figure 6.3a shows the focal conic textures obtained when an electric field of 6 V/µm is applied, and the domains are larger compared to those in Figure 6.2 in the absence of an electric field. The greater the electric field, the larger the size of the focal conic domains, as is observed in Figure 6.3b when 10 V/µm is applied to the sample (compared to Figure 6.3a at 6 V/µm). When the electric field (10 V/µm) is removed (in the $SmAP_F$ phase), streaks appear across the focal conics, as shown in the left half of Figure 6.3c. The right half of Figure 6.3c shows the non-ITO area of the cell that was not subjected to the electric field. The effect of the electric field on the size of the focal conic domains can be clearly observed in the left side of Figure 6.3c.

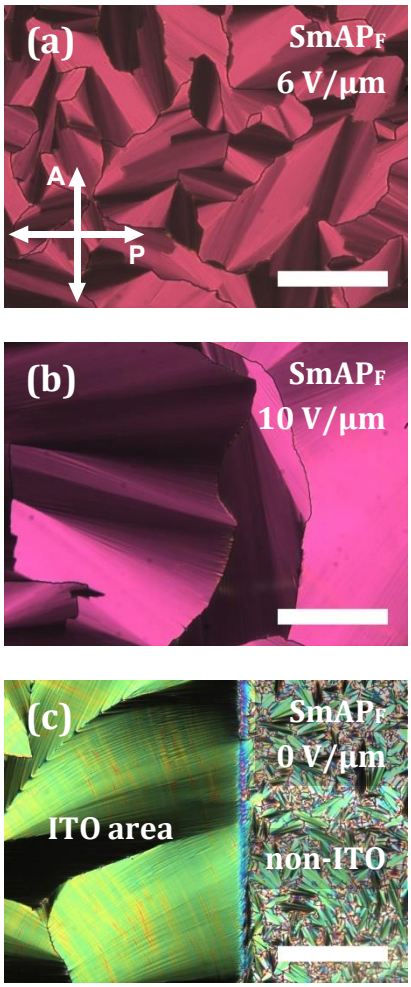

Figure 6.3: POM images of NT12 in a 10 µm planar cell at 100 °C ($SmAP_F$ phase) with an applied triangle wave of frequency 151 Hz. The electric fields applied are: (a) 6 V/µm, (b) 10 V/µm, and (c) 0 V/µm, after removing the 10 V/µm field – the small focal conic domains (right side of image) represent the non-ITO area of the cell that was not subjected to the electric field. The length of the scale bars is 100 µm.

The phase sequence temperatures of mesogen NT12 were analysed by differential scanning calorimetry (DSC). The data for the second heating cycle (bottom curve) and second cooling cycle (top curve) at a rate of 10 °C/min is given in Figure 6.4. Three phase transition peaks are observed in the second cooling cycle (top curve) of NT12. A first order isotropic to SmA transition occurs at 155.2 °C, with an associated enthalpy of 5.44 kJ/mol. A peak corresponding to the SmA to $SmAP_F$ transition occurs at 139.2 °C, with an associated enthalpy of 0.24 kJ/mol, which indicates a second order or weakly first order transition. The crystal transition is observed at 75.1 °C and has an associated enthalpy of 22.35 kJ/mol.

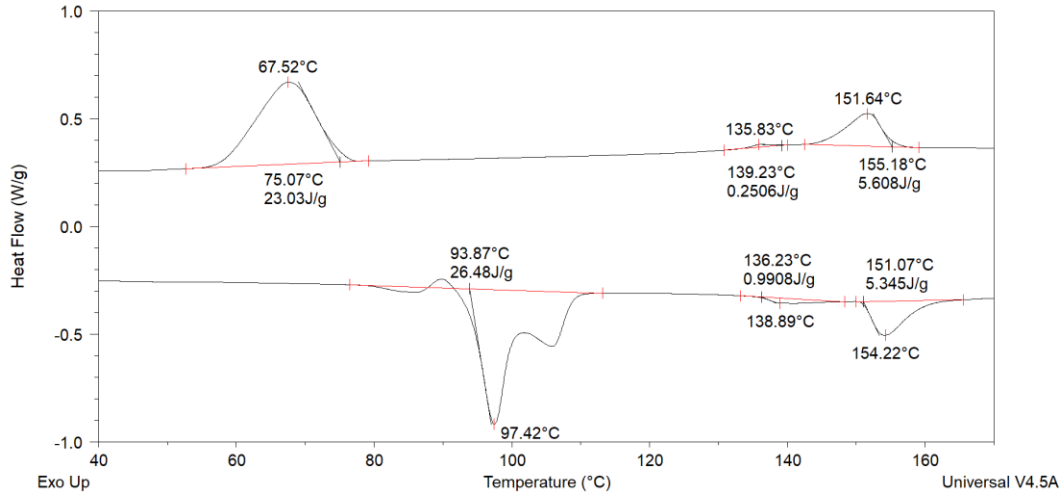

Figure 6.4: Second heating cycle (bottom curve) and second cooling cycle (top curve) of pure NT12 at a rate of 10 °C/min.

Small-angle X-ray scattering (SAXS) measurements were carried out on NT12 to confirm the presence of smectic phases. The layer spacing (in Å) for each temperature was calculated from the q values obtained from fitting the SAXS profiles to the Gaussian function (see section 2.3.6). The layer spacing was plotted as a function of temperature on cooling from 150 °C and the results are given in Figure 6.5. The SmA, $SmAP_F$ and crystal (Cr) phase ranges have been labelled – the SmA-$SmAP_F$ transition was obtained from a homeotropic cell and the $SmAP_F$-Cr transition was obtained from DSC data.

On cooling between 150 °C and 108 °C, there is a linear decrease (slope = 0.0216) in layer spacing in the range 60.5-61.5 Å, and this is similar to the values reported in literature (~61-62 Å).[219] As reported in literature, the layer spacing in the $SmAP_F$ phase is considerably greater than the calculated length of the most extended (all-trans) conformer of the material, with a layer spacing of 55 Å.[219] This suggests that

the $SmAP_F$ phase adopts a partially interdigitated layer structure, whereby the neighbouring aromatic parts of the bent-core molecules within the layer overlap, but the carbosilane tails alternate up and down between layers[236] (see Figure 5.2b). Similar behaviour was also observed for non-symmetric bent-core compounds exhibiting the antiferroelectric SmA ($SmAP_A$) phase.[228,237] Between 108 °C and 106 °C, however, there is an increase in layer spacing, from 60.7 Å to 64.2 Å, respectively. Cooling below 106 °C also shows a linear decrease in layer spacing, with a slope of 0.0225, which is similar to the slope of the linear decrease in layer spacing at temperatures 150-108 °C. This increase in layer spacing was observed for two separate SAXS measurements of NT12, however, the DSC data does not show any measurable peaks around the temperature 108-106 °C on cooling. The SAXS profile corresponding to 106 °C shows multiple sharp peaks emerging, which is characteristic of a crystalline transition, however, this needs to be further investigated. In addition, at higher q-values, a diffuse scattering peak corresponding to ~5 Å is observed, as reported by Reddy et al.[219] This value corresponds to the mean distance between the aromatic part of the bent-core molecules.

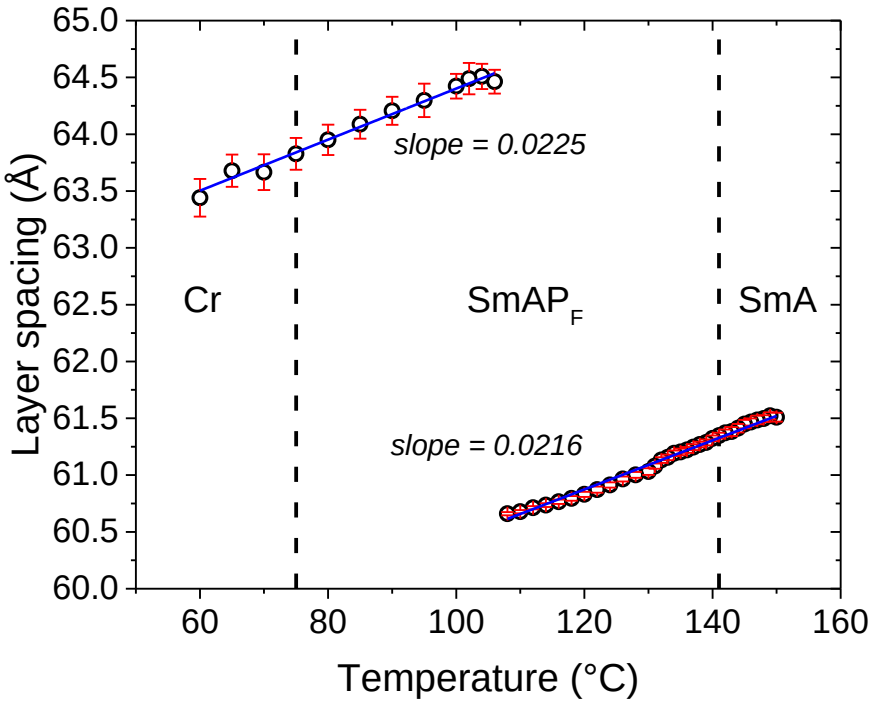

Figure 6.5: Temperature dependence of the layer spacing (in Å) for NT12 with labelled SmA, $SmAP_F$ and crystalline (Cr) phase ranges. Between 108 °C and 106 °C, there is an increase in the layer spacing. The error bars correspond to the errors obtained from the Gaussian fitting of the SAXS profiles. The slope of the linear fit in the range 150-108 °C is 0.0216, and in the range 106-60 °C, the slope is 0.0225.

Dielectric spectroscopy is an excellent technique to probe polar ordering in ferroelectric liquid crystals. The technique has been used to study the ferroelectric properties of calamitic mesogens exhibiting chiral SmA (SmA*) and chiral SmC (SmC*) phases.[238–241] The complex dielectric permittivity of ferroelectric materials (SmC*) is sensitive to temperature and frequency, and gives rise to two collective relaxation processes as a result of director fluctuations: the soft (amplitude) mode and the Goldstone (phason) mode. In the case of chiral smectic phases, the soft mode emerges in the SmA* phase, close to the SmA*-SmC* transition, and it is related to amplitude fluctuations in the tilt director. The Goldstone mode is related to collective distortions of the phase angle in the smectic tilt cone. In polar phases of bent-core liquid crystals, the Goldstone mode refers to the collective fluctuations in polarisation.

Figure 6.6 shows measurements of the real part of the dielectric permittivity (ε') and dielectric loss for NT12, over a range of temperatures on cooling from the isotropic phase. In Figure 6.6a, a plot of ε' as a function of temperature is given at 1 kHz, 10 kHz and 100 kHz on cooling from the isotropic state. The isotropic (I), SmA, $SmAP_F$ and crystal (Cr) phase temperature ranges are labelled. At the transition between the SmA and $SmAP_F$ phases, there is a significant increase in permittivity in the curve corresponding to 1 kHz, and the permittivity decreases at the transition between the $SmAP_F$ and Cr phases. Figure 6.6b shows a plot of dielectric loss as a function of frequency on cooling from the isotropic phase. A relaxation peak emerges on cooling between 150 °C and 140 °C. This relaxation is characteristic of a Goldstone mode with macroscopic polar order, and it arises in the paraelectric SmA phase due to the collective fluctuation of dipole moments.[236] The Goldstone mode can generally be suppressed by applying a DC bias field. The Goldstone mode was fitted to the Havriliak-Negami equation (2.8) to obtain its relaxation frequency (f_R) and dielectric strength ($\delta\varepsilon$). The plot of f_R (closed circle symbols) and $\delta\varepsilon$ (open circle symbols) as a function of temperature are given in Figure 6.6c, and the SmA and $SmAP_F$ phase regions have been labelled. The Goldstone mode emerges in the SmA phase around 150 °C, and the frequency at which the mode is observed generally decreases as the temperature decreases. In the SmA phase between 150 °C and 141 °C, the strength of the Goldstone mode increases from 0.3 to 1.3, respectively. As the sample transitions to the $SmAP_F$ phase, there is a significant increase in the strength of the mode, where at 130 °C, the strength is 7.1. Throughout the $SmAP_F$ phase between 130 °C and 90 °C, the strength of the mode remains fairly constant, being in the region between 7.1 and 7.8. As the sample approaches the crystalline transition (~75 °C), the strength of the mode significantly decreases from 7.5 at 90 °C to 0.5 at 80 °C.

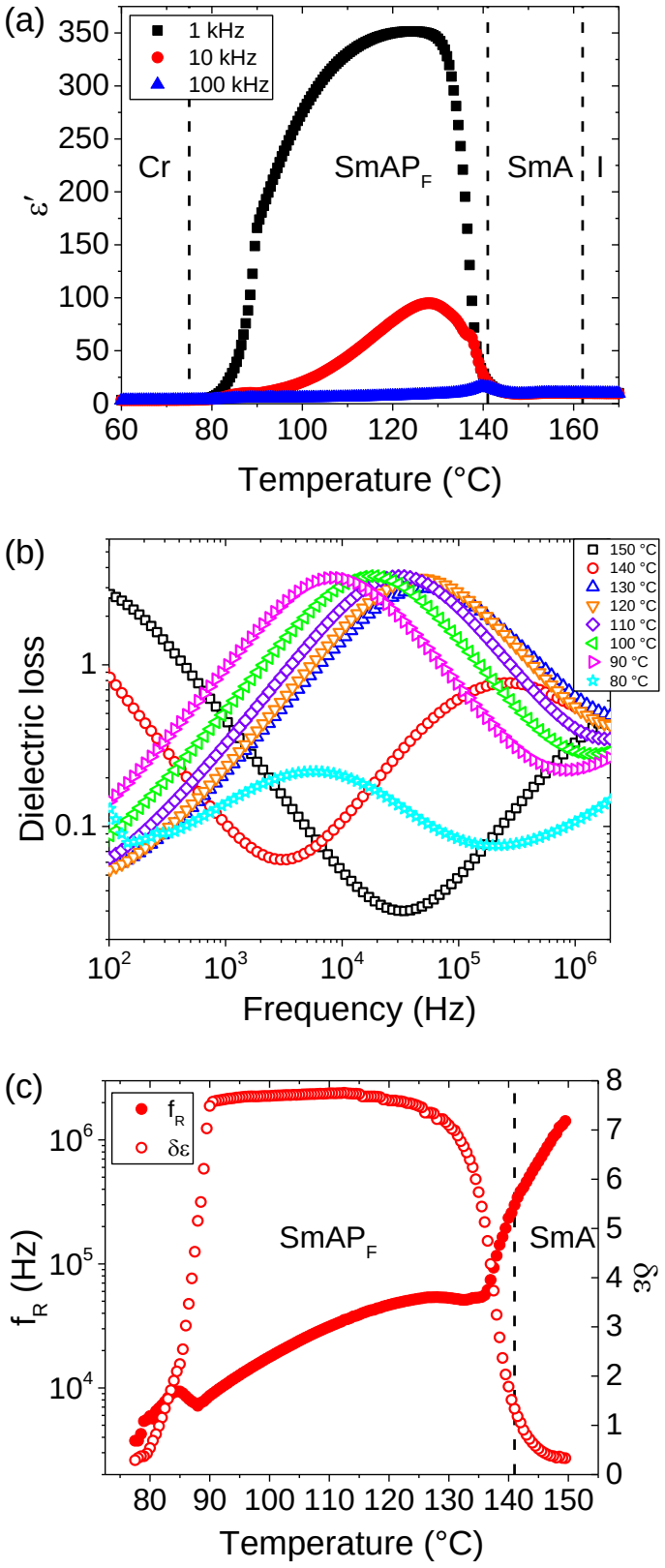

Figure 6.6: Dielectric spectroscopy data for NT12 measured at 0.1 V_{RMS} on cooling from the isotropic state. (a) Permittivity (ε') as a function of temperature at 1 kHz, 10 kHz and 100 kHz. (b) Dielectric loss as a function of frequency at temperatures 150-80 °C. (c) Relaxation frequency (f_R) and dielectric strength ($\delta\varepsilon$) of the Goldstone mode as a function of temperature.

As mentioned in section 2.3.5, a low frequency triangular waveform can be applied to polar liquid crystals to measure a flow of current due to the switching of the spontaneous polarisation. For ferroelectric liquid crystals such as NT12, a single current peak is seen in each half period of the triangle wave. The polarisation can be measured by integrating the area under the peak, and more information on how this is achieved is provided in section 2.3.5.

Figure 6.7a shows a plot of the current response of NT12 at 145 °C, 120 °C and 100 °C when 60 V_{RMS} was applied to the sample. It was previously determined, using a homeotropic cell, that the transition from the SmA to $SmAP_F$ occurs at 141 °C. In Figure 6.7a, however, a peak is observed at 145 °C (SmA phase). At 120 °C and 100 °C in the $SmAP_F$ phase, the intensity of the peak is greater compared to that of 145 °C. The single current peaks observed at each half period of the triangle wave were integrated to obtain values of spontaneous polarisation (in nC/cm^2). Figure 6.7b shows a plot of polarisation as a function of temperature for NT12 on cooling from the isotropic phase, and results corresponding to a range of applied voltages between 20 V_{RMS} and 100 V_{RMS} are given. The SmA and $SmAP_F$ phase regions are labelled (the temperature of the SmA-$SmAP_F$ transition was determined using a homeotropic cell). As is observed from the data in Figure 6.7b, current peaks emerge between 148 °C and 150 °C, whilst the sample is still in the SmA phase. Guo et al.,[236] however, do not observe a current peak in the SmA phase. It is possible that the applied electric field is inducing biaxiality in the SmA phase. However, the electro-optic behaviour of NT12 in a homeotropic cell needs to be further investigated by applying an in-plane electric field to the sample. If the electric field is inducing biaxiality in the SmA phase, then birefringence would be observed using polarising optical microscopy, as is the case in Figure 4.1b at 130 °C. The datasets for each applied voltage in Figure 6.7b show similar trends: (1) as the temperature decreases, the polarisation increases, and (2) the higher the electric field at eat set temperature, the greater the polarisation.

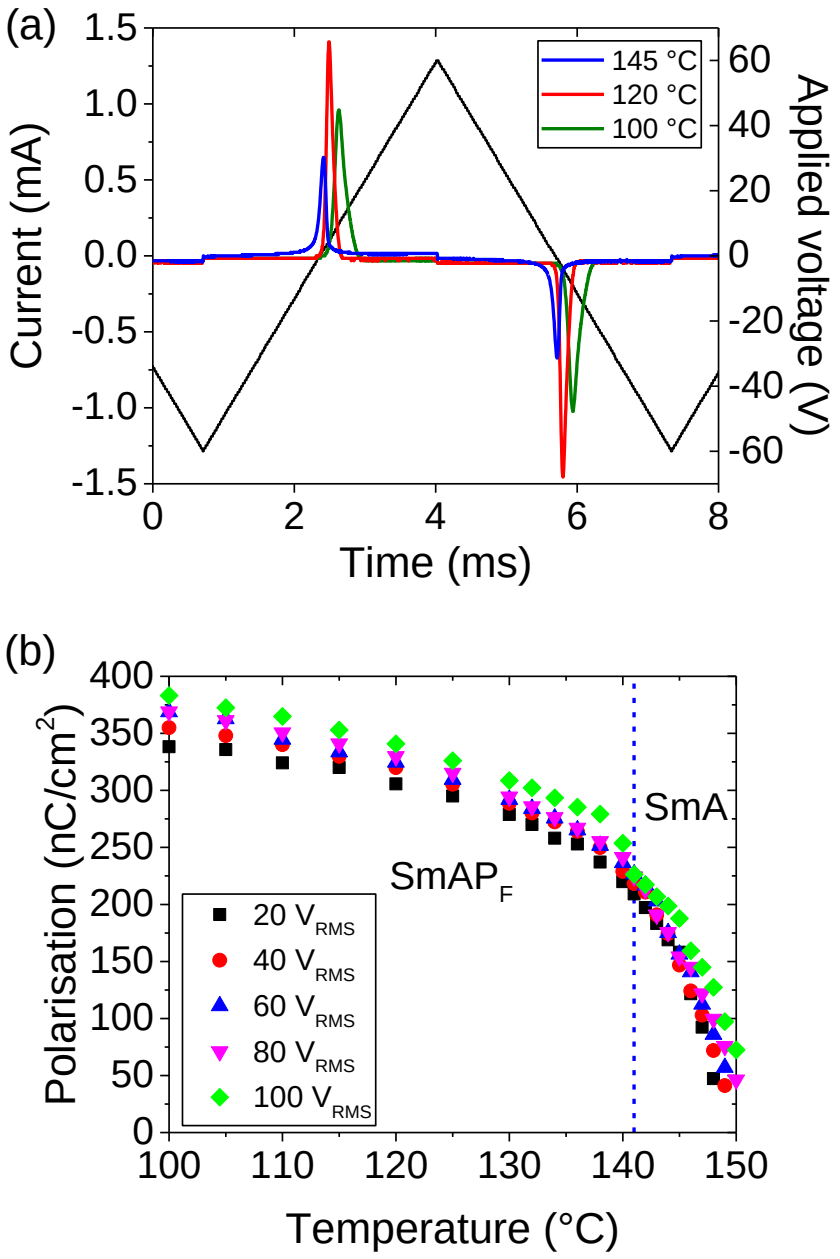

Figure 6.7: (a) The current response of NT12 measured at 145 °C, 120 °C and 100 °C (E = 6 V/μm; 60 V_{RMS}). (b) The temperature-dependent polarisation of NT12 with applied voltages in the range 20-100 V_{RMS}. The SmA and $SmAP_F$ phase regions are labelled. Measurements for both plots were taken in a 10 μm planar cell by applying a triangle wave of frequency 151 Hz.

6.2 Binary mixtures with a reactive mesogen

Binary mixtures of the $SmAP_F$ mesogen NT12 and reactive mesogen RM257 were prepared. Two concentrations of RM257 were considered, 10 wt% and 20 wt%, and the binary mixtures will be referred to as NT12-10 and NT12-20, respectively. These mixtures will be used in Chapter 7 to create templates of the $SmAP_F$ phase.

The phase transition temperatures of mixtures NT12-10 and NT12-20 were measured using DSC. The DSC curves for the second heating and cooling cycles, carried out at 10 °C/min, are given in Appendix I. Two peaks corresponding to the isotropic-SmA transition and the SmA-crystal transition are observed in the second cooling cycle of both mixtures, and these results are summarised in Table 6.1. As the concentration of monomer increases, the enthalpy of the isotropic to SmA phase transition decreases: for pure NT12 the enthalpy is 5.44 kJ/mol, and the addition of 20 wt% of RM257 (NT12-20) reduces the enthalpy of the transition by approx. half of its value, to 2.87 kJ/mol. As is seen in Table 6.1, the SmA to $SmAP_F$ transition of pure NT12 has an enthalpy of 0.24 kJ/mol, which indicates a second order or weakly first order transition, as discussed earlier in the chapter. Mixing NT12 with monomer RM257, however, reduces the energy associated with SmA-$SmAP_F$ phase transition. Therefore, mixtures NT12-10 and NT12-20 do not show any measurable enthalpies for the SmA-$SmAP_F$ transition, even though both mixtures exhibit ferroelectric switching (discussed later in the chapter).

Table 6.1: Phase transition temperatures and associated enthalpies (ΔH) for pure NT12 and mixtures NT12-10 and NT12-20. Values were determined from single measurement second cooling cycles at a rate of 10 °C/min.

Compound	Temperature (°C)	ΔH (kJ/mol)
NT12	155.2 (Iso-SmA)	5.44
	139.2 (SmA-$SmAP_F$)	0.24
	75.1 ($SmAP_F$-Cr)	22.35
NT12-10	146.6 (Iso-SmA)	4.71
	63.1 ($SmAP_F$-Cr)	18.84
NT12-20	140.5 (Iso-SmA)	2.87
	64.1 ($SmAP_F$-Cr)	16.67

The dielectric permittivity and the dielectric loss of the binary NT12+RM257 mixtures were measured on cooling from the isotropic phase. Figure 6.8a and Figure 6.8b show the plot of permittivity (ε') as a function of temperature for NT12-10 and NT12-20, respectively, at 1 kHz, 10 kHz and 100 kHz. The isotropic (I) phase has been labelled in both graphs. From the permittivity curves corresponding to 1 kHz, it is clear that there are ions in both mixtures. This is especially noticeable for the 20 wt% mixture in Figure 6.8b, where the permittivity in the isotropic region does not remain constant ($\varepsilon' \approx$ 22-31), and it is more than double in value compared to the isotropic permittivities of the 10 kHz and 100 kHz curves ($\varepsilon' \approx 8$). A decrease in permittivity is observed at ~80 °C for both mixtures (as is the case for pure NT12 in Figure 6.6a). This corresponds to the transition from the $SmAP_F$ to the crystalline phase, even though crystal transitions obtained from DSC experiments (Table 6.1) occur at lower temperatures (63-64 °C). The significant increase in permittivity in Figure 6.8a at ~120 °C corresponds to the SmA to $SmAP_F$ transition in mixture NT12-10, and in Figure 6.8b for mixture NT12-20, the increase in permittivity is observed at ~100 °C (the exact SmA-$SmAP_F$ transition temperature of mixtures NT12-10 and NT12-20 needs to be determined using homeotropic cells).

The plot of dielectric loss as a function of frequency at different temperatures for NT12-10 and NT12-20 are given in Figure 6.8c and Figure 6.8d, respectively. In both loss curves, the relaxation corresponding to the Goldstone mode is present and shifts to lower frequencies on cooling. For mixture NT12-10 in Figure 6.8c, the Goldstone mode emerges between 140 °C and 130 °C and the relaxation peak was fitted to the Havriliak-Negami equation (2.8). The frequency (f_R) and strength ($\delta\varepsilon$) of the Goldstone mode of mixture NT12-10 are given in Figure 6.8e. The Goldstone mode emerges at ~130 °C at a frequency of >1 MHz, and its frequency decreases on cooling, whilst its strength increases between ~130 °C and 110 °C, from 0.8 to 6.2. Throughout the $SmAP_F$ phase of NT12-10, there is a slight decrease in the strength of the mode, from 6.2 at 110 °C to 5.5 at 90 °C. There is a significant decrease in the strength of the mode from 5.3 at 88 °C to 0.2 at 80 °C, as the temperature approaches the crystalline transition. Similarly, for mixture NT12-20, the relaxation peak corresponding to the Goldstone mode in Figure 6.8c appears at ~110 °C and shifts towards lower frequencies on cooling. The frequency (f_R) and strength ($\delta\varepsilon$) of the peak are plotted as a function of temperature in Figure 6.8f. The strength of the mode continually increases from $\delta\varepsilon$ = 0.3 at 110 °C until it reaches a maximum strength of 2.1 at 84.5°C, before decreasing to 1.59 at 82.5 °C. The maximum strength of the Goldstone mode in

mixture NT12-20 ($\delta\varepsilon$ = 2.1 at 84.5 °C) is approx. three times smaller than that of mixture NT12-10 ($\delta\varepsilon$ = 6.3 at 109 °C).

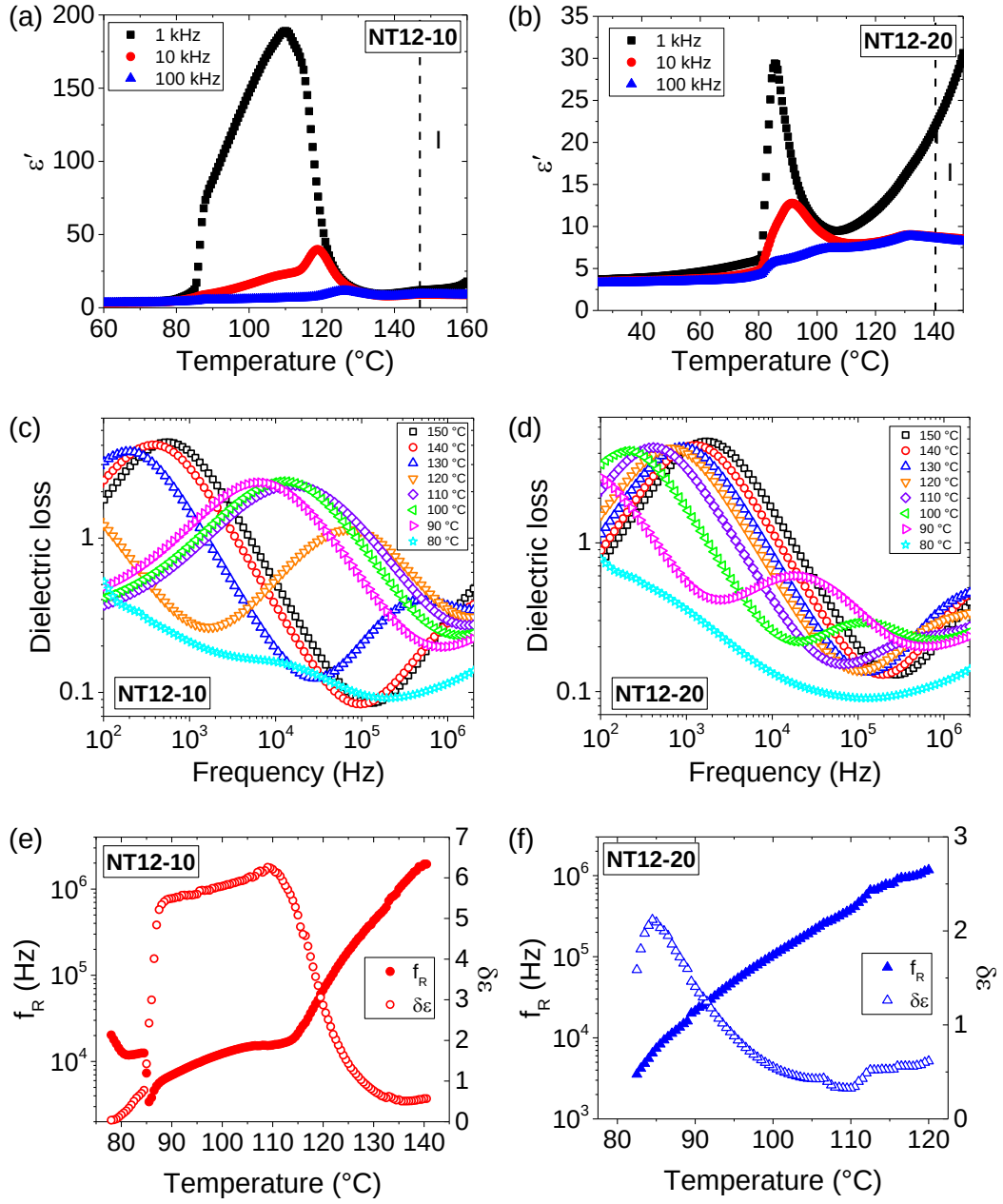

Figure 6.8: Dielectric spectroscopy data for mixtures NT12-10 and NT12-20 in 10 µm planar cells, measured at 0.1 V_{RMS} on cooling from the isotropic state. Permittivity (ε') as a function of temperature for: (a) NT12-10, and (b) NT12-20. The isotropic (I) phase has been labelled. Dielectric loss as a function of frequency for: (c) NT12-10, and (d) NT12-20. Relaxation frequency (f_R) and dielectric strength ($\delta\varepsilon$) of the Goldstone mode as a function of temperature for: (e) NT12-10, and (f) NT12-20.

A plot of polarisation as a function of temperature for mixtures NT12-10 (circle symbols) and NT12-20 (triangle symbols) is given in Figure 6.9. The mixtures were

cooled from the isotropic state and the electric fields applied to the samples are 4 V/µm for NT12-10, and 10 V/µm for NT12-20. Peaks due to ferroelectric switching appear at 123 °C for mixture NT12-10 and at 100 °C for mixture NT12-20. These two temperatures roughly correspond to the temperatures at which the increase in permittivity occurs for mixtures NT12-10 in Figure 6.8a (at ~120 °C) and NT12-20 in Figure 6.8b (at ~100 °C). The temperatures at which the Goldstone mode emerges for each mixture – i.e. at ~130 °C for NT12-10 (Figure 6.8c,e) and at ~110 °C for NT12-20 (Figure 6.8d,f) – are approx. 10 °C higher than the temperatures at which the polarisation becomes measurable in Figure 6.9. It is clear from Figure 6.9 that a lower concentration of RM257 in the binary mixtures results in the polarisation being measurable over a wider temperature window, i.e. the polarisation of NT12-10 is measurable between 123 °C and 90 °C, whereas the polarisation of NT12-20 is measurable between 100 °C and 81 °C. Mixture NT12-10 in Figure 6.9 shows a steady increase in spontaneous polarisation on cooling, from P_s = 73.5 nC/cm² at 123 °C to P_s = 252 nC/cm² at 90 °C. Mixture NT12-20 also shows a steady increase in polarisation on cooling, from P_s = 26 nC/cm² at 100 °C until a maximum of 118 nC/cm² is reached at 84 °C. On further cooling, the polarisation of NT12-20 begins to decrease as the temperature approaches the crystalline transition.

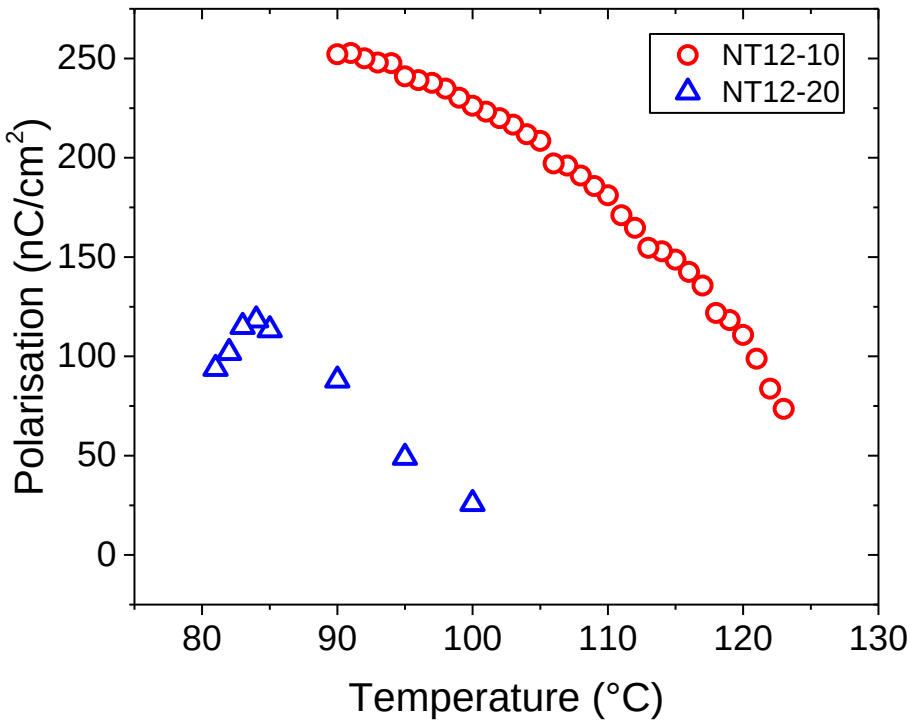

Figure 6.9: Polarisation as a function of temperature for mixtures NT12-10 (circle symbols, E = 4 V/µm) and NT12-20 (E = 10 V/µm, triangle symbols). A triangle wave of 151 Hz was applied for both mixtures.

6.3 Summary of results

Section 6.1 discussed the characterisation of mesogen NT12 exhibiting the SmA and $SmAP_F$ phases (synthesised in Chapter 5). The SmA and $SmAP_F$ phases were distinguished using a homeotropic cell, where the uniaxial SmA phase was optically dark when viewed using POM, and the biaxial $SmAP_F$ phase exhibited birefringence. In planar cells, the size of focal conic domains could be fine-tuned with the application of an external electric field. The DSC curve of NT12 shows a first order isotropic to SmA transition and a second order or weakly first order SmA to $SmAP_F$ transition. SAXS experiments confirmed the presence of a layered structure in both the SmA and $SmAP_F$ phases of NT12, with layer spacing in the range 60.5-61.5 Å. A diffuse scattering peak with a q value equivalent to ~5 Å was also observed in the SAXS profiles, and this corresponds to the mean distance between the aromatic parts of the bent-core molecules within the layers. The dielectric loss data for NT12 showed a relaxation peak emerge in the SmA phase at a frequency of >1 MHz, which corresponds to a Goldstone mode. The peak was fitted to the Havriliak-Negami equation (2.8) to obtain the frequency and strength of the relaxation. The Goldstone mode shifted to lower frequencies as the temperature decreased. As the sample transitioned from the SmA to the $SmAP_F$ phase, the strength of the mode significantly increased and remained relatively constant throughout the $SmAP_F$ phase. Current response measurements showed a peak due to ferroelectric switching in the SmA phase of NT12, close to the SmA to $SmAP_F$ transition, which was potentially due to the electric field inducing biaxiality in the SmA phase. The peak due to ferroelectric switching was integrated to obtain the polarisation across a range of temperatures, and it was found that the polarisation increases as the sample is cooled.

In section 6.2, binary mixtures of NT12 with RM257 were prepared using a 10 wt% and 20 wt% concentration of monomer, named NT12-10 and NT12-20, respectively. The addition of the monomer significantly reduced the energy associated with the SmA to $SmAP_F$ transition, and so there were no measurable enthalpies in the DSC curves for the two mixtures. A relaxation peak corresponding to the Goldstone mode was observed for both mixtures. The frequency of the mode decreased on cooling for both mixtures, and its strength is greater for mixture NT12-10 compared to NT12-20. The polarisation of the 10 wt% mixture was measurable over a wider temperature window (33 °C range) compared to the 20 wt% mixture (19 °C range). The spontaneous polarisation of each mixture generally increased on cooling. The maximum polarisation achieved for NT12-10 (P_s = 252 nC/cm^2) was over twice the value of the maximum polarisation of NT12-20 (P_s = 118 nC/cm^2).

CHAPTER 7:
Templating the $SmAP_F$ phase

For this chapter, the mixtures NT12-10 and NT12-20 from Chapter 6 will be used to create templates of the ferroelectric SmA ($SmAP_F$) phase. The $SmAP_F$ template formed from NT12-10 will be refilled with the nematic liquid crystal 5CB to investigate the influence of the templated structures on the physical properties of the refilled liquid crystal.

7.1 Photopolymerised $SmAP_F$ phases

Following on from results obtained in the previous chapter, photoinitiator BME (1 wt%) was added to the two binary mixtures of NT12 with RM257, NT12-10 and NT12-20, composed of 10 wt% and 20 wt% of RM257, respectively. Planar cells of 10 μm spacing were filled with the two polymerisable mixtures in the isotropic phase. An electric field of 7 V/μm (70 V_{RMS} triangle wave, 151 Hz) was applied to the samples on cooling from the isotropic phase, in order to obtain larger focal conic domains (see Figure 6.3). The samples NT12-10 and NT12-20 were cooled to the $SmAP_F$ phase (95 °C for both mixtures) and exposed to UV light for 2 hours, whilst subjected to the electric field. The current peak due to ferroelectric switching was monitored throughout the entire duration of UV exposure, to check if any significant changes occurred in the current response. The current response data for both NT12-10 and NT12-20 is given in Figure 7.1a and Figure 7.1b, respectively. Before UV exposure (the blue curves), the polarisation at 95 °C for NT12-10 and NT12-20 is ~233 nC/cm^2 and ~117 nC/cm^2, respectively. When the UV source is turned on, the polarisation of each mixture changes (to the red curves), and it is now ~308 nC/cm^2 for NT12-10 and ~278 nC/cm^2 for NT12-20. The polarisation has increased by ~75 nC/cm^2 for NT12-10 and by ~161 nC/cm^2 for NT12-20, compared to before UV exposure. The samples were kept under UV light for 2 hours (as was the case for polymerised N_{TB} mixtures in Chapter 4), and the polarisation did not change any further. When the UV source is turned off, the current peak is still present and there is little change in the appearance of focal conics before (Figure 7.1c) and after (Figure 7.1d) UV exposure. A polymer network is formed from RM257 when the polymerisable mixtures NT12-10 and NT12-20 are exposed to UV light, and so the polarisation of the polymerised samples will mainly be determined only from NT12 (note that the polarisation of pure NT12 at 100 °C in Figure 6.7b is ~370 nC/cm^2 at 6-8 V/μm),

whereas before polymerisation, the mixture of both NT12 and RM257 determined the polarisation. There is a lower concentration of NT12 in polymerised NT12-20 (the polymer network is denser), and so the polarisation of polymerised NT12-20 is smaller than that of polymerised NT12-10.

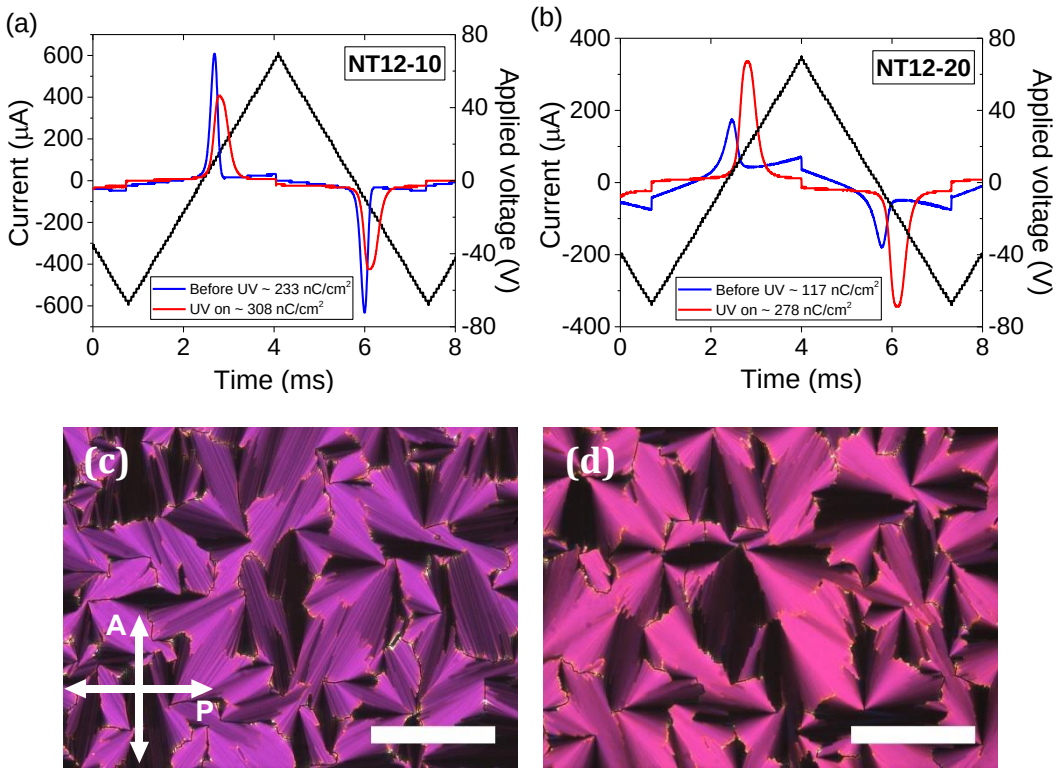

Figure 7.1: The current response measured at 70 V_{RMS} in 10 μm planar cells (E = 7 V/μm) before and after UV exposure for: (a) NT12-10, and (b) NT12-20. POM images of NT12-10 at E = 7 V/μm: (c) before UV exposure, and (d) after UV exposure. The length of the scale bar is 100 μm.

It was determined using POM that the isotropic transition of pure NT12 occurs at 162 °C. Before polymerisation, the isotropic transition is at 149 °C for NT12-10, and at 139 °C for NT12-20. After polymerisation, the isotropic transition is now at 161 °C for polymerised NT12-10, and at 160 °C for polymerised NT12-20, and above these temperatures, residual birefringence is observed in the polymer networks. The spontaneous polarisation was measured on cooling from the isotropic state and Figure 7.2 shows plots of polarisation as a function of reduced temperature for pure NT12 and mixtures NT12-10 and NT12-20, before and after polymerisation. The electric field applied to all these samples was 10 V/μm, apart from for mixture NT12-20 before polymerisation, where 4 V/μm was applied. The polarisation of pure NT12 is shown in black squares. The polarisation of the mixtures before (BP) and after

polymerisation (AP) is represented with open and closed symbols, respectively. After polymerisation, the polarisation of both mixtures increases significantly, compared to the samples before polymerisation. This is because, as mentioned in the previous paragraph, the RM257 forms a polymer network and the polarisation will mainly be determined only from NT12 in the liquid crystal/polymer matrix. After polymerisation, it is expected that the polarisation of NT12-20 (closed triangle symbols) is lower than that of NT12-10 (closed circle symbols), because there is a lower concentration of NT12 (80 wt%) in the liquid crystal/polymer matrix. Before polymerisation, the polarisation of NT12-10 is measurable from 26 °C below the isotropic-SmA transition ($T\text{-}T_{I\text{-}SmA}$ = -26 °C) over a range of 33 °C. Similarly, for the NT12-20 sample before polymerisation, the polarisation is measurable from 39 °C below the I-SmA transition and over a range of 19 °C. After polymerisation, the temperature window across which the polarisation is measurable is larger compared to before polymerisation, and of similar range to that of pure NT12. The shape of the curves after polymerisation are similar to the shape of the pure NT12 curve. Before polymerisation, the maximum polarisation achieved is 252 nC/cm^2 ($T\text{-}T_{I\text{-}SmA}$ = -59 °C) for NT12-10 and 118 nC/cm^2 ($T\text{-}T_{I\text{-}SmA}$ = -55 °C) for NT12-20. After polymerisation, the maximum polarisation achieved is 309 nC/cm^2 ($T\text{-}T_{I\text{-}SmA}$ = -66 °C) for NT12-10 and 273 nC/cm^2 ($T\text{-}T_{I\text{-}SmA}$ = -70 °C) for NT12-20.

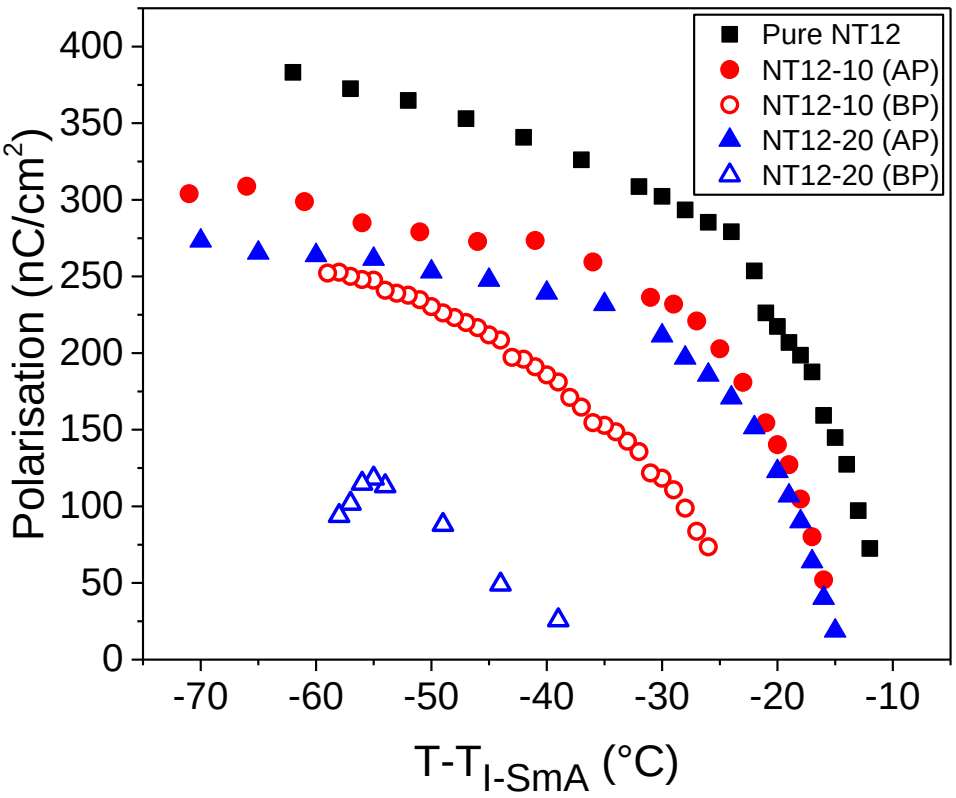

Figure 7.2: Polarisation as a function of reduced temperature for NT12-10 and NT12-20 before polymerisation (BP) and after polymerisation (AP) shown with open and closed symbols, respectively. Data for pure NT12 is also provided as a comparison. E = 10 V/µm for pure NT12, NT12-10 (BP), NT12-10 (AP) and NT12-20 (AP). E = 4 V/µm for NT12-20 (BP). A triangle wave of frequency 151 Hz was applied for all measurements.

Dielectric spectroscopy measurements of polymerised NT12-10 were taken to draw a comparison with pure NT12 and NT12-10 before polymerisation. Figure 7.3a shows the plot of dielectric permittivity (ε') as a function of temperature at 100 kHz for NT12-10 after polymerisation (AP, red closed circles), NT12-10 before polymerisation (BP, blue open triangles) and pure NT12 (black closed squares). Compared to before polymerisation, polymerised NT12-10 exhibits a wider temperature range over which the liquid crystal phase is present, which can be seen in the changes in permittivity at the isotropic-SmA transition (T-$T_{I\text{-}SmA}$ = 0) and ~80 °C below the transition. The changes in permittivity are similar to that of pure NT12. The drop in permittivity at approx. -80 °C for polymerised NT12-10 corresponds to the transition to the crystalline phase. The permittivity values in the region between -30 °C and -60 °C are similar before and after polymerisation. The permittivities of polymerised NT12-10 are lower than those of pure NT12 (e.g.

at -40 °C, ε' = 7.53 for pure NT12, whereas for polymerised NT12-10, ε' = 6.20), and this is most likely due to the presence of the polymer network in polymerised NT12-10. Such comparisons were also made for permittivities of the polymerised N_{TB} phase in section 4.1.4.

The plot of dielectric loss as a function of frequency for polymerised NT12-10 is given in Figure 7.3b. The curve corresponding to 150 °C (black open squares) shows a peak at ~1 kHz and this is due to ions. The relaxation peak corresponding to the Goldstone mode can be observed at the higher-frequency-end of the plot, and the peak becomes broader as the temperature decreases (it is not as prominent as the Goldstone mode for NT12-10 before polymerisation, in Figure 6.8c). The relaxation peak was fitted to the Havriliak-Negami equation (2.8), and its relaxation frequency (f_R) and strength ($\delta\varepsilon$) are plotted as a function of temperature in Figure 7.3c. The mode emerges at ~150 °C where $\delta\varepsilon$ = 0.4 and its strength reaches a maximum at 136 °C, where $\delta\varepsilon$ = 5.1. As the temperature decreases, the peak shifts to lower frequencies. Further cooling below 136 °C results in approx. a 4-fold decrease in the strength of the peak, where at 120 °C, $\delta\varepsilon$ = 1.2. Between 120 °C and 90 °C, the strength of the Goldstone mode is in the range 1.0-1.2. The Goldstone mode in the polymerised NT12-10 sample is present over a wider temperature range, compared to before polymerisation. After polymerisation, the mode emerges at ~150 °C (similar to pure NT12), whereas before polymerisation it emerges at ~130 °C (see Figure 6.8e). The strength of the Goldstone mode, however, is lower than that of pure NT12 and NT12-10 before polymerisation.

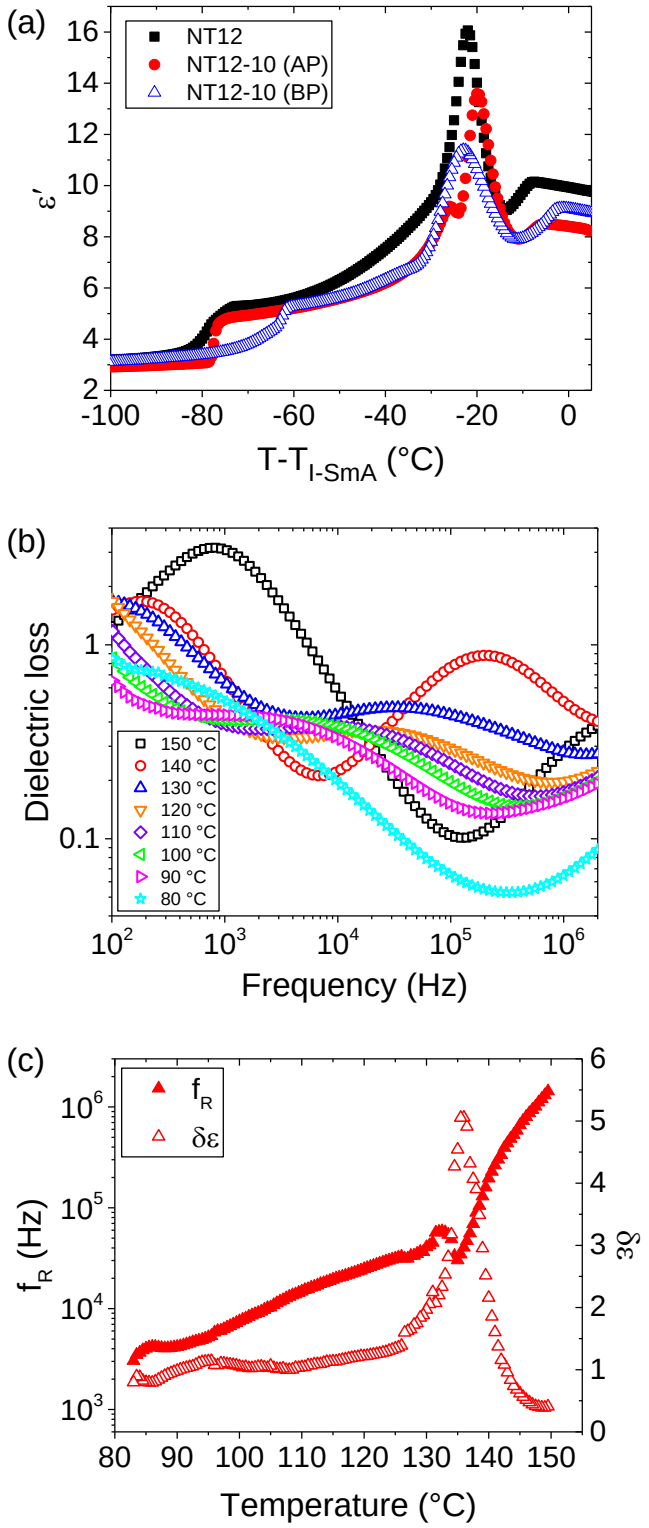

Figure 7.3: Dielectric spectroscopy data for NT12-10 after polymerisation (AP), measured at 0.1 V_{RMS} in a 10 µm planar cell. (a) Dielectric permittivity (ε') at 100 kHz as a function of reduced temperature. Data for pure NT12 and NT12-10 before polymerisation (BP) is also included as a comparison. (b) Dielectric loss as a function of frequency between 150 °C and 80 °C. (c) Relaxation frequency (f_R) and dielectric loss (δε) of the Goldstone mode as a function of temperature.

7.2 Templates of the $SmAP_F$ phase

To create the templates, the host liquid crystal was washed from the polymerised samples by placing the cell in acetone. As was the case in Chapter 4 for twist-bend nematic materials composed of CB7CB and 5CB, the mesogen NT12 also possesses a nitrile group. The polymer template made from RM257 does not possess a nitrile group (see Figure 2.1 for the chemical structures of NT12 and RM257). Of course, unlike RM257, NT12 also possesses a carbosilane tail, however, the -CN group will be traced instead for simplicity. Figure 7.4 shows the Raman spectra of the polymerised and washed NT12-20 samples (mixture of NT12 with 20 wt% RM257). The spectrum of the polymerised sample (black line) shows a peak at 2232 cm^{-1}, and this corresponds to the Raman shift of the nitrile (-CN) group of NT12. After washing (red line), this peak is no longer present, and so this confirms that the liquid crystal has been completely washed out.

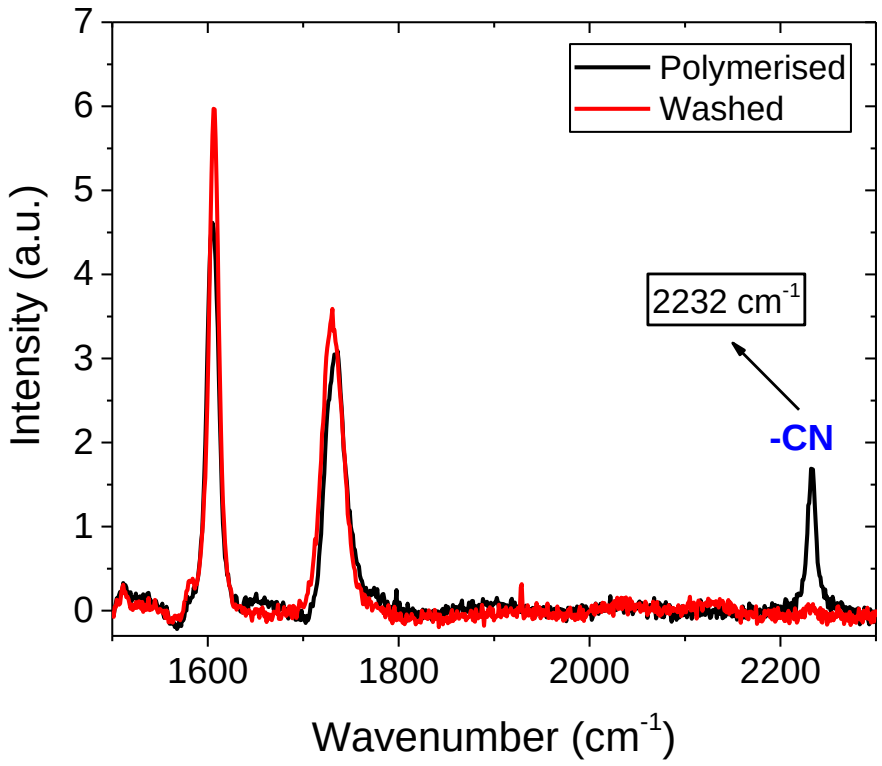

Figure 7.4: Raman spectra of the polymerised (black line) and washed (red line) NT12-20 sample (NT12 mixed with 20 wt% RM257). The nitrile (-CN) peak at 2232 cm^{-1} in the polymerised sample is absent after washing.

7.3 Morphologies of templates

Templated structures were imaged by scanning electron microscopy (SEM) to visualise the orientation of the polymer strands. The NT12-10 mixture (NT12 with 10 wt% RM257) was templated in both its SmA and $SmAP_F$ phases, and the two were compared.

The SmA template was formed by cooling NT12-10 from the isotropic state at 5 °C/min. The sample was contained in a 5 μm planar cell and a 40 V_{RMS} triangle wave (151 Hz) was applied to the sample on cooling for two reasons. The first was to obtain a neater alignment of the focal conic textures. The second was to check that the sample was in the SmA phase before exposing it to UV light, by monitoring the current response. At 130 °C, a current peak was not observed, therefore, the material was in its SmA phase. The electric field was removed, then the sample was exposed to UV light for 2 hours, followed by washing the liquid crystal out using acetone. The washed cell was then thoroughly dried on a hotplate at 30 °C and cracked open. Figure 7.5a-c shows SEM images of the SmA phase of NT12-10 at different magnifications, and the corresponding POM image of the SmA template (after washing) is given in Figure 7.5d. The width of individual polymer strands (labelled with a rectangle in Figure 7.5b) is in the range 50-100 nm, as was observed for templates of N_{TB} and SmA phases in section 4.2.6. The overall structure of the template shows focal conics, such as those observed in the corresponding POM image in Figure 7.5d, and the polymer strands follow a preferred alignment within each of the focal conic domains (Figure 7.5a). Additionally, 'wispy' areas of the sample were observed in Figure 7.5a (labelled with a green dashed oval) and Figure 7.5c. This was unusual because similar textures were observed for polymerised N_{TB} samples in Figure 4.14 (where the liquid crystal was still present in the sample). Raman spectroscopy, however, confirmed that the liquid crystal was removed during the washing procedure.

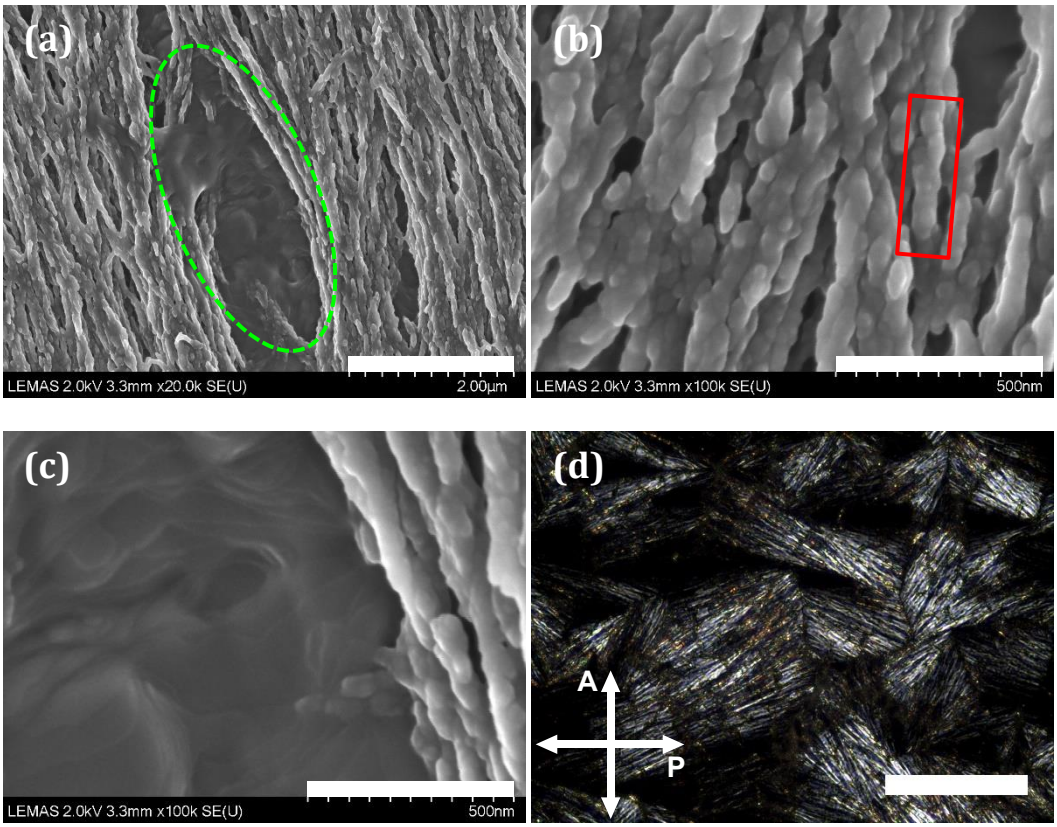

Figure 7.5: (a-c) SEM images of the SmA template formed from NT12-10. The scale bar for SEM images is labelled in each image. (d) The corresponding POM image of the washed SmA sample. The length of the scale bar in the POM image is 100 µm.

To further investigate these 'wispy' textures, a section of the sample was scanned using energy-dispersive X-ray spectroscopy (EDX), which provides information on the elements present in a particular area of a sample. Figure 7.6 shows an SEM image of the SmA template, where the darker sections represent the 'wispy' areas. EDX was used to analyse the central area of the SEM image that is labelled with a rectangle, and the corresponding EDX spectrum is provided. Carbon (C) and oxygen (O) are identified as the only elements in this labelled area (the polymer network is formed from these elements), and it can be confirmed that the wispy areas are not a result of leftover host liquid crystal in the template.

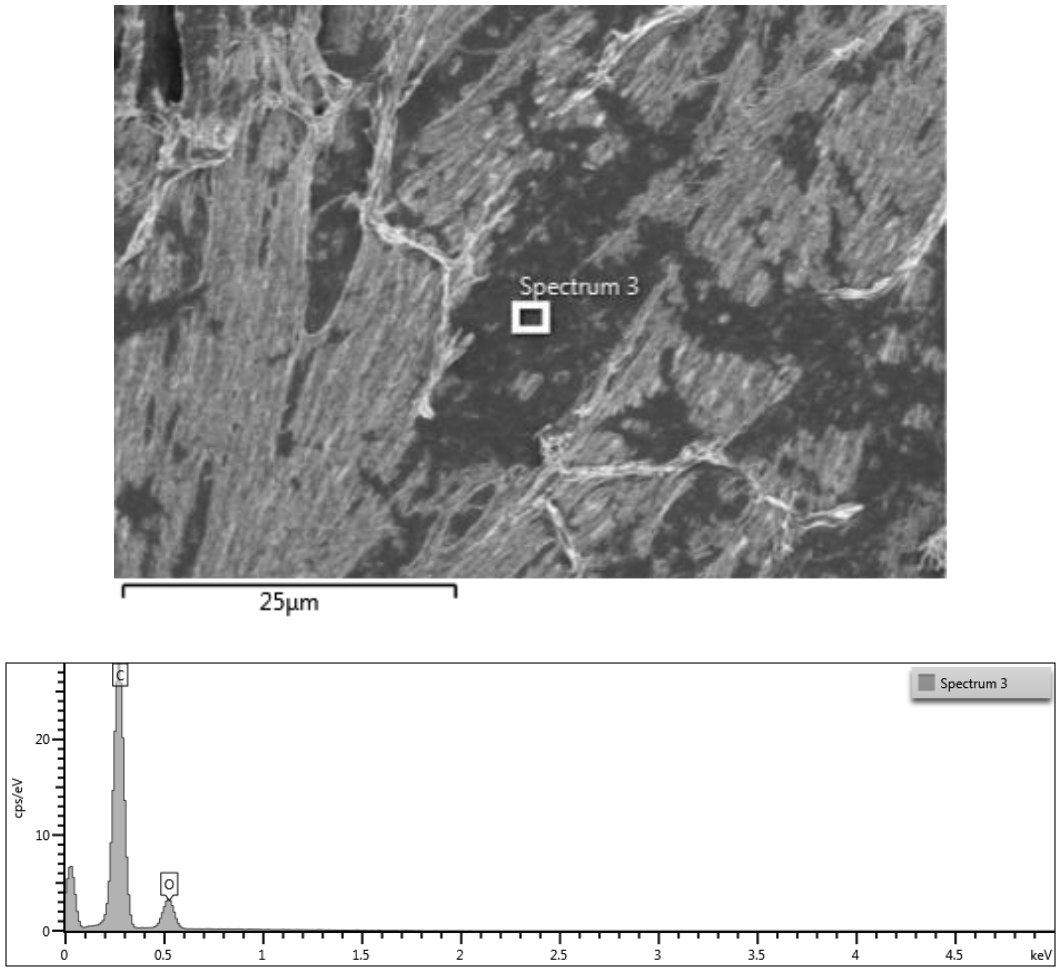

Figure 7.6: Top: SEM image of the SmA template formed from NT12-10, with the wispy region labelled with a rectangle in the centre of the image. Bottom: EDX analysis of the labelled area in the SEM image. The spectrum shows that carbon (C) and oxygen (O) are the only elements present in this area.

Next, the template of the $SmAP_F$ phase was visualised. The template was formed by cooling NT12-10 from the isotropic state at 5 °C/min in a 5 µm planar cell. As was the case for the SmA template, a triangle wave (151 Hz) of 40 V_{RMS} was applied on cooling for two reasons: to obtain neater focal conics and to ensure that the sample was in the $SmAP_F$ phase. At 95 °C, the current peak corresponding to ferroelectric switching was present, and so the sample was exposed to UV light for 2 hours. The sample was subjected to the electric field throughout the entire duration of UV exposure, then the host liquid crystal was washed out using acetone. SEM images of the $SmAP_F$ template are given in Figure 7.7a-c, and the corresponding POM image of the washed template is shown in Figure 7.7d. Figure 7.7a shows a focal conic of the $SmAP_F$ phase, where the polymer strands (labelled with green arrows) branch out at an angle of ~30° (β) from either side of a central strand (labelled with a red dashed line). The $SmAP_F$

template in Figure 7.7b and Figure 7.7c appears smoother compared to the SmA template in Figure 7.5a, which makes it more difficult to distinguish individual polymer strands; however, the width of the strand labelled with a rectangle in Figure 7.7c is in the range 50-100 nm.

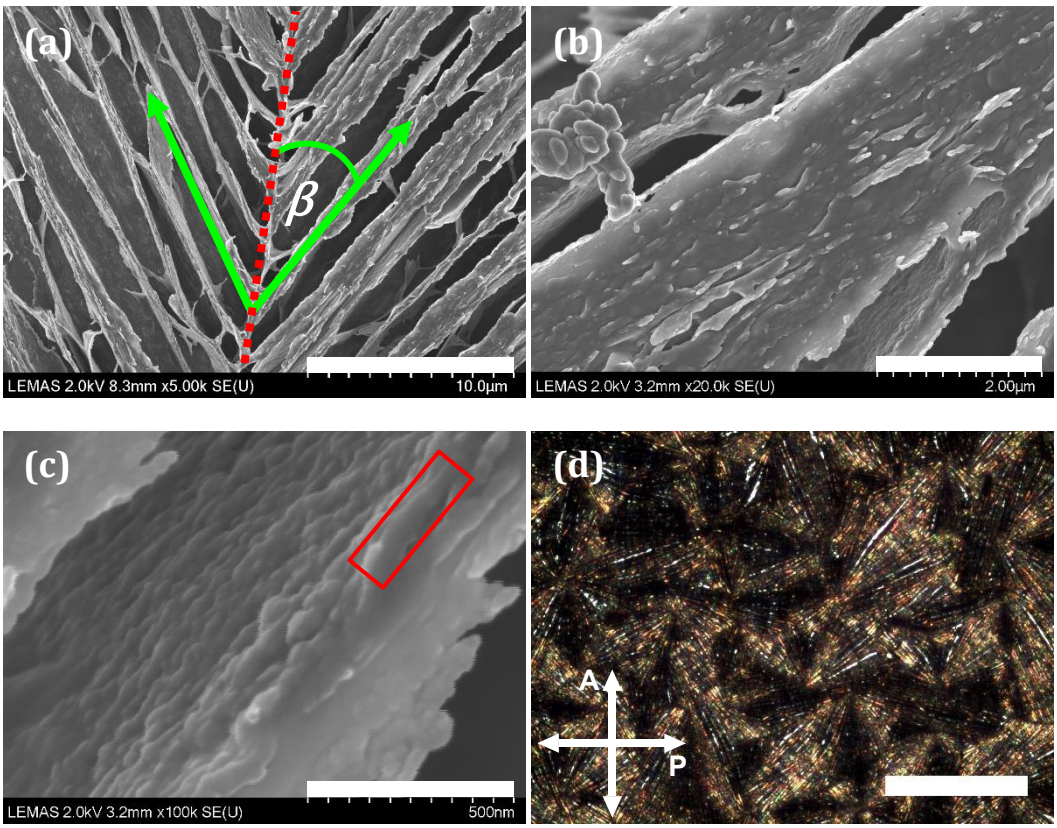

Figure 7.7: (a-c) SEM images of the $SmAP_F$ template formed from NT12-10. The scale bar for SEM images is labelled in each image. (d) The corresponding POM image of the washed $SmAP_F$ sample. The length of the scale bar in the POM image is 100 µm.

The $SmAP_F$ template did not show any wispy textures such as the ones observed in the SmA phase in Figure 7.5. However, EDX analysis was also performed on the $SmAP_F$ template, on the area of the sample labelled in the SEM image in Figure 7.8 (top). The four colour maps correspond to the labelled rectangular area in the SEM image and represent the distribution of particular elements in the scanned area. Carbon (C) and oxygen (O) have, of course, been detected, as the polymer network is composed of these elements. However, silicon (Si) has also been detected, and this is due to its presence in the glass substrates of the cell. Likewise, indium (In) has been detected due to the ITO (indium tin oxide) electrode of the cell. Traces of nitrogen (from the liquid crystal's nitrile groups) were not detected, which suggests that the host liquid crystal was removed during the washing procedure.

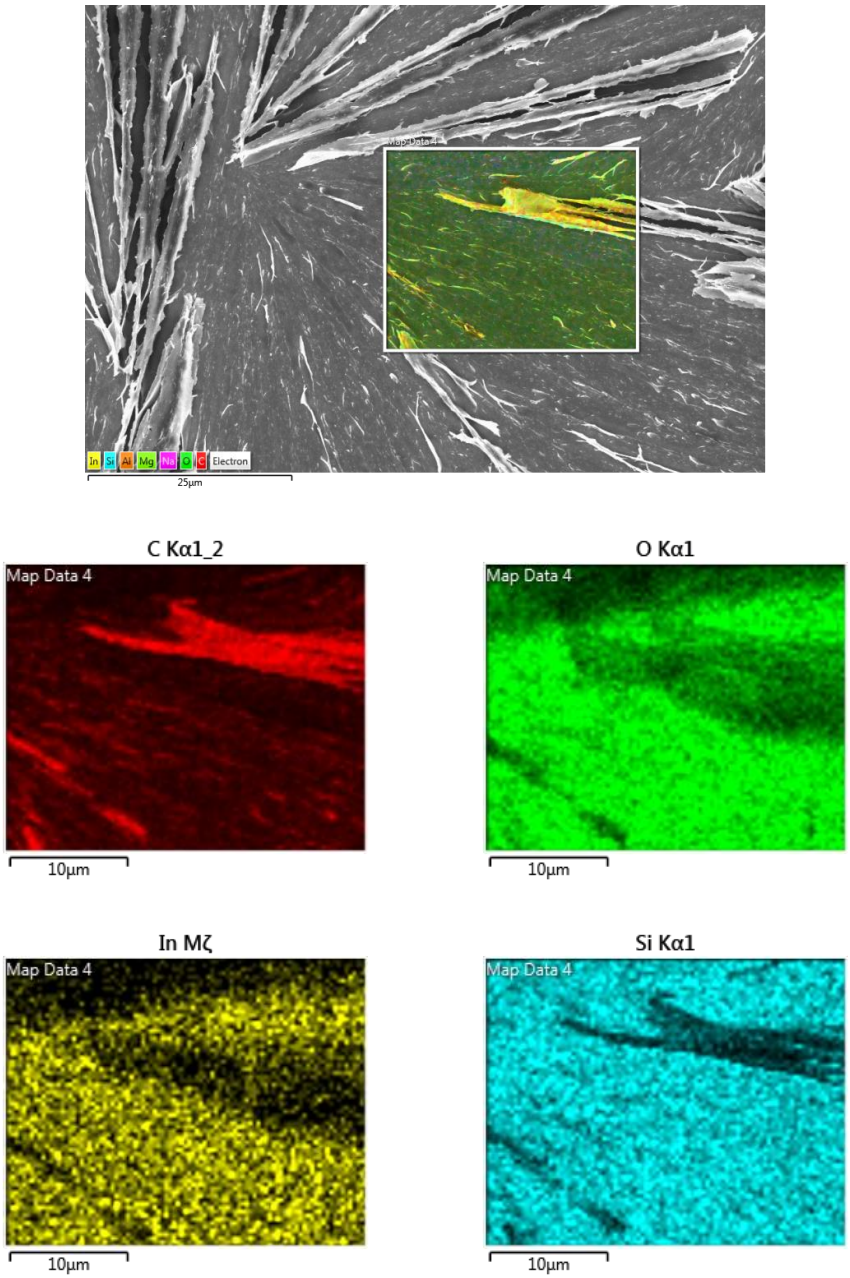

Figure 7.8: Top: SEM image of the $SmAP_F$ template formed from NT12-10. The area marked with a rectangle was analysed using EDX. Bottom: The four coloured EDX images show where the elements carbon (C), oxygen (O), indium (In) and silicon (Si) are present in the labelled SEM area.

7.4 Refilled $SmAP_F$ templates

The $SmAP_F$ template was refilled with the nematic liquid crystal 5CB to understand how the templated structure of the $SmAP_F$ phase affects the refilled nematic phase. The template of NT12-10 was refilled with 5CB at room temperature. Heating the refilled sample shows a decrease in birefringence between 35 °C and 36 °C, corresponding to the nematic-isotropic transition of pure 5CB (this was also the case for the refilled N_{TB} template in Chapter 4). Figure 7.9a-d shows POM images of the refilled template of NT12-10 at different temperatures, where 25 °C (Figure 7.9a) and 34 °C (Figure 7.9b) correspond to the nematic phase of the refilled liquid crystal. At 70 °C (Figure 7.9c), the liquid crystal is in the isotropic phase, but residual birefringence is observed, which suggests that the polymer is inducing order to the isotropic phase. After subjecting the refilled sample to an electric field, the textures in Figure 7.9d appear smoother compared to Figure 7.9a and Figure 7.9b, before an electric field was applied. The birefringence (Δn) of the refilled sample was measured over a range of temperatures using a Berek compensator, and the results are given in Figure 7.9e, where data for pure 5CB is also included as a comparison. The nematic and isotropic phase regions have been labelled. For the refilled template, it is possible to determine the birefringence in the isotropic phase, where $\Delta n = 0.02 \pm 0.01$. In the nematic phase, Δn of the refilled template increases to 0.11 ± 0.01 at 34.5 °C. On further cooling, Δn of both the refilled template and pure 5CB continue to increase, with Δn of pure 5CB being approx. 10% greater than Δn of the refilled template. The difference in birefringence between the refilled template and 5CB suggests that the template is inducing order in the refilled liquid crystal at the polymer/liquid crystal interface.

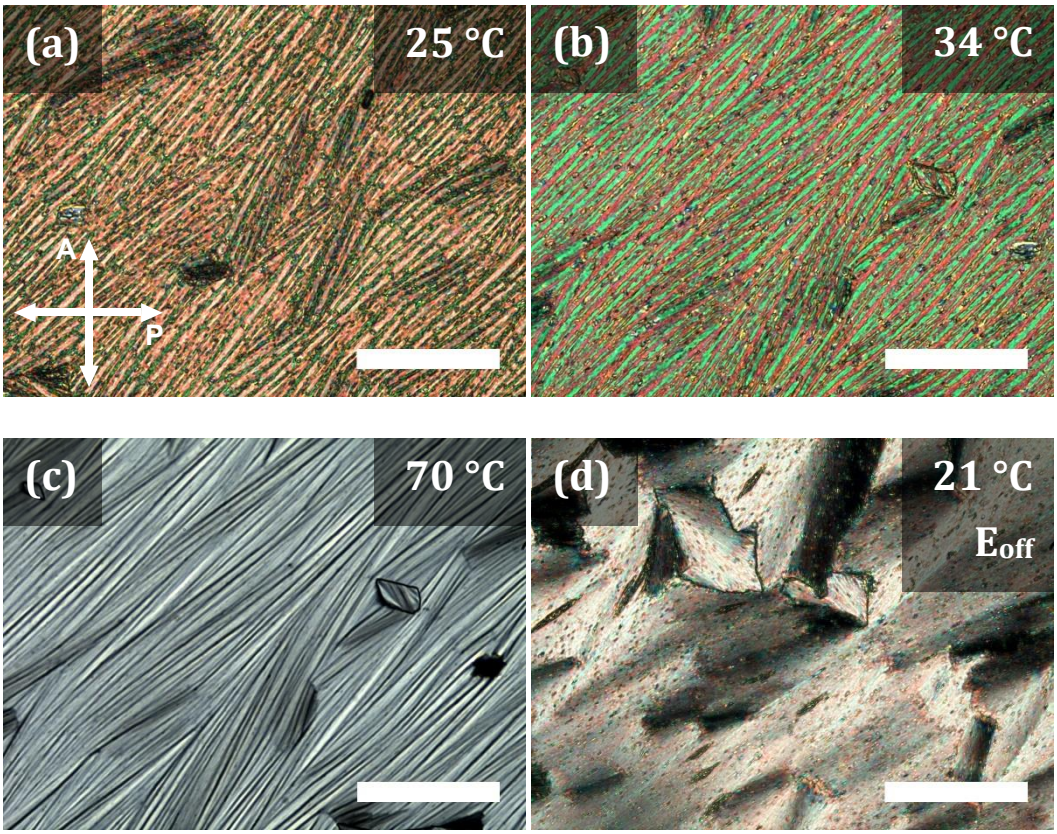

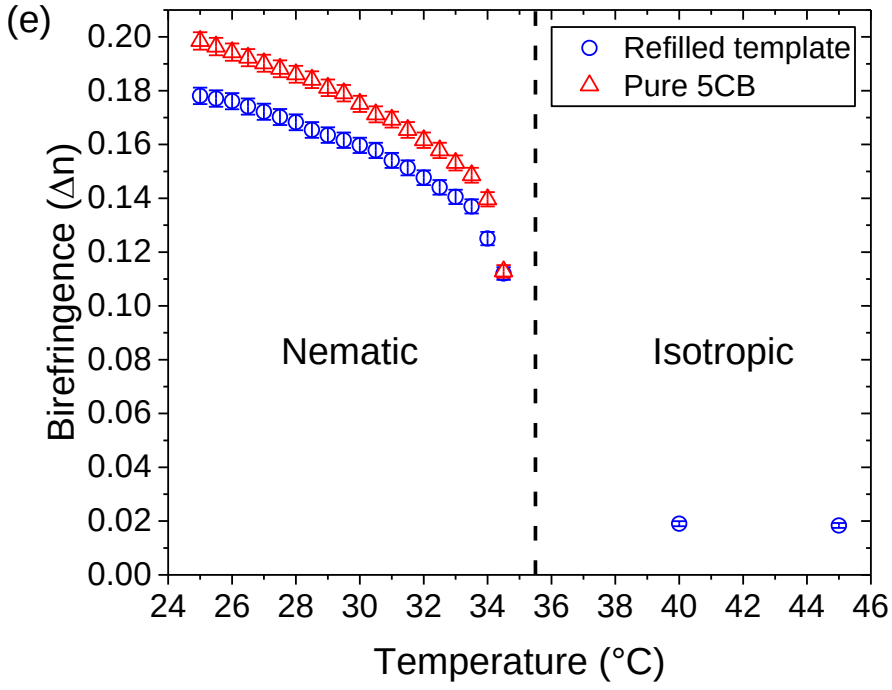

Figure 7.9: POM images of the refilled $SmAP_F$ template (NT12-10) at: (a) 25 °C, (b) 34 °C, (c) 70 °C, where residual birefringence is observed, and (d) 21 °C, after subjecting the sample to an electric field. The length of the scale bar is 100 µm. (e) Birefringence as a function of temperature for the refilled $SmAP_F$ template and 5CB.

Dielectric spectroscopy measurements were carried out on the refilled $SmAP_F$ template formed from NT12-10. A plot of permittivity (ε') at 10 kHz as a function of temperature for the refilled template is provided in Figure 7.10a (red circles), and data for pure 5CB (black squares) is included as a comparison. The refilled template and pure 5CB show similar shapes of the curve; there is a change in permittivity at ~35 °C for the refilled template, corresponding to the isotropic transition. The main differences between the refilled template and pure 5CB are the values of permittivity in the isotropic phase region (above 35 °C) and the nematic phase region (below 35 °C), both labelled in Figure 7.10a. The permittivities in the isotropic region of pure 5CB are almost twice the value of the isotropic permittivities of the refilled template. In the liquid crystal region, below 35 °C, the permittivity of the refilled template is approx. 50% lower than that of pure 5CB. The difference in permittivity corresponding to 25 °C and 40 °C for the refilled template is ~1.7, whereas for pure 5CB it is ~3.9. This difference in permittivity is more than twice lower for the refilled template compared to pure 5CB. For the refilled N_{TB} template in section 4.2.7, a similar small change in permittivity between the liquid crystal and isotropic regions was observed. The dielectric loss of the refilled $SmAP_F$ template was measured as a function of frequency on cooling from the isotropic state, to test for any relaxation peaks corresponding to the Goldstone mode. The data is shown in Figure 7.10b and no relaxations are observable in the measured frequency window. Permittivity as a function of voltage for several temperatures was also measured on cooling from the isotropic state, and the data is given in Figure 7.10c. The curves corresponding to 36 °C and 40 °C (isotropic phase) show almost no change in permittivity over the measured voltage range. The permittivity in the liquid crystal region between 24 °C and 32 °C increases linearly as the threshold voltage at ~3-4 V is passed (the threshold electric field is approx. 0.3-0.4 V/μm). Compared to 5CB, the curves of the refilled templates in Figure 7.10c show no sign of saturation. The threshold electric fields of pure 5CB, discussed in section 4.2.7, are <0.1 V/μm, and the threshold electric fields of the refilled $SmAP_F$ template in Figure 7.10c are in the range 0.3-0.4 V/μm, i.e. greater than those of pure 5CB. This suggests that the $SmAP_F$ template is inducing an anchoring effect onto the 5CB liquid crystal at the liquid crystal/polymer interface.

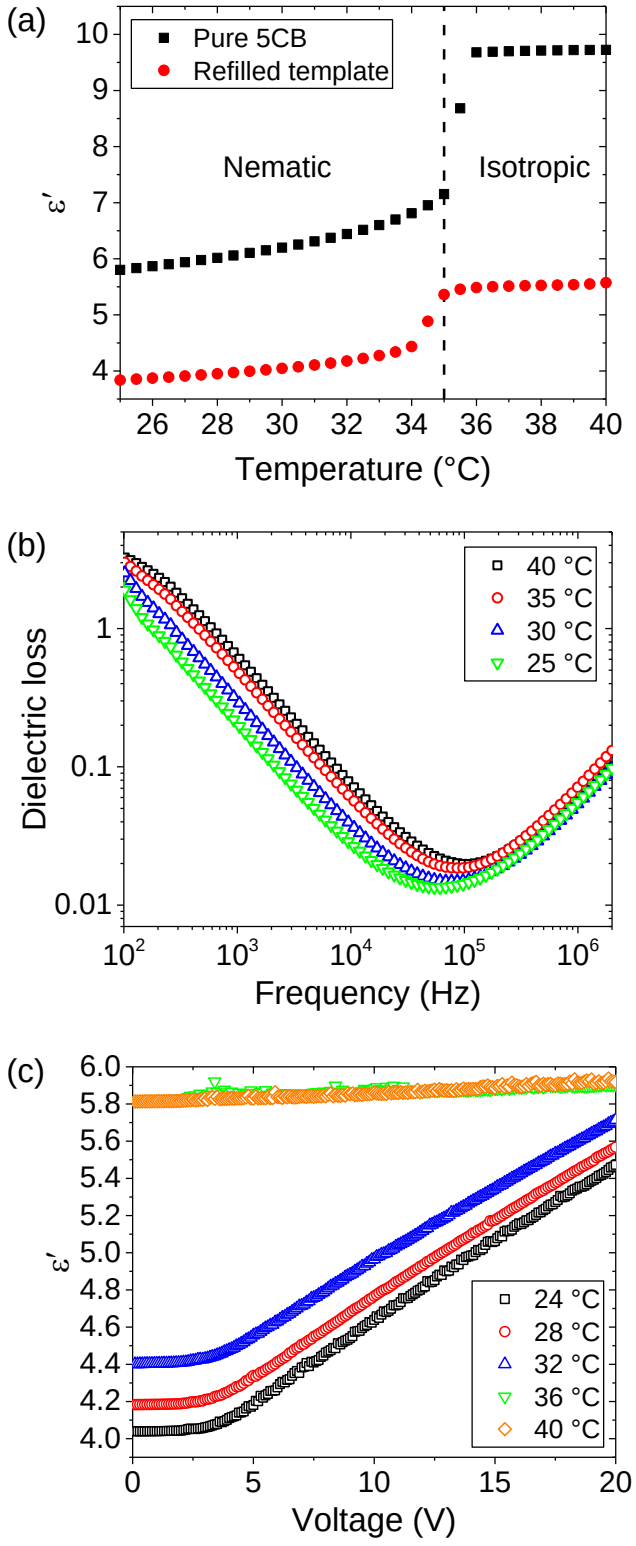

Figure 7.10: Dielectric spectroscopy measurements of the refilled $SmAP_F$ template formed from NT12-10 on cooling from the isotropic state (10 μm planar cell). (a) Dielectric permittivity (ε') at 10 kHz as a function of temperature (data for pure 5CB is also included). (b) Dielectric loss as a function of frequency between 40 °C and 25 °C. (c) ε' as a function of voltage at temperatures 40-24 °C.

Furthermore, the current response of the refilled template (NT12-10) was also measured to check for ferroelectric switching across a range of temperatures (25-35 °C: nematic phase, 40-50 °C: isotropic phase). A 50 V_{RMS} triangle wave (E = 5 V/μm, 11 Hz) was applied to the refilled template and the current response is given in Figure 7.11a. A peak is observed in the current response curves across all measured temperatures from 25 °C to 50 °C (i.e. the nematic and isotropic phases). The current response of pure 5CB was also measured across the temperature range from 25 °C to 50 °C to check if similar behaviour was observed in the pure material. The current response for 5CB is given in Figure 7.11b and the curves also show a peak across all measured temperatures. Comparing the shapes of the curves, the peaks for the refilled template in Figure 7.11a appear broader than those in Figure 7.11b for pure 5CB. The peaks observed in the refilled template and pure 5CB are most likely due to ions in the sample. The peak at each measured temperature was integrated and the area under the peaks is given as a function of temperature in Figure 7.11c for both the refilled template and pure 5CB. It can be seen that the curves for both the refilled sample and pure 5CB follow a similar trend: as the temperature increases, the area under the peak increases and the area at each temperature is of similar value for both samples.

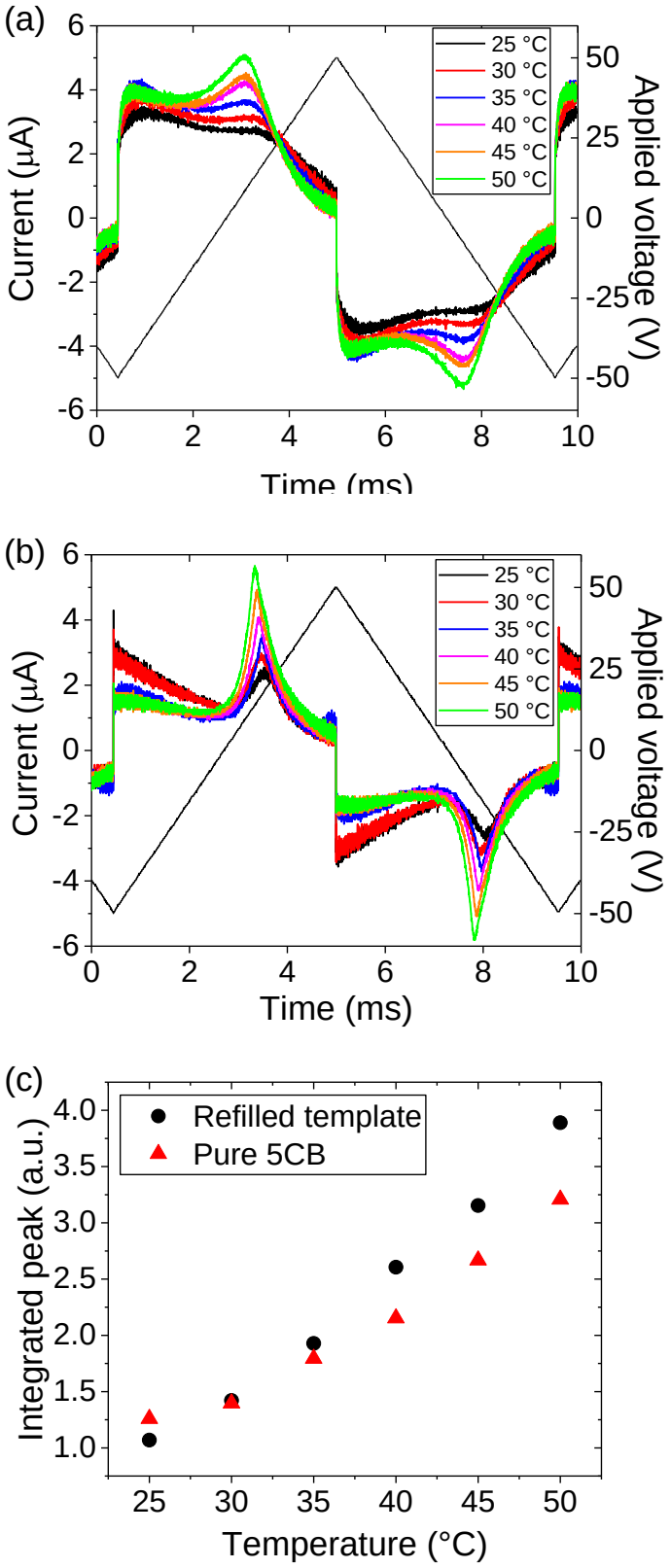

Figure 7.11: Current response measured in 10 μm planar cells at E = 5 V/μm (triangle wave, 11 Hz) for: (a) the refilled template, (b) pure 5CB. (c) Integrated area under the peak as a function of temperature for the refilled template (circle symbols) and pure 5CB (triangle symbols).

The fact that (1) the refilled template formed from 10wt% monomer concentration does not exhibit a relaxation peak corresponding to the Goldstone mode in dielectric loss data, and (2) the peak observed in current response data is most likely due to ions in the liquid crystal, it is suggested that ferroelectricity has not been templated onto the polymer network formed from 10 wt% of monomer (NT12-10). However, results for the refilled template formed from 20wt% of monomer (NT12-20) need to be investigated. It is possible that a template formed from a higher concentration of monomer (20 wt% instead of 10 wt%) could induce polar order onto the refilled liquid crystal because the interface between the liquid crystal and polymer would be greater. As discussed in section 4.2.7, a relaxation peak characteristic of the N_{TB} phase appeared to emerge in the refilled N_{TB} template formed from 20 wt% of monomer.

7.5 Summary of results

This chapter discussed templating of the $SmAP_F$ phase using the mixtures NT12-10 and NT12-20 formed in Chapter 6. The $SmAP_F$ phase was photopolymerised whilst subjected to an electric field, to obtain larger sizes of focal conic domains. The polymerised samples had isotropic transition temperatures very similar to those of pure NT12, and residual birefringence was observed in the isotropic phase. Subjecting the polymerised samples to an electric field showed that polarisation is measurable over a wider temperature window after polymerisation, compared to the unpolymerised samples, and is of similar range to that of pure NT12. After polymerisation, higher polarisation values are measured, compared to unpolymerised samples. This is because the polarisation in polymerised samples is mainly determined only from NT12 in the liquid crystal/polymer matrix (formed from RM257), whereas before polymerisation the polarisation was determined from the mixture of both NT12 and RM257. Permittivity as a function of temperature shows that the polymerised sample exhibits a wider temperature range over which the liquid crystal phase is present, compared to the unpolymerised sample. A relaxation peak corresponding to a Goldstone mode was observed in dielectric loss measurements of polymerised NT12-10. The peak was fitted to the Havriliak-Negami equation and the mode shifts to lower frequencies on cooling. In the polymerised sample, the mode is present over a wider temperature range compared to before polymerisation – it emerges at ~150 °C, which is similar to pure NT12 (before polymerisation it emerges at ~130 °C). The strength of the mode is lower than that of pure NT12 and the unpolymerised sample.

Raman spectroscopy was used to ensure the host liquid crystal was washed out when forming the templates. SEM imaging of the SmA and $SmAP_F$ templates (formed from the same material) showed that the general mesoscopic structure of the phases had been templated and that the width of polymer strands is in the range 50-100 nm, as was observed for N_{TB} templates. The SmA polymer strands follow a preferred alignment within each of the focal conic domains. Regions with 'wispy' textures were observed in the SmA template. EDX analysis confirmed that there was no nitrogen present in the wispy regions, which suggests that the wispy regions were not due to leftover (unwashed) host liquid crystal in the template. The $SmAP_F$ phase template shows smoother textures compared to the SmA template.

The $SmAP_F$ templates were refilled with the nematic liquid crystal 5CB. For the refilled template, it is possible to determine the birefringence in the isotropic phase, due to residual birefringence. In the liquid crystal phase, the birefringence of the refilled template is approx. 10% lower than the birefringence of pure 5CB, which suggests that the template is inducing order in the refilled liquid crystal. Dielectric spectroscopy measurements show that the permittivity in the isotropic region (>35 °C) of the refilled template is ~50% lower than that of pure 5CB. In the liquid crystal region (<35 °C), the permittivity of the refilled template is also ~50% lower than that of pure 5CB. There are no relaxations in the measured frequency window for dielectric loss measurements of the refilled template. Plots of permittivity as a function of voltage show no sign of saturation. Current response measurements of the refilled template formed from 10 wt% monomer showed a single peak in the liquid crystal and isotropic phases; however, this was also observed for pure 5CB. This suggests that the peak was most likely due to ions. This, and the fact that a Goldstone mode was not observed in dielectric loss data, suggests that polar ordering and ferroelectricity has not been imprinted onto the polymer network formed from 10 wt% of monomer. However, further investigations need to be made for the refilled template formed from 20 wt% of monomer.

CHAPTER 8:
Conclusion

The process of liquid crystal templating offers great potential in understanding interfacial interactions between the host liquid crystals and guest polymers at the nanoscale. In the last three decades, a vast amount of research has been carried out on templating the lyotropic liquid crystal phases. Most of this research focuses on using the templates as mesoporous nanostructures to carry out catalytic chemical reactions, encapsulate drugs, and functionalise templates for sensing applications. On the other hand, templating thermotropic liquid crystal phases is a relatively recent topic of study, and most of the studies so far focussed on templating the structural features of the cholesteric and liquid crystal blue phases. Very little is known about what characteristics of liquid crystals can be imprinted and what the nanoscopic interaction is between the polymer and liquid crystal that leads to the templating effect. The aim of this project was to improve the understanding of (1) the process of surface modification of polymers through which templates are created, and (2) what sort of properties of the host liquid crystal can be templated.

The work undertaken in this thesis focuses on two novel liquid crystal phases: the twist-bend nematic (N_{TB}) phase and the polar SmA phase that exhibits ferroelectric switching ($SmAP_F$). The N_{TB} phase is a type of nematic phase that not only exhibits orientational order, but also a spontaneous self-arrangement of mesogens into helical structures of nanoscale pitch. Due to its high viscosity, it is extremely difficult to measure the properties of the N_{TB} phase in pure materials. Templating the N_{TB} phase and refilling the template with another nematic liquid crystal provided an additional benefit of understanding the electrical and mechanical properties of the phase. The $SmAP_F$ phase is a biaxial phase that exhibits macroscopic polarisation. In this project a bent-core mesogen exhibiting the $SmAP_F$ phase was synthesised. The aim was to see if the physical and structural properties of the $SmAP_F$ phase such as the biaxiality, layered arrangement of mesogens and ferroelectric switching can be imprinted into the polymer matrix.

Even though the process of thermotropic liquid crystal templating has been reported before, the materials and procedures are not universal, and it was necessary to optimise them according to our experimental requirements and conditions. In order to create templates, appropriate mixtures of liquid crystals and mesogenic monomer were investigated first. It is preferable to have the liquid crystal phase of interest at

room temperature during templating. The liquid crystal used for templating the N_{TB} phase was the dimer CB7CB that exhibits the nematic and N_{TB} phases, and the nematic liquid crystal 5CB was also included in order to reduce the nematic to N_{TB} transition temperature, as the N_{TB} phase is generally observed well above room temperature. The concentration of monomer used for N_{TB} templating was 20 wt%, and for $SmAP_F$ templating, 10 wt% was chosen. Next, the phases were photopolymerised by exposing the samples contained in cells to UV light, at a temperature at which the phase of interest exists. This process formed thermodynamically-stabilised phases and metastable room temperature N_{TB} phases were achieved via this process. The polymer networks of all polymerised phases formed in this thesis exhibited residual birefringence when the liquid crystal was in the isotropic state, which was most likely a result of induced orientational order stemming from the interface of the liquid crystal and aligned polymer. The thermal and dielectric properties of the photopolymerised N_{TB} and $SmAP_F$ phases were similar to those of the pure host liquid crystals used for polymerisation. This is because the properties of unpolymerised samples are determined both from the host liquid crystal and the mesogenic monomer, whereas when the sample is polymerised, a polymer network is formed from the mesogenic monomer, resulting in a matrix of polymer and the host liquid crystal.

Templates were created by washing the host liquid crystal from the polymerised sample. Raman spectroscopy proved to be a useful tool in ensuring that the templates were not contaminated with leftover host liquid crystal that had not been washed out. This was possible because all host liquid crystals used for templating possessed nitrile groups, whereas the monomer did not, and so the peak in Raman spectra corresponding to the nitrile group could be traced. Dielectric spectroscopy was used as a technique of measuring the porosity of the templates. It was observed that different templates formed from the same material (same concentration of monomer) showed similar porosities, regardless of the phase they were polymerised in.

Visualisation of the templates using SEM showed a clear difference in the morphology of different templated phases. It was clear that the general mesoscopic structure of the host liquid crystal phase had been templated. Individual polymer strands showed similar diameters for all templated phases, whereas their textures varied between different phases. Templates of the N_{TB} phase showed a particular arrangement of polymer strands and it was suggested that this related to the direction of the director and helical axis of the N_{TB} phase.

The N_{TB} and $SmAP_F$ templates were refilled with the nematic liquid crystal 5CB to determine if any of the physical properties of the host liquid crystal phases were imprinted onto the polymer networks (besides the general mesoscopic structure of the phases). Both the refilled N_{TB} and $SmAP_F$ templates induced order in the surrounding nematic liquid crystal. As a result, the templates refilled with 5CB exhibited different physical behaviour compared to pure 5CB, and this was especially evident when comparing the permittivities and threshold electric field values of the refilled templates to 5CB. In addition, the refilled N_{TB} sample showed the emergence of a dielectric relaxation that is characteristic of the N_{TB} phase in pure liquid crystals and corresponds to the flip-flop motion of the cyanobiphenyl units in bent conformers. This suggests that the nanofeatures of the N_{TB} phase have also been templated on the polymer network. For the refilled $SmAP_F$ template, a dielectric relaxation peak corresponding to the Goldstone mode was not observed in the measured frequency window, and in addition to this, current response measurements did not show a current peak as expected of a mesogen exhibiting ferroelectric switching.

The reason why the refilled N_{TB} template gives an indication of imprinted physical properties of the host liquid crystal phase, whereas the refilled $SmAP_F$ template does not, could be to do with the concentration of monomer used in forming the templates. For the N_{TB} template, 20 wt% of monomer was used, whereas 10 wt% of monomer was used for the $SmAP_F$ template. Therefore, it is necessary to further examine the properties of the refilled $SmAP_F$ template formed from 20 wt% monomer. The work could not be carried out due to time constraints. Templates formed from higher monomer concentrations might (1) create a stronger polymer film, and (2) enable a greater surface of polymer to be exposed to the surrounding (refilled) liquid crystal, and this would, in turn, allow a greater chance of inducing physical properties of the host liquid crystal on the refilled liquid crystal. Mixture work undertaken in this thesis showed that N_{TB} phases were formed when CB7CB was mixed with up to 40 wt% of monomer.

The questions of whether the helical arrangement of the N_{TB} phase and layered structure of the $SmAP_F$ phase have been templated are yet to be answered. Visualisation of the templates using SEM did not show any discernible features on the polymer strands, however, other visualisation methods with higher resolution such as freeze-fracture transmission electron microscopy (FF-TEM) could be used to provide an answer to these questions. Of course, with thermotropic liquid crystal templating being a relatively novel topic of research, there are a vast array of other

approaches that could be undertaken to further develop this work, from using different types of monomer for polymerisation and determining optimal curing temperatures, to investigating different liquid crystals for refilling the templates. More broadly, templating thermotropic liquid crystal phases is a field that is yet to be explored, and the potential of understanding interaction mechanisms of an array of soft matter systems at the nanoscale is what makes this field of research so fascinating.

References

[1] M. Mitov, *Soft Matter* **2017**, *13*, 4176–4209.

[2] F. Reinitzer, *Monatsh. Chem.* **1888**, *9*, 421–441.

[3] O. Lehmann, *Flüssige Kristalle: Sowie Plastizität von Kristallen Im Allgemeinen, Molekulare Umlagerungen Und Aggregatzustandsänderungen*, Verlag Von Wilhelm Engelmann, Leipzig, **1904**.

[4] C. Tschierske, *Curr. Opin. Colloid Interface Sci.* **2002**, *7*, 355–370.

[5] P. Yeh, C. Gu, *Optics of Liquid Crystal Displays*, Wiley, Hoboken, N.J, **2010**.

[6] B. Bahadur, Ed. , *Liquid Crystals: Applications and Uses. Vol. 1*, World Scientific, Singapore, **1995**.

[7] E. P. Raynes, in *Reference Module in Materials Science and Materials Engineering*, Elsevier, **2016**.

[8] H.-W. Chen, J.-H. Lee, B.-Y. Lin, S. Chen, S.-T. Wu, *Light Sci. Appl.* **2018**, *7*, 17168.

[9] J. Beeckman, *Opt. Eng.* **2011**, *50*, 081202.

[10] H. Coles, S. Morris, *Nat. Photonics* **2010**, *4*, 676–685.

[11] D. Cupelli, F. Pasquale Nicoletta, S. Manfredi, M. Vivacqua, P. Formoso, G. De Filpo, G. Chidichimo, *Sol. Energy Mater. Sol. Cells* **2009**, *93*, 2008–2012.

[12] H.-K. Kwon, K.-T. Lee, K. Hur, S. H. Moon, M. M. Quasim, T. D. Wilkinson, J.-Y. Han, H. Ko, I.-K. Han, B. Park, B. K. Min, B.-K. Ju, S. M. Morris, R. H. Friend, D.-H. Ko, *Adv. Energy Mater.* **2015**, *5*, 1401347.

[13] J. Mo, G. Milleret, M. Nagaraj, *Liquid Crystals Reviews* **2017**, *5*, 69–85.

[14] S. J. Woltman, G. D. Jay, G. P. Crawford, *Nat. Mater.* **2007**, *6*, 929–938.

[15] S. W. Ula, N. A. Traugutt, R. H. Volpe, R. R. Patel, K. Yu, C. M. Yakacki, *Liq. Cryst. Rev.* **2018**, *6*, 78–107.

[16] R. Narayan, J. E. Kim, J. Y. Kim, K. E. Lee, S. O. Kim, *Adv. Mater.* **2016**, *28*, 3045–3068.

[17] L. Wang, Q. Li, *Adv. Funct. Mater.* **2016**, *26*, 10–28.

[18] S. V. Pasechnik, V. G. Chigrinov, D. V. Shmeliova, *Liquid Crystals Viscous and Elastic Properties*, Wiley-VCH, Weinheim, **2009**.

[19] D. W. Bruce, R. Deschenaux, B. Donnio, D. Guillon, in *Comprehensive Organometallic Chemistry III*, Elsevier, **2007**, pp. 195–293.

[20] H. Stegemeyer, Ed. , *Liquid Crystals*, Steinkopff; Springer, Darmstadt; New York, **1994**.

[21] S. Chandrasekhar, *Liquid Crystals*, Cambridge University Press, Cambridge, **1992**.

[22] G. W. Gray, K. J. Harrison, J. A. Nash, *Electron. Lett.* **1973**, *9*, 130 – 131.

[23] M. Nagaraj, *Liq. Cryst* **2016**, *43*, 2244–2253.

[24] D. Vorländer, *Ber. dtsch. Chem. Ges. A/B* **1929**, *62*, 2831–2835.

[25] D. Vorländer, A. Apel, *Ber. dtsch. Chem. Ges. A/B* **1932**, *65*, 1101–1109.

[26] H. Takezoe, Y. Takanishi, *Jpn. J. Appl. Phys.* **2006**, *45*, 597–625.

[27] R. A. Reddy, C. Tschierske, *J. Mater. Chem.* **2006**, *16*, 907–961.

[28] M. B. Ros, J. L. Serrano, M. R. de la Fuente, C. L. Folcia, *J. Mater. Chem.* **2005**, *15*, 5093.

[29] J. Etxebarria, M. Blanca Ros, *J. Mater. Chem.* **2008**, *18*, 2919.

[30] G. Pelzl, S. Diele, W. Weissflog, *Adv. Mater.* **1999**, *11*, 707–724.

[31] D. Vorländer, *Z. Phys. Chem* **1927**, *126U*, 449–472.

[32] C. T. Imrie, in *Liquid Crystals II* (Ed.: D.M.P. Mingos), Springer Berlin Heidelberg, Berlin, Heidelberg, **1999**, pp. 149–192.

[33] I. Dierking, in *Polymer-Modified Liquid Crystals* (Ed.: I. Dierking), Royal Society Of Chemistry, Cambridge, **2019**, pp. 37–44.

[34] I. Dierking, *Adv. Mater.* **2000**, *12*, 167–181.

[35] D. J. Broer, J. Boven, G. N. Mol, G. Challa, *Die Makromolekulare Chemie* **1989**, *190*, 2255–2268.

[36] D. J. Broer, R. G. Gossink, R. A. M. Hikmet, *Angew. Makromol. Chemie* **1990**, *183*, 45–66.

[37] R. A. M. Hikmet, *Liq. Cryst.* **1991**, *9*, 405–416.

[38] R. A. M. Hikmet, J. Lub, J. A. Higgins, *Polymer* **1993**, *34*, 1736–1740.

[39] P. Archer, I. Dierking, *Soft Matter* **2009**, *5*, 835–841.

[40] H. Kikuchi, M. Yokota, Y. Hisakado, H. Yang, T. Kajiyama, *Nat. Mater.* **2002**, *1*, 64–68.

[41] H. J. Coles, M. N. Pivnenko, *Nature* **2005**, *436*, 997–1000.

[42] D. J. Broer, I. Heynderickx, *Macromolecules* **1990**, *23*, 2474–2477.

[43] D. J. Broer, J. Lub, G. N. Mol, *Nature* **1995**, *378*, 467–469.

[44] A. Varanytsia, L.-C. Chien, *J. Appl. Phys.* **2016**, *119*, 014502.

[45] D.-K. Yang, in *Polymer-Modified Liquid Crystals* (Ed.: I. Dierking), Royal Society Of Chemistry, Cambridge, **2019**, pp. 166–194.

[46] H. Furue, T. Miyama, Y. Iimura, H. Hasebe, H. Takatsu, *Jpn. J. Appl. Phys.* **1997**, *36*, L1517–L1519.

[47] C. A. Guymon, E. N. Hogga, D. M. Walba, N. A. Clark, C. N. Bowman, *Liq. Cryst.* **1995**, *19*, 719–727.

[48] I. Dierking, L. Komitov, S. T. Lagerwall, T. Wittig, R. Zentel, *Liq. Cryst.* **1999**, *26*, 1511–1519.

[49] P. Rudquist, D. Elfstrom, S. Lagerwall, R. Dabrowski, *GFER* **2006**, *344*, 177–188.

[50] J. Strauss, H. -S. Kitzerow, *Appl. Phys. Lett.* **1996**, *69*, 725–727.

[51] H. Furue, H. Yokoyama, *Jpn. J. Appl. Phys.* **2003**, *42*, 6180–6182.

[52] C. T. Kresge, M. E. Leonowicz, W. J. Roth, J. C. Vartuli, J. S. Beck, *Nature* **1992**, *359*, 710–712.

[53] H. Ishikawa, T. Kikuchi, *J. Mater. Chem.* **1998**, *8*, 1783–1786.

[54] S. Che, A. E. Garcia-Bennett, T. Yokoi, K. Sakamoto, H. Kunieda, O. Terasaki, T. Tatsumi, *Nat. Mater.* **2003**, *2*, 801–805.

[55] E. W. Shin, H. S. Choi, T.-D. Nguyen-Phan, J. S. Chung, E. J. Kim, *J. Ind. Eng. Chem.* **2008**, *14*, 510–514.

[56] J. B. Joo, Q. Zhang, I. Lee, M. Dahl, F. Zaera, Y. Yin, *Adv. Funct. Mater.* **2012**, *22*, 166–174.

[57] S. L. Burkett, S. D. Sims, S. Mann, *ChemComm* **1996**, 1367–1368.

[58] C. B. Vidal, A. L. Barros, C. P. Moura, A. C. A. de Lima, F. S. Dias, Luiz. C. G. Vasconcellos, P. B. A. Fechine, R. F. Nascimento, *J. Colloid Interface Sci.* **2011**, *357*, 466–473.

[59] A. Monnier, F. Schuth, Q. Huo, D. Kumar, D. Margolese, R. S. Maxwell, G. D. Stucky, M. Krishnamurty, P. Petroff, A. Firouzi, M. Janicke, B. F. Chmelka, *Science* **1993**, *261*, 1299–1303.

[60] W. Lin, J. Chen, Y. Sun, W. Pang, *J. Chem. Soc., Chem. Commun.* **1995**, 2367.

[61] S. H. Tolbert, *Science* **1997**, *278*, 264–268.

[62] L. Sierra, J.-L. Guth, *Microporous Mesoporous Mater.* **1999**, *27*, 243–253.

[63] E. Zhao, S. E. Hardcastle, G. Pacheco, A. Garcia, A. L. Blumenfeld, J. J. Fripiat, *Microporous Mesoporous Mater.* **1999**, *31*, 9–21.

[64] V. Antochshuk, M. Jaroniec, *Chem. Mater.* **2000**, *12*, 2496–2501.

[65] M. A. Karakassides, A. Bourlinos, D. Petridis, L. Coche-Guerènte, P. Labbè, *J. Mater. Chem.* **2000**, *10*, 403–408.

[66] Y. Bennadja, P. Beaunier, D. Margolese, A. Davidson, *Microporous Mesoporous Mater.* **2001**, *44–45*, 147–152.

[67] A. Vinu, V. Murugesan, M. Hartmann, *Chem. Mater.* **2003**, *15*, 1385–1393.

[68] B. G. Trewyn, I. I. Slowing, S. Giri, H.-T. Chen, V. S.-Y. Lin, *Acc. Chem. Res.* **2007**, *40*, 846–853.

[69] L. Jin, S. M. Auerbach, P. A. Monson, *Langmuir* **2013**, *29*, 766–780.

[70] J. L. Blin, F. Michaux, M. J. Stébé, *Colloids Surf. A Physicochem. Eng. Asp.* **2016**, *510*, 104–112.

[71] T. Zhao, A. Elzatahry, X. Li, D. Zhao, *Nat. Rev. Mater.* **2019**, *4*, 775–791.

[72] Z. ALOthman, *Materials* **2012**, *5*, 2874–2902.

[73] A. Sayari, in *Studies in Surface Science and Catalysis*, Elsevier, **1996**, pp. 1–46.

[74] M. Vallet-Regi, A. Rámila, R. P. del Real, J. Pérez-Pariente, *Chem. Mater.* **2001**, *13*, 308–311.

[75] Y. Wang, Q. Zhao, N. Han, L. Bai, J. Li, J. Liu, E. Che, L. Hu, Q. Zhang, T. Jiang, S. Wang, *Nanomedicine* **2015**, *11*, 313–327.

[76] M. Vallet-Regí, L. Ruiz-González, I. Izquierdo-Barba, J. M. González-Calbet, *J. Mater. Chem.* **2006**, *16*, 26–31.

[77] Z. Li, J. C. Barnes, A. Bosoy, J. F. Stoddart, J. I. Zink, *Chem. Soc. Rev.* **2012**, *41*, 2590.

[78] W. Zeng, X.-F. Qian, Y.-B. Zhang, J. Yin, Z.-K. Zhu, *Mater. Res. Bull.* **2005**, *40*, 766–772.

[79] A. Suwalski, H. Dabboue, A. Delalande, S. F. Bensamoun, F. Canon, P. Midoux, G. Saillant, D. Klatzmann, J.-P. Salvetat, C. Pichon, *Biomaterials* **2010**, *31*, 5237–5245.

[80] I. Izquierdo-Barba, L. Ruiz-González, J. C. Doadrio, J. M. González-Calbet, M. Vallet-Regí, *Solid State Sci.* **2005**, *7*, 983–989.

[81] D. P. Serrano, G. Calleja, J. A. Botas, F. J. Gutierrez, *Ind. Eng. Chem. Res.* **2004**, *43*, 7010–7018.

[82] E. Petala, K. Dimos, A. Douvalis, T. Bakas, J. Tucek, R. Zbořil, M. A. Karakassides, *J. Hazard. Mater.* **2013**, *261*, 295–306.

[83] A. Heidari, H. Younesi, Z. Mehraban, *Chem. Eng. J.* **2009**, *153*, 70–79.

[84] A. Sayari, S. Hamoudi, Y. Yang, *Chem. Mater.* **2005**, *17*, 212–216.

[85] J. A. S. Costa, R. A. de Jesus, D. O. Santos, J. F. Mano, L. P. C. Romão, C. M. Paranhos, *Microporous Mesoporous Mater.* **2020**, *291*, 109698.

[86] D. Das, J.-F. Lee, S. Cheng, *ChemComm* **2001**, 2178–2179.

[87] M. Jia, A. Seifert, W. R. Thiel, *Chem. Mater.* **2003**, *15*, 2174–2180.

[88] Y. Qiao, C. Miao, Y. Yue, Z. Xie, W. Yang, W. Hua, Z. Gao, *Microporous Mesoporous Mater.* **2009**, *119*, 150–157.

[89] I. Jiménez-Morales, M. Moreno-Recio, J. Santamaría-González, P. Maireles-Torres, A. Jiménez-López, *Appl. Catal. B* **2015**, *164*, 70–76.

[90] F. Deng, N. Li, S. Tang, C. Liu, H. Yue, B. Liang, *Chem. Eng. J.* **2018**, *334*, 1943–1953.

[91] H. Zhang, Y. Sun, K. Ye, P. Zhang, Y. Wang, *J. Mater. Chem.* **2005**, *15*, 3181.

[92] F. Wang, J. Yang, K. Wu, *Anal. Chim. Acta* **2009**, *638*, 23–28.

[93] R. Qi, X. Lin, J. Dai, H. Zhao, S. Liu, T. Fei, T. Zhang, *Sens. Actuators B Chem.* **2018**, *277*, 584–590.

[94] C. L. Lester, S. M. Smith, C. D. Colson, C. A. Guymon, *Chem. Mater.* **2003**, *15*, 3376–3384.

[95] M. Antonietti, R. A. Caruso, C. G. Göltner, M. C. Weissenberger, *Macromolecules* **1999**, *32*, 1383–1389.

[96] J. D. Clapper, C. A. Guymon, *Macromolecules* **2007**, *40*, 1101–1107.

[97] C. L. Lester, S. M. Smith, C. A. Guymon, *Macromolecules* **2001**, *34*, 8587–8589.

[98] M. A. DePierro, K. G. Carpenter, C. A. Guymon, *Chem. Mater.* **2006**, *18*, 5609–5617.

[99] B. S. Forney, C. Baguenard, C. A. Guymon, *Chem. Mater.* **2013**, *25*, 2950–2960.

[100] M. A. DePierro, C. A. Guymon, *Macromolecules* **2014**, *47*, 5728–5738.

[101] J. Jennings, B. Green, T. J. Mann, C. A. Guymon, M. K. Mahanthappa, *Chem. Mater.* **2018**, *30*, 185–196.

[102] J. Guo, H. Cao, J. Wei, D. Zhang, F. Liu, G. Pan, D. Zhao, W. He, H. Yang, *Appl. Phys. Lett.* **2008**, *93*, 201901.

[103] M. E. McConney, V. P. Tondiglia, J. M. Hurtubise, T. J. White, T. J. Bunning, *ChemComm* **2011**, *47*, 505–507.

[104] M. E. McConney, V. P. Tondiglia, J. M. Hurtubise, L. V. Natarajan, T. J. White, T. J. Bunning, *Adv. Mater.* **2011**, *23*, 1453–1457.

[105] M. E. McConney, T. J. White, V. P. Tondiglia, L. V. Natarajan, D. Yang, T. J. Bunning, *Soft Matter* **2012**, *8*, 318–323.

[106] J. Guo, H. Wu, F. Chen, L. Zhang, W. He, H. Yang, J. Wei, *J. Mater. Chem.* **2010**, *20*, 4094.

[107] S. S. Choi, S. M. Morris, W. T. S. Huck, H. J. Coles, *Adv. Mater.* **2010**, *22*, 53–56.

[108] M. Mitov, N. Dessaud, *Nat. Mater.* **2006**, *5*, 361–364.

[109] Y. Li, Y. J. Liu, H. T. Dai, X. H. Zhang, D. Luo, X. W. Sun, *J. Mater. Chem. C* **2017**, *5*, 10828–10833.

[110] Y. Zhao, L. Zhang, Z. He, G. Chen, D. Wang, H. Zhang, H. Yang, *Liq. Cryst.* **2015**, *42*, 1120–1123.

[111] F. Castles, F. V. Day, S. M. Morris, D.-H. Ko, D. J. Gardiner, M. M. Qasim, S. Nosheen, P. J. W. Hands, S. S. Choi, R. H. Friend, H. J. Coles, *Nat. Mater.* **2012**, *11*, 599–603.

[112] H.-C. Jau, W.-M. Lai, C.-W. Chen, Y.-T. Lin, H.-K. Hsu, C.-H. Chen, C.-C. Wang, T.-H. Lin, *Opt. Mater. Express* **2013**, *3*, 1516.

[113] J. Xiang, O. D. Lavrentovich, *Appl. Phys. Lett.* **2013**, *103*, 051112.

[114] M. Ravnik, J. Fukuda, *Soft Matter* **2015**, *11*, 8417–8425.

[115] S. Zha, H. Zhang, C. Sun, Y. Feng, J. Lu, *Crystals* **2019**, *9*, 451.

[116] M. Stimulak, M. Ravnik, *Soft Matter* **2014**, *10*, 6339–6346.

[117] C.-W. Chen, C.-T. Hou, C.-C. Li, H.-C. Jau, C.-T. Wang, C.-L. Hong, D.-Y. Guo, C.-Y. Wang, S.-P. Chiang, T. J. Bunning, I.-C. Khoo, T.-H. Lin, *Nat. Commun.* **2017**, *8*, 727.

[118] S. Havriliak, S. Negami, *Polymer* **1967**, *8*, 161–210.

[119] V. Fréedericksz, A. Repiewa, *Z. Phys.* **1927**, *42*, 532–546.

[120] K. Miyasato, S. Abe, H. Takezoe, A. Fukuda, E. Kuze, *Jpn. J. Appl. Phys.* **1983**, *22*, L661–L663.

[121] Ph. Martinot-Lagarde, *J. Physique Lett.* **1977**, *38*, 17–19.

[122] H. Takezoe, *Mol. Cryst. Liq. Cryst.* **2017**, *646*, 46–65.

[123] J. R. DeVore, *J. Opt. Soc. Am.* **1951**, *41*, 416.

[124] V. P. Panov, M. Nagaraj, J. K. Vij, Yu. P. Panarin, A. Kohlmeier, M. G. Tamba, R. A. Lewis, G. H. Mehl, *Phys. Rev. Lett.* **2010**, *105*, 167801.

[125] V. P. Panov, R. Balachandran, M. Nagaraj, J. K. Vij, M. G. Tamba, A. Kohlmeier, G. H. Mehl, *Appl. Phys. Lett.* **2011**, *99*, 261903.

[126] R. J. Mandle, E. J. Davis, C.-C. A. Voll, C. T. Archbold, J. W. Goodby, S. J. Cowling, *Liq. Cryst.* **2014**, 1–16.

[127] C. S. P. Tripathi, P. Losada-Pérez, C. Glorieux, A. Kohlmeier, M.-G. Tamba, G. H. Mehl, J. Leys, *Phys. Rev. E* **2011**, *84*, 041707.

[128] M. Cestari, S. Diez-Berart, D. A. Dunmur, A. Ferrarini, M. R. de la Fuente, D. J. B. Jackson, D. O. Lopez, G. R. Luckhurst, M. A. Perez-Jubindo, R. M. Richardson, J. Salud, B. A. Timimi, H. Zimmermann, *Phys. Rev. E* **2011**, *84*, 031704.

[129] A. Hoffmann, A. G. Vanakaras, A. Kohlmeier, G. H. Mehl, D. J. Photinos, *Soft Matter* **2015**, *11*, 850–855.

[130] R. Balachandran, V. P. Panov, Y. P. Panarin, J. K. Vij, M. G. Tamba, G. H. Mehl, J. K. Song, *J. Mater. Chem. C* **2014**, *2*, 8179–8184.

[131] D. O. López, N. Sebastian, M. R. de la Fuente, J. C. Martínez-García, J. Salud, M. A. Pérez-Jubindo, S. Diez-Berart, D. A. Dunmur, G. R. Luckhurst, *J. Chem. Phys.* **2012**, *137*, 034502.

[132] A. A. Dawood, M. C. Grossel, G. R. Luckhurst, R. M. Richardson, B. A. Timimi, N. J. Wells, Y. Z. Yousif, *Liq. Cryst.* **2016**, *43*, 2–12.

[133] C. Meyer, G. R. Luckhurst, I. Dozov, *Phys. Rev. Lett.* **2013**, *111*, 067801.

[134] V. Borshch, Y.-K. Kim, J. Xiang, M. Gao, A. Jákli, V. P. Panov, J. K. Vij, C. T. Imrie, M. G. Tamba, G. H. Mehl, O. D. Lavrentovich, *Nat. Commun.* **2013**, *4*, 2635.

[135] D. Chen, J. H. Porada, J. B. Hooper, A. Klittnick, Y. Shen, M. R. Tuchband, E. Korblova, D. Bedrov, D. M. Walba, M. A. Glaser, J. E. Maclennan, N. A. Clark, *Proc. Natl. Acad. Sci. U.S.A.* **2013**, *110*, 15931–15936.

[136] R. B. Meyer, in *Les Houches Summer School in Theoretical Physics, 1973. Molecular Fluids* (Eds.: R. Balian, G. Weil), Gordon And Breach, New York, **1976**, pp. 273–373.

[137] I. Dozov, *EPL* **2001**, *56*, 247–253.

[138] V. P. Panov, R. Balachandran, J. K. Vij, M. G. Tamba, A. Kohlmeier, G. H. Mehl, *Appl. Phys. Lett.* **2012**, *101*, 234106.

[139] A. Varanytsia, L.-C. Chien, *Sci. Rep.* **2017**, *7*, 41333.

[140] M. Šepelj, A. Lesac, U. Baumeister, S. Diele, H. L. Nguyen, D. W. Bruce, *J. Mater. Chem.* **2007**, *17*, 1154–1165.

[141] D. A. Paterson, J. P. Abberley, W. T. Harrison, J. M. Storey, C. T. Imrie, *Liq. Cryst.* **2017**, *44*, 127–146.

[142] R. J. Mandle, E. J. Davis, C. T. Archbold, S. J. Cowling, J. W. Goodby, *J. Mater. Chem. C* **2014**, *2*, 556–566.

[143] Y. Wang, G. Singh, D. M. Agra-Kooijman, M. Gao, H. K. Bisoyi, C. Xue, M. R. Fisch, S. Kumar, Q. Li, *CrystEngComm* **2015**, *17*, 2778–2782.

[144] R. J. Mandle, J. W. Goodby, *RSC Adv.* **2016**, *6*, 34885–34893.

[145] D. Chen, M. Nakata, R. Shao, M. R. Tuchband, M. Shuai, U. Baumeister, W. Weissflog, D. M. Walba, M. A. Glaser, J. E. Maclennan, N. A. Clark, *Phys. Rev. E* **2014**, *89*, 022506.

[146] S. P. Sreenilayam, V. P. Panov, J. K. Vij, G. Shanker, *Liq. Cryst.* **2016**, *44*, 244–253.

[147] K. Merkel, A. Kocot, J. K. Vij, G. Shanker, *Phys. Rev. E* **2018**, *98*, 022704.

[148] P. A. Henderson, C. T. Imrie, *Liq. Cryst.* **2011**, *38*, 1407–1414.

[149] C.-J. Yun, M. R. Vengatesan, J. K. Vij, J.-K. Song, *Applied Physics Letters* **2015**, *106*, 173102.

[150] K. Adlem, M. Čopič, G. R. Luckhurst, A. Mertelj, O. Parri, R. M. Richardson, B. D. Snow, B. A. Timimi, R. P. Tuffin, D. Wilkes, *Physical Review E* **2013**, *88*, 022503.

[151] S. Parthasarathi, D. S. S. Rao, N. B. Palakurthy, C. V. Yelamaggad, S. Krishna Prasad, *The Journal of Physical Chemistry B* **2016**, *120*, 5056–5062.

[152] R. Balachandran, V. P. Panov, J. K. Vij, A. Kocot, M. G. Tamba, A. Kohlmeier, G. H. Mehl, *Liquid Crystals* **2013**, *40*, 681–688.

[153] B. Robles-Hernández, N. Sebastián, M. R. de la Fuente, D. O. López, S. Diez-Berart, J. Salud, M. B. Ros, D. A. Dunmur, G. R. Luckhurst, B. A. Timimi, *Phys. Rev. E* **2015**, *92*, 062505.

[154] S. Parthasarathi, D. S. S. Rao, N. B. Palakurthy, C. V. Yelamaggad, S. Krishna Prasad, *J. Phys. Chem. B* **2016**, *120*, 5056–5062.

[155] G. Cukrov, Y. Mosaddeghian Golestani, J. Xiang, Yu. A. Nastishin, Z. Ahmed, C. Welch, G. H. Mehl, O. D. Lavrentovich, *Liq. Cryst.* **2016**, *44*, 219–231.

[156] C. Greco, G. R. Luckhurst, A. Ferrarini, *Soft Matter* **2014**, *10*, 9318–9323.

[157] D. A. Dunmur, M. R. de la Fuente, M. A. Perez Jubindo, S. Diez, *Liq. Cryst.* **2010**, *37*, 723–736.

[158] D. A. Dunmur, G. R. Luckhurst, M. R. de la Fuente, S. Diez, M. A. Peréz Jubindo, *J. Chem. Phys.* **2001**, *115*, 8681–8691.

[159] D. A. Dunmur, *Liq. Cryst.* **2005**, *32*, 1379–1387.

[160] N. Sebastián, M. R. de la Fuente, D. O. López, M. A. Pérez-Jubindo, J. Salud, S. Diez-Berart, M. B. Ros, *J. Phys. Chem. B* **2011**, *115*, 9766–9775.

[161] N. Sebastián, D. O. López, B. Robles-Hernández, M. R. de la Fuente, J. Salud, M. A. Pérez-Jubindo, D. A. Dunmur, G. R. Luckhurst, D. J. B. Jackson, *Phys. Chem. Chem. Phys.* **2014**, *16*, 21391–21406.

[162] N. Sebastián, B. Robles-Hernández, S. Diez-Berart, J. Salud, G. R. Luckhurst, D. A. Dunmur, D. O. López, M. R. de la Fuente, *Liq. Cryst.* **2017**, *44*, 177–190.

[163] M. Stocchero, A. Ferrarini, G. J. Moro, D. A. Dunmur, G. R. Luckhurst, *J. Chem. Phys.* **2004**, *121*, 8079.

[164] C. T. Archbold, R. J. Mandle, J. L. Andrews, S. J. Cowling, J. W. Goodby, *Liq. Cryst.* **2017**, 1–10.

[165] M. R. Tuchband, M. Shuai, K. A. Graber, D. Chen, L. Radzihovsky, A. Klittnick, L. Foley, A. Scarbrough, J. H. Porada, M. Moran, E. Korblova, D. M. Walba, M. A. Glaser, J. E. Maclennan, N. A. Clark, *arXiv:1511.07523 [cond-mat.soft]* **2015**.

[166] D. A. Paterson, M. Gao, Y.-K. Kim, A. Jamali, K. L. Finley, B. Robles-Hernández, S. Diez-Berart, J. Salud, M. R. de la Fuente, B. A. Timimi, H. Zimmermann, C. Greco, A. Ferrarini, J. M. D. Storey, D. O. López, O. D. Lavrentovich, G. R. Luckhurst, C. T. Imrie, *Soft Matter* **2016**, *12*, 6827–6840.

[167] V. P. Panov, J. K. Vij, G. H. Mehl, *Liq. Cryst.* **2017**, *44*, 147–159.

[168] D. O. López, J. Salud, M. R. de la Fuente, N. Sebastián, S. Diez-Berart, *Phys. Rev. E* **2018**, *97*, 012704.

[169] K. Merkel, A. Kocot, C. Welch, G. H. Mehl, *Phys. Chem. Chem. Phys.* **2019**, *21*, 22839–22848.

[170] K. Merkel, C. Welch, Z. Ahmed, W. Piecek, G. H. Mehl, *J. Chem. Phys.* **2019**, *151*, 114908.

[171] A. Knežević, I. Dokli, M. Sapunar, S. Šegota, U. Baumeister, A. Lesac, *Beilstein J. Nanotechnol.* **2018**, *9*, 1297–1307.

[172] V. P. Panov, S. P. Sreenilayam, Y. P. Panarin, J. K. Vij, C. J. Welch, G. H. Mehl, *Nano Lett.* **2017**, *17*, 7515–7519.

[173] T. Sergan, I. Dozov, V. Sergan, R. Voss, *Phys. Rev. E* **2017**, *95*, 052706.

[174] M. Brun, A. Lallemand, J.-F. Quinson, C. Eyraud, *Thermochim. Acta* **1977**, *21*, 59–88.

[175] J. Mitchell, J. Webber, J. Strange, *Phys. Rep.* **2008**, *461*, 1–36.

[176] G. Rohman, D. Grande, F. Lauprêtre, S. Boileau, P. Guérin, *Macromolecules* **2005**, *38*, 7274–7285.

[177] Y. Hu, S. R. Winn, I. Krajbich, J. O. Hollinger, *J. Biomed. Mater. Res.* **2003**, *64A*, 583–590.

[178] I. N. Savina, V. M. Gun'ko, V. V. Turov, M. Dainiak, G. J. Phillips, I. Yu. Galaev, S. V. Mikhalovsky, *Soft Matter* **2011**, *7*, 4276.

[179] J. P. Butler, R. W. Mair, D. Hoffmann, M. I. Hrovat, R. A. Rogers, G. P. Topulos, R. L. Walsworth, S. Patz, *J. Phys. Condens. Matter* **2002**, *14*, L297–L304.

[180] E. Kizilkan, J. Strueben, X. Jin, C. F. Schaber, R. Adelung, A. Staubitz, S. N. Gorb, *R. Soc. Open Sci.* **2016**, *3*, 150700.

[181] C. Meyer, G. R. Luckhurst, I. Dozov, *J. Mater. Chem. C* **2015**, *3*, 318–328.

[182] C. V. Rajaram, S. D. Hudson, L. C. Chien, *Chem. Mater.* **1995**, *7*, 2300–2308.

[183] I. Dierking, L. L. Kosbar, A. C. Lowe, G. A. Held, *Liq. Cryst.* **1998**, *24*, 387–395.

[184] C.-J. Hsu, Z.-H. Gu, C.-C. Wu, C.-Y. Huang, *Liq. Cryst.* **2019**, *46*, 560–569.

[185] T. Nakata, T. Gotoh, M. Satoh, E. Hasegawa, *Mol. Cryst. Liq. Cryst. Sci. Tech. Mol. Cryst. Liq. Cryst.* **1997**, *299*, 389–394.

[186] F. Liu, H. Cao, Q. Mao, P. Song, H. Yang, *Liq. Cryst.* **2012**, *39*, 419–424.

[187] S. H. Kim, L.-C. Chien, *Jpn. J. Appl. Phys.* **2004**, *43*, 7643–7647.

[188] K. Kang, L. C. Chien, S. Sprunt, *Liq. Cryst.* **2002**, *29*, 9–18.

[189] I. Dierking, L. L. Kosbar, A. Afzali-Ardakani, A. C. Lowe, G. A. Held, *Appl. Phys. Lett.* **1997**, *71*, 2454–2456.

[190] B. Kim, *Polymer* **2000**, *41*, 1325–1335.

[191] R. Basu, A. Garvey, D. Kinnamon, *J. Appl. Phys.* **2015**, *117*, 074301.

[192] A. Eremin, A. Jákli, *Soft Matter* **2013**, *9*, 615–637.

[193] R. B. Meyer, *Mol. Cryst. Liq. Cryst.* **1977**, *40*, 33–48.

[194] R. G. Petschek, K. M. Wiefling, *Phys. Rev. Lett.* **1987**, *59*, 343–346.

[195] P. Palffy-Muhoray, M. A. Lee, R. G. Petschek, *Phys. Rev. Lett.* **1988**, *60*, 2303–2306.

[196] R. H. Tredgold, *J. Phys. D* **1990**, *23*, 119–120.

[197] F. Tournilhac, L. M. Blinov, J. Simon, S. V. Yablonsky, *Nature* **1992**, *359*, 621–623.

[198] J. Lee, S.-D. Lee, *Mol. Cryst. Liq. Cryst. Sci. Tech. Mol. Cryst. Liq. Cryst.* **1994**, *254*, 395–403.

[199] F. Biscarini, C. Zannoni, C. Chiccoli, P. Pasini, *Mol. Phys.* **1991**, *73*, 439–461.

[200] J. Watanabe, Y. Nakata, K. Simizu, *J. Phys. II France* **1994**, *4*, 581–588.

[201] P. E. Cladis, H. R. Brand, *Liq. Cryst.* **1993**, *14*, 1327–1349.

[202] Y. Matsunaga, S. Miyamoto, *Mol. Cryst. Liq. Cryst. Sci. Tech. Mol. Cryst. Liq. Cryst.* **1993**, *237*, 311–317.

[203] T. Akutagawa, Y. Matsunaga, K. Yasuhara, *Liq. Cryst.* **1994**, *17*, 659–666.

[204] E. M. Terentjev, M. A. Osipov, T. J. Sluckin, *J. Phys. A* **1994**, *27*, 7047–7059.

[205] A. Jakli, A. Saupe, *Liq. Cryst.* **1997**, *22*, 309–316.

[206] B. Park, Y. Kinoshita, H. Takezoe, J. Watanabe, *Jpn. J. Appl. Phys.* **1998**, *37*, L136–L138.

[207] H. Takezoe, J. Watanabe, *Mol. Cryst. Liq. Cryst. Sci. Tech. Mol. Cryst. Liq. Cryst.* **1999**, *328*, 325–332.

[208] J. Watanabe, Y. Hirose, M. Tokita, T. Watanabe, S. Miyata, *Macromolecules* **1998**, *31*, 5937–5939.

[209] H. R. Brand, P. E. Cladis, H. Pleiner, *Macromolecules* **1992**, *25*, 7223–7226.

[210] J. C. Jones, M. J. Towler, J. R. Hughes, *Displays* **1993**, *14*, 86–93.

[211] Y. Ma, A. M. W. Tam, X. T. Gan, L. Y. Shi, A. K. Srivastava, V. G. Chigrinov, H. S. Kwok, J. L. Zhao, *Opt. Express* **2019**, *27*, 10079.

[212] S. J. Elston, *J. Mod. Opt.* **1995**, *42*, 19–56.

[213] J. W. Goodby, T. M. Leslie, *Mol. Cryst. Liq. Cryst.* **1984**, *110*, 175–203.

[214] D. M. Walba, *Science* **1995**, *270*, 250–250.

[215] T. Niori, T. Sekine, J. Watanabe, T. Furukawa, H. Takezoe, *J. Mater. Chem.* **1996**, *6*, 1231.

[216] A. Eremin, S. Diele, G. Pelzl, H. Nádasi, W. Weissflog, J. Salfetnikova, H. Kresse, *Phys. Rev. E* **2001**, *64*, 051707.

[217] D. Pociecha, M. Čepič, E. Gorecka, J. Mieczkowski, *Phys. Rev. Lett.* **2003**, *91*, 185501.

[218] Y. Shimbo, E. Gorecka, D. Pociecha, F. Araoka, M. Goto, Y. Takanishi, K. Ishikawa, J. Mieczkowski, K. Gomola, H. Takezoe, *Phys. Rev. Lett.* **2006**, *97*, 113901.

[219] R. A. Reddy, C. Zhu, R. Shao, E. Korblova, T. Gong, Y. Shen, E. Garcia, M. A. Glaser, J. E. Maclennan, D. M. Walba, N. A. Clark, *Science* **2011**, *332*, 72–77.

[220] H. Takezoe, Y. Takanishi, *Jpn. J. Appl. Phys.* **2006**, *45*, 597–625.

[221] C. Zhu, R. Shao, R. A. Reddy, D. Chen, Y. Shen, T. Gong, M. A. Glaser, E. Korblova, P. Rudquist, J. E. Maclennan, D. M. Walba, N. A. Clark, *J. Am. Chem. Soc.* **2012**, *134*, 9681–9687.

[222] D. R. Link, *Science* **1997**, *278*, 1924–1927.

[223] L. Bergquist, C. Zhang, R. R. Ribeiro de Almeida, B. Pellegrene, M. Salamonczyk, M. Kim, J.-I. Hwang, K.-J. Kim, J.-H. Lee, A. Jákli, T. Hegmann, *ChemistryOpen* **2017**, *6*, 196–200.

[224] S. P. Sreenilayam, Y. P. Panarin, J. K. Vij, V. P. Panov, A. Lehmann, M. Poppe, M. Prehm, C. Tschierske, *Nat. Commun.* **2016**, *7*, 11369.

[225] L. E. Hough, H. T. Jung, D. Krüerke, M. S. Heberling, M. Nakata, C. D. Jones, D. Chen, D. R. Link, J. Zasadzinski, G. Heppke, J. P. Rabe, W. Stocker, E. Körblova, D. M. Walba, M. A. Glaser, N. A. Clark, *Science* **2009**, *325*, 456–460.

[226] Z. Li, P. Salamon, A. Jakli, K. Wang, C. Qin, Q. Yang, C. Liu, J. Wen, *Liq. Cryst.* **2010**, *37*, 427–433.

[227] M. Poppe, M. Alaasar, A. Lehmann, S. Poppe, M.-G. Tamba, M. Kurachkina, A. Eremin, M. Nagaraj, J. K. Vij, X. Cai, F. Liu, C. Tschierske, *J. Mater. Chem. C* **2020**, 10.1039.C9TC06456G.

[228] B. K. Sadashiva, R. Amaranatha Reddy, R. Pratibha, N. V. Madhusudana, *J. Mater. Chem.* **2002**, *12*, 943–950.

[229] K. Gomola, L. Guo, E. Gorecka, D. Pociecha, J. Mieczkowski, K. Ishikawa, H. Takezoe, *ChemComm* **2009**, 6592.

[230] Y. Jang, V. P. Panov, A. Kocot, J. K. Vij, A. Lehmann, C. Tschierske, *Appl. Phys. Lett.* **2009**, *95*, 183304.

[231] Y. P. Panarin, M. Nagaraj, J. K. Vij, C. Keith, C. Tschierske, *EPL* **2010**, *92*, 26002.

[232] H. Yoon, S.-W. Kang, M. Lehmann, J. O. Park, M. Srinivasarao, S. Kumar, *Soft Matter* **2011**, *7*, 8770.

[233] Y.-K. Kim, B. Senyuk, S.-T. Shin, A. Kohlmeier, G. H. Mehl, O. D. Lavrentovich, *Soft Matter* **2014**, *10*, 500–509.

[234] E. Korblova, E. Guzman, J. Maclennan, M. Glaser, R. Shao, E. Garcia, Y. Shen, R. Visvanathan, N. Clark, D. Walba, *Materials* **2017**, *10*, 1284.

[235] L. Guo, S. Dhara, B. K. Sadashiva, S. Radhika, R. Pratibha, Y. Shimbo, F. Araoka, K. Ishikawa, H. Takezoe, *Phys. Rev. E* **2010**, *81*, 011703.

[236] L. Guo, E. Gorecka, D. Pociecha, N. Vaupotič, M. Čepič, R. A. Reddy, K. Gornik, F. Araoka, N. A. Clark, D. M. Walba, K. Ishikawa, H. Takezoe, *Phys. Rev. E* **2011**, *84*, 031706.

[237] R. A. Reddy, B. K. Sadashiva, *J. Mater. Chem.* **2004**, *14*, 310.

[238] F. Gouda, K. Skarp, S. T. Lagerwall, *Ferroelectrics* **1991**, *113*, 165–206.

[239] A. Levstik, T. Carlsson, C. Filipic, I. Levstik, B. Zeks, *Phys. Rev. A* **1987**, *35*, 3527–3534.

[240] T. Carlsson, B. Žekš, C. Filipič, A. Levstik, *Phys. Rev. A* **1990**, *42*, 877–889.

[241] S. U. Vallerien, F. Kremer, H. Kapitza, R. Zentel, W. Frank, *Phys. Lett. A* **1989**, *138*, 219–222.

Appendix I:

DSC curves

Pure materials

CB7CB: second heating/cooling cycles

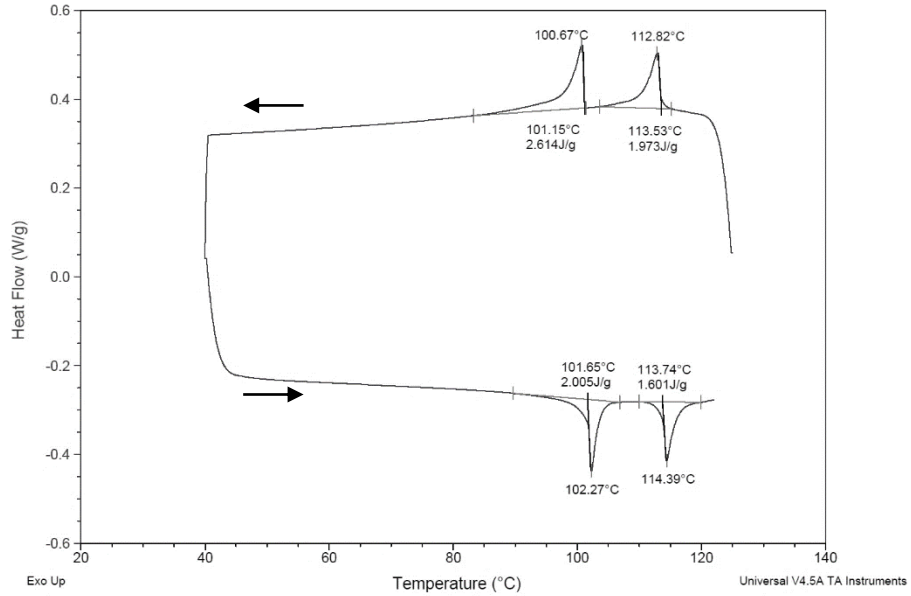

5CB: second cooling cycle

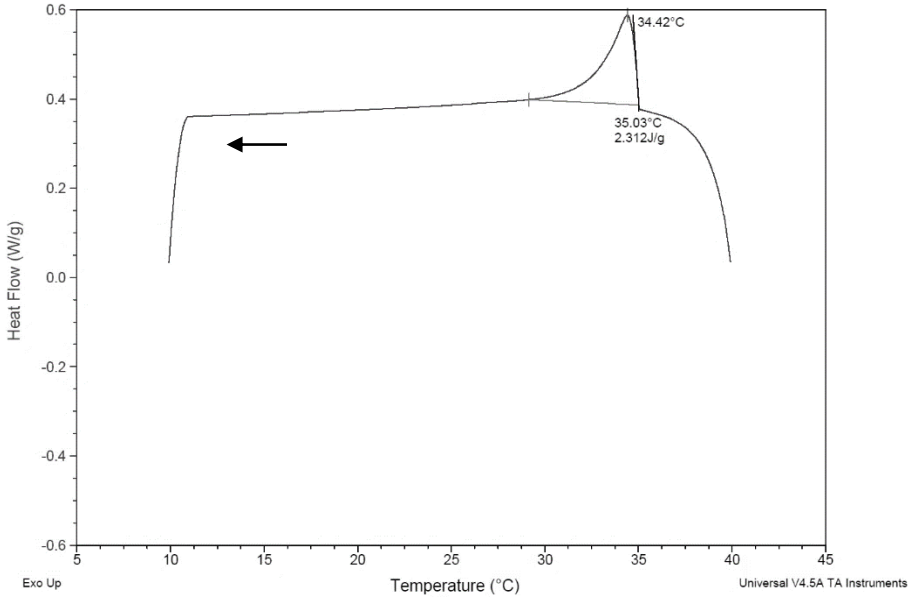

8CB: second heating/cooling cycles

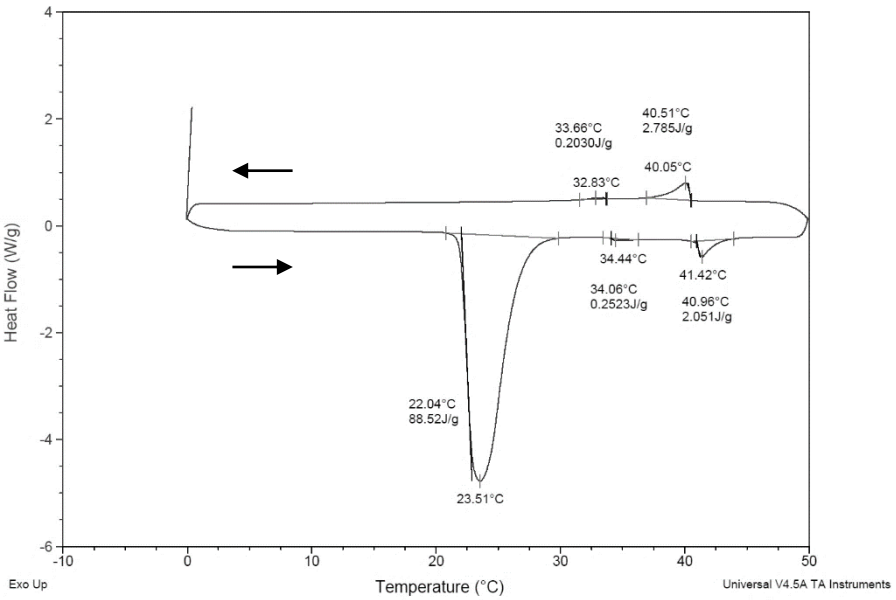

Mixtures

M10: second heating/cooling cycles

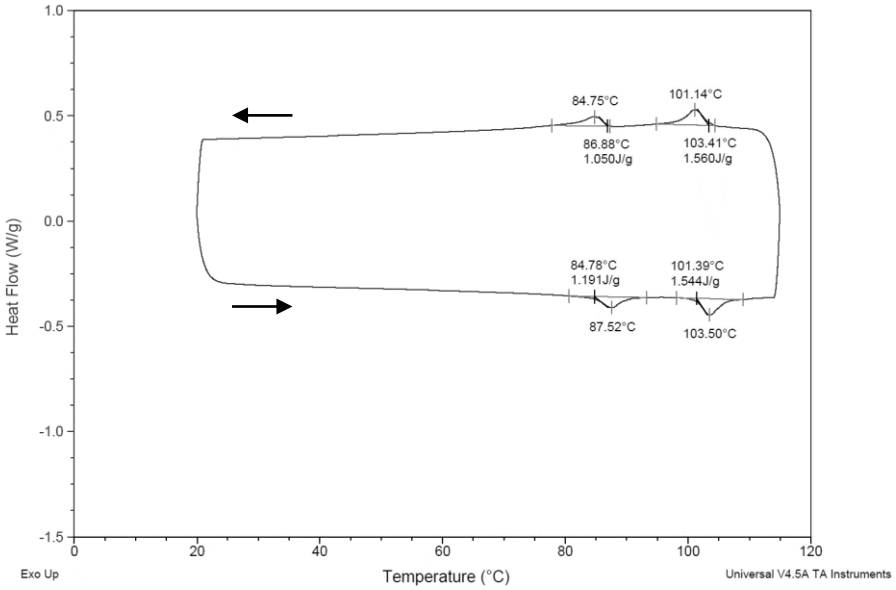

M40: second heating/cooling cycles

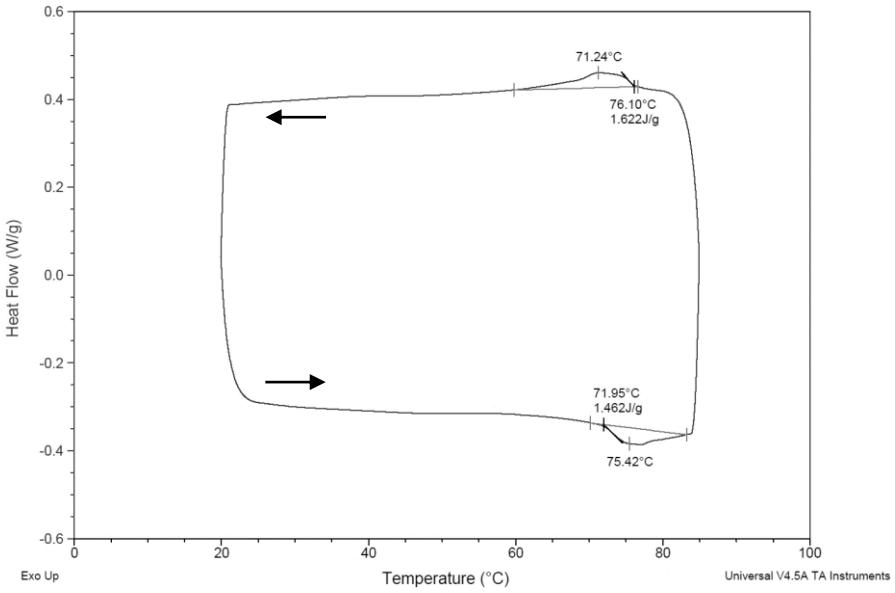

PM20 – polymerised: second heating/cooling cycles

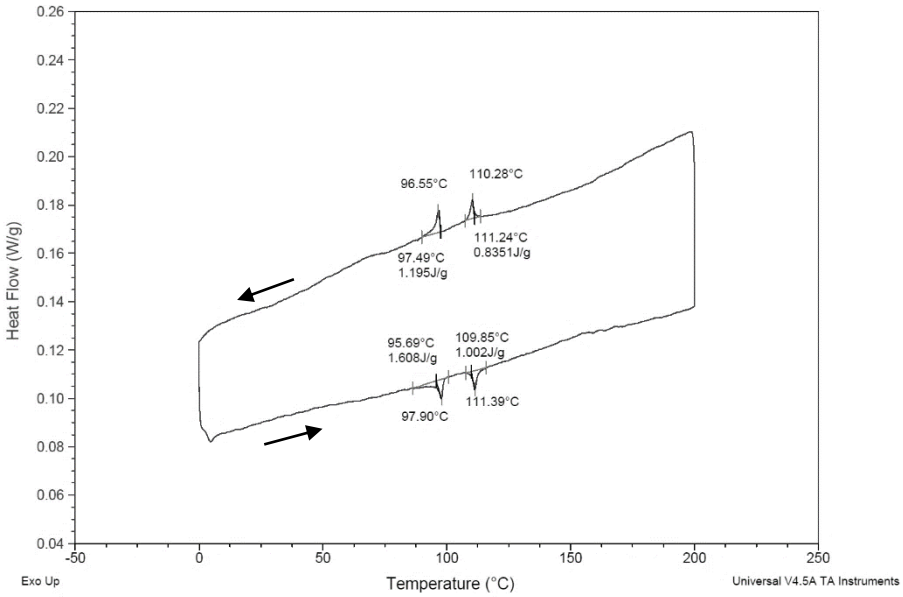

8CB-RM-10 – polymerised: second heating/cooling cycles

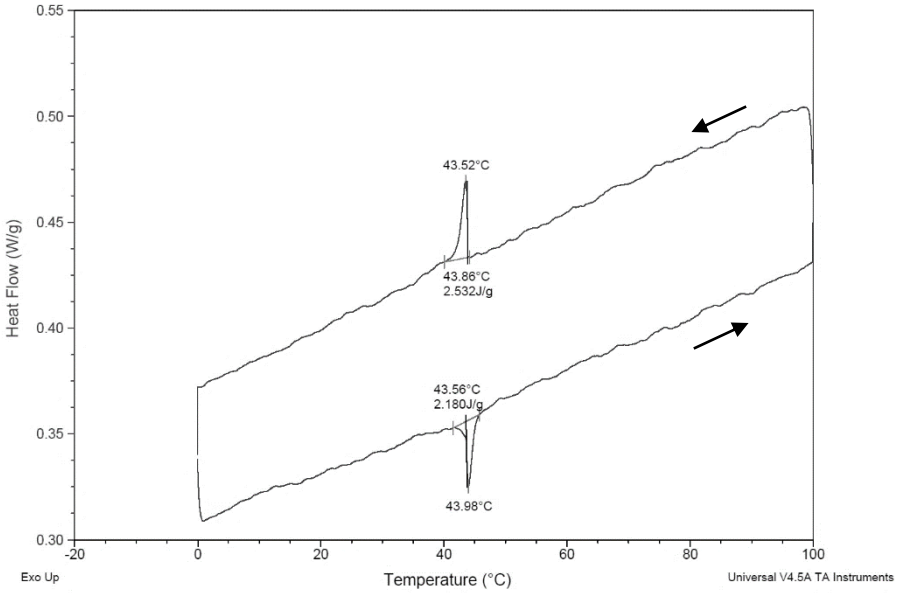

NT12-10: second heating/cooling cycles

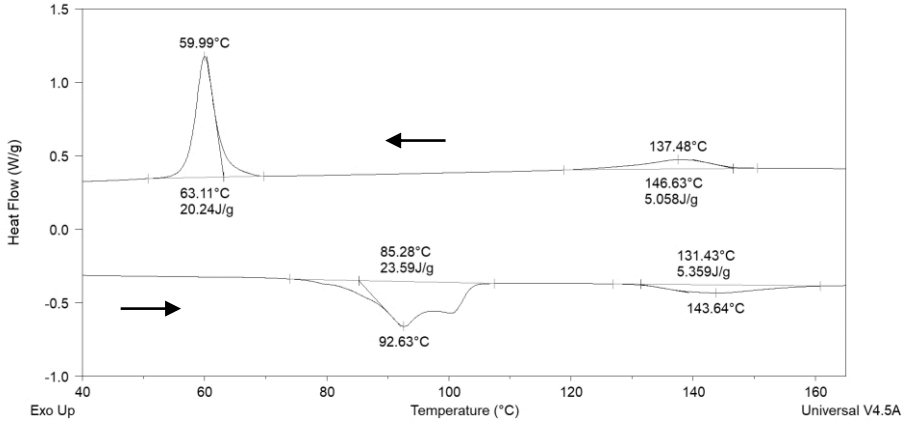

NT12-20: second heating/cooling cycles

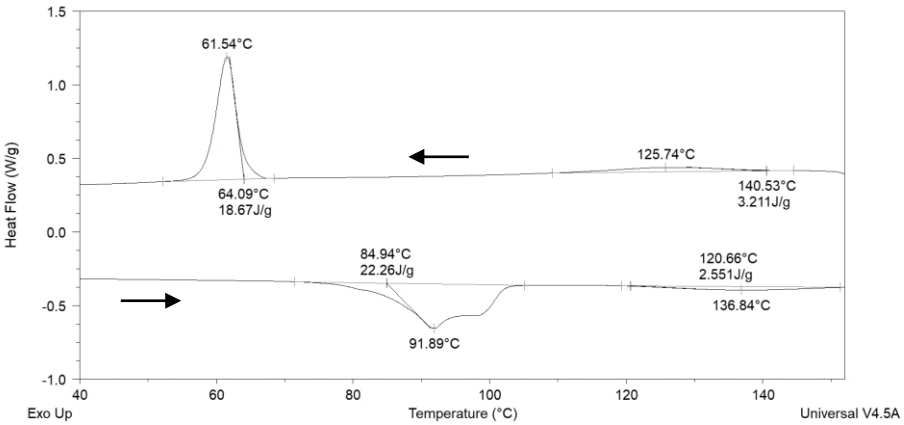

Appendix II:

Spectroscopic data

NMR spectra

NT01:

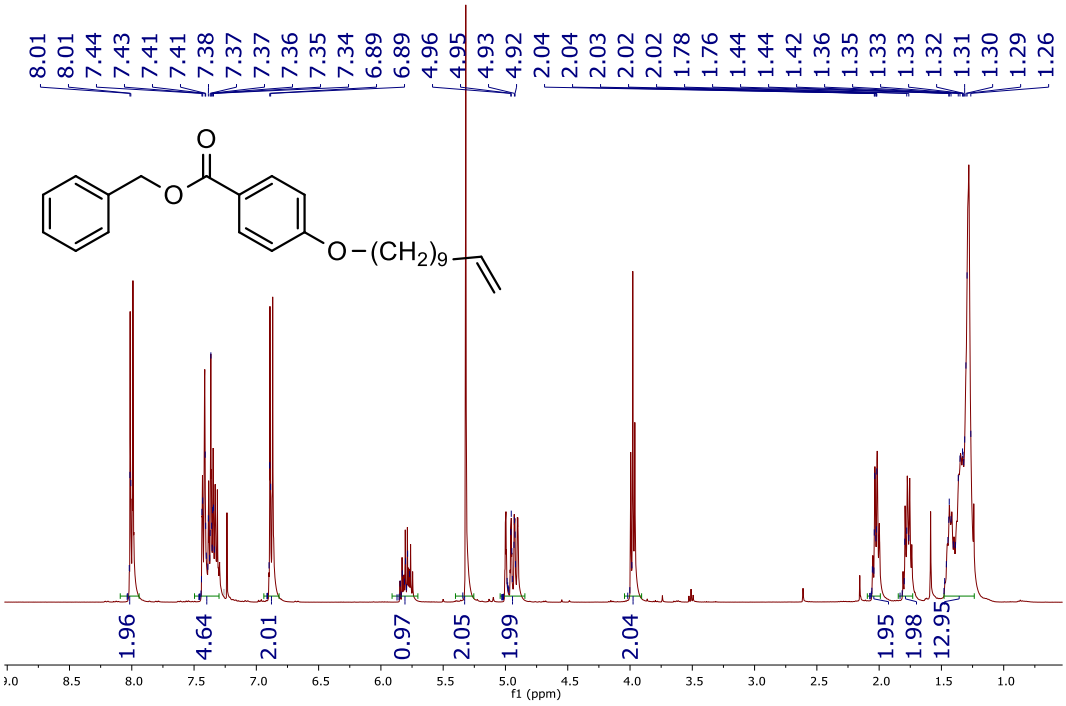

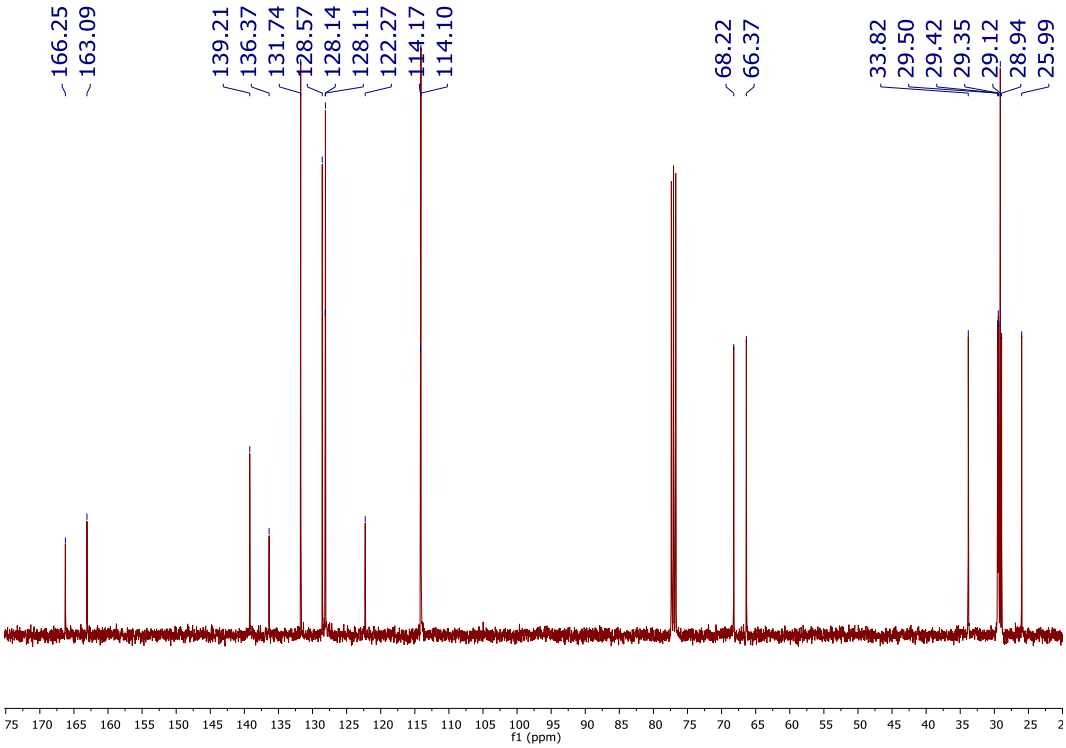

NT02:

Si
Si
Cl

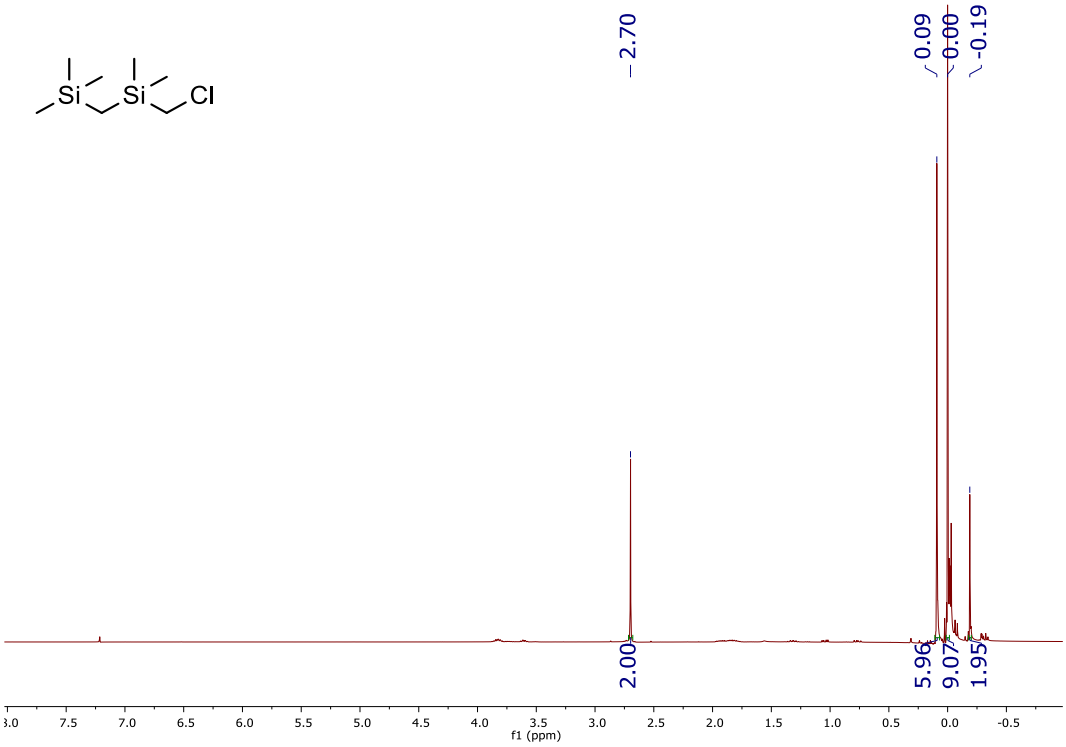
2.70
0.09
0.00
-0.19
2.00
5.96
9.07
1.95
f1 (ppm)

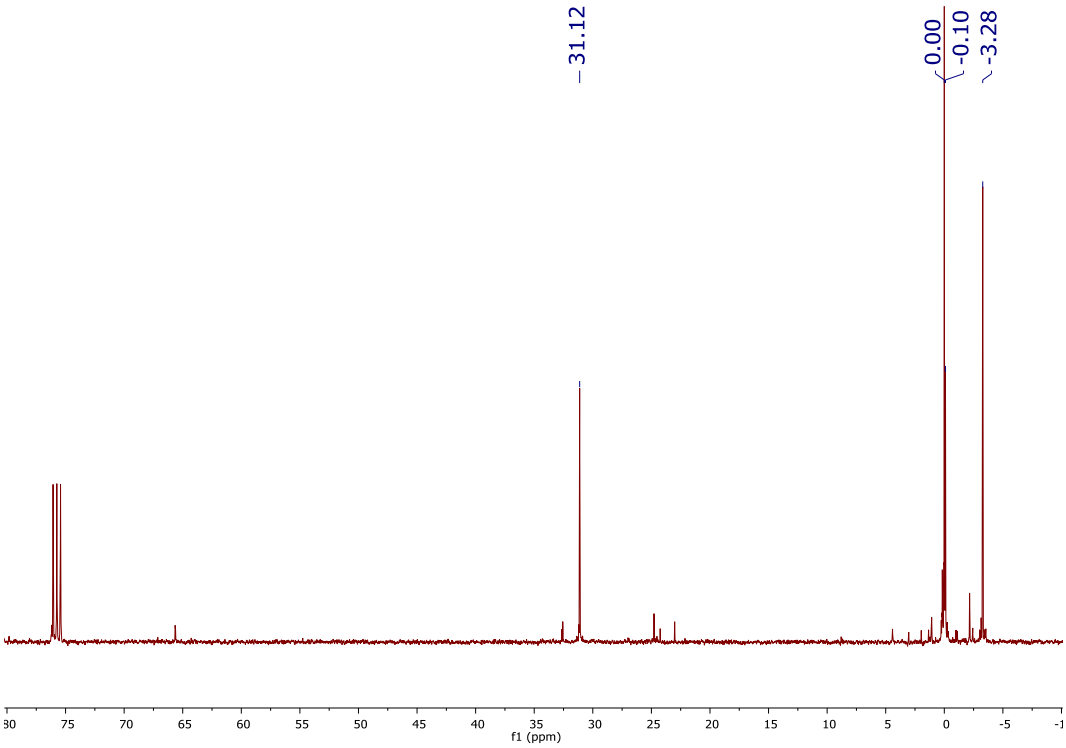
31.12
0.00
-0.10
-3.28
f1 (ppm)

NT03:

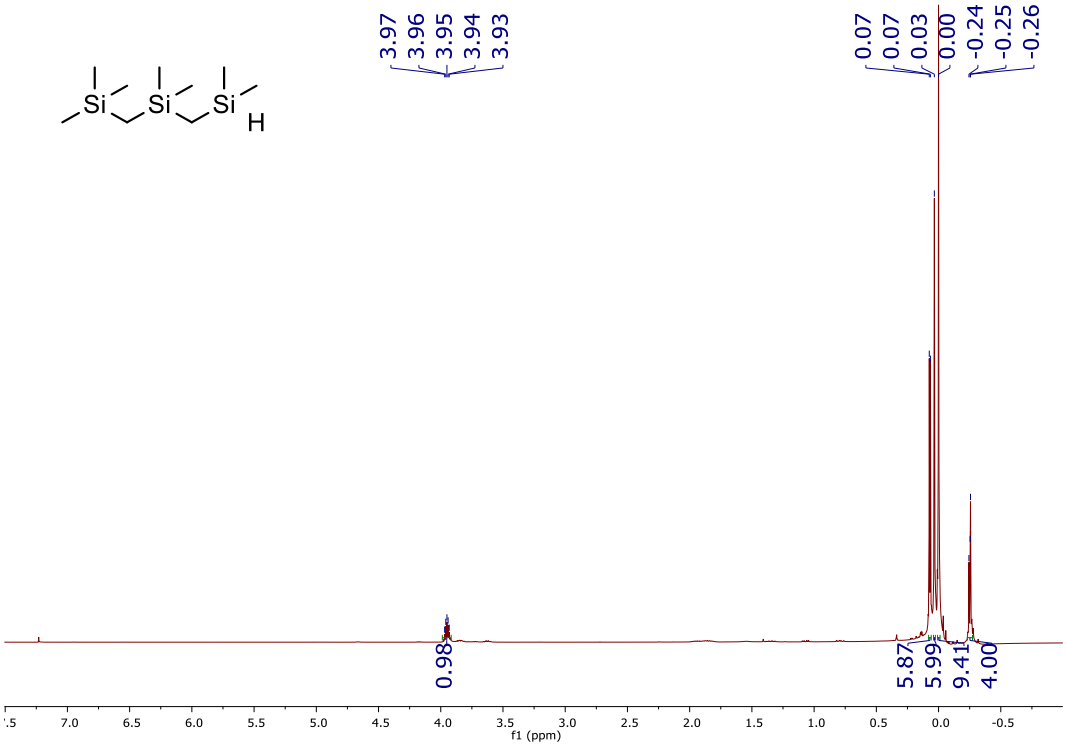
Si
Si
Si
H
3.97
3.96
3.95
3.94
3.93
0.07
0.07
0.03
0.00
-0.24
-0.25
-0.26
0.98
5.87
5.99
9.41
4.00
f1 (ppm)

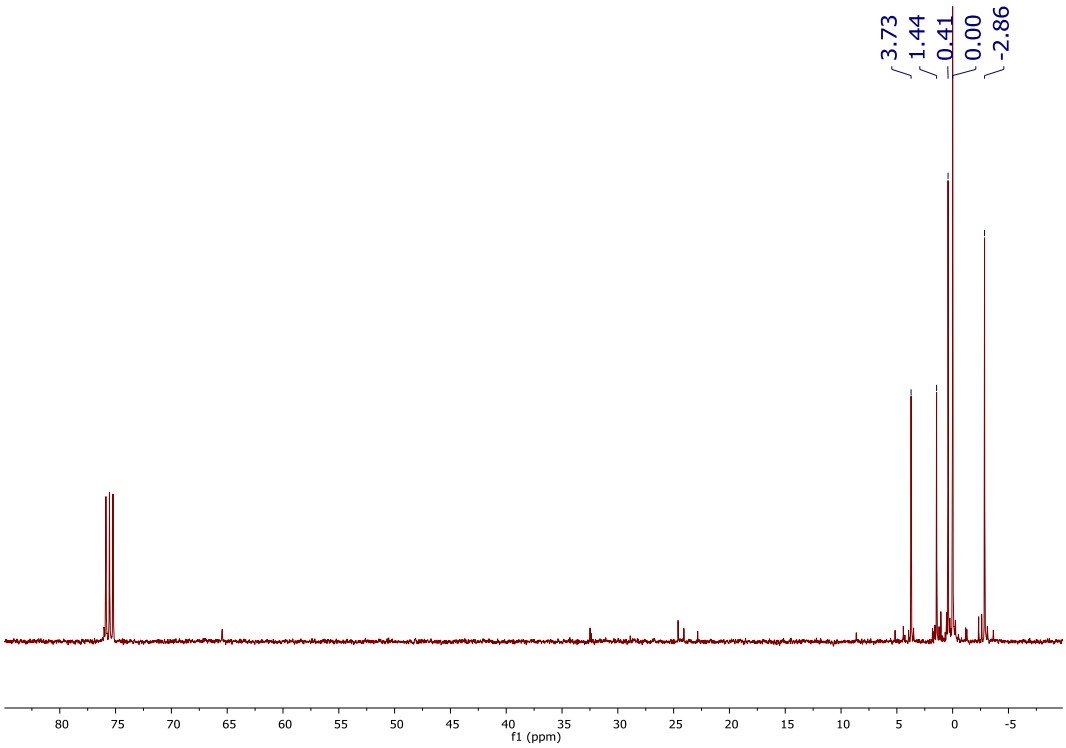
3.73
1.44
0.41
0.00
-2.86
f1 (ppm)

NT04:

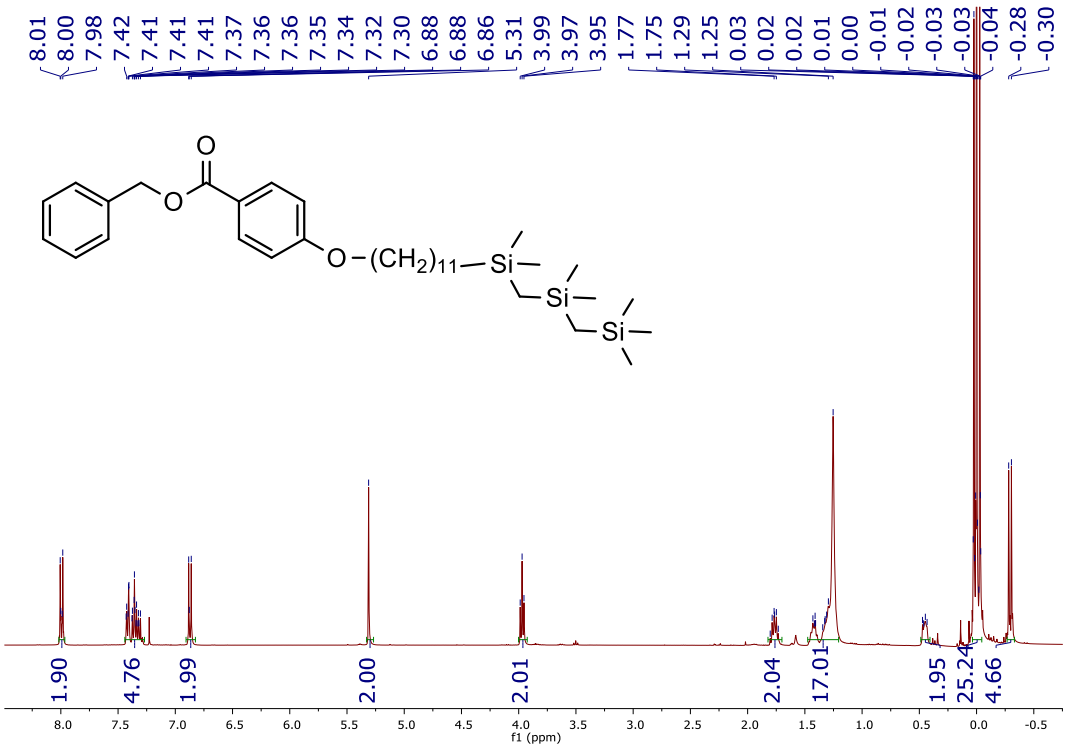
8.01 8.00 7.98 7.42 7.41 7.41 7.41 7.37 7.36 7.36 7.35 7.34 7.32 7.30 6.88 6.88 6.86 5.31 3.99 3.97 3.95 1.77 1.75 1.29 1.25 0.03 0.02 0.02 0.01 0.00 -0.01 -0.02 -0.03 -0.03 -0.04 -0.28 -0.30
O
O
O−(CH2)11−Si
Si
Si
1.90 4.76 1.99 2.00 2.01 2.04 17.01 1.95 25.24 4.66
8.0 7.5 7.0 6.5 6.0 5.5 5.0 4.5 4.0 3.5 3.0 2.5 2.0 1.5 1.0 0.5 0.0 -0.5
f1 (ppm)

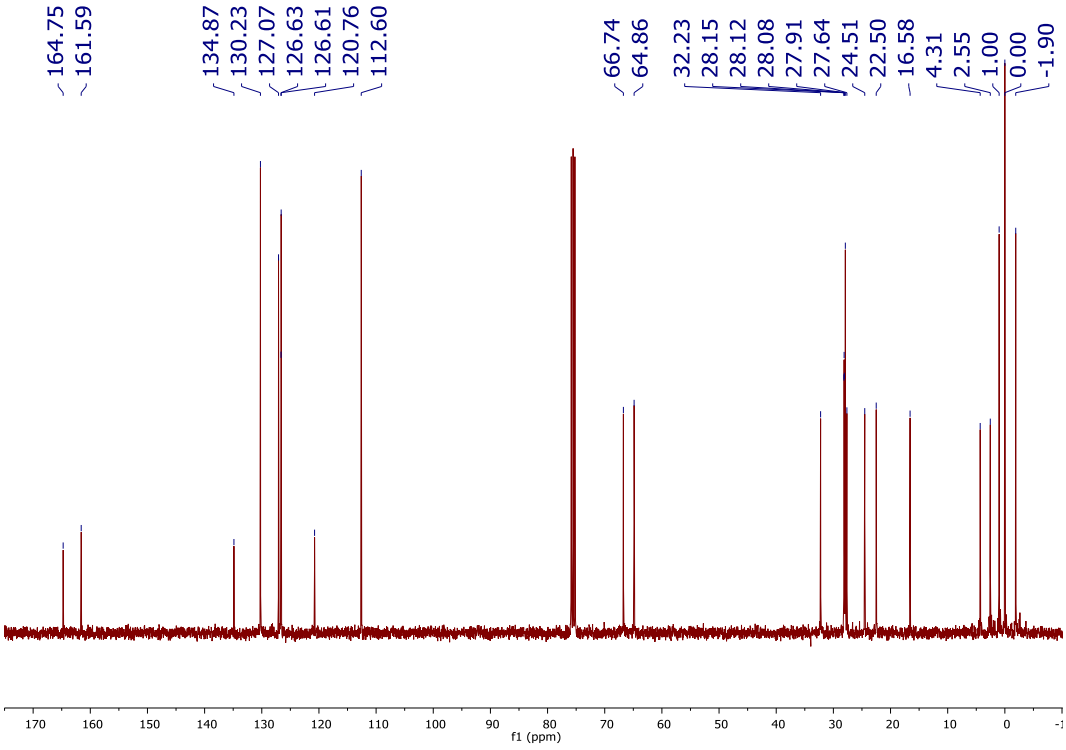
164.75 161.59 134.87 130.23 127.07 126.63 126.61 120.76 112.60 66.74 64.86 32.23 28.15 28.12 28.08 27.91 27.64 24.51 22.50 16.58 4.31 2.55 1.00 0.00 -1.90
170 160 150 140 130 120 110 100 90 80 70 60 50 40 30 20 10 0
f1 (ppm)

NT05:

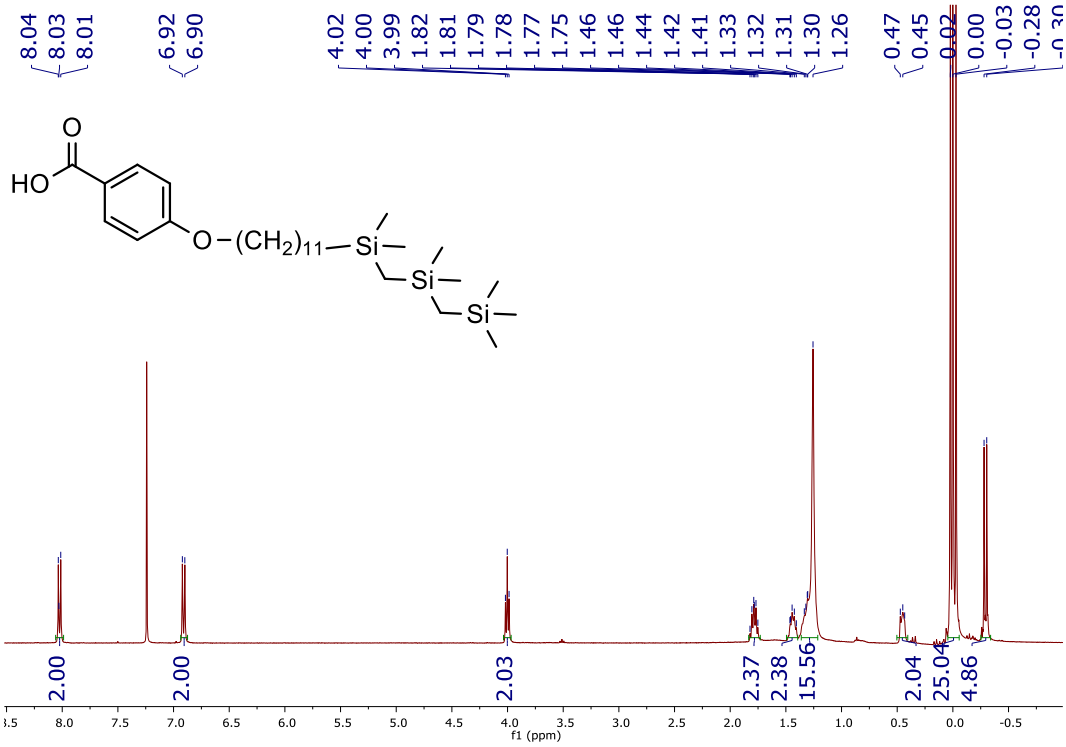
8.04
8.03
8.01
6.92
6.90
4.02
4.00
3.99
1.82
1.81
1.79
1.78
1.77
1.75
1.46
1.46
1.44
1.42
1.41
1.33
1.32
1.31
1.30
1.26
0.47
0.45
0.02
0.00
-0.03
-0.28
HO
O
O−(CH2)11−Si
Si
Si
2.00
2.00
2.03
2.37
2.38
15.56
2.04
25.04
4.86
f1 (ppm)

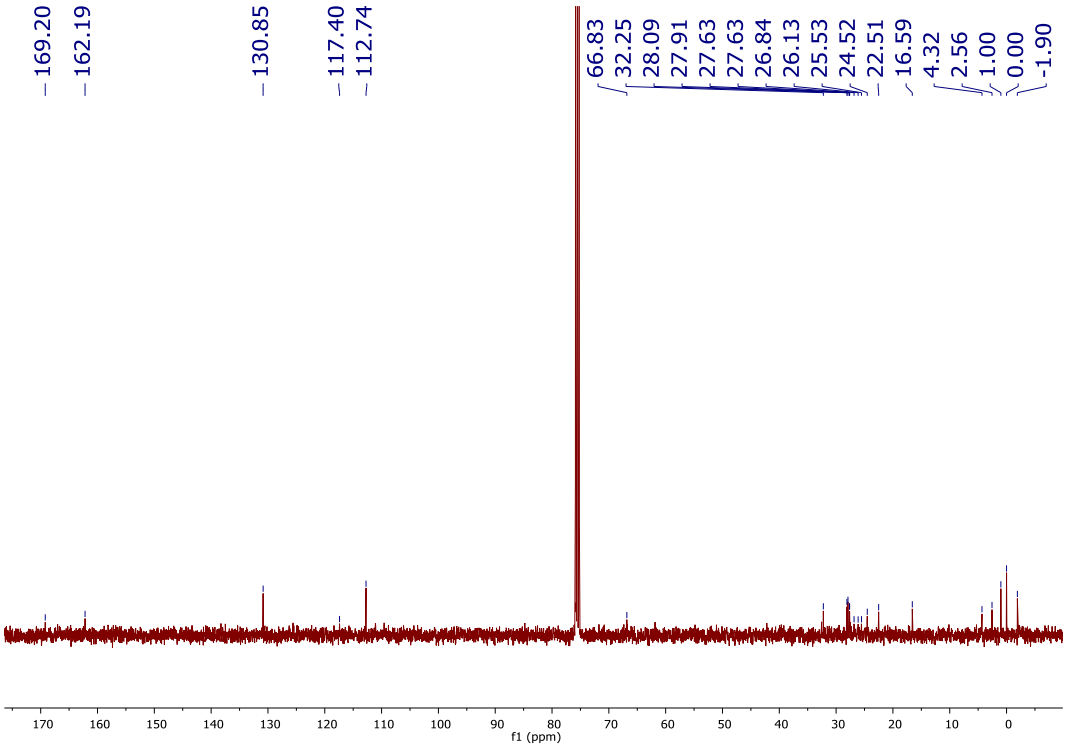
169.20
162.19
130.85
117.40
112.74
66.83
32.25
28.09
27.91
27.63
27.63
26.84
26.13
25.53
24.52
22.51
16.59
4.32
2.56
1.00
0.00
-1.90
f1 (ppm)

NT06:

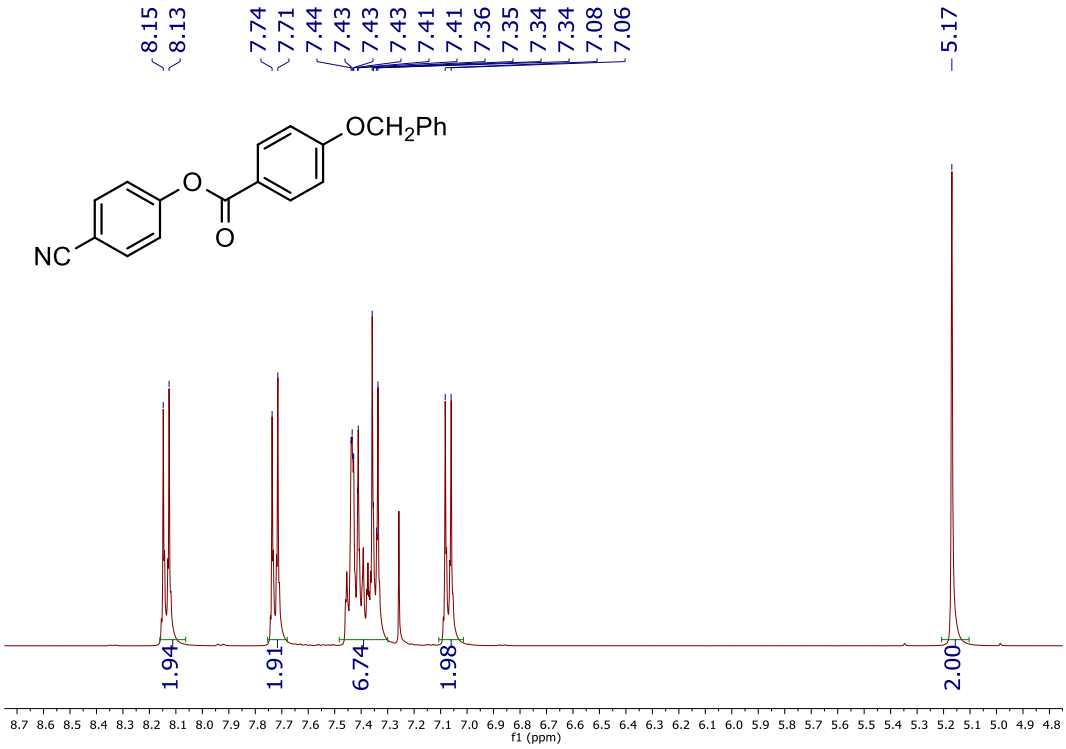
8.15
8.13
7.74
7.71
7.44
7.43
7.43
7.43
7.41
7.41
7.36
7.35
7.34
7.34
7.08
7.06
5.17
OCH2Ph
O
O
NC
1.94
1.91
6.74
1.98
2.00
f1 (ppm)

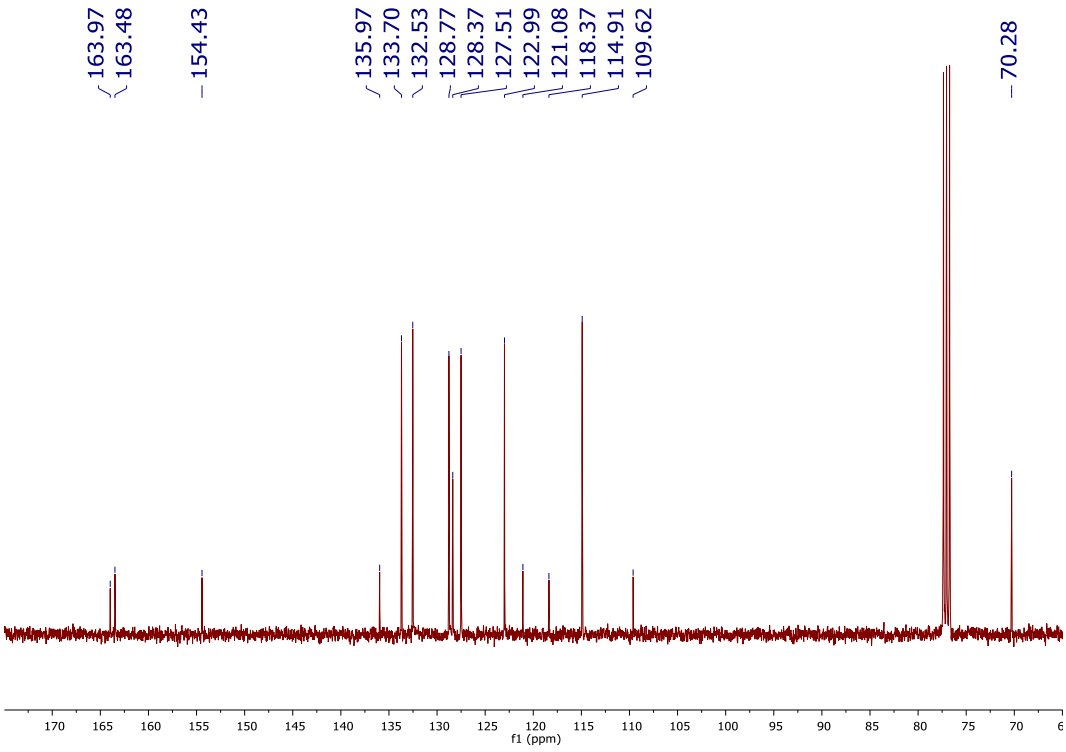
163.97
163.48
154.43
135.97
133.70
132.53
128.77
128.37
127.51
122.99
121.08
118.37
114.91
109.62
70.28
f1 (ppm)

NT07:

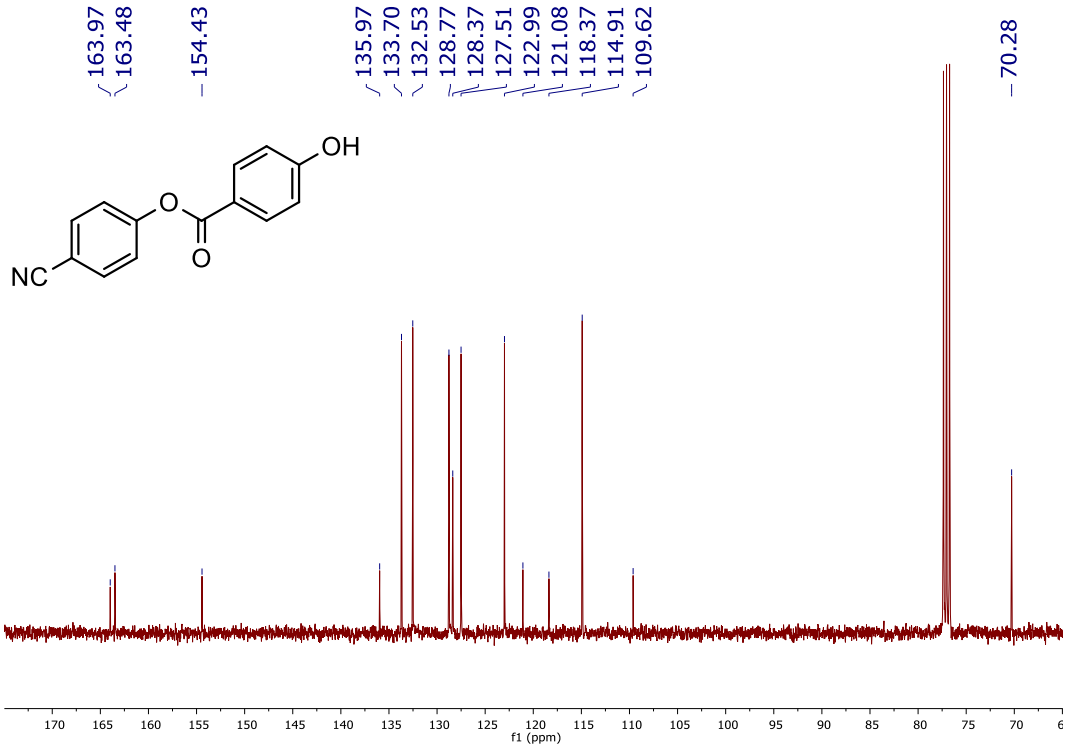
163.97
163.48
154.43
135.97
133.70
132.53
128.77
128.37
127.51
122.99
121.08
118.37
114.91
109.62
70.28
OH
O
O
NC
170 165 160 155 150 145 140 135 130 125 120 115 110 105 100 95 90 85 80 75 70
f1 (ppm)

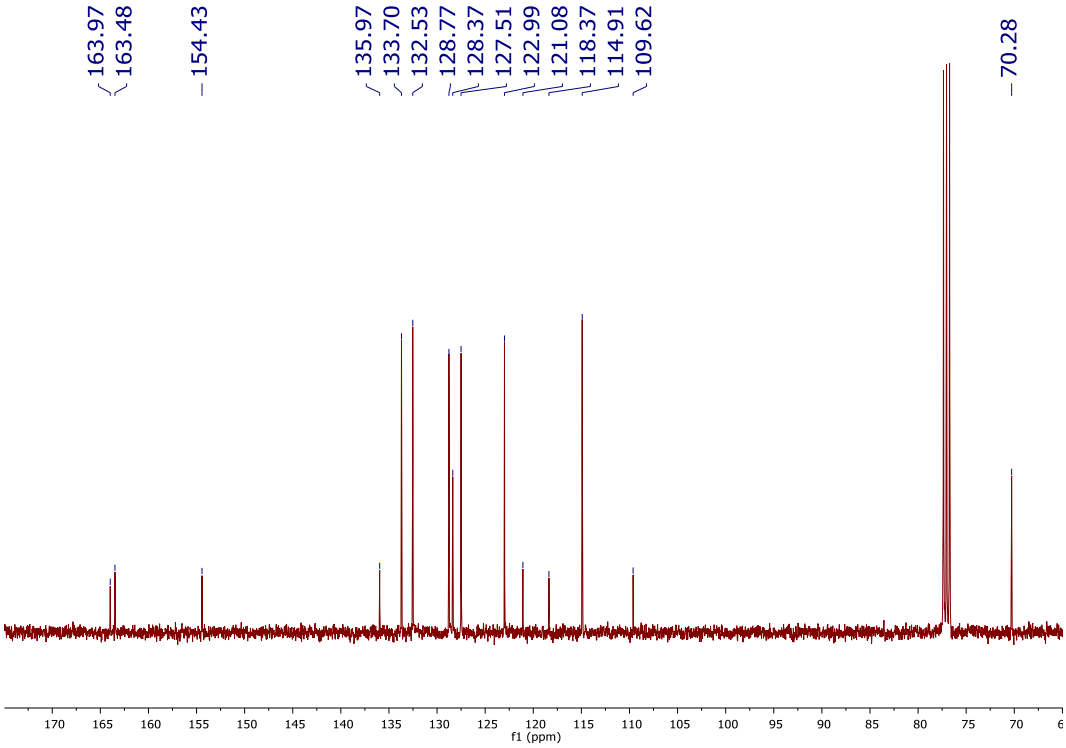
163.97
163.48
154.43
135.97
133.70
132.53
128.77
128.37
127.51
122.99
121.08
118.37
114.91
109.62
70.28
170 165 160 155 150 145 140 135 130 125 120 115 110 105 100 95 90 85 80 75 70
f1 (ppm)

NT08:

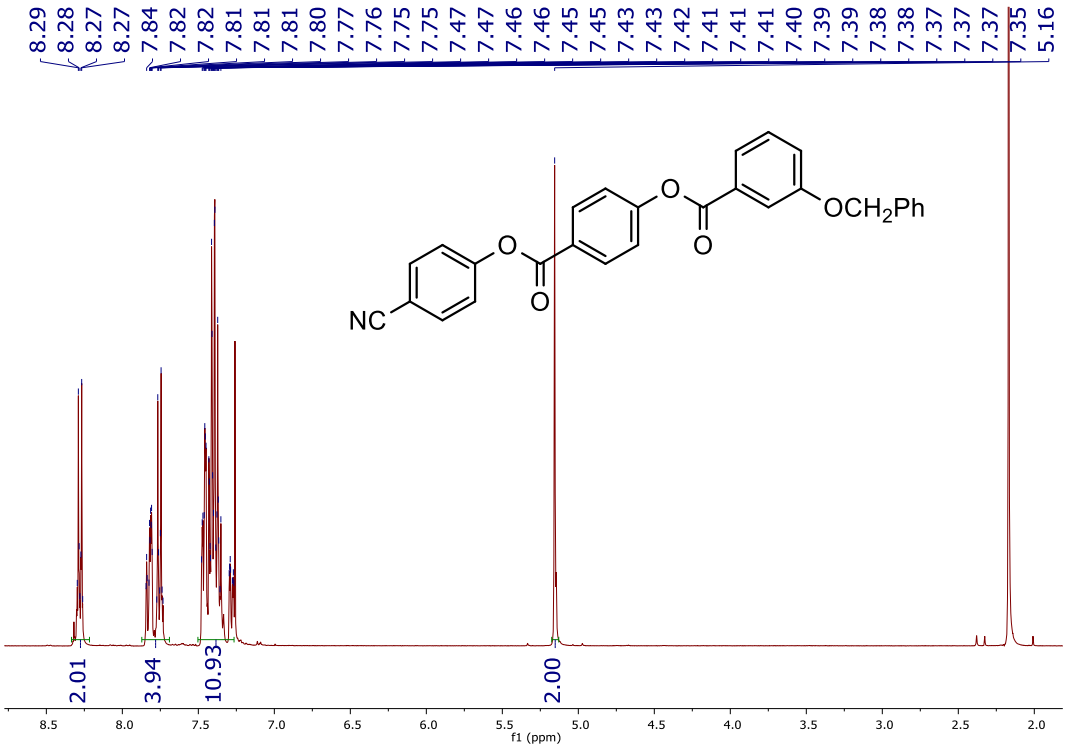
8.29
8.28
8.27
8.27
7.84
7.82
7.82
7.81
7.81
7.81
7.80
7.77
7.76
7.75
7.75
7.47
7.47
7.46
7.46
7.45
7.45
7.43
7.43
7.42
7.41
7.41
7.41
7.40
7.39
7.39
7.38
7.38
7.37
7.37
7.37
7.35
5.16
O
O
O
O
OCH2Ph
NC
2.01
3.94
10.93
2.00
f1 (ppm)

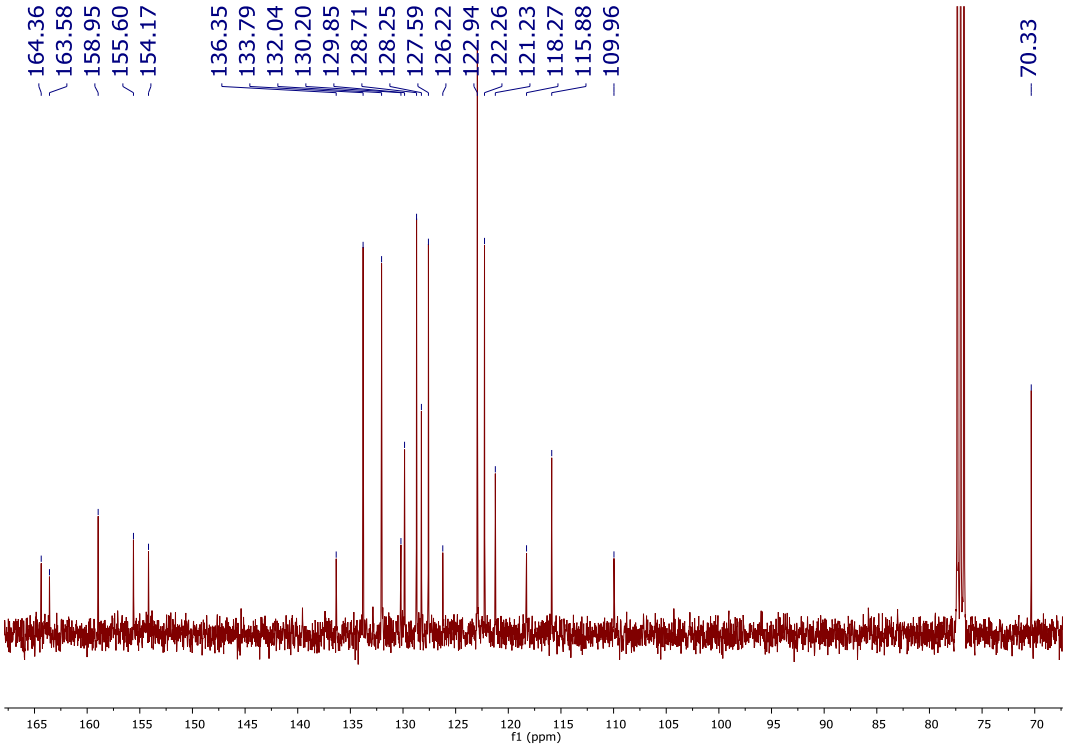
164.36
163.58
158.95
155.60
154.17
136.35
133.79
132.04
130.20
129.85
128.71
128.25
127.59
126.22
122.94
122.26
121.23
118.27
115.88
109.96
70.33
f1 (ppm)

NT09:

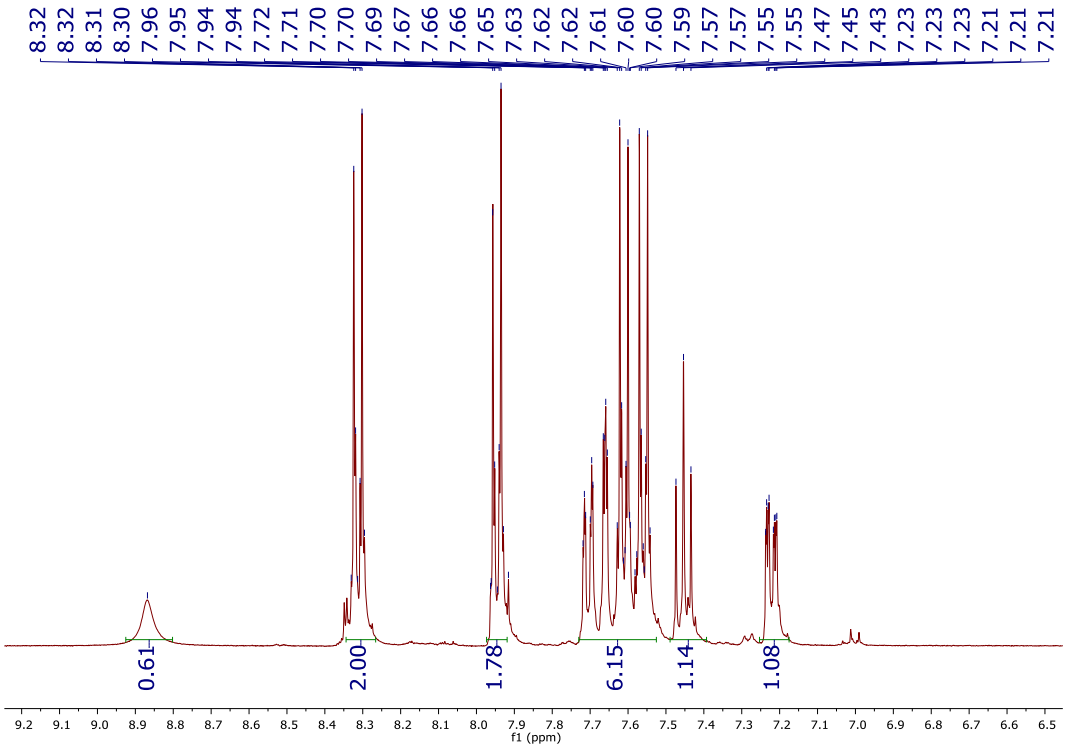
8.32 8.32 8.31 8.30 7.96 7.95 7.94 7.94 7.72 7.71 7.70 7.70 7.69 7.67 7.66 7.66 7.65 7.63 7.62 7.62 7.61 7.60 7.60 7.59 7.57 7.57 7.55 7.55 7.47 7.45 7.43 7.23 7.23 7.23 7.21 7.21 7.21
0.61
2.00
1.78
6.15
1.14
1.08
f1 (ppm)

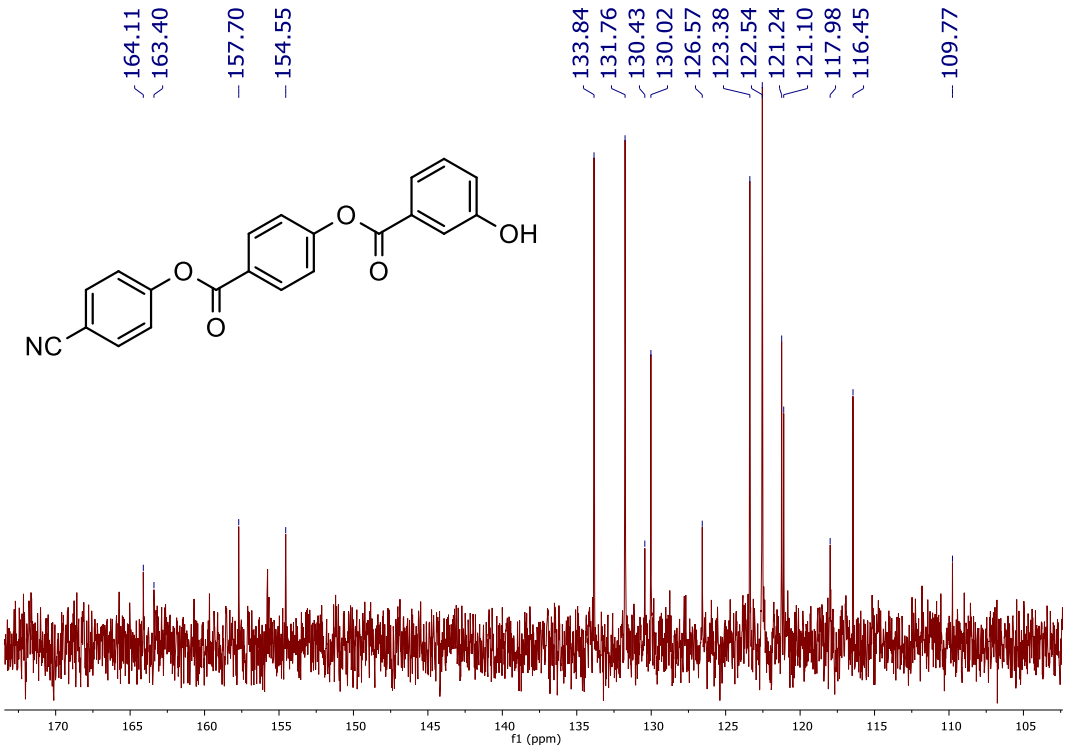
164.11
163.40
157.70
154.55
133.84
131.76
130.43
130.02
126.57
123.38
122.54
121.24
121.10
117.98
116.45
109.77
NC
O
O
O
O
OH
f1 (ppm)

NT10:

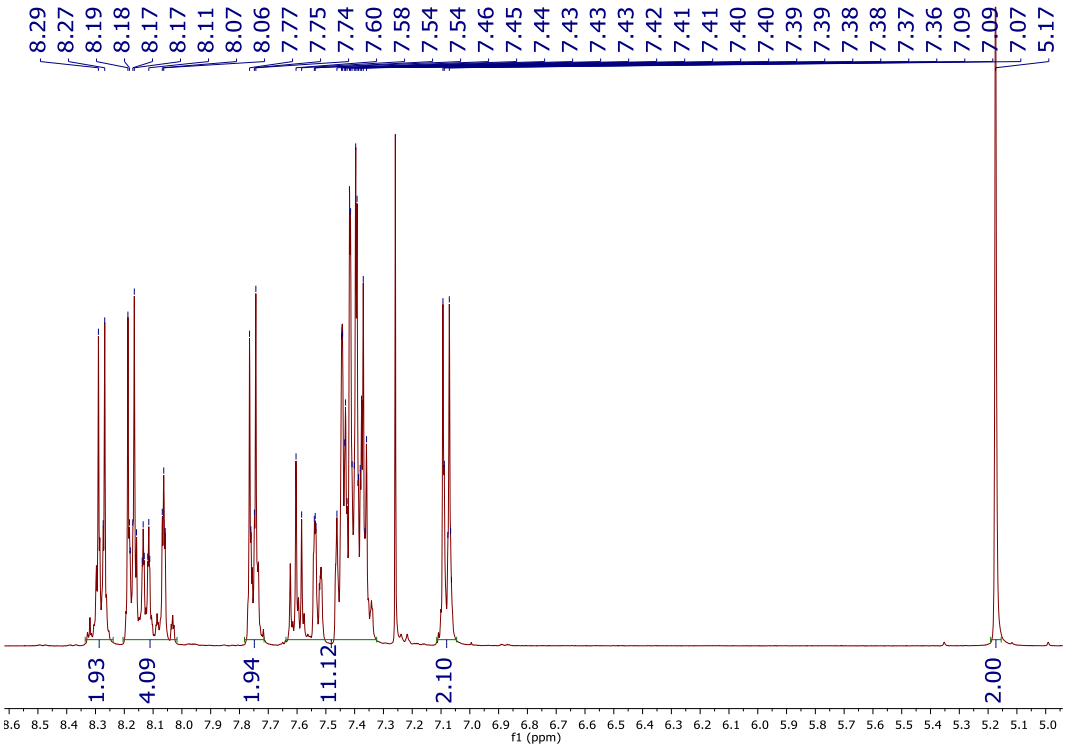
8.29
8.27
8.19
8.18
8.17
8.17
8.11
8.07
8.06
7.77
7.75
7.74
7.60
7.58
7.54
7.54
7.46
7.45
7.44
7.43
7.43
7.43
7.42
7.41
7.41
7.40
7.40
7.39
7.39
7.38
7.38
7.37
7.36
7.09
7.09
7.07
5.17
1.93
4.09
1.94
11.12
2.10
2.00
f1 (ppm)

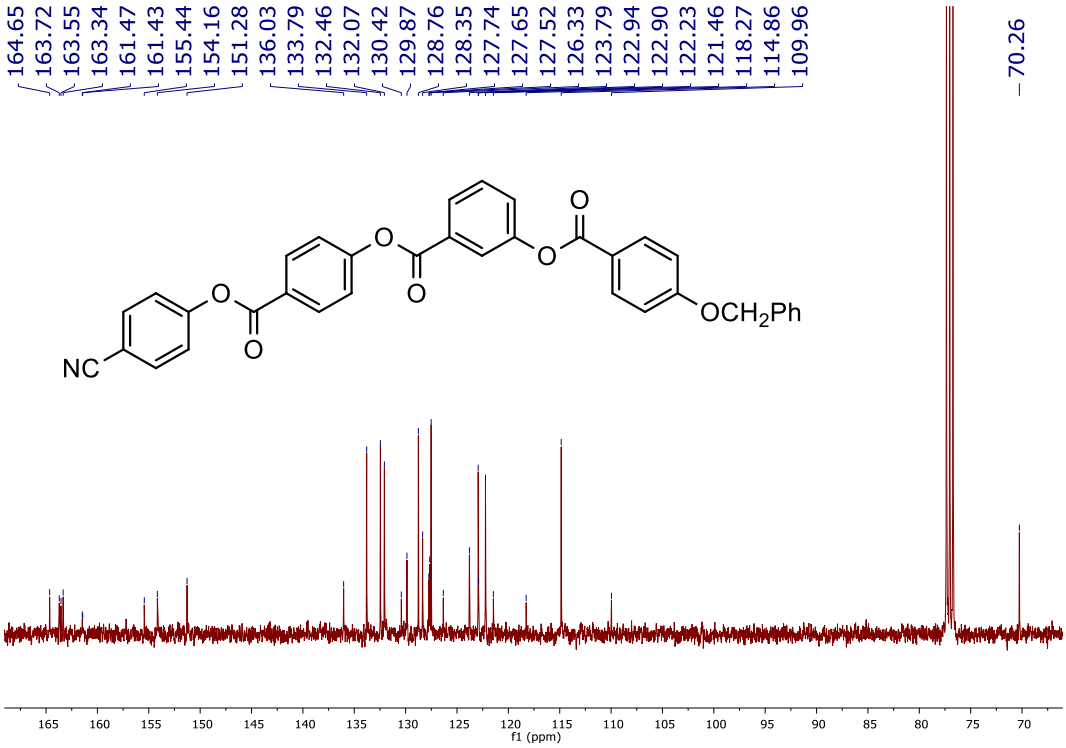
164.65
163.72
163.55
163.34
161.47
161.43
155.44
154.16
151.28
136.03
133.79
132.46
132.07
130.42
129.87
128.76
128.35
127.74
127.65
127.52
126.33
123.79
122.94
122.90
122.23
121.46
118.27
114.86
109.96
70.26
O
O
O
O
O
O
NC
OCH2Ph
f1 (ppm)

NT11:

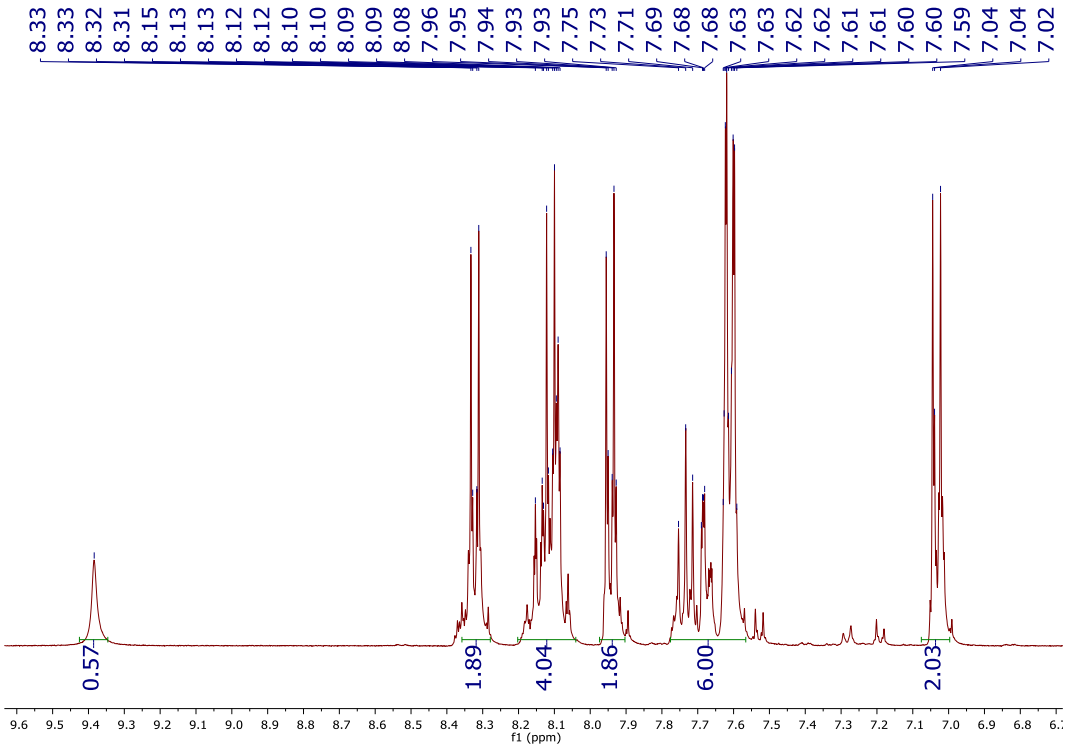
8.33
8.33
8.32
8.31
8.15
8.13
8.13
8.12
8.12
8.10
8.10
8.09
8.09
8.08
7.96
7.95
7.94
7.93
7.93
7.75
7.73
7.71
7.69
7.68
7.68
7.63
7.63
7.62
7.62
7.61
7.61
7.60
7.60
7.59
7.04
7.04
7.02
0.57
1.89
4.04
1.86
6.00
2.03
f1 (ppm)

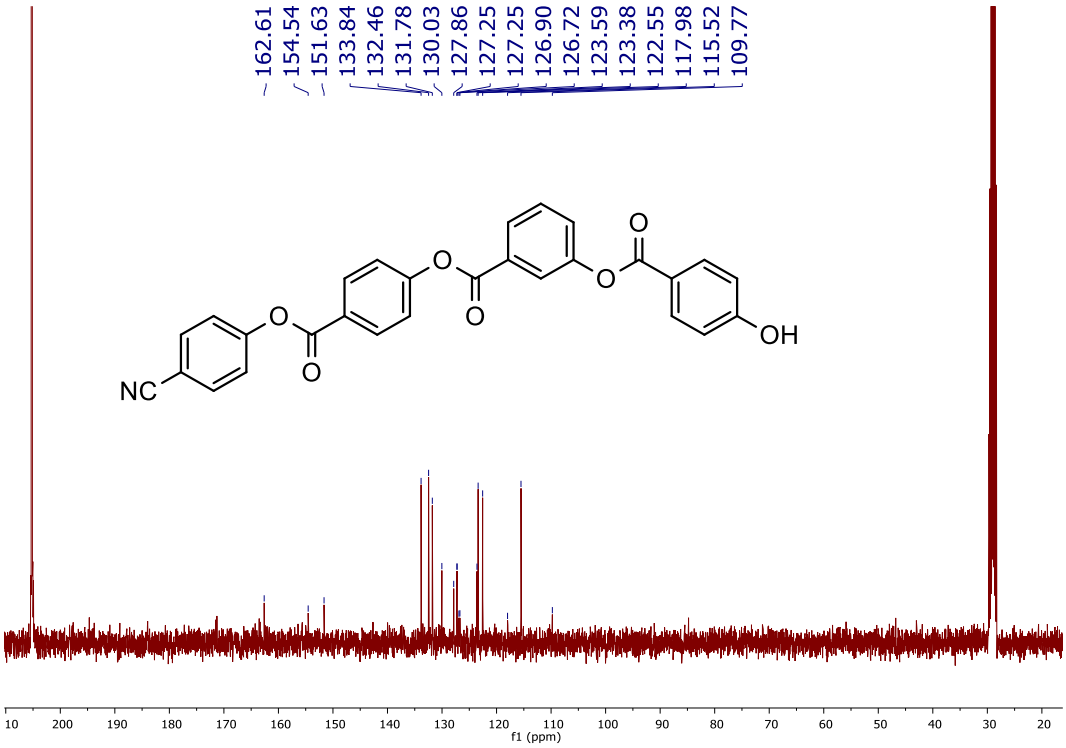
162.61
154.54
151.63
133.84
132.46
131.78
130.03
127.86
127.25
127.25
126.90
126.72
123.59
123.38
122.55
117.98
115.52
109.77
O
O
O
O
O
O
NC
OH
f1 (ppm)

NT12:

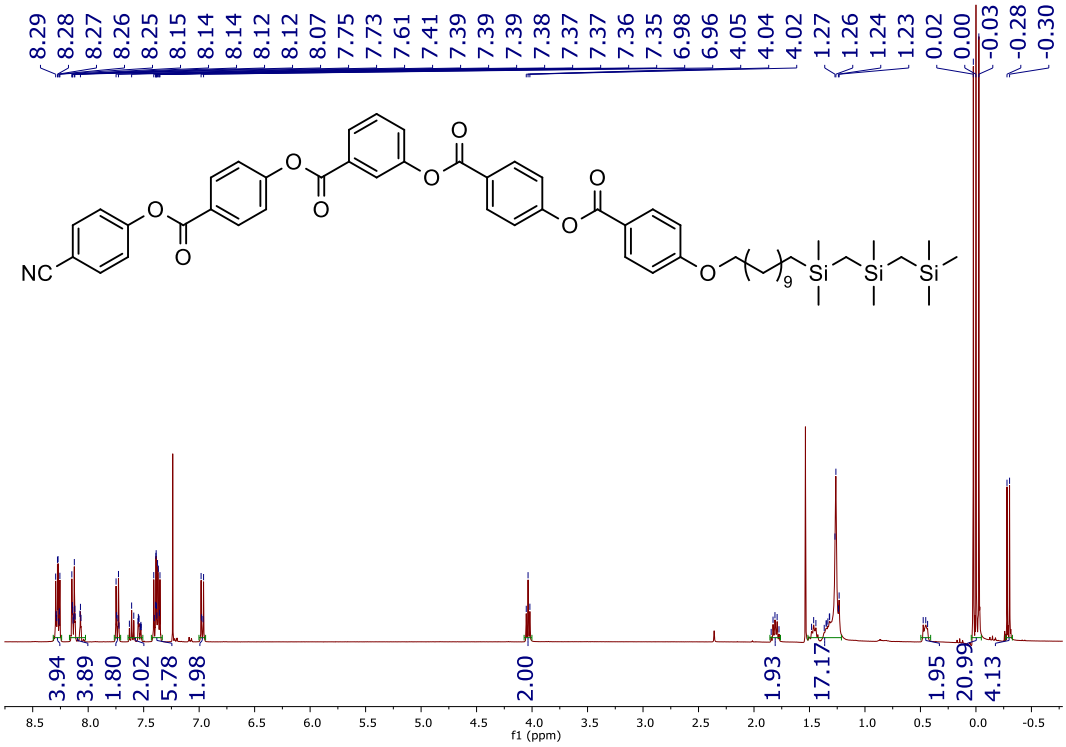
8.29 8.28 8.27 8.26 8.25 8.15 8.14 8.14 8.12 8.12 8.07 7.75 7.73 7.61 7.41 7.39 7.39 7.39 7.38 7.37 7.37 7.36 7.35 6.98 6.96 4.05 4.04 4.02 1.27 1.26 1.24 1.23 0.02 0.00 -0.03 -0.28 -0.30
NC
O
Si
9
3.94 3.89 1.80 2.02 5.78 1.98 2.00 1.93 17.17 1.95 20.99 4.13
8.5 8.0 7.5 7.0 6.5 6.0 5.5 5.0 4.5 4.0 3.5 3.0 2.5 2.0 1.5 1.0 0.5 0.0 -0.5
f1 (ppm)

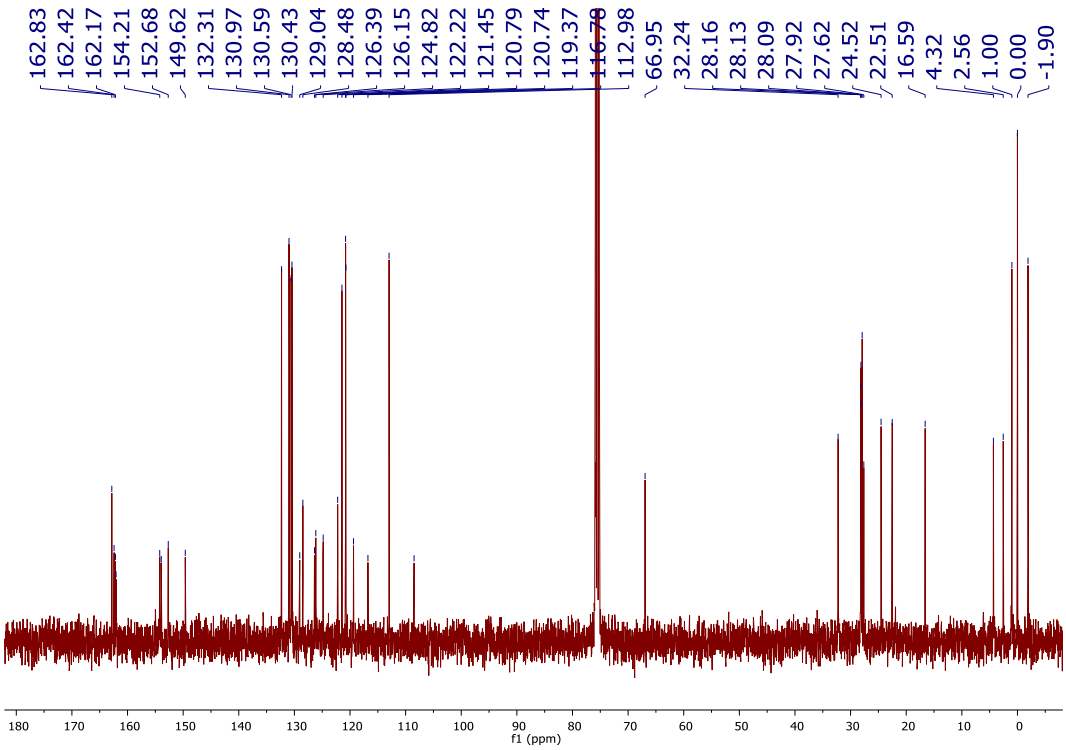
162.83 162.42 162.17 154.21 152.68 149.62 132.31 130.97 130.59 130.43 129.04 128.48 126.39 126.15 124.82 122.22 121.45 120.79 120.74 119.37 116.70 112.98 66.95 32.24 28.16 28.13 28.09 27.92 27.62 24.52 22.51 16.59 4.32 2.56 1.00 0.00 -1.90
180 170 160 150 140 130 120 110 100 90 80 70 60 50 40 30 20 10 0
f1 (ppm)

FT-IR spectra

NT01:

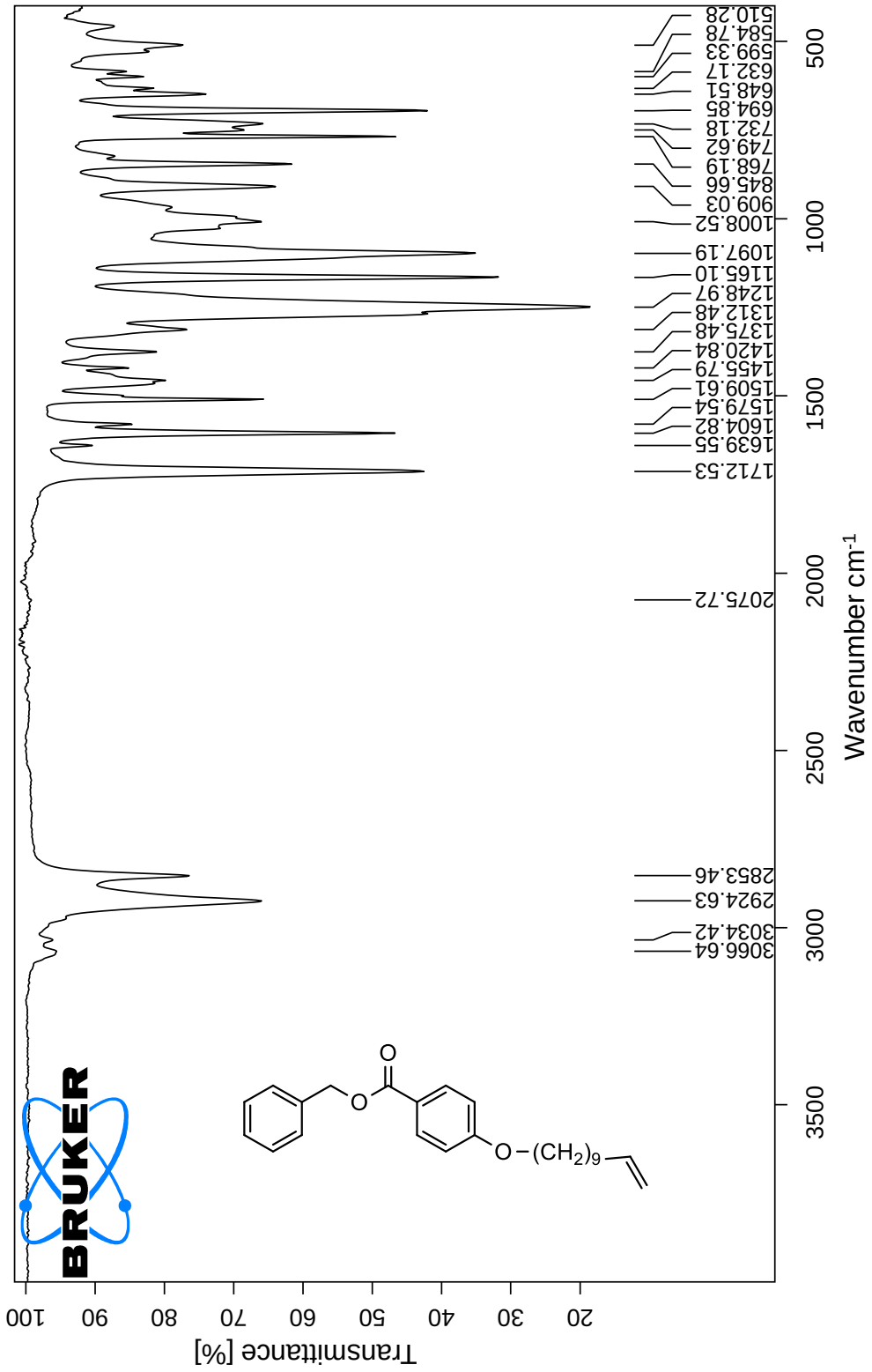

NT02:

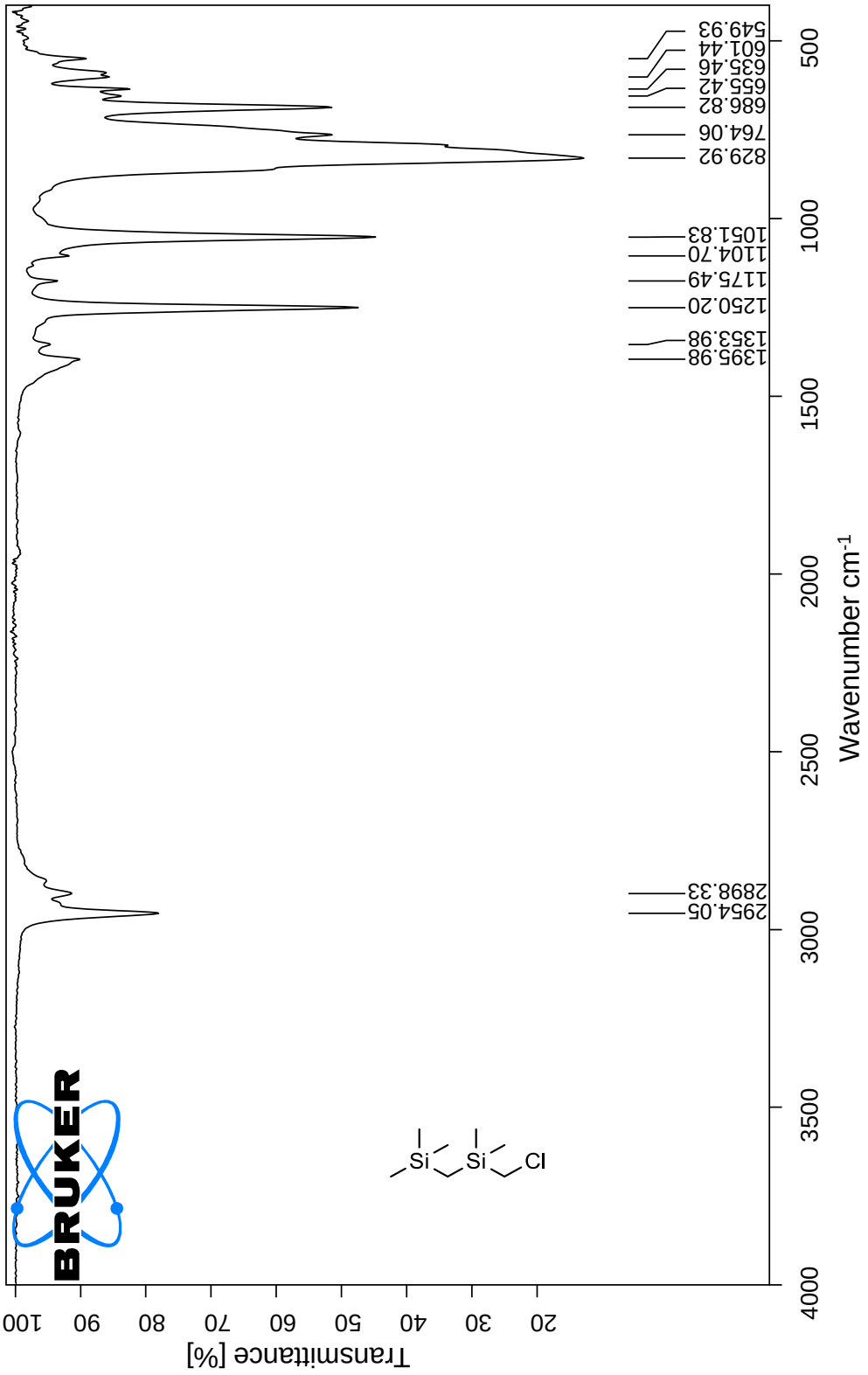
Transmittance [%]
100
90
80
70
60
50
40
30
20
Wavenumber cm-1
4000
3500
3000
2500
2000
1500
1000
500
2954.05
2898.33
1395.98
1353.98
1250.20
1175.49
1104.70
1051.83
829.92
764.06
686.82
655.42
635.46
601.44
549.93
Si
Si
Cl
BRUKER

NT03:

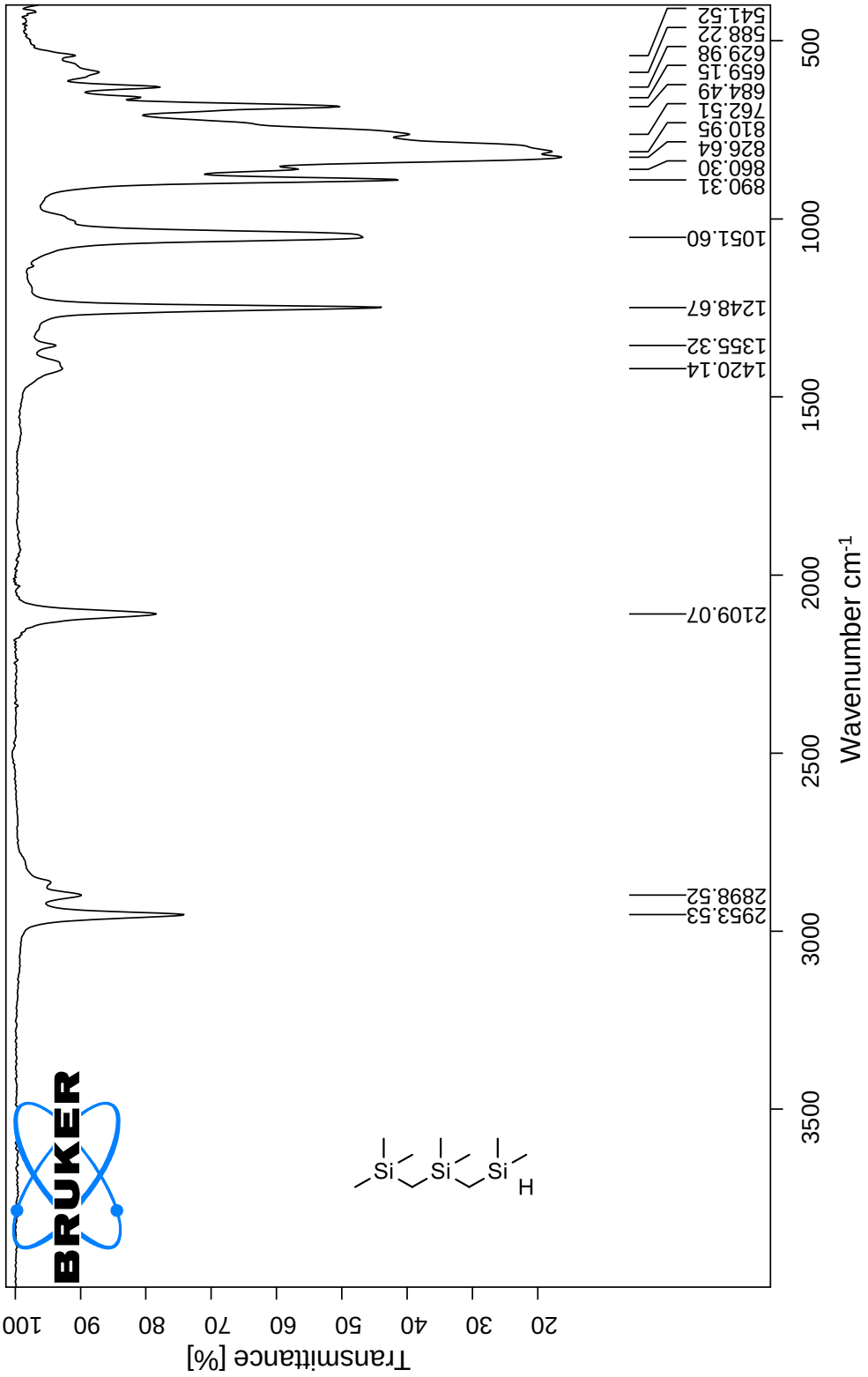
Transmittance [%]
20
30
40
50
60
70
80
90
100
Wavenumber cm-1
3500
3000
2500
2000
1500
1000
500
2953.53
2898.52
2109.07
1420.14
1355.32
1248.67
1051.60
890.31
860.30
826.64
810.95
762.51
684.49
659.15
629.98
588.22
541.52
Si
Si
Si
H
BRUKER

NT04:

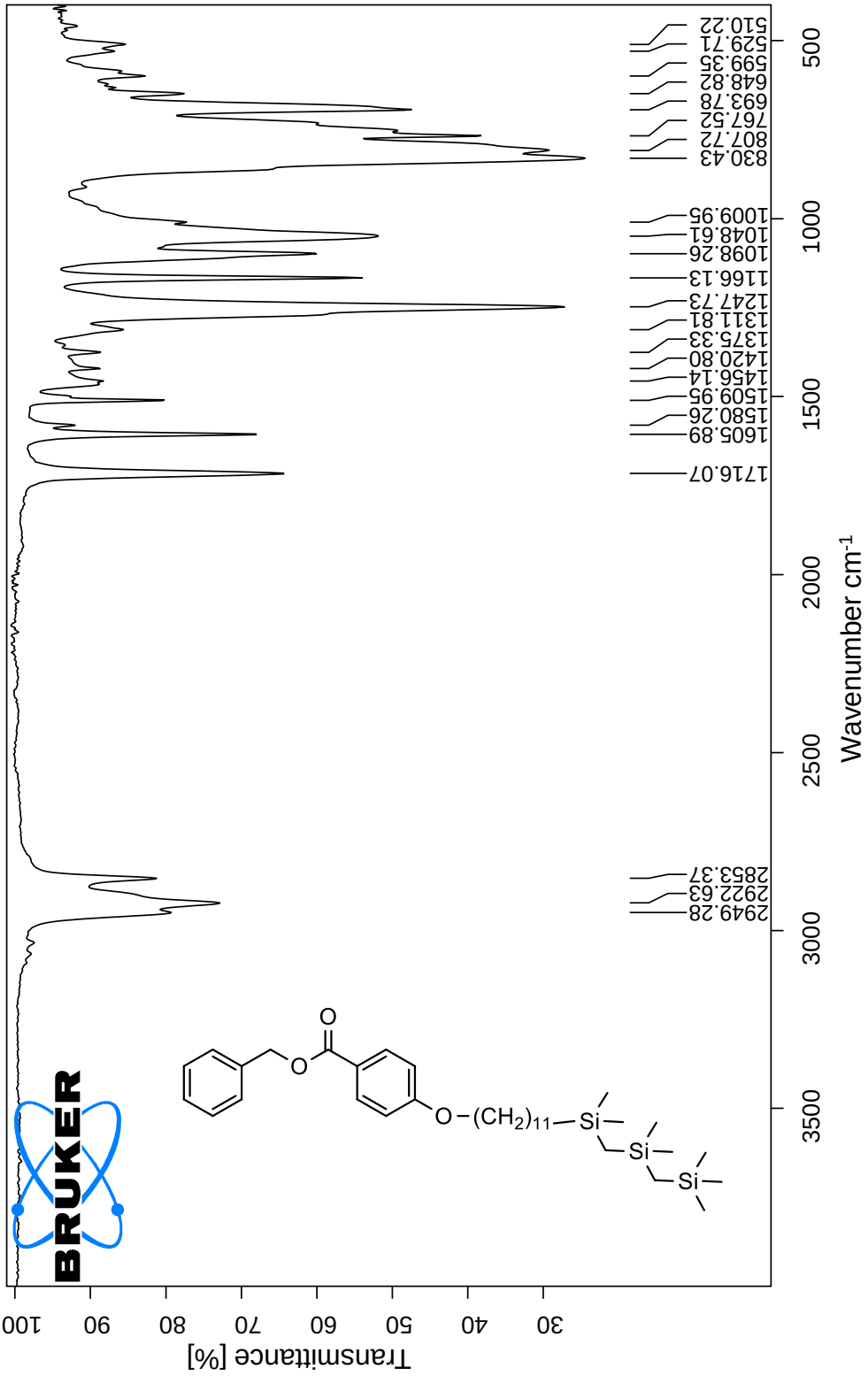
Transmittance [%]
100
90
80
70
60
50
40
30
Wavenumber cm-1
3500
3000
2500
2000
1500
1000
500
2853.37
2922.63
2949.28
1716.07
1605.89
1580.26
1509.95
1456.14
1420.80
1375.33
1311.81
1247.73
1166.13
1098.26
1048.61
1009.95
830.43
807.72
767.52
693.78
648.82
599.35
529.71
510.22
BRUKER
O
O
O
O
(CH2)11
Si
Si
Si

NT05:

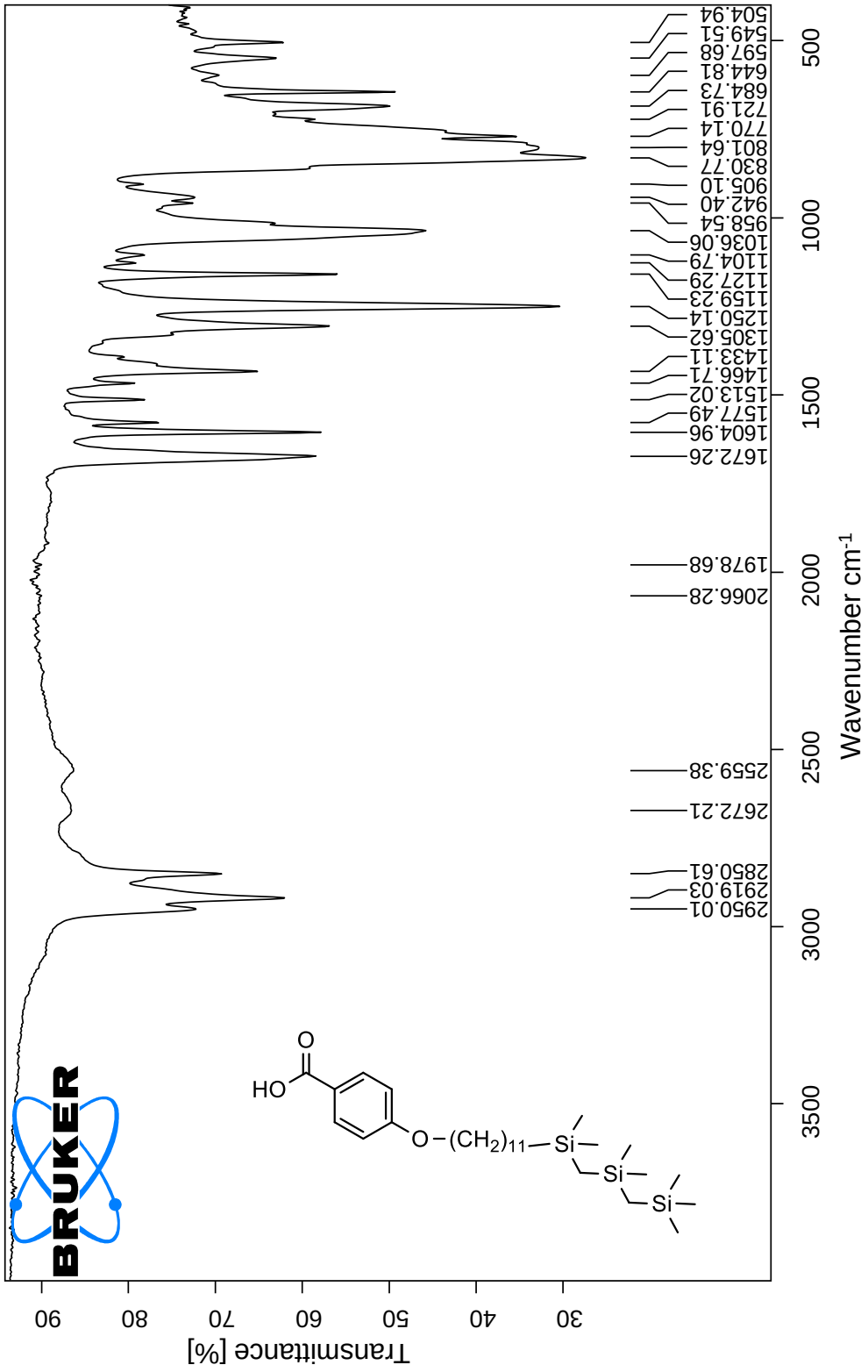
Transmittance [%]
30
40
50
60
70
80
90
Wavenumber cm-1
3500
3000
2500
2000
1500
1000
500
2950.01
2919.03
2850.61
2672.21
2559.38
2066.28
1978.68
1672.26
1604.96
1577.49
1513.02
1466.71
1433.11
1305.62
1250.14
1159.23
1127.29
1104.79
1036.06
958.54
942.40
905.10
830.77
801.64
770.14
721.91
684.73
644.81
597.68
549.51
504.94
HO
O
O–(CH2)11–Si
Si
Si
BRUKER

NT06:

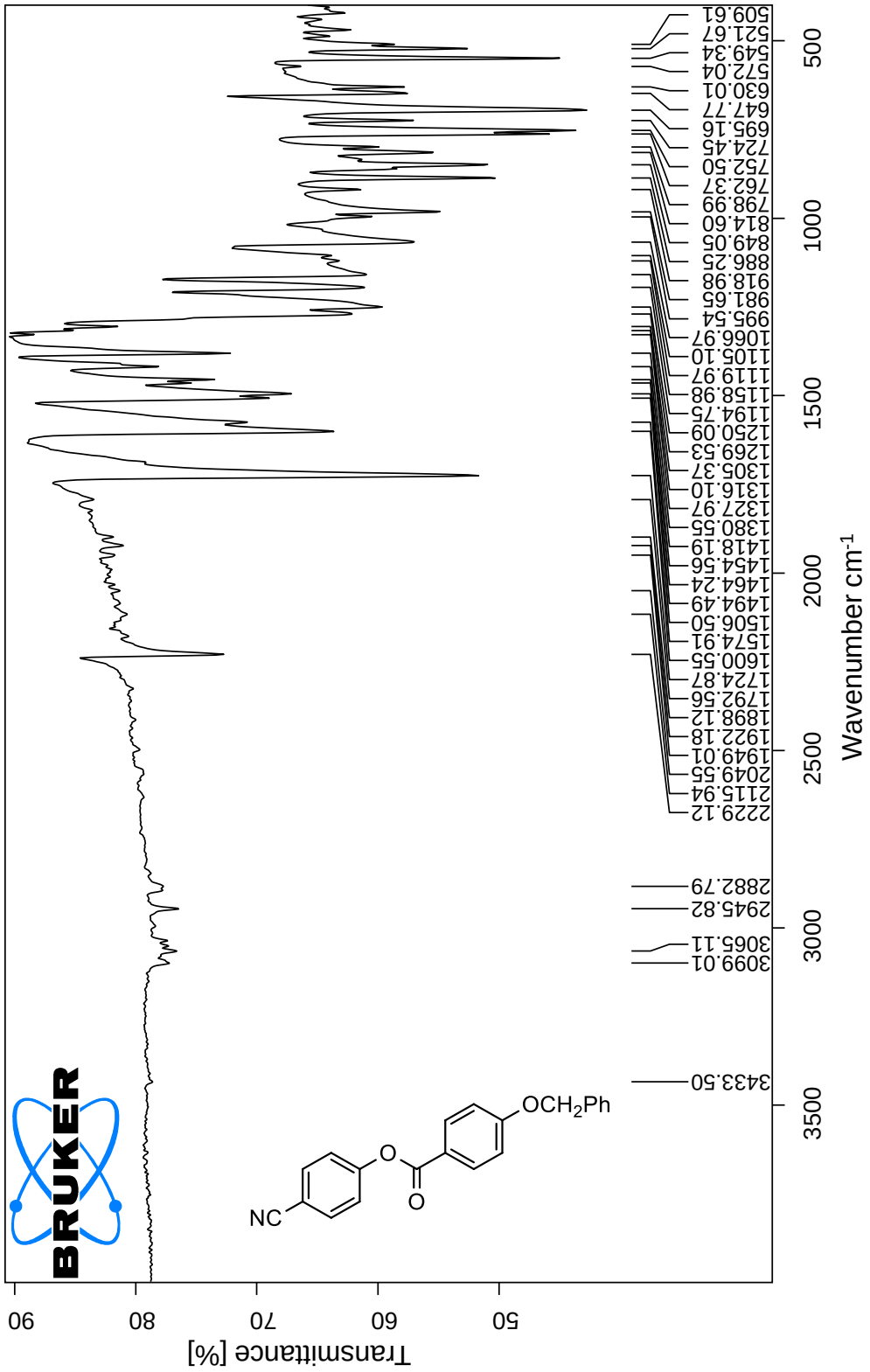
Transmittance [%]
90
80
70
60
50
Wavenumber cm-1
3500
3000
2500
2000
1500
1000
500
3433.50
3099.01
3065.11
2945.82
2882.79
2229.12
2115.94
2049.55
1949.01
1922.18
1898.12
1792.56
1724.87
1600.55
1574.91
1506.50
1494.49
1464.24
1454.56
1418.19
1380.55
1327.97
1316.10
1305.37
1269.53
1250.09
1194.75
1158.98
1119.97
1105.10
1066.97
995.54
981.65
918.98
886.25
849.05
814.60
798.99
762.37
752.50
724.45
695.16
647.77
630.01
572.04
549.34
521.67
509.61
NC
O
O
OCH2Ph
BRUKER

NT07:

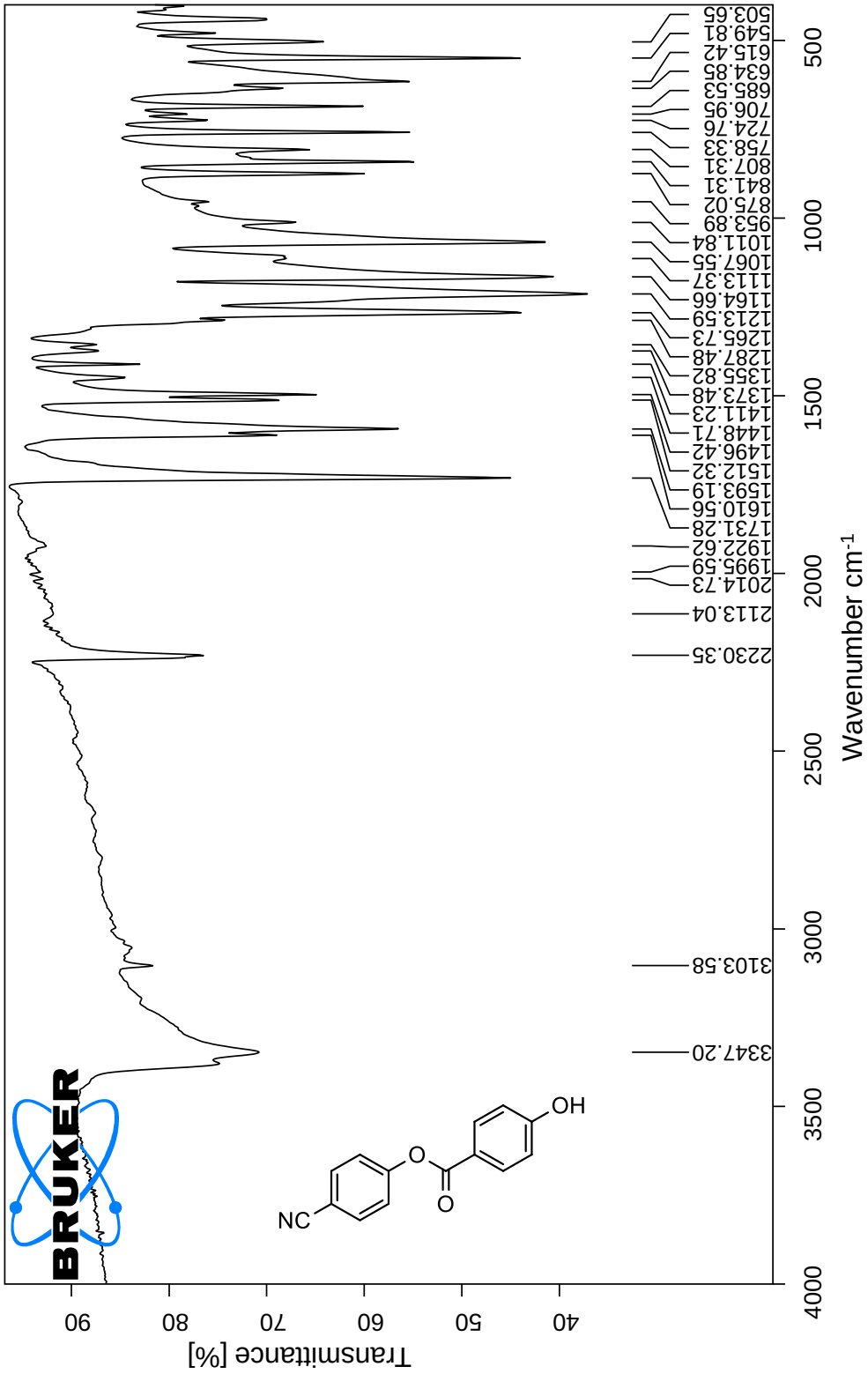
BRUKER
NC
O
O
OH
Transmittance [%]
Wavenumber cm-1
4000
3500
3000
2500
2000
1500
1000
500
3347.20
3103.58
2230.35
2113.04
2014.73
1995.59
1922.62
1731.28
1610.56
1593.19
1512.32
1496.42
1448.71
1411.23
1373.48
1355.82
1287.48
1265.73
1213.59
1164.66
1113.37
1067.55
1011.84
953.89
875.02
841.31
807.31
758.33
724.76
706.95
685.53
634.85
615.42
549.81
503.65

NT08:

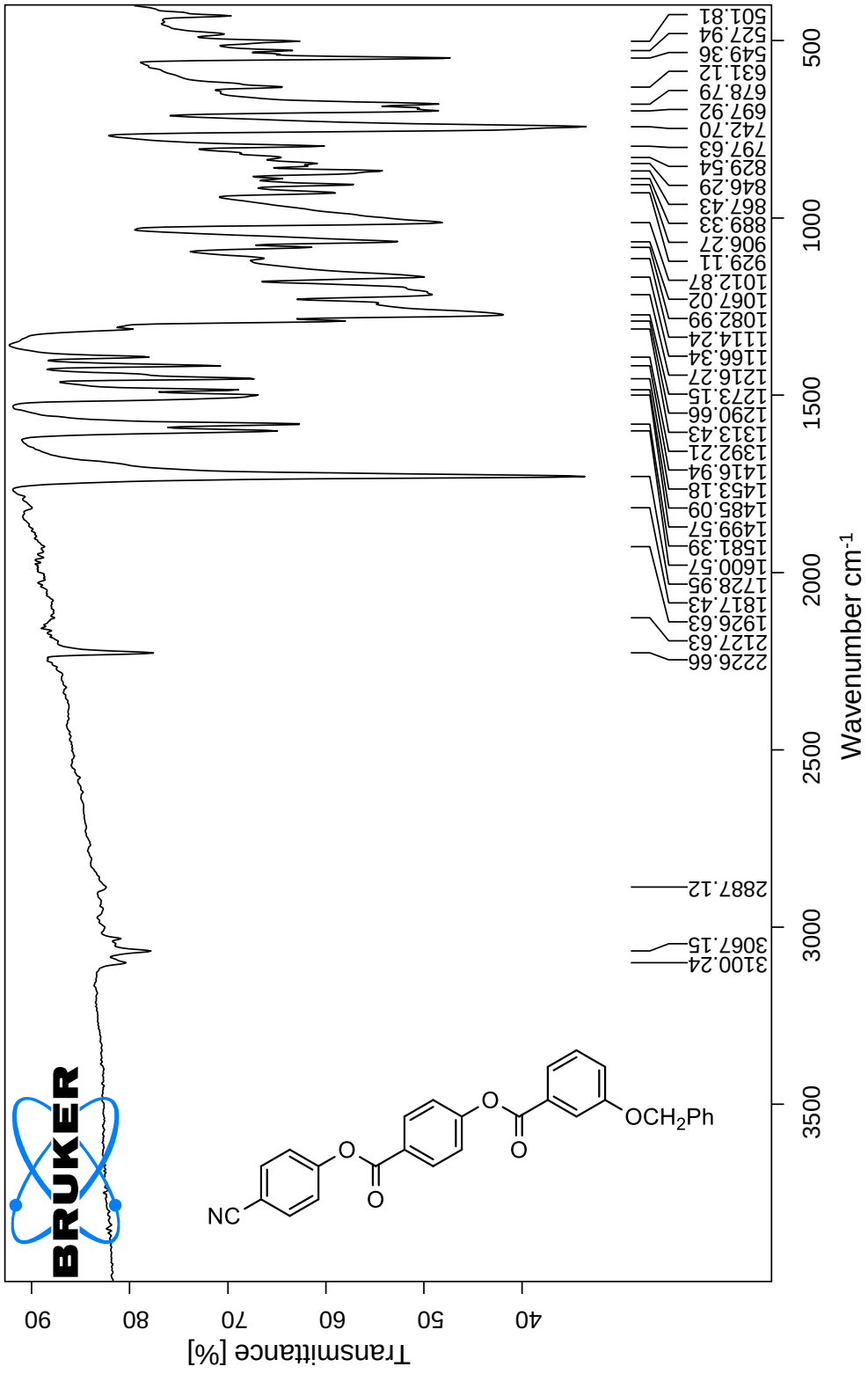
Transmittance [%]
90
80
70
60
50
40
Wavenumber cm-1
3500
3000
2500
2000
1500
1000
500
3100.24
3067.15
2887.12
2226.66
2127.63
1926.63
1817.43
1728.95
1600.57
1581.39
1499.57
1485.09
1453.18
1416.94
1392.21
1313.43
1290.66
1273.15
1216.27
1166.34
1114.24
1082.99
1067.02
1012.87
929.11
906.27
889.33
867.43
846.29
829.54
797.63
742.70
697.92
678.79
631.12
549.36
527.94
501.81
NC
O
O
O
O
OCH2Ph
BRUKER

NT09:

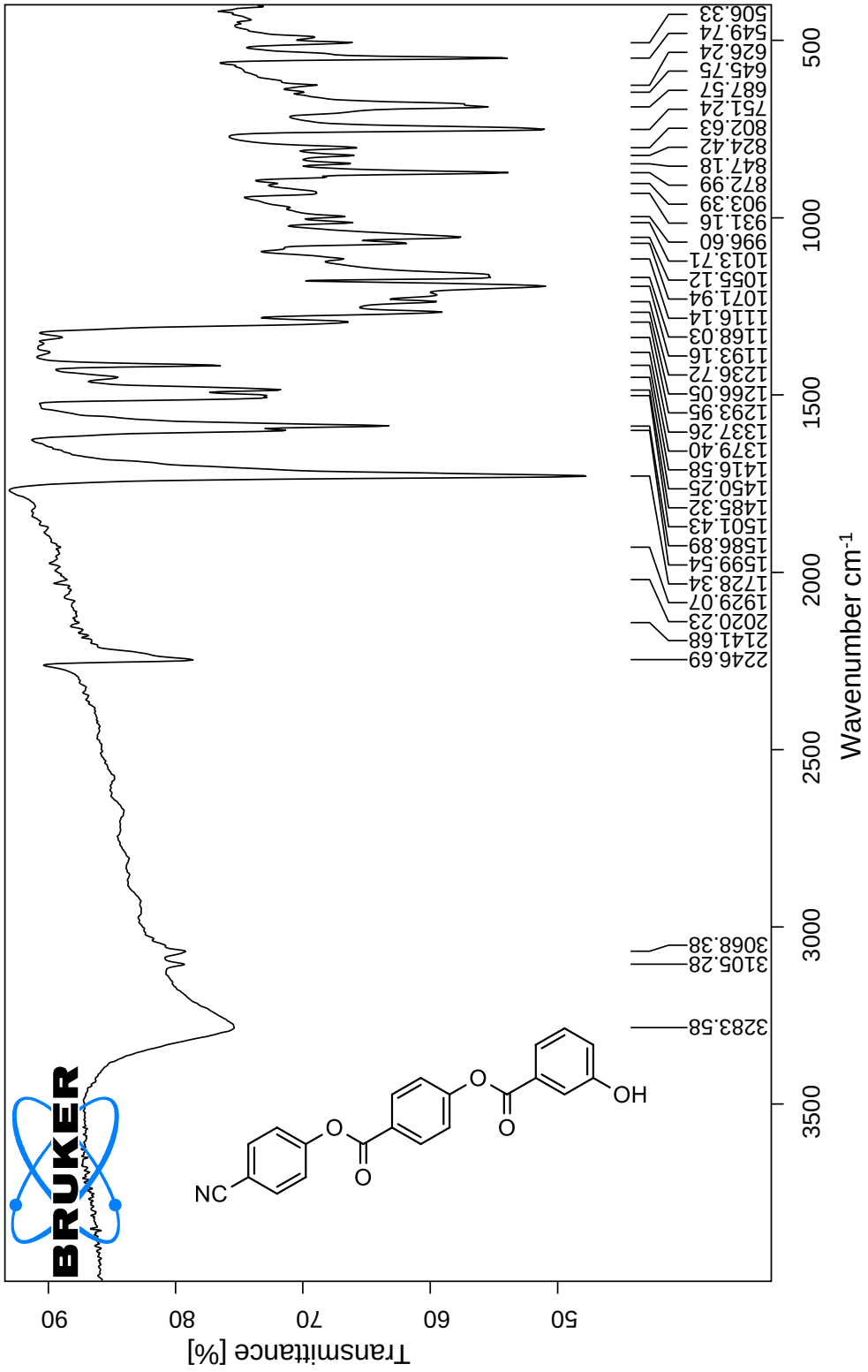
Transmittance [%]
90
80
70
60
50
Wavenumber cm-1
3500
3000
2500
2000
1500
1000
500
3283.58
3105.28
3068.38
2246.69
2141.68
2020.23
1929.07
1728.34
1599.54
1586.89
1501.43
1485.32
1450.25
1416.58
1379.40
1337.26
1293.95
1266.05
1236.72
1193.16
1168.03
1116.14
1071.94
1055.12
1013.71
996.60
931.16
903.39
872.99
847.18
824.42
802.63
751.24
687.57
645.75
626.24
549.74
506.33
NC
O
O
O
O
HO
BRUKER

NT10:

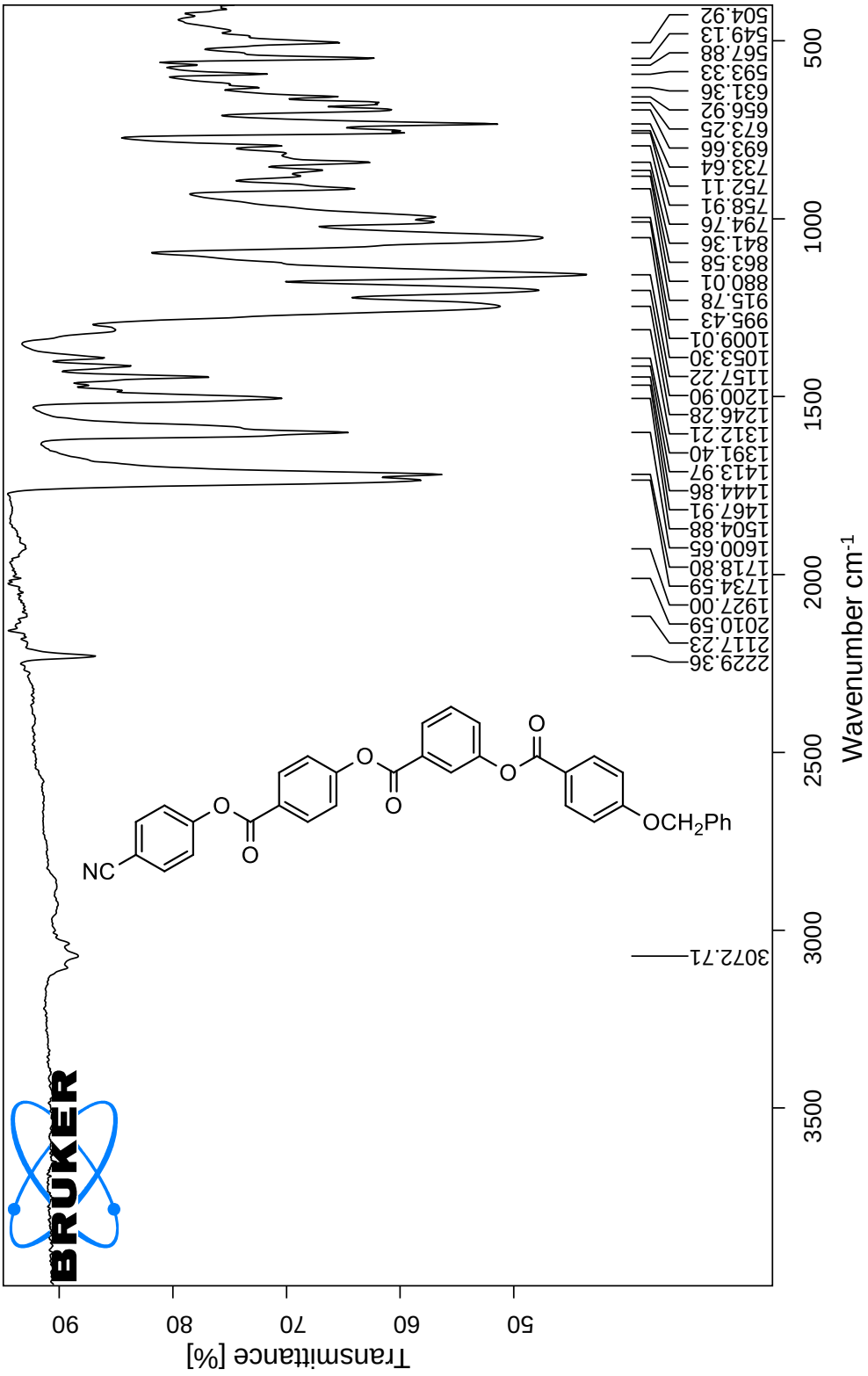
Transmittance [%]
90
80
70
60
50
Wavenumber cm-1
3500
3000
2500
2000
1500
1000
500
3072.71
2229.36
2117.23
2010.59
1927.00
1734.59
1718.80
1600.65
1504.88
1467.91
1444.86
1413.97
1391.40
1312.21
1246.28
1200.90
1157.22
1053.30
1009.01
995.43
915.78
880.01
863.58
841.36
794.76
758.91
752.11
733.64
693.66
673.25
656.92
631.36
593.33
567.88
549.13
504.92
NC
OCH2Ph
O
BRUKER

NT11:

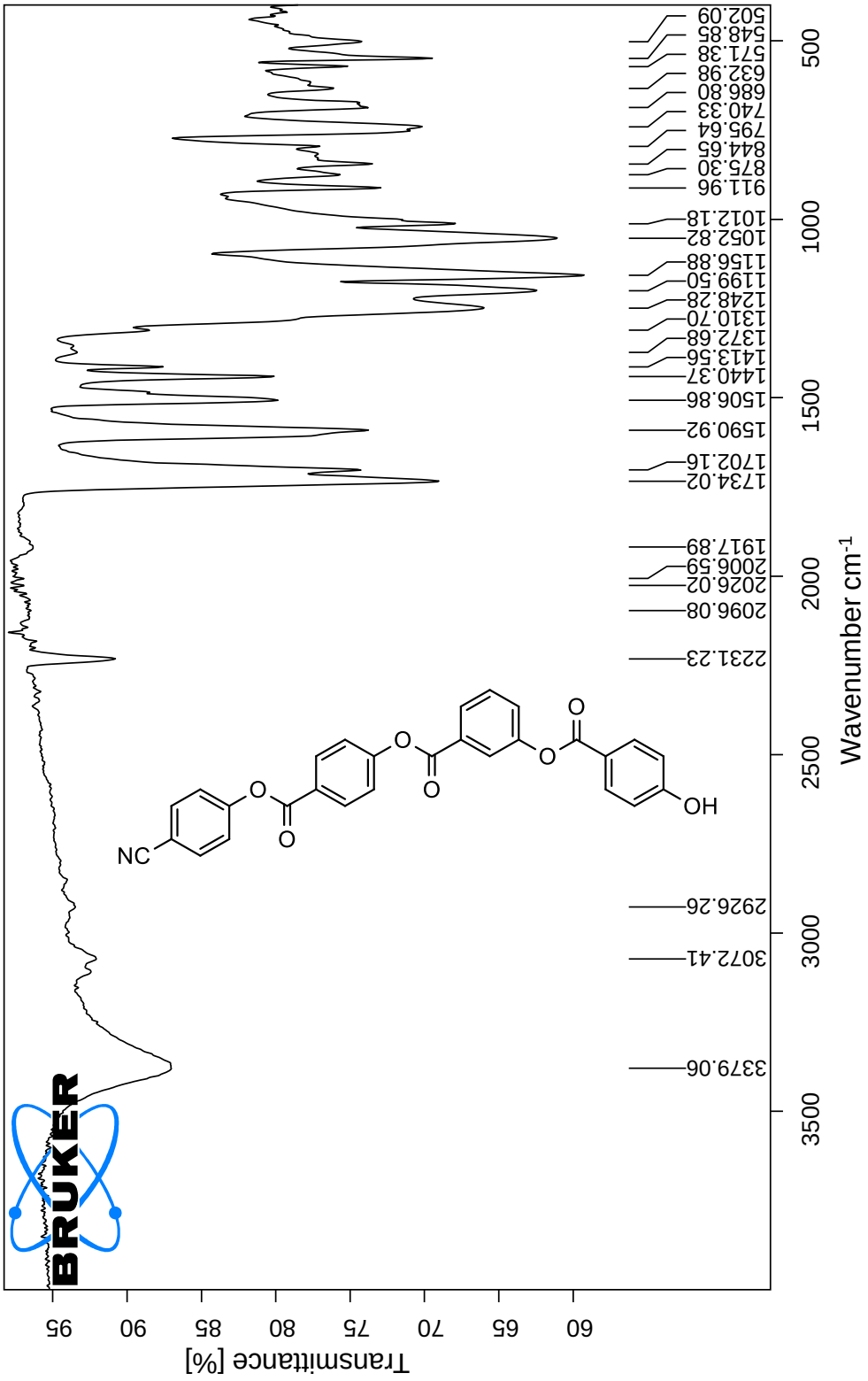
Transmittance [%]
95
90
85
80
75
70
65
60
Wavenumber cm-1
3500
3000
2500
2000
1500
1000
500
3379.06
2926.26
3072.41
2231.23
2096.08
2026.02
2006.59
1917.89
1734.02
1702.16
1590.92
1506.86
1440.37
1413.56
1372.68
1310.70
1248.28
1199.50
1156.88
1052.82
1012.18
911.96
875.30
844.65
795.64
740.33
686.80
632.98
571.38
548.85
502.09
NC
O
O
O
O
O
O
OH
BRUKER

NT12:

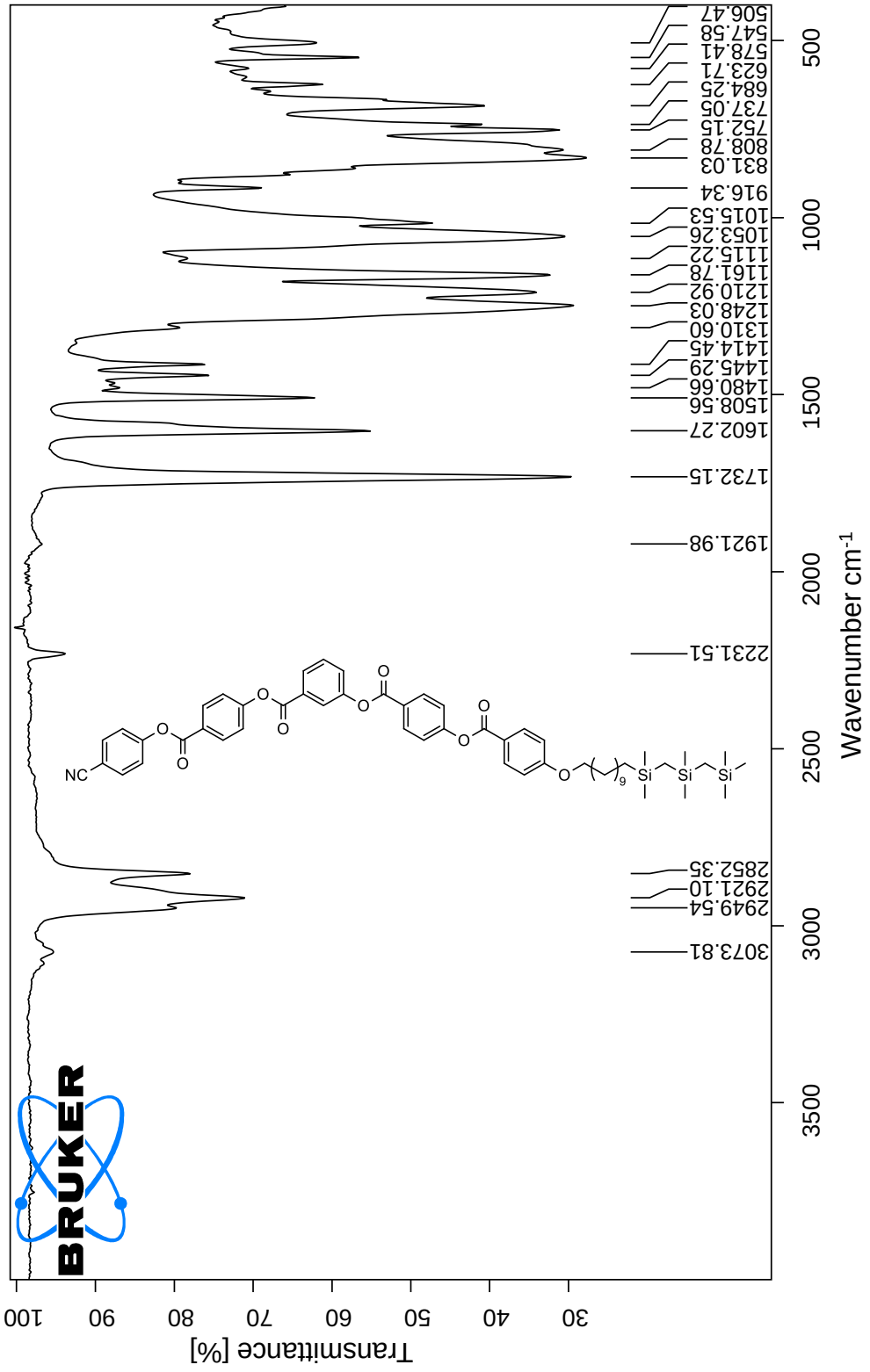
Transmittance [%]
100
90
80
70
60
50
40
30
Wavenumber cm-1
3500
3000
2500
2000
1500
1000
500
3073.81
2949.54
2921.10
2852.35
2231.51
1921.98
1732.15
1602.27
1508.56
1480.66
1445.29
1414.45
1310.60
1248.03
1210.92
1161.78
1115.22
1053.26
1015.53
916.34
831.03
808.78
752.15
737.05
684.25
623.71
578.41
547.58
506.47
NC
O
Si
9